UNIVERSITY OF BIRMINGHAM

Studies into the Ion Exchange and Intercalation Properties of $AlH_2P_3O_{10}\cdot 2H_2O$

by

Thomas P. Marsh

A thesis submitted to
The University of Birmingham
for the degree of
Doctor of Philosophy

The School of Chemistry

College of Engineering and Physical Sciences

The University of Birmingham

April 2011

Abstract

This thesis describes investigations performed into the ion exchange and intercalation properties of aluminium triphosphate, $AlH_2P_3O_{10}\cdot 2H_2O$ (AlTP). Materials synthesised were characterised using a variety of techniques, including powder neutron and X-ray diffraction, Rietveld analysis, thermogravimetic analysis and environmental scanning microscopy.

Monovalent ion exchange (with Na, K, Rb, Cs and Ag) gave complete and facile exchange of the host's hydrogen ions and gave crystalline products. A thermodynamically favoured phase with two waters of crystallisation was observed for all monovalent cation exchanges. The alkali metals also showed metastable phases with differing numbers of waters of crystallisation, four for Na and one for K, Rb and Cs. Unit cells have been assigned to the exchanged phases, with all showing a more than doubling of the *a* parameter. Structural characterisation of the rubidium and caesium phases show this to be a result of a change of symmetry to C2/c causing adjacent layers to shift half a unit cell along [010] with respect to one another. Ion exchange with divalent cations (Cu, Mn, Zn, Ca and Sr) has also been shown to be possible, with phases showing altered XRD patterns and decomposition products.

Intercalation with a range of increasingly complex amines was found to be possible in AlTP. Multifunctional molecules, including amino acids, were also found to intercalate into AlTP, with evidence in the intercalation of 6-aminohexanoic acid that interactions between intercalated molecules within the inter-lamellar region are possible. Trends were found to be similar to other layered phosphates with respect to the amounts and angles of intercalation of simple monoamines and the effects of pK_b and sterics upon an amines ability to intercalate into AlTP. In addition, intercalation with silver exchanged AlTP was also found to be possible. This was able to intercalate several similar amines to AlTP, but showed its own unique intercalation properties including the ability to intercalate thiols.

Acknowledgements

Thanks must first go to my supervisor Dr. Adrian Wright for his help and support (and putting up with me) for the past 4½ years.

I would like to thank many members of the 5th floor for not only making it an enjoyable place to work, but also somewhere where help was never hard to find. Many thanks to my 'predecessors' Dr. Phil Chater, for always being willing to share his genius, and the starbucks gang Dr. Eirin McBride, and particularly Dr. Jenny Readman and Dr. Matt Cave for all their help with so many things early on, and for teaching me the answer to most things is a hot chocolate with cream.

Thanks also to many of the current members of the floor. Yasmin, my main gofer whilst writing this and who was always around to help chew over a problem and Evin, who despite constant attempts at usurping my lab was always willing to help run the odd ESEM image I'd forgotten to, and for the pair of them always willing to have fun at my expense. Ben, the hardest working person I know, for putting up with all the (good natured) stick I've given him and still being willing to lend a helping hand. Finally the 'newbie's' Julie, my other gofer, Mariana and Tom, and Annabelle because she insisted and made me cakes.

Many thanks to Dr. Jackie Deans, whose door was always open and who was always willing to give help and advice on the new instruments at the drop of a hat, or just stop for a friendly chat.

And finally my family and outside uni friends, particularly Amy, Nicola and Chris (and his mom) for their continued support and Dr. Frankie Yates for lots of encouragement and help during my write up.

Abbreviations

α-ZrP	α-Zirconium Phosphate, α-$Zr(HPO_4)_2 \cdot H_2O$
AlTP	Aluminium Triphosphate, $AlH_2P_3O_{10} \cdot 2H_2O$
AlTP-Ag	Silver exchanged Aluminium Triphosphate, $AlAg_2P_3O_{10} \cdot 2H_2O$
AlTP-Cs	Caesium exchanged Aluminium Triphosphate, $AlCs_2P_3O_{10} \cdot 2H_2O$
AlTP-K	Potassium exchanged Aluminium Triphosphate, $AlK_2P_3O_{10} \cdot 2H_2O$
AlTP-K·1	Potassium exchanged Aluminium Triphosphate, $AlK_2P_3O_{10} \cdot H_2O$
AlTP-Na	Sodium exchanged Aluminium Triphosphate, $AlNa_2P_3O_{10} \cdot 2H_2O$
AlTP-Na·4	Sodium exchanged Aluminium Triphosphate, $AlNa_2P_3O_{10} \cdot 4H_2O$
AlTP-Rb	Rubidium exchanged Aluminium Triphosphate, $AlRb_2P_3O_{10} \cdot 2H_2O$
ESEM	Environmental Scanning Electron Microscopy
GSAS	General Structure Analysis System
MTP	Metal (III) Triphosphate, $M^{III}H_2P_3O_{10} \cdot 2H_2O$
TGA	Thermogravimetric Analysis
XRD	X-ray Diffraction

Contents

Chapter 1

Introduction

There is much current interest in inorganic host materials capable of accommodating ions and molecules within their structure for applications such as ion entrapment, catalysis and drug delivery. This thesis describes a detailed study into a family of layered triphosphate materials, encompassing their synthesis, structure, ion exchange and intercalation properties.

1.1 Introduction to Phosphate Materials

'Phosphate' is the term used to describe oxyanions of phosphorus (V), which can range from simple orthophosphate units, to chains and rings, through to infinite networks. There are a large number of known phosphates both synthesised and found as natural minerals in rocks and living organisms. The diversity and chemistry of phosphates results from variations of the phosphate species, their ability to coordinate with a large number of cations and their tolerance for other anions or molecules, such as water or ammonia.

Three main classes of phosphates exist: monophosphates, condensed phosphates and oxyphosphates. Monophosphates, also known as orthophosphates, are salts derived from phosphoric acid (H_3PO_4). They are characterised by isolated PO_4^{3-} anions groups, consisting of four oxygens atoms surrounding a central phosphorus in a tetrahedral arrangement. Condensed phosphate species contain a condensed phosphoric anion which has at least one

P-O-P linkage; these types of phosphate are described in more detail in Section 1.2. Oxyphosphates, which were incorrectly referred to as "basic phosphates" for a time, include oxygen atoms not belonging to the phosphate group in their crystal structure. The phosphoric anion is an isolated PO_4 tetrahedron in all such compounds reported to date, for example $Co(VO)_2(PO_4)_2$[1]. Oxyphosphates may therefore be defined as phosphates with a general formula containing an oxygen to phosphorus ratio greater than 4:1.

Phosphates are often comparable to solid silicates, this is largely due to both the phosphate anion (PO_4^{3-}) and silicate anion (SiO_4^{4-}) (also the sulphate (SO_4^{2-}) and perchlorate (ClO_4^-) anions) having similar tetrahedral configurations. Classical valency formulations show these XO_4^{n-} ions to form a series with decreasing amounts of covalent character going from chlorate to silicate. It is generally recognised that all four bonds within the tetrahedra are equivalent and modern theories describe the PO_4 group in terms of σ bonds formed through sp^3 hybridisation and π-bonding using the d orbitals.

Many phosphates are resistant to chemical attack and thermally stable to high temperatures, in excess of 1400 °C in some cases[2]. Such properties have lead to much interest and attention over the past 60 years, in many fields including dyes[3], detergents[4], fertilizers[5] and molecular sieves[6]. In recent years the interest has shifted to biomaterials[7], phosphate glasses[8], magnetic phosphates[9], ferroelectric properties in phosphates such as KH_2PO_4[10], non-linear optics in phosphates such as KTP[11] and the discovery of the first stoichiometric laser in the ultraphosphate family[12].

1.2 Condensed Phosphates

Condensed phosphates form an important and intricate part of phosphate chemistry. The chemistry of condensed phosphates, when compared to that of condensed silicates, is still relatively poorly understood. A condensed phosphate can be defined as any phosphoric anion

which contains one or more P-O-P bonds, or alternatively any phosphoric anion containing an oxygen to phosphorus ratio of less than 4:1. This ratio is a result of condensed phosphates being built up of basic PO_4 tetrahedra units. The P-O-P bonds can be formed in a variety of ways, the simplest of which is the elimination of water when combining two hydrogen monophosphates units, Figure 1.1.

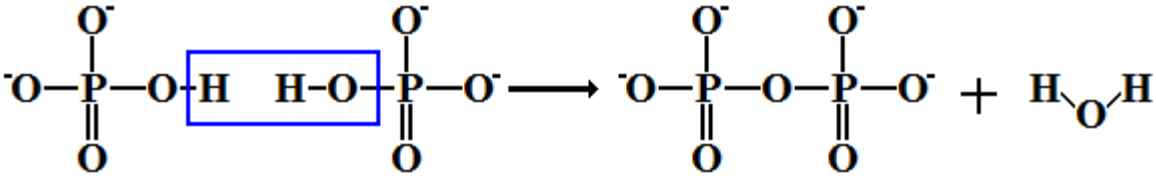

Figure 1.1 *Schematic representation of two monophosphates condensing to form a condensed phosphate*

This type of condensation is capable of generating large numbers of phosphoric anions, with numerous geometries, with the three main building units of condensed phosphates shown in Figure 1.2.

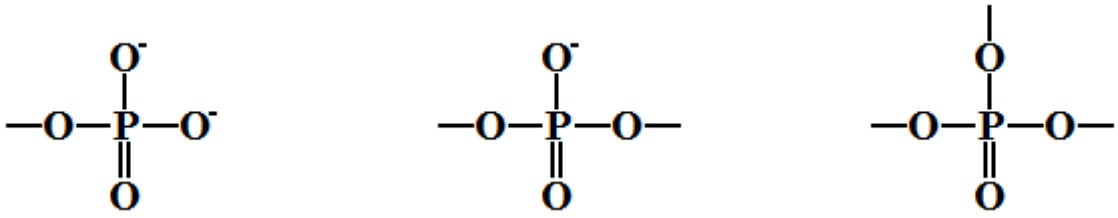

End Unit Middle Unit Branching Unit

Figure 1.2 *The three main building units of condensed phosphates*

These different phosphate environments can easily be distinguished by techniques such as ^{31}P NMR spectroscopy, or sometimes simply via their acidity. Combinations of the three units give rise to four main types of condensed phosphate:

1. *Finite chain phosphates*, built of linear linkages with the general formula $[P_nO_{3n+1}]^{(n+2)-}$. These have been isolated for n = 1 to 16, with the lower members of the series (n = 2 to 5) commonly labelled oligophosphates.

2. *Infinite chain phosphates* with the general formula $[(PO_3)_n]^{n-}$.
3. *Cyclic metaphosphates* also with general formula $[(PO_3)_n]^{n-}$, with $n \geq 3$. These phosphates often form P_nO_{3n} rings and are often referred to as cyclophosphates.
4. *Ultraphosphates.* These are a class of P_2O_5 rich phosphates containing branching units. P_4O_{10} is considered the ultimate ultraphosphate containing only branching units.

As mentioned in Section 1.1, the condensed phosphates are relatively stable to chemical attack, as they contain fully oxidised phosphorus atoms. They are, however, vulnerable to hydrolysing reactions. The condensed phosphate anion dominates most of the chemical and physical properties of these materials, but the cations present may play important roles, for example influencing the nature of reactions occurring during thermal decomposition leading to variations in the anionic products formed from a given phosphorus anion.

1.2.1 Structure Types

When combined with metal cations, the four types of condensed phosphates, described in Section 1.2, can adopt various structural types, varying in framework connectivity and this has significant influence on chemical properties. The most common are those in which the phosphate anions link to metal cations in such a way to build a rigid three-dimensional framework (see Figure 1.3a). Much less common is a structure type in which the metals and phosphate anions connect together in a two-dimensional array, with these held together in the third dimension by relatively weak bonding, often hydrogen bonding (see Figure 1.3b).

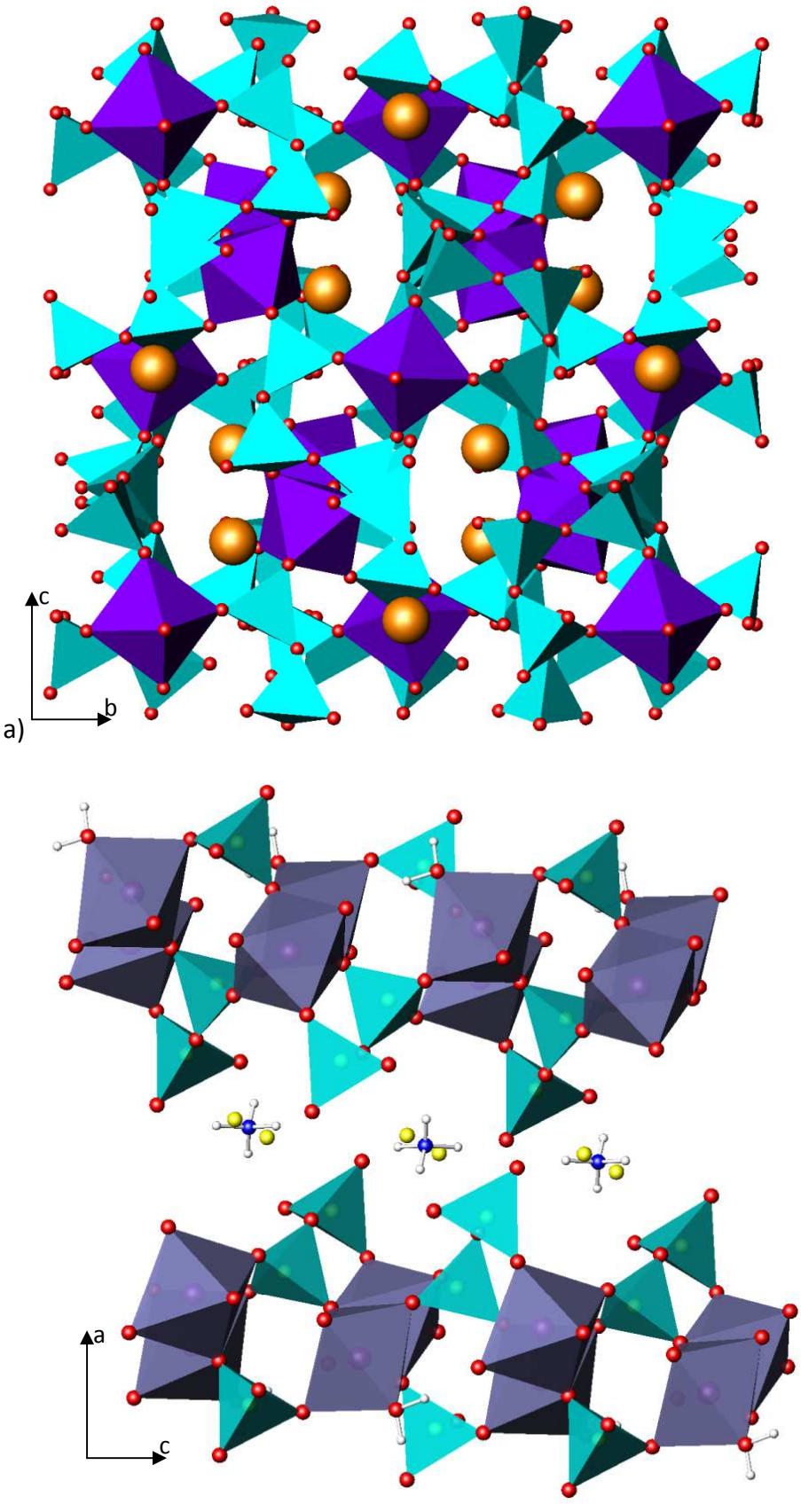

Figure 1.3 *a) Three-dimensional structure of $Cs_3(V_3P_{12}O_{36})$[13], purple octahedra VO_6, blue tetrahedra PO_4 and orange spheres caesium b) Two-dimensional layered structure of $Na(NH_4)(Ni_3(P_2O_7)_2(H_2O)_2)$[14], purple octahedra NiO_6, blue tetrahedra PO_4, blue spheres nitrogen, yellow spheres sodium and white spheres hydrogen*

1.2.2 Triphosphates

The simplest condensed phosphate is the diphosphate $P_2O_7^{4-}$. However in this thesis study will focus on the next in the series, the triphosphate $P_3O_{10}^{5-}$. Somewhat surprisingly, there was formal dispute over the existence of oligophosphates above n = 2 for over 60 years after the initial report of sodium triphosphate in 1895 by Schwarz[15]. This was despite Morey and Ingerson producing equilibrium phase diagrams for the $NaPO_3$ – $Na_4P_2O_7$ system[16-18] which clearly showed the existence of $Na_5P_3O_{10}$. The resolution of the crystal structure of one of the forms of $Na_5P_3O_{10}$, with XRD analysis and paper chromatography by Davis and Corbridge in 1958[19] ended this dispute. Triphosphates have received interest since, with an increasing number of crystal structures being solved[20-25].

Most of the well characterised triphosphates have been discovered by investigations of their various systems by flux methods at relatively high temperatures, which may be explained by the fact that most triphosphates are difficult to crystallise in aqueous media. One notable exception is the $M^{III}H_2P_3O_{10}\cdot nH_2O$ family (the aluminium member of which is the focus of this project), several of which can be obtained through aqueous acid fluxes at relatively low temperatures. This family is discussed in greater detail in Section 1.6.

1.2.2.1 The Triphosphate Anion

The ICSD[26] currently has over 70 crystal structures containing the P_3O_{10} triphosphate unit, with others reported elsewhere[27, 28]. There are three main features used to describe P_3O_{10} groups, the P-P distances, the P-O-P angles and the P-P-P angles, which are shown in Figure 1.4. Values reported in the literature for P-P distances range from 2.82 to 2.99 Å. The literature values for P-O-P angles have a larger variation ranging from 112.6 to 142.5 ° with the P-P-P values having an even larger variation, ranging from 84.5 to 151.3 °. These large variations result from the different sizes and bonding preferences of the large number of cations forming the triphosphate phases (over 30 in reported crystal structures, from all four

blocks of the periodic table, examples including H^{+}, Be^{2+}, Ca^{2+}, Cs^{+}, Ni^{2+}, Cu^{2+}, Y^{3+}, Cd^{2+}, Ta^{5+}, Al^{3+}, In^{3+}, Pb^{2+}, Bi^{3+}, Pr^{3+}, Yb^{3+}, Th^{4+}, U^{4+}, U^{6+} and NH_4^{+}), and are consistent with long chain phosphates and large ring anions such as cyclohexaphosphate. Around half of the reported triphosphate crystal structures exhibit a 2-fold symmetry of the triphosphate anions, with the others displaying no internal symmetry, see Figure 1.4.

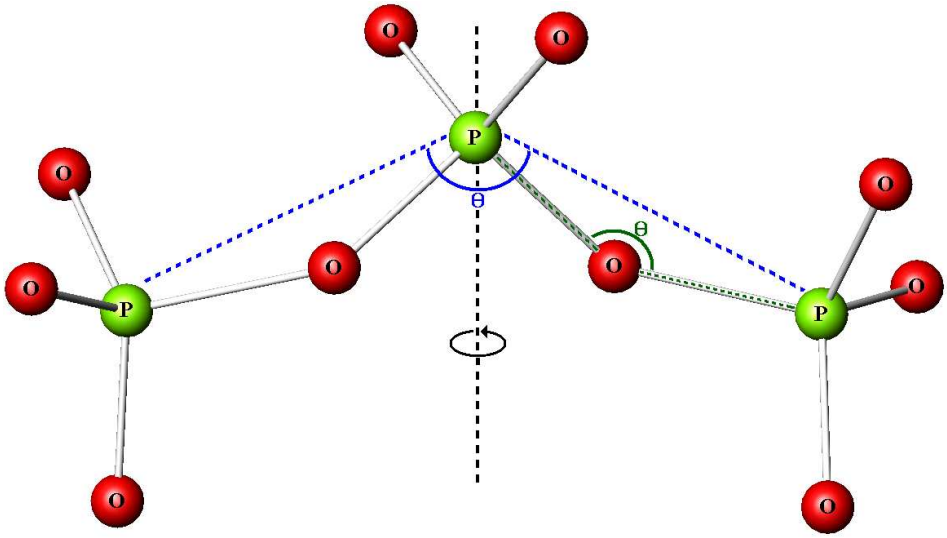

Figure 1.4 *Geometry of a triphosphate unit showing the P-P-P angle (blue), P-O-P angle (green) and P-P distances. The internal axis of symmetry is also shown*

1.2.3 History of Condensed Phosphates

The present knowledge of the geometry and types of condensed phosphate anions is a result of nearly 200 years of research into the field. Berzelius[29] described the changes to the properties of phosphoric acid after ignition in 1816, which was the first observation of condensation of the acid, thus isolating the first reported condensed phosphate. Over 30 years later, in 1848, Fleitmann and Henneberg[30] proposed the following reaction scheme, to explain their own results:

$$nH_3PO_4 \rightarrow H_{n+2}P_nO_{3n+1} + (n\text{-}1)H_2O$$

This scheme lead to the general formula of polyphosphates. The first report of a triphosphate (as mentioned in Section 1.2.2) came from Schwarz in 1895[15] who reported several mixed triphosphates and sodium triphosphate, which was later characterised as having the $P_3O_{10}^{5-}$ polyphosphate anion.

In 1900, Knorre[31] published a detailed review of all the work to date into condensed phosphates and reported results from his own investigations into the preparation of sodium cyclophosphate. Boulle also worked in the area of cyclophosphates and in 1938 reported a procedure for the preparation of water soluble cyclotriphosphates[32]. Boulle's procedure has been extensively used to synthesis cyclotriphosphates, and many other classes of condensed phosphates, and remains a key process for the preparation of these types of phosphate. Around the same time, Bonneman-Bemia[33] undertook a detailed investigation into triphosphate chemistry using the latest methods of synthesis and X-ray diffraction. This study confirmed the existence of the previously reported triphosphates and detailed a number of new examples.

The development of X-ray structural analysis also played a significant role in the development of the condensed phosphate field. Possible geometric conformations had been suggested for condensed phosphate anions in the past, through various techniques, but had not been confirmed. The application of diffraction was slow to be realised in this field, however, with the first crystal structure of a condensed phosphate, $Zr_2P_2O_7$ only reported in 1935 by Levi and Peyronel[34], while by that time many silicates had been structurally characterised.

The 1950s saw a true resurgence of condensed phosphate chemistry, with the discovery of thin-layer chromatography by Westman and Scott[35] and Ebel[36] and increased use of X-ray structural analysis. These techniques allowed easy establishment of the degree of

condensation possible, and showed several previously reported compounds to actually be mixtures of condensed phosphates. This also allowed the beginnings of well controlled and reproducible preparation methods to be established.

Recognising the possibilities these methods offered, Thilo[37] undertook a detailed and systematic investigation into condensed phosphate materials. This produced a large number of fundamental results, which have formed the basic chemical foundation for many subsequent investigations into the condensed phosphate field. Around the same time van Wazer and Griffiths[38] undertook a significant investigation into the properties of and reproducible synthetic routes to condensed phosphates. This provided several new synthetic routes to various condensed phosphates.

In more recent years interest in condensed phosphates has remained constant, with groups such as that of Selevich and Lyutsko investigating many of the triphosphates discussed in Section 1.6, and detailing crystal structures for many other condensed phosphates[39-43].

1.3 Aluminium Phosphates

There is a large diversity in composition of aluminium phosphates, with examples existing from all the types of phosphate anion described in Sections 1.1 and 1.2, leading them to form a large and complex family.

This large composition range leads to a rich structural chemistry, currently with over 100 reported crystal structures in the ICSD containing just the basic Al, P and O required to form an aluminium phosphate. This number jumps to over 150 with the inclusion of hydrogen and over 560 when the other elements are included. The crystal structures of aluminium phosphates are highly diverse (see Figure 1.5), ranging from three-dimensional frameworks built from simple mono or oxyphosphates such as $Al_3(PO_4)_2(OH)_3(H_2O)_6$[44]

(Figure 1.5b), phosphate chains (for example $Al(PO_3)_3$[45] Figure 1.5e), phosphate rings (for example $Al_2(P_6O_{18})$[46], Figure 1.5a) or even oxygen deficient phosphates such as $Al4(PO_3H)_6$[47] (Figure 1.5f), to layered phosphates such as $AlH_2P_3O_{10}\cdot 2H_2O$ (see Section 1.6.1) or $Al_6P_8O_{32}$[48] (Figure 1.5c), to zeolitic type open frameworks such as that of $Al(PO_4)(H_2O)_{2.1}$[49] (Figure 1.5d).

Their diversity in composition and structure means aluminium phosphates are able to display a range of properties such as ion exchange[50], intercalation[51], ionic conduction[52] and catalysis[53]. These properties in turn lead to a wealth of applications with aluminium phosphates being used in environmental remediation[54], as additives in baking powders[55], anti-corrosive agents in paints[56], dental and biomedical implants implants[57] and as fire retardants[58].

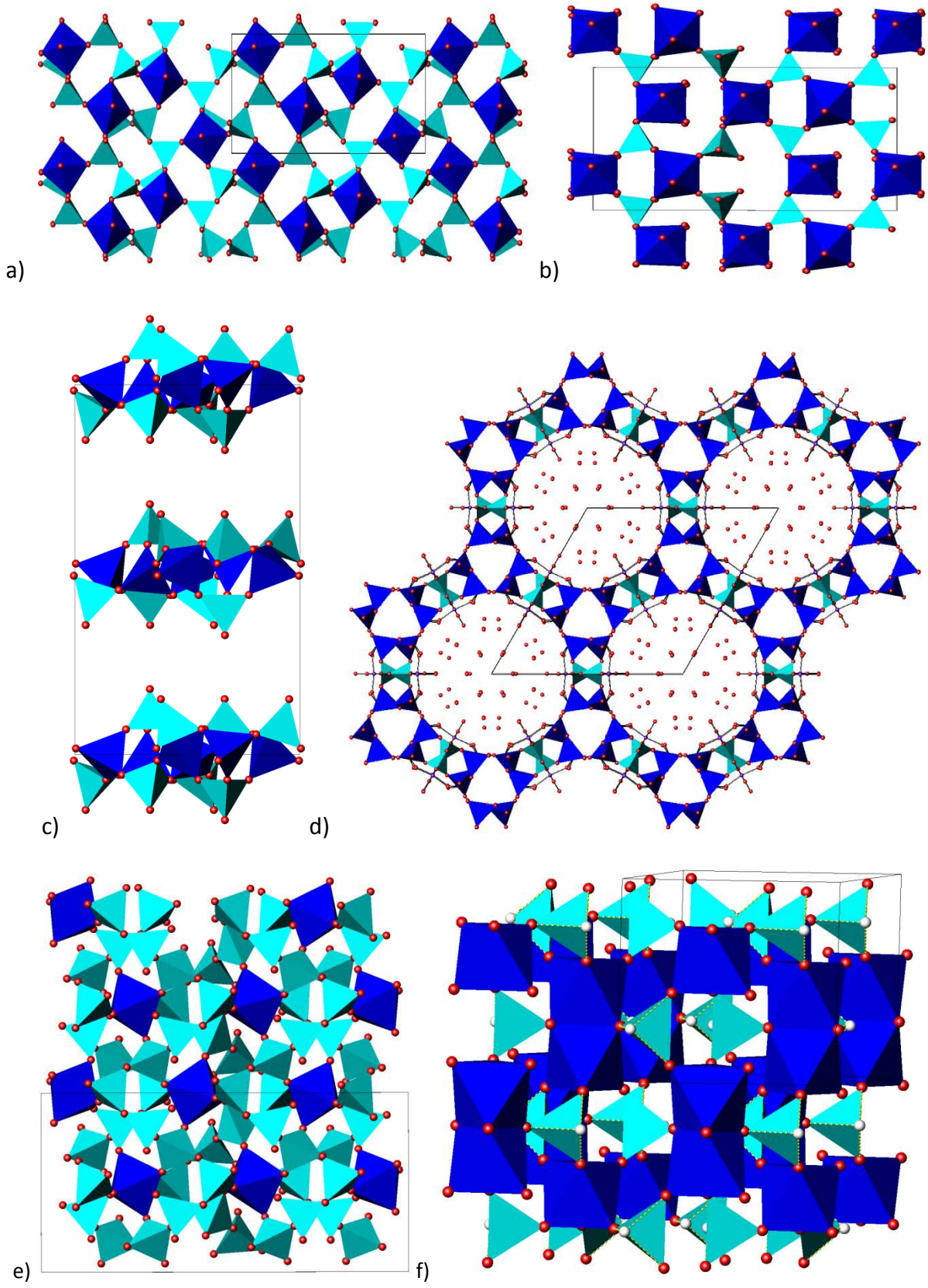

Figure 1.5 *a) $Al_2(P_6O_{18})$[46], b) $Al_3(PO_4)_2(OH)_3(H_2O)_6$[44], c) $Al_6P_8O_{32}$[48], d) $Al(PO_4)(H_2O)_{2.1}$[49], e) $Al(PO_3)_3$[45] and f) $Al4(PO_3H)_6$[47]. Blue octahedra AlO_6, dark blue tetrahedra AlO_4, light blue tetrahedra PO_4, red spheres oxygen and white spheres hydrogen.*

1.4 Layered Materials

Layered phosphates are the focus of this thesis but it is important to be aware that several other forms of inorganic layered materials exist, which share many similar properties to and chemistry with layered phosphates.

1.4.1 Clays

Clays are natural layered ceramic materials composed mainly of silicate, alumina and water. Many types of clays exist, which are classified by their structure type as one of: allophane, kaolinite, halloysite, illite, chlorite, vermiculite, smectite and attapulgite-palygorskite-sepiolite or as containing mixed layers.

The crystal structures (see Figure 1.6) of these clays consist of layers built of a central sheet of magnesium or aluminium octahedra between two sheets of silica tetrahedra, with the connectivity of these determining the structure type. These negatively-charged sheets are separated by inter-lamellar regions occupied by hydrated cations, which provide the clays with high ion exchange capability, and are held together by weak dipolar or van der Waals forces. These weak forces allow the intercalation of other cations, extra water molecules or even organic molecules, causing expansion in the lattice parameter perpendicular to the inorganic layers.

Smectic clays have received the most attention due to their large surface area, high swelling capacity and high cation exchange capabilities. Clays and their nanocomposites are used in numerous applications ranging from food packaging to automotive components, and numerous catalysis reactions are able to occur at the surface of different clays, such as the nucleophilic substitution of hydroxyl groups in α-aryl alcohols being catalysed by tin ion exchanged montmorillonite[59]. Catalysis reactions show a significant weakness of clays, as only relatively mild conditions are possible to ensure the structure of the clays remains intact.

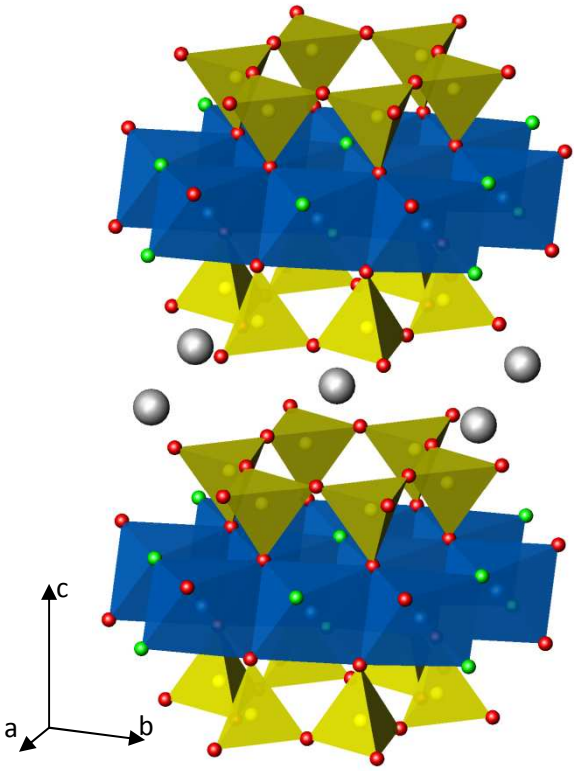

Figure 1.6 *Crystal structure of $Cs_{0.6}(Li_{0.6}Mg_{2.4})(Si_4O_{10})F_2$[60]. Blue octahedra MgO_4F_2/LiO_4F_2, yellow tetrahedra SiO_4 and grey spheres Cs*

1.4.2 Layered double hydroxides

Layered double hydroxides are an unusual family of layered inorganic materials, in that the layers are positively-charged with balancing anions residing within the inter-lamellar region. The layers are similar to those of brucite[61], being built up of $M(OH)_6$ octahedra of single layer thickness, with the hydrogens directed into the inter-lamellar region towards the anions and water molecules residing there (see Figure 1.7). Most layered double hydroxides can be represented by the formula $[M^{2+}_{1-x}M^{3+}_{x}(OH)_2]^{x+}(A^{n-})_{x/n}\cdot yH_2O$, where M^{2+} includes Ca^{2+}, Mg^{2+}, Mn^{2+}, Fe^{2+}, Co^{2+}, Cu^{2+}, Ni^{2+} and Zn^{2+}, M^{3+} includes Al^{3+}, Ga^{3+}, $Cr^{3+}$and Fe^{3+} and A^{n-} can be either organic (such as carbonates) or inorganic (such as halides or nitride).

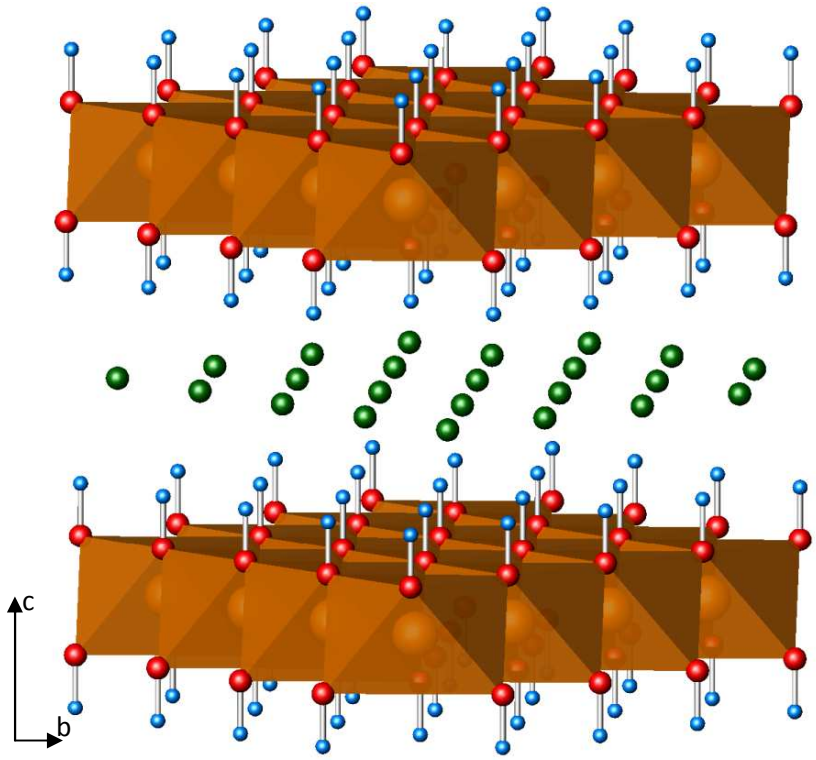

Figure 1.7 *Structure of* $[Zn_{0.65}Al_{0.35}(OH)_2]Cl_{0.336}{\cdot}0.336H_2O$[62]*. Orange octahedra* ZnO_6/AlO_6*, blue spheres H and green spheres partially occupied Cl sites, inter-lamellar* H_2O *not shown*

Layered double hydroxides exhibit a number of desirable properties, such as intercalation[63], catalytic activity[64] and ion exchange[65], based on the exchange of negative ions. They have a number of applications in biology and medicine[66], as additives in polymers[67, 68], environmental remediation[69] and as precursors to magnetic materials[70-72].

1.5 Layered Phosphates

1.5.1 Zirconium Phosphates

The zirconium phosphates are one family of layered ortho-phosphates to receive considerable interest. The two main forms are α-$Zr(HPO_4)_2{\cdot}H_2O$ (α-ZrP) and γ-$Zr(PO_4)(H_2PO_4){\cdot}2H_2O$ (γ-ZrP), with others existing but of less relevance to this project.

1.5.1.1 α-ZrP

α-ZrP forms the structural archetype for a family of metal phosphates consisting of Zr[73], Ti[74], Hf[75], Ge[76], Sn[77], Pb[77] or a mixed metal framework[78]. The structure of α-ZrP[73] is built upon a monoclinic unit cell with space group $P2_1/c$ and unit cell parameters of a = 9.076(3) Å, b = 5.298(6) Å, c = 16.22(2) Å and β = 111.5(1) °. The structure (Figure 1.8) consists of layers built up of corner sharing PO_4 tetrahedra and ZrO_6 octahedra, with each PO_4 sharing three corners with ZrO_6 groups, with the fourth corner containing a hydroxide group which protrudes into the inter-lamellar region. This gives the phase clay-like layers with a thickness of 6.4 Å. Each inter-lamellar water only participates in intralayer hydrogen bonding with the terminal hydroxyl group from a single layer, as a result the layers in α-ZrP are held together through van der Waals forces alone[79, 80].

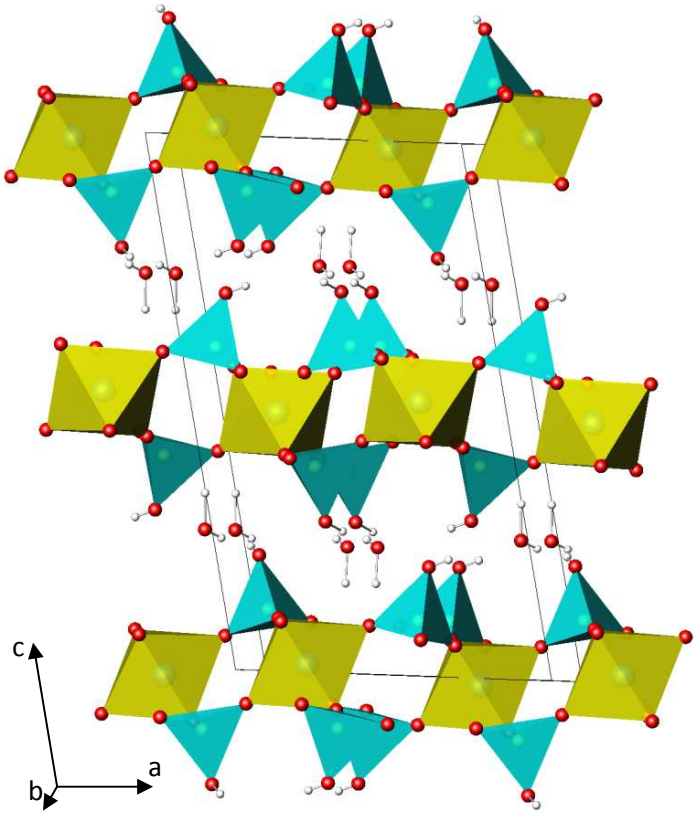

Figure 1.8 *Structure of α-ZrP. Yellow octahedra ZrO_6, blue tetrahedra PO_4, unit cell shown*

The interlayer spacing of α-ZrP measures ~7.55 Å. The inter-lamellar region can be considered as a zeolite-like cavity, with passageways between oxygens measuring 2.62 Å[81], which gives relatively easy access to the protruding hydroxide group. Most of the chemistry of α-ZrP exploits this ease of access manipulating the proton or hydroxide, through processes such as ion exchange[80-84] and intercalation[85-88], which are discussed in more detail in subsequent chapters.

1.5.1.2 γ-ZrP

γ-ZrP also forms the structural archetype for a family of metal phosphates consisting of Zr[89], Ti[90] and Hf[91]. The structure of γ-ZrP (Figure 1.9) has a monoclinic unit cell with space group $P2_1$ and unit cell parameters of a = 5.3825(2) Å, b = 6.6337(1) Å, c = 12.4102(4) Å and β = 98.687(2) ° [89]. The layered structure is built up of ZrO_6 octahedra corner sharing with two PO_4 tetrahedral environments. One PO_4 unit is situated in the centre of the layer and shares all four corners with four neighbouring ZrO_6 octahedra, the other PO_4 unit is situated on the edges of the layer sharing two corners with adjacent octahedra, with the other two protruding into the inter-lamellar region as hydroxyl groups, each being only half as acidic, on average, as the terminal hydroxide in α-ZrP. This structural arrangement gives γ-ZrP a greater layer rigidity and thickness than α-ZrP, being 9.3 Å thick. Both hydroxyl groups participate in hydrogen bonding with waters in the inter-lamellar region, which in turn form hydrogen bonds to other inter-lamellar waters and the adjacent layer. This hydrogen bonding network, which holds the layers together, is a result of γ-ZrP having two inter-lamellar waters per formula unit, whilst α-ZrP only has one. The interlayer spacing of γ-ZrP is also larger than that of α-ZrP at ~12.2 Å.

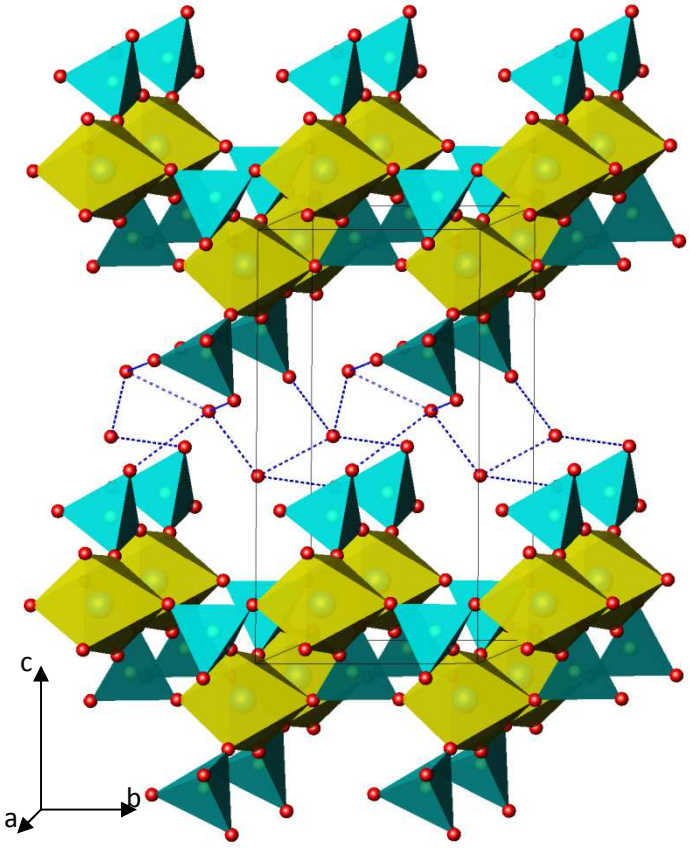

Figure 1.9 *Structure of γ-ZrP. Yellow octahedra ZrO_6, blue tetrahedra PO_4. Hydrogens bonds and unit cell shown*

1.6 $MH_2P_3O_{10}\cdot nH_2O$ Family

Aluminium triphosphate, $AlH_2P_3O_{10}\cdot 2H_2O$ (AlTP) belongs to a family of layered tertiary metal triphosphates with the general formula $M^{III}H_2P_3O_{10}\cdot nH_2O$ where M = Al, Ga, Cr, V, Mn and Fe[92-96] and n = 0, 1 or 2. The aluminium phase was first identified by D'Yvoire in 1962[92] who noted the existence of two forms of $AlH_2P_3O_{10}$: the first a layered structure with two waters of hydration denoted type-I, and the second an anhydrous form with a three-dimensional framework denoted type-II. D'Yvoire also made note of two iron phases isotopic to the two aluminium phases.

Numerous reports of other members of this family followed over the following years, with the type-I layered phases of Ga being reported by Mel'nikov[93], Mn by Selevich and Lyutsko[97] and Guzeeva[98] and V by Lyutsko and Selevich[94], but no crystal structures were

reported in these early studies. There have also been several reports of the type-II with isostructural crystal structures being reported for Al[99] (see Figure 1.10), Ga[100], Cr[101], Fe[102], V[103] and In[104] with other reports but no crystal structures for $MnH_2P_3O_{10}$[97, 98].

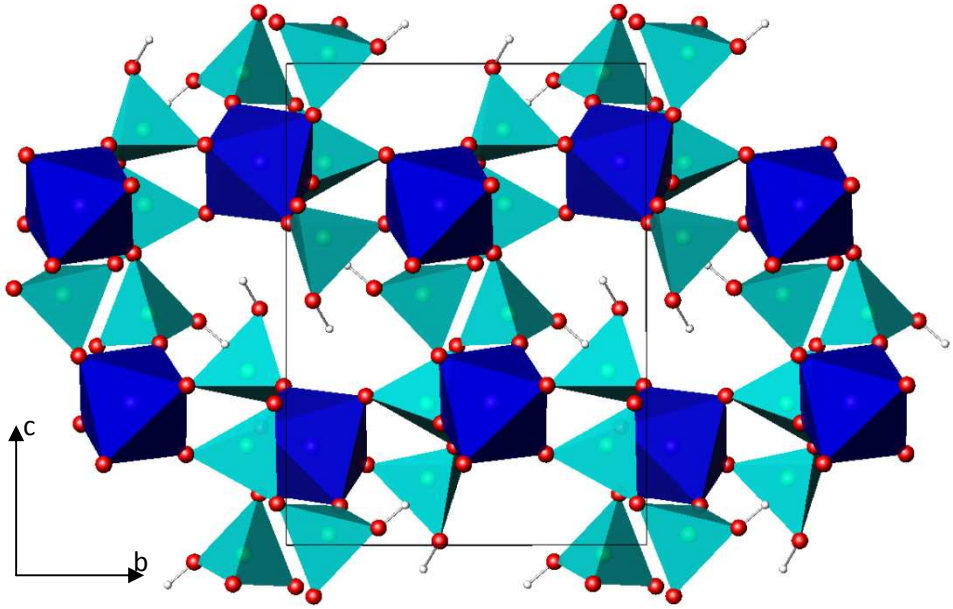

Figure 1.10 *Structure of type-II $AlH_2P_3O_{10}$. Dark blue octahedra AlO_6, light blue tetrahedra PO_4, unit cell shown*

The crystal structure of the layered type-I triphosphates remained unknown for over 40 years, with only implied structural similarities to α-ZrP[73, 89], until the structure of AlTP (see Section 1.6.1) was solved by Rishi in 2006[105]. This was quickly followed by the elucidation of the crystal structures of the Ga and Cr phases[27, 28] showing these to be isostructural to AlTP.

There are also crystal structures for two phases containing one water of hydration. The first an iron phase discovered by Averbuch and Guitel[106], has a three-dimensional crystal structure similar to that of the anhydrous iron phase, but expanded to allow the incorporation of water molecules. The second, a vanadium phase reported by Rishi[28], has a layered structure (see Figure 1.11) different to those of the type-I dihydrate members of the family.

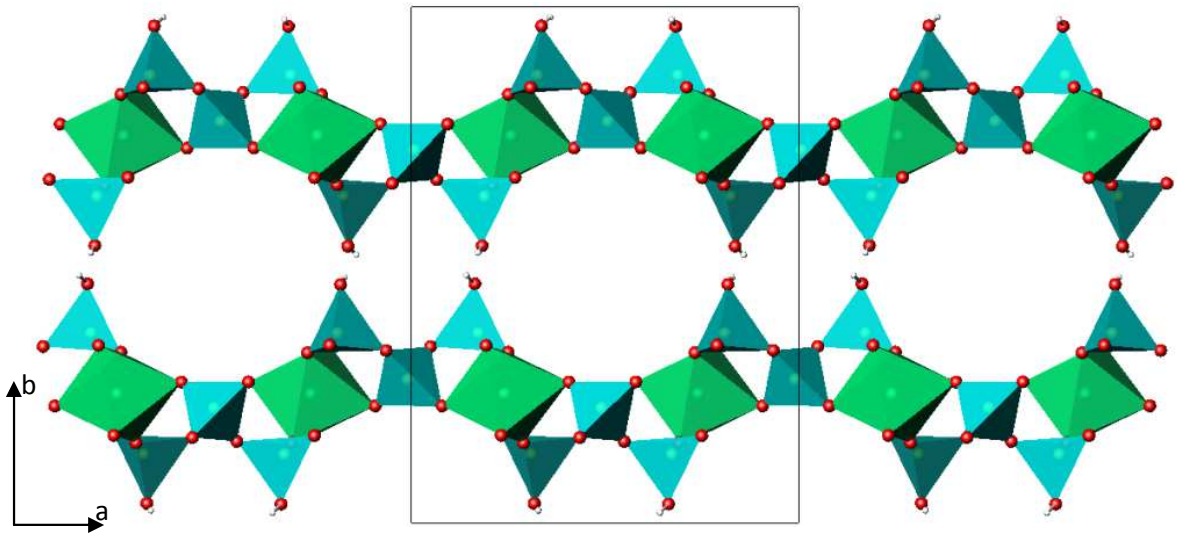

Figure 1.11 *Crystal Structure of $VH_2P_3O_{10}{\cdot}H_2O$[28]. Green octahedra VO_6, blue tetrahedra PO_4, unit cell shown*

1.6.1 AlTP Structure

The crystal structure of AlTP is built upon a unit cell of monoclinic symmetry, space group P2/c with parameters of a = 7.9497(2) Å, b = 4.9302(1) Å, c = 11.6564(2) Å and β = 95.72(2) °. The structure (Figure 1.12) consists of layers in the *bc* plane built of $H_2P_3O_{10}$ spanning across the layer connecting to AlO_6 octahedra. Each AlO_6 octahedron connects to four triphosphate units, two sharing a corner from both a terminal and the central PO_4, with the second terminal PO_4 unit attaching to a neighbouring Al^{3+} cation, and two more connecting through only a terminal PO_4 tetrahedra with the other two phosphate units connecting to neighbouring Al^{3+} cations. The hydroxyl groups from the terminal PO_4 units protrude into the inter-lamellar region and participate in hydrogen bonding with the inter-lamellar water molecules which in turn hydrogen bond with the adjacent layer, this hydrogen bonding network holds the layers and structure together.

The terminal PO_4 units protruding into the inter-lamellar region give AlTP similar structure properties to α-ZrP, most importantly the terminal hydroxide group protruding into the inter-lamellar region. As mentioned in Section 1.5.1.2, manipulation of this hydroxide is

involved in most of the chemistry of α-ZrP, so the presence of a similar hydroxide in AlTP implies similar chemistry may be feasible in this phase.

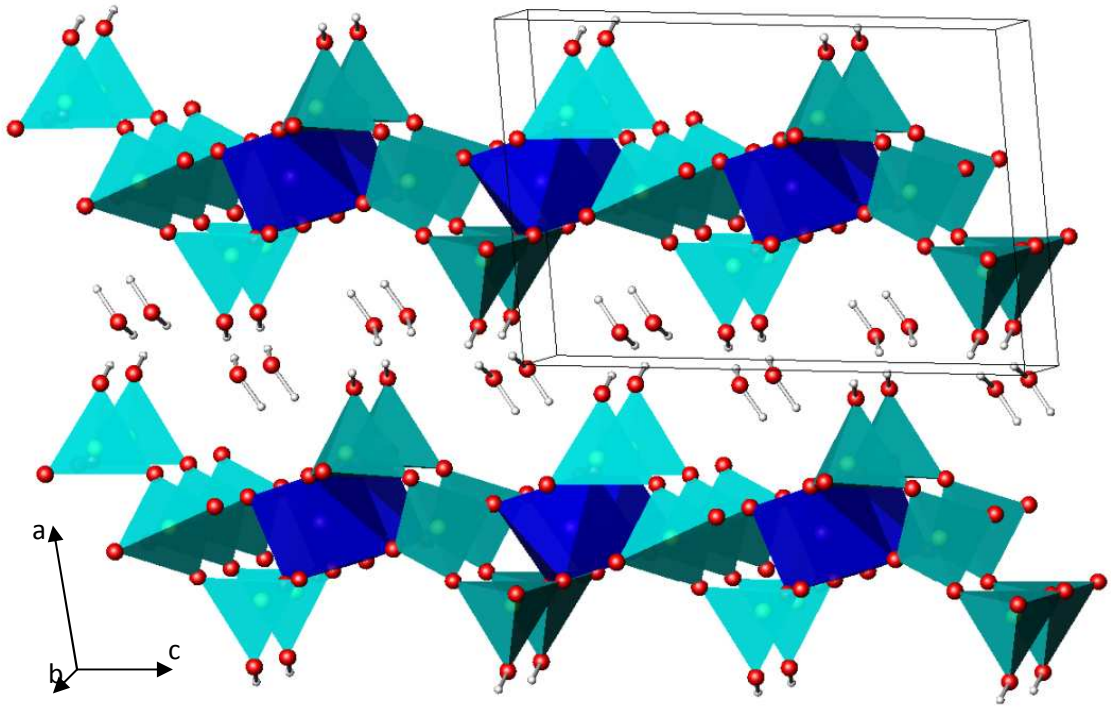

Figure 1.12 *Structure of AlTP. Dark blue octahedra AlO_6, light blue tetrahedra PO_4, unit cell shown*

In spite of only recently being structurally characterised, AlTP has been commercially available for a number of years with numerous international patents for its industrial applications. It is commonly used as an anticorrosive additive in paints and metal surface coatings, preferential to less environmentally friendly lead and chromium alternatives, with several patents existing for its use as such[107-109]. A number of patents also exist for the use of composites of AlTP as catalysts for exhaust gas purification[110], hardening agents for resins[111] and as chemical absorbents in odour eaters removing odours like ammonia and hydrogen sulphide[112].

AlTP displays a trait common to many inorganic layered materials, especially phosphates, in which the d_{100} reflection (or d_{010} or d_{001} depending on the orientation of inorganic layers) in the XRD pattern is a direct measure of the interlayer spacing

(Figure 1.13). This provides an easy method of monitoring any changes occurring as a result of intercalation or ion exchange reactions.

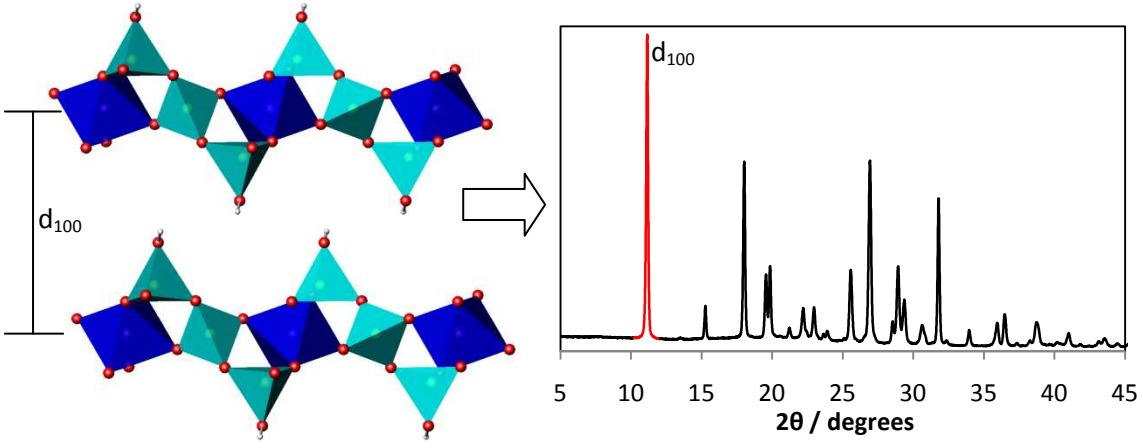

Figure 1.13 *Schematic of d_{100} peak directly showing interlayer spacing*

1.7 Project Aims

The primary aim of this project was to investigate the properties and potential of the $M^{III}P_3O_{10}\cdot 2H_2O$ family, with the focus on the aluminium member of the family as this was the easiest member to synthesis and the most widely studied. Results from the investigations with AlTP could then be expanded to study other members of this isostructural family of layered triphosphates.

The initial aim was to study the ion exchange properties of AlTP, expanding upon the few studies already reported[28, 113, 114], and knowing the structural similarities between AlTP and α-ZrP, utilise the wealth of knowledge of α-ZrPs ion exchange properties to attempt to optimise exchange in AlTP. Resulting products were to have the amount of exchange quantified, then attempts would be made to structurally characterise these phases.

Another aim of the project was to investigate the intercalation potential of AlTP, as with ion exchange, exploiting the similarities to α-ZrP and making use of the understanding of intercalation into α-ZrP and similar phases. These investigations were to assess the diversity of possible intercalated molecules and compare with other known host structures.

Of particular interest were complex molecules that had potential to offer unusual properties. It was also hoped to determine the structural implications of these intercalation reactions.

References

1. S. Kaoua, P. Gravereau, J. P. Chaminade, S. Pechev, S. Krimi and A. El Jazouli, *Sol. Stat. Sci.*, 2009, **11**, 628.
2. E. Thilo and H. Grunze, *Z. Anorg. Allg. Chem.*, 1955, **263**, 263.
3. S. K. Doughty, J. G. Simpson and K. L. Rowlen, *J. Am. Chem. Soc.*, 1998, **120**, 7997.
4. J. B. Williams and D. Taber, *J. Am. Oil Chem. Soc.*, 1972, **49**, 539.
5. W. L. Hill, D. S. Reynolds, S. B. Hendricks and K. D. Jacob, *J. Assoc. Offic. Agricult. Chem.*, 1945, **28**, 105.
6. J. B. Parise, *Chem Comm*, 1985, **9**, 606.
7. L. E. Jackson, L. M. Grover and A. J. Wright, *Bioceram., Vol 20, Pts 1 and 2*, 2008, **361-363**, 11.
8. C. Mercier, G. Palavit, L. Montagne and C. Follet-Houttemane, *C.R. Acad. Sci. II C.*, 2002, **5**, 693.
9. F. C. Coomer, N. J. Checker and A. J. Wright, *Inorg. Chem.*, 2010, **49**, 934.
10. S. P. Dolin, A. A. Levin and T. Y. Mikhailova, *J. Molec. Struct.*, **972**, 115.
11. A. Mitra, H. Yoshida, H. Fujita and M. Nakatsuka, *Opt. Commun.*, 2006, **261**, 342.
12. H. P. Weber, T. C. Damen, H. G. Danielme and B. C. Tofield, *Appl. Phys. Lett.*, 1973, **22**, 534.
13. A. V. Lavrov, V. P. Nikolaev, G. G. Sadikov and M. J. Vojtenkov, *Dokla. Akad. Nauk Sssr*, 1981, **259**, 103.
14. W. Liu, X. X. Yang, H. H. Chen, Y. X. Huang, W. Schnelle and J. T. Zhao, *Sol. Stat. Sci.*, 2004, **6**, 1375.
15. F. Schwarz, *Z. Annorg. Chem.*, 1895, **9**, 249.
16. E. Ingerson and G. W. Morey, *Am. Mineralog.*, 1943, **28**, 48.
17. G. W. Morey and E. Ingerson, *Am. J. Sci.*, 1944, **242**, 1.
18. G. W. Morey, *J. Am. Chem. Soc.*, 1954, **76**, 4724.
19. D. R. Davies and D. E. C. Corbridge, *Acta Crystallogra.*, 1958, **11**, 315.
20. K. K. Palkina, S. I. Maksimova and V. G. Kuznetsov, *Inorg. Mater.*, 1979, **15**, 1704.
21. A. S. Lyakhov, V. A. Lyutsko, L. I. Prodan and K. K. Palkina, *Inorg. Mater.*, 1991, **27**, 845.
22. A. S. Lyakhov, V. A. Lyutsko, T. N. Galkova and K. K. Palkina, *Zhurn. Neorg. Khim.*, 1991, **36**, 3053.
23. P. O. Jouini, M. Dabbabi, M. T. Averbuch-Pouchot, A. Durif and J. C. Guitel, *Acta Crystallogr. Sec. C-Cryst. Struct. Comm.*, 1984, **40**, 728.
24. F. Erragh, A. Boukhari and E. M. Holt, *Acta Crystallogr. Sec. C-Cryst. Struct. Comm.*, 1996, **52**, 1867.
25. D. E. C. Corbridge, *Acta Crystallogr.*, 1960, **13**, 263.
26. ICSD, *Inorganic Crystal Structure Database*, http://www.cds.dl.ac.uk/datasets/crys/icsd/llicsd.html.
27. L. S. Ivashkevich, A. S. Lyakhov and A. F. Selevich, *Phosph. Res. Bull.*, 2010, **24**, 6.
28. S. K. Rishi, Ph.D thesis, University of Birmingham, 2006.
29. J. Berzelius, *Ann. Physik.*, 1816, **54**, 31.
30. T. Fleitmann and W. Henneberg, *Liebigs Ann. Chem.*, 1848, **65**, 304.
31. G. Knorre, *Z. Annorg. Chem.*, 1900, **24**, 369.
32. A. Boulle, *C.R. Acad. Sci.*, 1938, 517.
33. P. Bonneman-Bemia, *Anal. Chim.*, 1941, **206**, 395.
34. G. R. Levi and G. Peyronel, *Zeitsch. Kristallogr.*, 1935, **92**, 190.
35. A. E. R. Westman and A. E. Scott, *Nature (London)*, 1951, **168**, 740.
36. J. P. Ebel, *Bull. Soc. Chim. Fr*, 1968, 1663.

37. E. Thilo, *Bull. Soc. Chim. Fr*, 1968, 1726.
38. J. R. van Wazer and Griffiths, *Phosphorus and its Compounds*, interscience, New York, 1966.
39. L. S. Ivashkevich, K. A. Selevich, A. I. Lesnikovich and A. F. Selevich, *Acta Crysta. E - Struct. Rep. Online*, 2007, **63**, i70.
40. A. S. Lyakhov, K. K. Palkina and A. F. Selevich, *Zhurn. Neorg. Khim.*, 1994, **39**, 1438.
41. L. S. Ivashkevich, A. S. Lyakhov, A. F. Selevich, D. Ilieva and A. I. Lesnikovich, *Zeitsch. Kristallogr.*, 2002, **217**, 605.
42. L. S. Ivashkevich, A. S. Lyakhov, A. F. Selevich and A. I. Lesnikovich, *Zeitsch. Kristallogr.*, 2003, **218**, 32.
43. L. S. Ivashkevich, A. F. Selevich, A. S. Lyakhov and A. I. Lesnikovich, *Zhurn. Neorg. Khim.*, 2007, **52**, 1359.
44. P. Q. Fu, *Ti Chi. Ko Hsu.*, 1966, **2**, 116.
45. H. van der Meer, *Acta Crystallogr. B*, 1976, **32**, 2423.
46. A. Oudahmane, A. Mbarek, M. El-Ghozzi and D. Avignant, *Acta Crysta. E - Struct. Rep. Online*, 2010, **66**, I17.
47. N. Li, Y. Ma, S. Xiang and N. Guan, *Chem. Mat.*, 2006, **18**, 975.
48. E. R. Parnham, E. A. Drylie, P. S. Wheatley, A. M. Z. Slawin and R. E. Morris, *Angew. Chem. Int. Ed.*, 2006, **45**, 4962.
49. D. M. Poojary and A. Clearfield, *Zeolites*, 1993, **13**, 542.
50. A. Naeem, S. Mustafa, S. Murtaza, B. D. Ara and A. Hamid, *J. Chem. Soc. Pak.*, 2001, **23**, 133.
51. A. Hayashi, H. Nakayama, M. Tsuhako, T. Eguchi and N. Nakamura, *J. Inclus. Phenom. Macrocyc. Chem.*, 1999, **34**, 401.
52. T. Savitha, S. Selvasekarapandian, C. S. Ramya, M. S. Bhuvaneswari, G. Hirankumar, R. Baskaran and P. C. Angelo, *J. Pow. Sourc.*, 2006, **157**, 533.
53. K. Srinivas, P. P. Reddy, P. Jayaprakash, P. K. Dubey and A. K. Chakravarthy, *Asian J. Chem.*, 2011, **23**, 138.
54. L. Filippov, F. Thomas, I. Filippova, J. Yvon and A. Morillon-Jeanmaire, *J Haz. Mat.*, 2009, **171**, 731.
55. S. M. Saiyed and R. A. Yokel, *Food Addit. Contam.*, 2005, **22**, 234.
56. D. El-Hamid, G. Blustein, M. Deya, B. del Amo and R. Romagnoli, *Mater. Chem. Phys.*, 2011, **127**, 353.
57. V. Medri, M. Mazzocchi and A. Bellosi, *J. Mater. Sci.-Mater. Med.*, 2010, **22**, 229.
58. U. Braun, H. Bahr and B. Schartel, *e-Polymers*, 2010, 14.
59. J. C. Wang, Y. Masui and M. Onaka, *Synlett*, 2010, 2493.
60. J. Breu, W. Seidl and A. Stoll, *Zeitsch. Anorg. Allgem. Chem.*, 2003, **629**, 503.
61. G. Isetti, *Peirodi. Mineral.*, 1965, **34**, 327.
62. G. M. Lombardo, G. C. Pappalardo, F. Punzo, U. Costantino and M. Sisani, *Euro. J. Inorg. Chem.*, 2005, 5026.
63. Y. Z. Xi and R. J. Davis, *Inorg. Chem.*, 2010, **49**, 3888.
64. D. French, P. Schifano, J. Cortes-Concepcion and S. Hargrove-Leak, *Catal. Comm.*, 2010, **12**, 92.
65. A. M. Fogg, J. S. Dunn, S. G. Shyu, D. R. Cary and D. O'Hare, *Chem. Mat.*, 1998, **10**, 351-355.
66. D. Stefanakis and D. F. Ghanotakis, *J. Nanopart. Res.*, 2010, **12**, 1285.
67. E. Kafunkova, K. Lang, P. Kubat, M. Klementova, J. Mosinger, M. Slouf, A. L. Troutier-Thuilliez, F. Leroux, V. Verney and C. Taviot-Gueho, *J. Mater. Chem.*, 2010, **20**, 9423.

68. L. A. Hollingbery and T. R. Hull, *Polym. Degrad. Stabil.*, 2010, **95**, 2213.
69. L. L. Skovbjerg, B. C. Christiansen, S. Nedel, K. Dideriksen and S. L. S. Stipp, *Radiochim. Acta*, 2010, **98**, 607-612.
70. F. Li and X. Duan, *Struct. Bonding*, 2006, **119**, 193.
71. D. O'Hare and A. I. Khan, *J. Mater. Chem.*, 2002, **12**, 3191.
72. V. Rives, *Layered Double Hydroxides: Present and Future*, Nova Science Publishers, Inc., New York, 2001.
73. A. Clearfield and G. D. Smith, *Inorg. Chem.*, 1969, **8**, 431.
74. M. A. Salvado, P. Pertierra, J. R. Garcia-Granda, J. Rodriguez and M. T. Fernandez-Diaz, *Acta Crystallogr. B*, 1997, **53**, 188.
75. I. Nakai, K. Imai, T. Kawashima, K. Ohsumi, F. Izumi and I. Tomita, *Anal. Sci.*, 1990, **6**, 689.
76. R. Romano, A. I. Ruiz and O. L. Alves, *J. Sol. Stat. Chem.*, 2004, **177**, 1520.
77. S. Bruque, M. A. G. Aranda, E. R. Losilla, P. Olivera-Pastor and P. Maireles-Torres, *Inorg. Chem.*, 1995, **34**, 893.
78. V. A. Burnell, J. E. Readman, C. C. Tang, J. E. Parker, S. P. Thompson and J. A. Hriljac, *J. Sol. Stat. Chem.*, 2010, **183**, 2196.
79. J. M. Troup and A. Clearfield, *Inorg. Chem.*, 1977, **16**, 3311.
80. J. Albertsson, A. Oskarsson, R. Tellgren and J. O. Thomas, *J. Phys. Chem.*, 1977, **81**, 1574.
81. A. Clearfield, W. L. Duax, A. S. Medina, G. D. Smith and J. R. Thomas, *J. Phys. Chem.*, 1969, **73**, 3423.
82. A. Clearfield, *Annu. Rev. Mater. Sci.*, 1984, **14**, 205.
83. C. H. Kim and H. S. Kim, *Synth. Metals*, 1995, **71**, 2051.
84. G. Alberti, U. Costanti and M. Pellicci, *J. Inorg. & Nucl. Chem.*, 1973, **35**, 1327.
85. T. Kijima, S. Ueno and M. Goto, *J. Chem. Soc. - Dalt. Trans.*, 1982, 2499.
86. Y. Ding, D. J. Jones, P. Maireles-Torres and J. Roziere, *Chem Mater.*, 1995, **7**, 562.
87. U. Costantino, *J. Chem. Soc. - Dalt. Trans.*, 1979, 402.
88. R. M. Tindwa, D. K. Ellis, G. Z. Peng and A. Clearfield, *J. Chem. Soc.-Farad. Trans. I*, 1985, **81**, 545.
89. D. M. Poojary, B. Shpeizer and A. Clearfield, *J. Chem. Soc. - Dalt. Trans.*, 1995, 111.
90. J. R. Garcia-Granda, S. A. Khainakov, A. Espina, J. R. Garcia, G. R. Castro, J. Rocha and L. Mafra, *Inorg. Chem.*, 2010, **49**, 2630.
91. M. Suarez, L. M. Barcina, R. Llavona, J. Rodriguez, M. A. Salvado, P. Pertierra and J. R. Garcia-Granda, *J. Chem. Soc., Dalton Trans., Inorg. Chem.*, 1998, **1998**, 99.
92. F. D'Yvoire, *Bull. Soc. Chim. Fr*, 1962, **6**, 1224.
93. P. P. Mel'nikov, V. A. Efremov, A. K. Stepanov, T. S. Romanova and L. N. Komissarova, *Russ. J Inorg. Chem.*, 1976, **21**, 26.
94. V. A. Lyutsko and A. F. Selevich, *Z. Neorg. Khim.*, 1983, **28**, 923.
95. M. A. G. Aranda, J. Chaboy and S. Bruque, *Inorg. Chem.*, 1991, **30**, 2394.
96. P. Remy and A. Boulle, *Bull. Soc. Chim. Fr*, 1972, **6**, 2213.
97. A. F. Selevich and V. A. Lyutsko, *Russ. J. Inorg. Chem.*, 1984, **29**, 364.
98. L. S. Guzeeva, A. V. Lavrov and I. V. Tananaev, *Izv. Akad. Nauk. SSSR, Neorg. Mater.*, 1982, **18**, 1850.
99. E. A. Genkina, Y. A. Gorbunov, B. A. Maksimov, A. A. Shternberg and O. K. Mel'Kinov, *Sov. Phys. Crystallogr.*, 1984, **29**, 128.
100. N. N. Chudinova, M. A. Avaliani and L. S. Guzeeva, *Izv. Akad. Nauk. SSSR, Neorg. Mater.*, 1977, **13**, 2229.
101. P. Remy and A. Boulle, *C.R. Acad. Sci.*, 1964, **258**, 927.
102. V. A. Lyutsko and G. Johansson, *Acta Chem. Scand.*, 1988, **A38**, 663.

103. A. S. Lyakhov, K. K. Palkina, V. A. Lyutsko, S. I. Maksimova and N. T. Chibiskova, *Izv. Akad. Nauk. SSSR, Neorg. Mater.*, 1990, **26**, 1064.
104. K. A. Selevich, L. S. Ivashkevich and A. F. Selevich, *Russ. J. Inorg. Chem.*, 2006, **51**, 1565.
105. S. K. Rishi, B. M. Kariuki, N. J. Checker, J. Godber and A. J. Wright, *Chem Comm*, 2006, 747.
106. M. T. Averbuch and J. C. Guitel, *Acta Crystallogr. Sect. B-Struct. Sci.*, 1977, **33**, 1613.
107. K. Noriyuki, M. Mashiko and I. Daisaku, *JP. Pat. 2004099943*, 2004.
108. Y. Taketani and H. Kondo, *Eur. Pat. 0845508*, 1998.
109. M. Hideyuki, O. Yoshinobu and D. Masamichi, *US Pat. 5576558*, 1996.
110. T. Koichi, Y. Koji and S. Satoschi, *JP. Pat. 61283350*, 1986.
111. M. Yukinori and S. Kazuhisa, *JP. Pat. 10237391*, 1998.
112. M. Okuda and M. Kobayashi, *JP. Pat. 4109954*, 1992.
113. V. A. Lyutsko, M. V. Nikanovich, K. N. Lapko and V. F. Tikavyi, *Z. Neorg. Khim.*, 1983, **28**, 1949.
114. A. Hayashi, H. Saimen, N. Watanabe, H. Kimura, A. Kobayashi, H. Nakayama and M. Tsuhako, *Langmuir*, 2005, **21**, 7238.

Chapter 2

Experimental Techniques

2.1 Synthesis

AlTP was synthesised using an acid flux technique as described previously[1, 2]. Aluminium oxide was swirled in phosphoric acid [85 wt%, Sigma-Aldrich] in an alumina crucible, with a phosphorus to aluminium molar ratio of 6:1. This mixture was heated to 240 °C for 24 hours then allowed to cool to room temperature over a 48 hour period. The resulting white powder was collected *via* vacuum filtration and washed with copious amounts of water.

The synthesis techniques used for ion exchanging and intercalating AlTP will be discussed in their relevant chapters.

2.2 Diffraction in Solids

Crystalline solids are capable of diffracting waves of both X-rays and neutrons. A basic understanding of diffraction and some basic principles of crystallinity is required to explain how this occurs.

2.2.1 Diffraction

Waves travelling through the same medium can interact with each other and undergo the process of superposition, which can give rise to both constructive and destructive interference. For two waves, of the same wavelength, travelling in the same direction, the observed intensity at any one point is determined by the phase shift between the two waves (Figure 2.1). This is normally a linear shift, Δ, in the length units of the wavelength. A phase shift of zero results in completely constructive interference, showing as increased intensity (Figure 2.1a), while a phase shift of a half the wavelength results in completely destructive interference, showing as no intensity (Figure 2.1b).

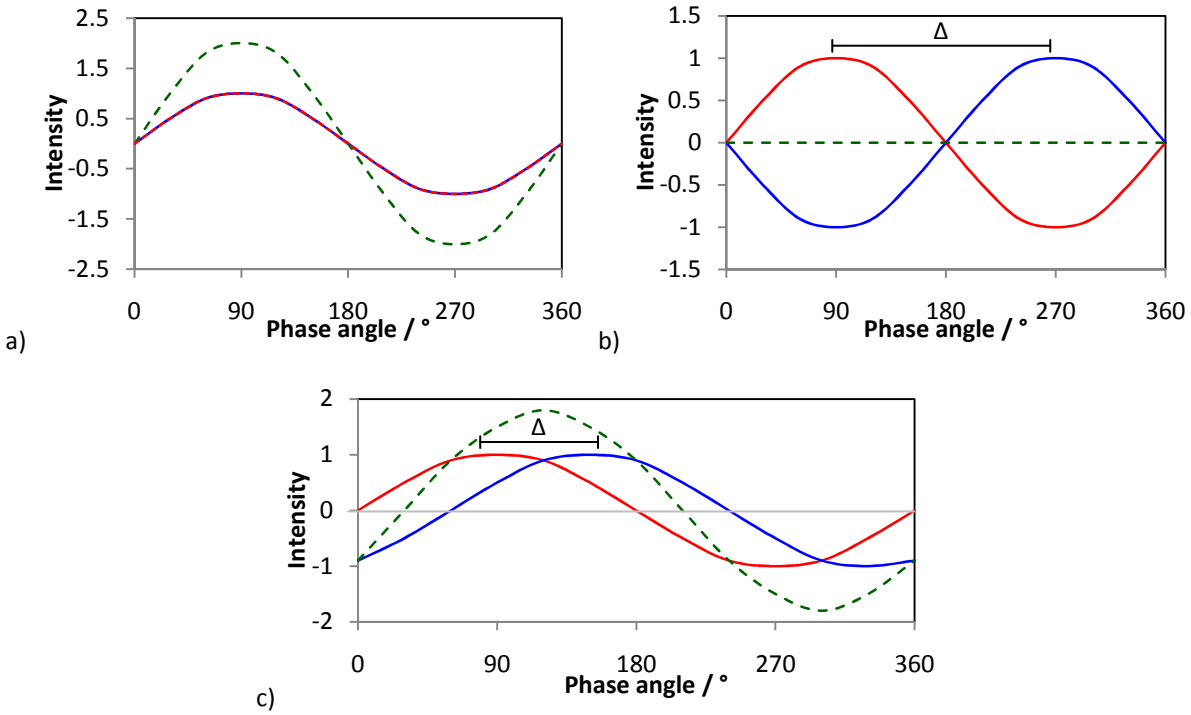

Figure 2.1 *Superposition of two waves (red and blue) giving an interference wave (green). a) zero phase shift, b) half wavelength phase shift and c) one third of a wavelength phase shift*

Diffraction in crystalline materials occurs when waves are scattered from atoms at different positions within the material. There is a phase shift between waves, created by the different path lengths to different atoms, which causes superposition of the waves and thus

differences in observed intensity. This can then give information about the positions of atoms within the crystalline material.

Diffraction is only able to occur when the wavelength of radiation is consistent with the distance between the scattering atoms. The wavelengths of X-rays and neutrons (see Sections 2.3 and 2.4 respectively) can be of the same order of scale as atomic separations so are ideal for diffraction of crystalline materials.

2.2.2 Fundamental Crystallography

The atoms making up a crystalline solid adopt a regular arrangement with respect to each other through three dimensions, building up what is known as a crystalline lattice. The smallest repeating unit which contains all the symmetry of the crystal structure is called the unit cell. This cell is built up of three axes, labelled *a*, *b* and *c*, and three angles, labelled α, β and γ, arranged such that α lies between *b* and *c* (opposite *a*). Variations of these axes and angles give rise to seven crystal systems (cubic, tetragonal, trigonal, hexagonal, orthorhombic, monoclinic and triclinic), of which the monoclinic system is of primary interest in this project, in which $a \neq b \neq c$, $\alpha = \gamma = 90° \neq \beta$. Combination of these crystal systems with lattice centring gives a total of 14 lattice types, known as the Bravais lattices[3] (Figure 2.2).

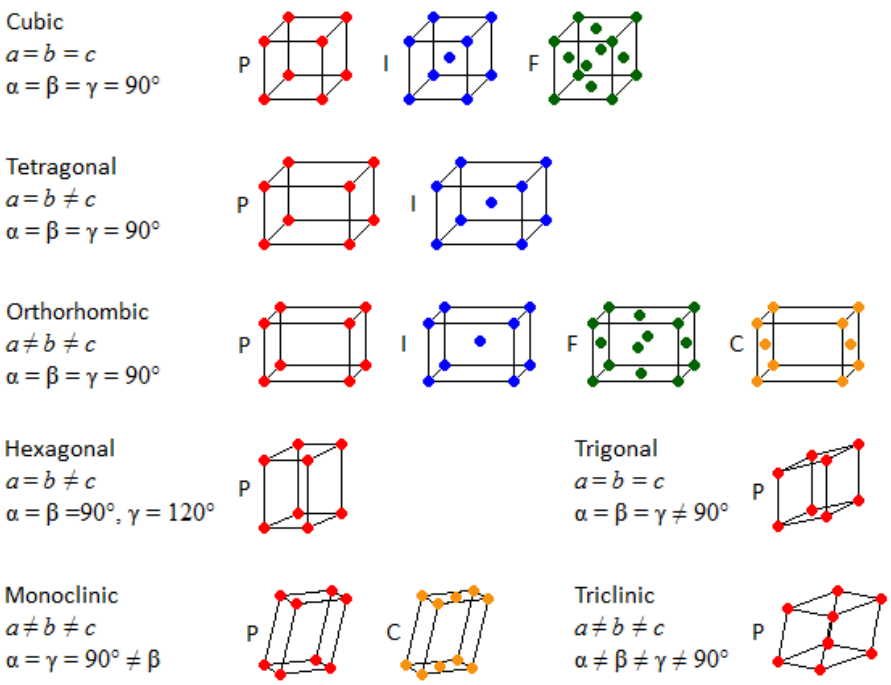

Figure 2.2 *The 7 Crystal systems and 14 Bravais lattices (adapted from [4])*

With the addition of atoms to the unit cell, whose positions are given as fractional coordinates for each of the three axes from one corner of the unit cell, it becomes apparent further translational symmetry is required alongside that describing the Bravais lattice. The addition of these extra symmetry elements, such as glide planes and screw axes, to those of the Bravais lattices in all possible arrangements gives rise to 230 spacegroups[5]. These spacegroups completely describe the symmetry of a crystal structure[3].

Crystals can be described in terms of a series of lattice planes, which provide a reference grid on which the atoms making up a crystal structure may be referred. Each plane cuts through the three cell axes and is defined as the fraction of the cell edge. The planes are labelled in terms of the reciprocal of these intercepts, and are referred to as Miller indices and labelled as (*hkl*) for the plane (Figure 2.3).

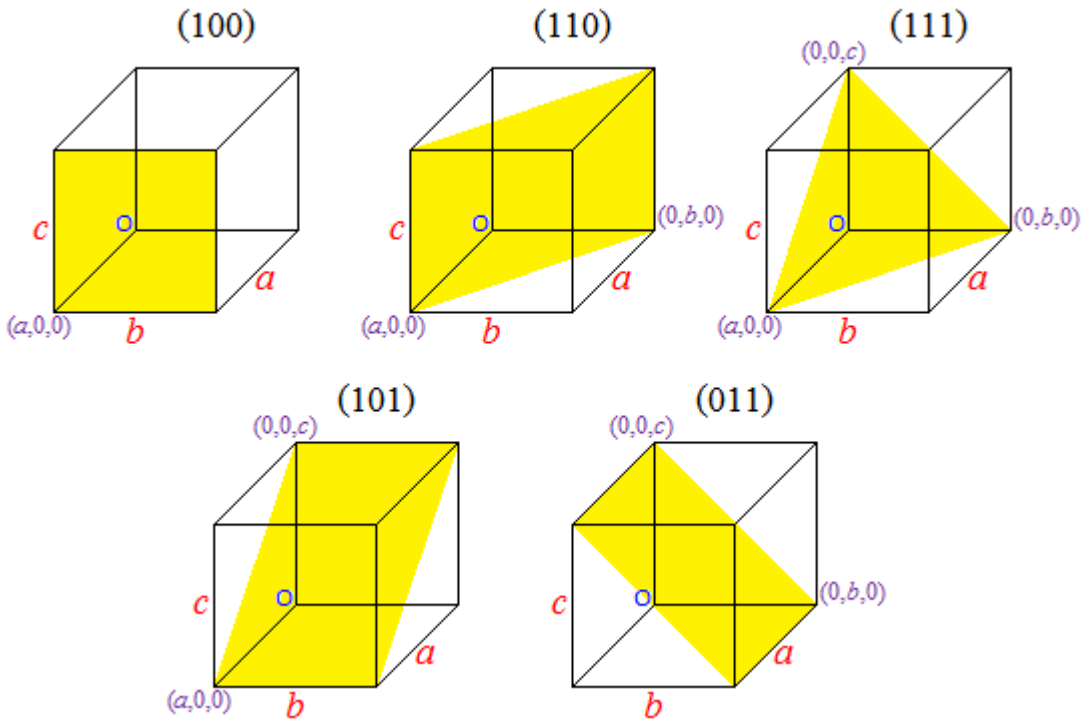

Figure 2.3 *Examples of lattice planes and their Miller indices. O marks the unit cell origin*

Dependent upon the symmetry of the system, some of the lattice planes will be equivalent, such as (100), (010) and (001) in a cubic lattice, with the number of equivalent planes known as the multiplicity. Lattice planes are usually defined as a plane in a single unit cell, but they exist as an infinite number of equivalent parallel planes running throughout the whole crystal lattice, which are separated by a perpendicular distance known as d-spacing often denoted d_{hkl}. For a monoclinic system, such as those in this project, the d-spacing of any set of planes can be calculated through Equation 1:

$$\frac{1}{d_{hkl}^2} = \frac{1}{\sin^2\beta}\left(\frac{h^2}{a^2} + \frac{k^2\sin^2\beta}{b^2} + \frac{l^2}{c^2} - \frac{2hl\cos\beta}{ac}\right) \qquad \textbf{Equation 1}$$

2.2.3 Bragg's Law

Bragg[6] derived his equation describing the relationship of reflected neutrons or X-rays by lattice planes shortly after the discovery that crystals could diffract X-rays, and this is now used universally as the basis to describe diffraction. Bragg's law describes a crystal in terms

of reflecting lattice planes, and treats diffraction as the reflection of X-rays from lattice planes of the same Miller indices (Figure 2.4).

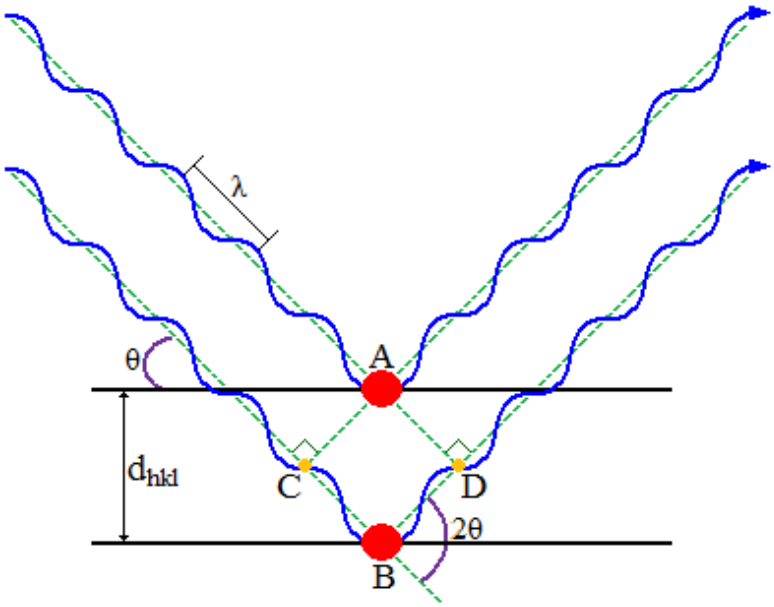

Figure 2.4 *Schematic representation of Bragg's Law*

For two X-rays scattering from adjacent planes (Figure 2.4) the second must travel a longer path (from C to B to D). Bragg's law gives this path difference in this in terms of the radiations incident angle (θ) and the plane separation (d_{hkl}) giving the equation:

$$CB + BD = 2d_{hkl} \sin\theta \qquad \textbf{Equation 2}$$

Constructive interference from superposition only occurs for this equation if the path difference is equal to an integer number of wavelengths (i.e. the waves are in phase), with non integer numbers of wavelengths leading to destructive interference. This allows Equation 2 to be modified to the Bragg equation:

$$n\lambda = 2d_{hkl} \sin\theta \qquad \textbf{Equation 3}$$

2.3 X-Ray Diffraction

X-ray diffraction (XRD) is one of the most fundamental and important techniques employed for characterisation of crystalline materials. It is able to provide phase

identification and assess sample purity using a database of known XRD patterns (such as the JCPDS[7]), as well as much more complex interpretations and investigations allowing full structural determinations of materials of interest. XRD was the primary technique used to characterise materials synthesised throughout this project.

2.3.1 Generation of X-rays

Laboratory X-ray diffractometers use an X-ray tube as the source of their X-rays. This tube is an evacuated enclosure in which an electric current is passed through a tungsten wire filament, producing electrons which are accelerated through a potential difference of ~40 kV and collided with a metal anode target. This target is usually copper (used exclusively in this project), but other metals such as molybdenum, chromium, iron and cobalt are also commonly used. This electron beam ionizes core electrons from the K shell (1s) of the copper atoms, causing vacancies which are filled with electrons from higher L (2p) or M (3p) shells, the relaxation of which produces X-rays of a characteristic wavelength, K_α and K_β radiation respectively for L and M (Figure 2.5a). The two possible spin states of the relaxing electrons creates two different wavelengths from each shell (e.g. $K_{\alpha1}$ = 1.5406 Å, $K_{\alpha2}$ = 1.5442 Å) in a 2:1 ratio[8-10]. Alongside these characteristic X-ray peaks is a continuous background which is known as the Bremsstrahlung ("brake radiation") caused by X-rays released from the deceleration of the high energy electrons after they collide with the metal target (Figure 2.5b).

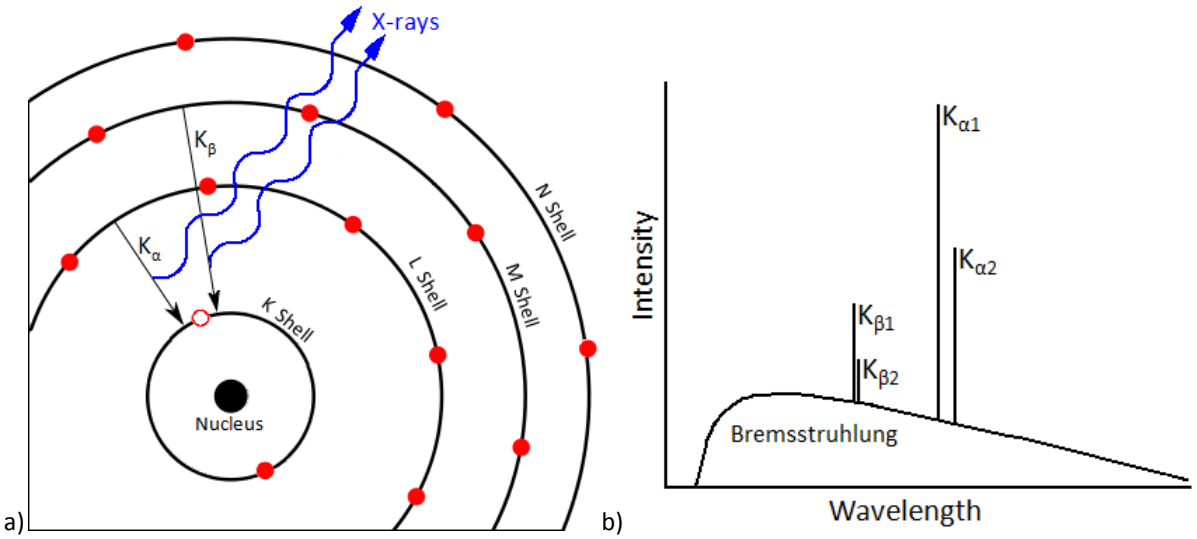

Figure 2.5 *a) X-ray produced through vacancy filling b) X-ray spectrum for copper*

2.3.2 Powder diffraction

X-ray diffraction of a single crystal results in a pattern containing spots of intensity which can usually be assigned to a single *hkl* value (Figure 2.6a). A powder sample, being studied with powder X-ray diffraction, contains a substantial number of crystallites randomly orientated, covering all possible angles of lattice planes. This means X-rays are diffracted at all possible angles defined by Bragg's law causing the spots observed in single crystal XRD to be smeared into rings (Figure 2.6c), with each ring being a peak in the XRD pattern. This causes a loss of direct data compared to single crystal XRD, but different aspects of the powder XRD pattern still contain amounts of data (Figure 2.7) which can aid in understanding the crystal structure of the material being studied.

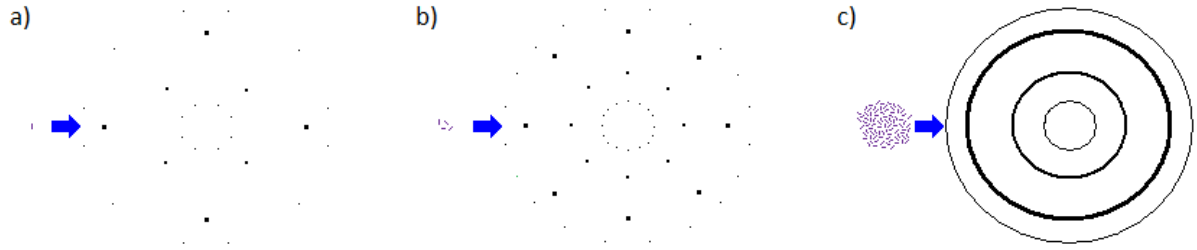

Figure 2.6 a) single crystal giving XRD spots, b) several differently orientated crystals causing extra rotated XRD spots, c) large number of crystals giving XRD rings

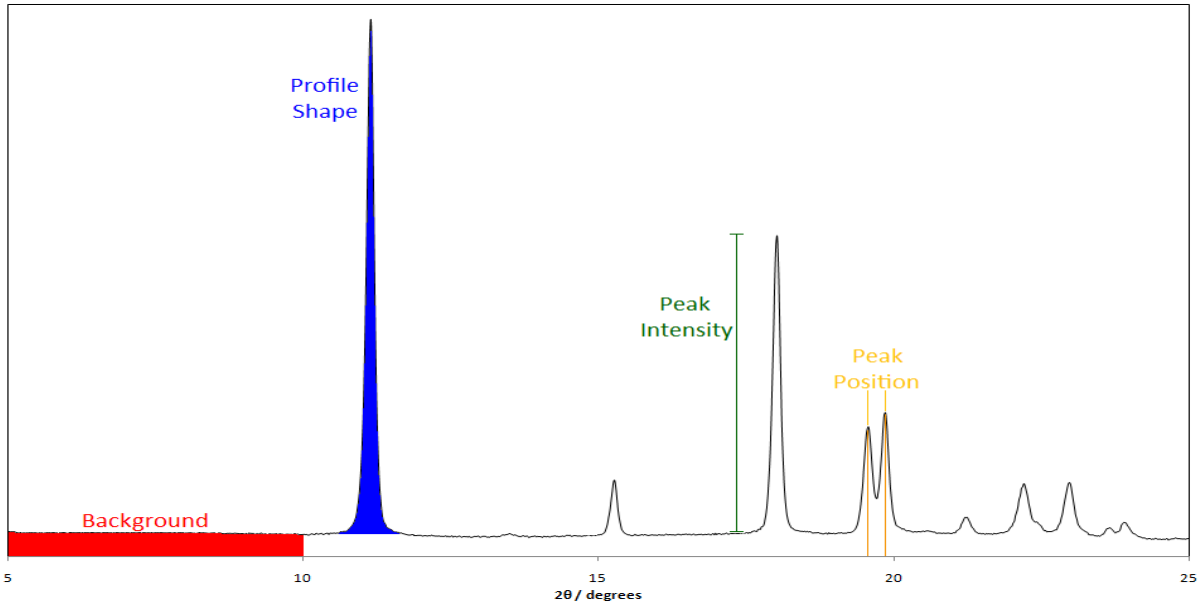

Figure2.7 *Aspects making up an XRD pattern*

The *Background* of an XRD pattern has an element caused through instrumental and experimental factors such as detector noise and the sample holder. The rest is a result of sample effects including things such as amorphous materials, incoherent scattering, local effects and X-ray absorbance and fluorescence. The background is usually disregarded during analysis of XRD patterns, although Pair Distribution Function analysis (see Section 2.6) utilises the diffuse scattering component.

The *peak positions* are determined by the phase's unit cell size and symmetry. Following Bragg's law the positions correspond to the separation distances of the lattice planes within the unit cell. The zero point error of the diffractometer used also has an effect on the peak position.

There are a number of contributing factors to a peaks *profile shape*. The diffractometers setup and radiation source have an effect, as does the phases crystallite size. For Bragg's law to be completely true the crystallite size must be effectively infinite, a finite sized crystal will spread the diffracted intensity over a small region related to its size and

shape. The amount of broadening resulting from the sample can be used to estimate the crystallite size using equations such as the Scherrer equation[11-13]:

$$\tau = \frac{K\lambda}{\beta \cos\theta} \qquad \textbf{Equation 4}$$

Where K is the shape factor (typically around 0.9), λ the X-ray wavelength, β the line broadening at full width half maximum of the diffraction peak, θ the Bragg angle of the diffraction peak and τ the mean size of the crystallite.

The *peak intensity* is affected in several ways by many different factors. The intensity can be expressed by various forms of the equation[14-16]:

$$\mathrm{I}_{hkl} = KF_{hkl}^2 mALP \qquad \textbf{Equation 5}$$

Where:

- F_{hkl} is the structure factor, the most important factor affecting the intensity of a diffracted peak. It represents the sum of the scattering power of all the atoms present within the unit cell.
- K is a proportionality constant
- m is the multiplicity of the *hkl* planes, accounting for the number of planes contributing to the same reflection, e.g. (100), (010) and (001) in a cubic system have the same d-spacing and contribute to the same peak in an XRD pattern
- A is the absorption factor, accounting for the amount of incident and diffracted X-rays that are absorbed by the crystalline material. This amount depends on a number of factors, such as the thickness of the sample and diffraction geometry
- L is the Lorentz factor, a geometric factor varying with θ, correcting for the diffractometer geometry

- P is the polarisation factor, accounting for the polarisation of the X-ray beam. This is often combined with the Lorentz factor.

There are still, however, other factors influencing the intensities observed in XRD patterns. As mentioned previously a small crystallite size broadens a peaks profile shape, this in turn causes a reduction of the peaks intensity. If a phase consists of crystallites containing one long crystal axis, often giving it a needle or plate like appearance (such as AlTP), the crystallites may align with each other, rather than having a completely random orientation as expected in a powder. This phenomenon is known as preferred orientation and increases the amount of diffracted intensity from lattice planes in the aligned crystallographic axis.

Experimental factors such as the collection time of the data and the intensity of the radiation source will define the absolute intensity of and XRD pattern. Multi-phased samples will have relative intensities of one phase to another, which will be dependent on the abundance of each phase.

2.3.3 Laboratory Diffractometers

Three different laboratory diffractometers were used throughout this project. A Siemens D5000 and a Brüker D8 were used routinely for the characterisation and identification of samples. For both diffractometers the sample was mounted on Scotch® 3M magic tape™, which gives negligible X-ray scattering, which was in turn attached to the diffractometers sample holder. A Siemens D5005 was used for variable temperature XRD studies. For the D5005 the sample filled a shallow alumina boat, which was inserted into the diffractometer furnace.

2.3.3.1 Siemens D5000

The D5000 operates with a copper X-ray tube and a germanium monochromator providing Cu $K_{\alpha 1}$ (λ = 1.54056 Å). The diffractometer is set up in transmission geometry, in

which the X-ray source is held in a constant position and the position sensitive detector (PSD) and sample are rotated through a circumference of between 5 – 100° 2θ. The PSD itself covers 8° 2θ and rotates with a step size of 0.02° 2θ. The samples were rotated in the plane perpendicular to the X-ray beam whilst data were being collected.

2.3.3.2 Brüker D8

Much like the D5000, the Brüker D8 operates in transition geometry, with a copper X-ray tube and germanium monochromator providing Cu $K_{\alpha1}$ radiation. The PSD is a more advanced solid state Linxeye model covering 3° 2θ and having a variable step size (around 0.02° was used for this project) and rotating through a circumference of between 2 – 90° 2θ.

2.3.3.3 Siemens D5005

The D5005 again contains a copper X-ray tube but employs a Göbel mirror as a wide beam monochromator. This removes the bremsstruhlung, but is unable to strip away the $K_{\alpha2}$, giving a mix of Cu $K_{\alpha1}$ and $K_{\alpha2}$ with an average wavelength of λ = 1.5418 Å. The diffractometer operates in a reflection (or θ-θ) geometry in which the sample is held in a constant position and the X-ray source and detector move synchronously through a range of 2θ. The static sample allows the D5005 to be fitted with various sample stages allowing diffraction to be carried out in different environments. In this project a high temperature Anton-Paar HTK 1200 stage, capable of temperatures up to 1000 °C, was used to monitor XRD '*in-situ*' at varying temperatures.

2.4 Neutron Diffraction

Neutrons that possess wavelengths of similar magnitude to the separation of atoms will undergo diffraction from crystalline materials following Bragg's law in a similar manner to X-rays. However, there is one significant difference, in that where X-rays interact with the electron cloud surrounding a nucleus, neutrons predominately interact with the nuclei

themselves. As a result neutron scattering power does not vary linearly with atomic number but follows a complex pattern[17]. This can lead to significant variation in scattering power between elements of similar atomic number and also different isotopes of the same element, especially in the case of hydrogen and deuterium. This makes neutron diffraction an excellent probe for light atoms, such as hydrogen and oxygen, even in the presence of heavier atoms.

Neutrons possess a spin and therefore a magnetic moment, meaning they can undergo magnetic scattering from paramagnetic atoms (atoms with unpaired electrons), resulting from interactions with the electron cloud. This magnetic scattering of neutrons gives information about the alignment of electron spins allowing determination of the magnetic unit cell and magnetic ordering of a crystal structure.

Neutrons are produced in two different ways leading to two types of experimental facilities. The first produces neutrons *via* spallation, a process in which a metal target is bombarded with high energy protons generating a pulsed neutron beam, commonly used in *time of flight* (TOF) neutron experiments. TOF experiments use diffraction from a range of wavelengths of the neutrons and detectors at fixed angles (θ) a known distance from the sample. The intensity of diffracted neutrons is then recorded as a function of the time of flight.

The second method involves the fission of uranium in a nuclear reactor, producing a continuous beam of high velocity neutrons, which need to be slowed with heavy water to produce wavelengths suitable for diffraction studies. Specific wavelengths can be selected by passing the beam through a monochromator (Cu, Ge or Si). This gives a continuous beam of neutrons with a constant wavelength and diffraction can be measured as a function of θ. These are known as *constant wavelength* (CW) experiments. This method of diffraction has a high loss of neutrons through the monochromation process, meaning longer periods of data

collection are often required to compensate for the low intensity of the neutron beam. All the neutron diffraction studies performed during this project were from constant wavelength experiments.

Both of these methods are expensive and therefore only available at national facilities. Neutron diffraction studies also require a large amount of sample, often using around 5g for each experiment.

Neutron diffraction studies in this study were performed at the Institut Laue Langevin (ILL) in Grenoble, France on the D2B high-resolution two-axis diffractometer. D2B (Figure 2.8) is fitted with a Ge monochromator, allowing the selection of wavelengths in the range 1.05 Å to 2.4 Å (a wavelength of 1.59432 Å was used during experiments in this project), and 64 detectors spaced at 2.5° intervals.

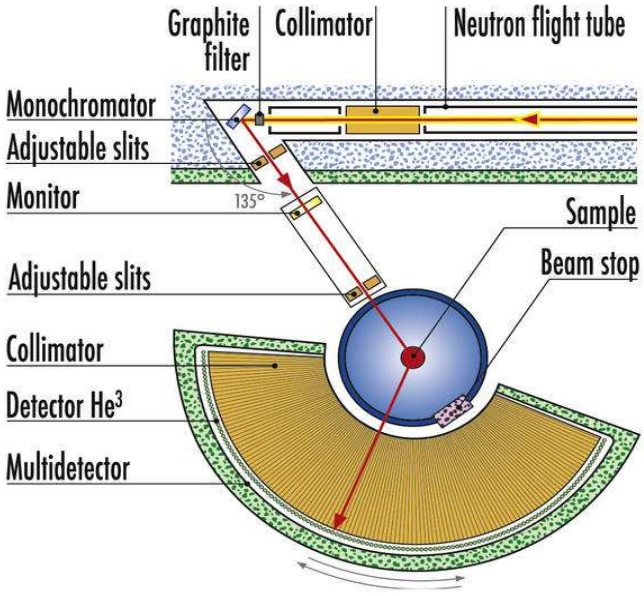

Figure 2.8 *Layout of instrument D2B at the ILL*[18]

2.5 Rietveld Analysis

Until the late 1960s unless a material possessed high symmetry with no overlapping Bragg peaks in its powder pattern, or single crystal diffraction could be preformed, detailed

structural analysis was often problematic and limited to simple pattern matching. This was overcome in the late 1960s when Rietveld proposed a technique to refine nuclear and magnetic structures from neutron powder diffraction data[19, 20], which was afterwards adapted for use with powder X-ray diffraction data and is now commonly known as Rietveld analysis or the Rietveld method[21].

The Rietveld method requires a full structural model, containing a unit cell, spacegroup and atom positions, which is combined with instrument parameters such as wavelength to calculate a powder pattern. This model is then modified and refined to obtain the best fit between the calculated powder pattern and the real observed pattern. The method uses nonlinear least-squares refinement to fit observed intensities, y_i, for all data points, i, in the powder pattern through:

$$S_y = \sum_i w_i (y_i - y_{ci})^2 \qquad \textbf{Equation 6}$$

Where S_y is the residual, y_i is the observed intensity of the i^{th} data point and y_{ci} is the calculated intensity of the i^{th} data point and w_i is the weight assigned to the i^{th} data point which is equal to y_i^{-1} in the absence of a background.

The quality of fit of a Rietveld refinement can be assessed visually with a difference plot of the observed and calculated powder patterns, which ideally should be a flat line. There are also a number of statistical Figures of merit, known as R-factors, used to evaluate the quality of fit including the Bragg residual, R_B:

$$R_B = \frac{\sum |I_{hkl} - I_{chkl}|}{\sum I_{hkl}} \qquad \textbf{Equation 7}$$

Where I_{hkl} and I_{chkl} are the observed and calculated intensity of Bragg peaks respectively. The Bragg residual is based upon the intensity of the Bragg peaks determined by the unit cell, and

is therefore a good indication of the accuracy of the staring model. There are also several R-factors based on the whole pattern such as R-profile:

$$R_p = \frac{\sum|y_i - y_{ci}|}{\sum y_i} \quad \textbf{Equation 8}$$

And R-weighted profile:

$$R_{wp} = \left[\frac{\sum w_i(y_i - y_{ci})^2}{\sum w_i(y_i)^2}\right]^{\frac{1}{2}} \quad \textbf{Equation 9}$$

And the R-expected:

$$R_{exp} = \left[\frac{N - P - C}{\sum w_i(y_i)^2}\right]^{\frac{1}{2}} \quad \textbf{Equation 10}$$

Where y_i and y_{ci} are the observed and calculated intensity of the i^{th} data point respectively, w_i is the weight assigned to the i^{th} data point, N is the number of observables, P is the number of refined parameters and C the number of constrains used.

Combining R_{wp} and R_{exp} gives the 'goodness of fit' value, χ^2, which in a perfect refinement would equal one, but in reality this is not achieved.

$$\chi^2 = \left[\frac{R_{wp}}{R_{exp}}\right]^2 \quad \textbf{Equation 11}$$

There are a several pieces of software available for performing Rietveld refinements. The most widely used are the freely available GSAS suite of programs[22], which were used in this project. Other programs include Fullprof[23] and the newer commercially available Topas[23].

2.6 Pair Distribution Function Analysis

While XRD and Rietveld analysis are effective tools for analysing crystalline material, they are much less effective for materials with poorer long-range order such as glasses, nanocrystals and amorphous materials. Pair distribution function analysis[24-26] (PDF),

however, is a total scattering technique combining both Bragg and diffuse scattering, which enables probing of the short and medium range order of less crystalline materials.

PDF uses the Fourier relationship between the real-space arrangement of atom pairs and diffraction intensities. It can be defined either as a Fourier transform of scattered X-ray or neutron intensities, or directly defined in real-space in terms of atomic coordinates. This latter definition makes PDF an intuitive function as PDF peaks result directly from the distances between atom pairs, i.e. a peak with an *r* value of 2 Å represents a distance of 2 Å between two atoms.

Both X-rays and neutrons can be used in PDF experiments, although the X-ray experiments are almost exclusively preformed with synchrotron X-rays. This is because to provide high accuracy and adequate real-space resolution of the PDF peaks, it is important to measure data over a wide range of q-space (Q), typically 25-50 $Å^{-1}$, and as $Q = 4\pi \sin\theta / \lambda$ (for elastic scattering), high energy, short wavelength X-rays or neutrons are required. X-rays between λ = 0.12 Å and λ = 0.27 Å (100 keV and 45 keV respectively) are typically used, thus mostly ruling out laboratory X-ray sources, though lab based diffractometers are being developed using Mo and Ag X-ray sources to allow in-house PDF.

The atomic PDF, G(*r*), can be defined from the atomic pair density, $\rho(r)$, the average atomic number, ρ_o, and a radial distance, *r*, through the equation:

$$\mathrm{G}(r) = 4\pi r[\rho(r) - \rho_o] \qquad \textbf{Equation 12}$$

It is also possible to obtain G(*r*) experimentally as it relates to the measured X-ray / neutron diffraction pattern through the Fourier transform:

$$\mathrm{G}(r) = (2\pi) \int_{Q=0}^{Q_{max}} Q[S(Q) - 1] \sin(Qr) dQ \qquad \textbf{Equation 13}$$

Where S(Q) is the total scattering structure function, containing the measured intensity from an isotropic sample, which is in turn calculated through the equation:

$$S(Q) = \frac{I^{coh}(Q) - \sum c_i |f_i(Q)|^2}{|\sum c_i f_1(Q)|^2} + 1 \qquad \textbf{Equation 14}$$

Where $I^{coh}(Q)$ is the measured scattering intensity from a sample which has been corrected for experimental effects and normalised by the flux and number of atom in the sample. c_i and f_i are the atomic concentration and X-ray form factor respectively for the atomic species *i*. For neutron experiments the *f* terms are replaced by *b* terms which are Q-independent neutron scattering lengths and the sums are run over all isotopes and spin states in the sample as well as the atomic species.

Structural models can be refined against G(*r*) in a similar fashion to that of Rietveld refinement with X-ray diffraction. Various programs[27-29] exist to do this, such as PDFFIT[30], which uses least-squares refinement similar to Rietveld. Unlike Rietveld refinement, which can only use long range order to give an average structure, PDF can be used to refine long, medium and short range order by refining different ranges of *r*. This allows structural refinement of local as well as average structure, and allows structural probing of local defects within a material, and of glasses and amorphous materials with no long range order.

PDF data for this project were collected at station 11-ID-B at the Advanced Photon Source (APS), Argonne in Chicago by Dr. Joseph Hriljac, Dr. Jennifer Readman and Victoria Burnell. The instrument is capable of delivering synchrotron X-rays at a range of wavelengths (λ = 0.13702 Å was used for this project) and is fitted with a silicon monochromator and germanium amorphous silicon image plate detector.

2.7 Thermogravimetric Analysis

Thermogravimetric analysis (TGA) is a technique used for monitoring mass changes of a material as a function of temperature. TGA analysers themselves are, effectively, very accurate weighing balances (±0.00005g) inside a furnace, which continually record the mass of a sample as the temperature is increased, decreased or held constant over a period of time. Analysers are capable of operating under a number of different environments such as normal air, N_2, O_2, H_2, etc, or under vacuum.

Most TGA analysers also have a differential thermal analysis (DTA) unit, which monitors heat flow and energy changes within the material being studied. This is achieved through comparison to a reference material (such as α-Al_2O_3) throughout the experiment. DTA can be used to monitor phase changes in a material as a function of temperature and is particularly useful for polymorphic phase changes where no changes in mass are observed but endo- or exothermic events occur. The technique can be calibrated to give accurate quantitive values for thermal events, or, as in the case of this project, simply to indicate if a thermal event is exo- or endothermic.

All measurements in this project were performed with a small amount of sample (~20-40 mg) placed in an alumina boat, which was in turn mounted on a fine platinum balance within the TGA analyser. This was then heated, in an atmosphere of air, at a rate of 3 °C/min to a set temperature where it was held over a 30 minute period. The measurements in this project were performed using a Rheometric Scientific STA 1500, and the changes in mass of the ion exchanged AlTP samples used to calculate the content of water in each phase.

2.8 Scanning Electron Microscopy

The study of the topology of a material's surface is often important in many fields of science. Optical microscopy is the classical method of studying surfaces, but has limited

resolution. Scanning electron microscopy[31] (SEM) allows a greater depth of focus and better resolution allowing materials to be viewed at over 100,000 times magnification.

A high energy electron beam (typically above 10kV) is scanned across the surface of a material, causing the generation of low energy secondary electrons, many of which escape the surface. These secondary electrons are attracted to a phosphor screen, causing it to glow. The intensity of this light is measured by a photomultiplier tube and converted into an image. Samples which are good electron conductors are easiest to study as the unimpeded flow of electrons aids the process. Poorly conducting samples may be coated in a thin film of gold or carbon to aid their conductivity, but there is a delicate balance between the thickness of this coating and obstructing the surfaces features.

SEM units operate under high vacuums (typically 10^{-4} Torr or less), as the molecules in an atmosphere would scatter the secondary electrons affecting the images being produced. This causes problems for hydrated samples such as AlTP as the high vacuum can cause decomposition of the sample. These problems have been overcome with the development of environmental scanning electron microscopy[32, 33] (ESEM), which operate under low vacuum, allowing vapour pressure of up to 10 Torr and relative humidity of up to 100%, allowing hydrated samples to remain stable.

Samples observed in this project were thinly applied to a sticky carbon pad and coated with a thin layer of carbon. These were then observed using a Philips XL30 ESEM-FEG operating at 4.6 Torr with a 15.0 kV electron beam at the Electron Microscopy Centre at the University of Birmingham.

2.9 Energy Dispersive X-ray Spectroscopy

Energy dispersive X-ray spectroscopy[34] (EDX) is a technique to determine the elemental composition of a material using X-rays. An EDX system can be attached to both

SEM and ESEM systems, allowing the microscopes to be described as analytical electron microscopes (AEM).

An electron beam, typically in the energy range 10-20 kV, is scanned across the surface of the material under investigation, causing the elements making up the material to emit X-rays. These X-rays strike the SiLi semiconductor detector, which generates a pulse of current proportional to the energy of the X-ray, thus allowing an X-ray spectrum to be created giving information on the materials elemental composition.

The silicon-lithium detector is usually protected by a beryllium window, which absorbs X-rays produced by elements with an atomic number below 11, making detection of elements below sodium difficult.

2.10 Flame Emission Photometry[35]

This technique has its basis in the simple flame test and the century old knowledge that flames produced from the combustion of gases are capable of exciting elements to emit characteristic radiation. It uses a flame as a source of energy to first vaporise a compound into a molecular gas and then dissociate this into a gas of free atoms. A fraction of these free atoms then absorb further energy and enter an excited state. When the atoms return to the ground state they re-emit this energy as a characteristic atomic line spectrum (Figure 2.9). If the excitation conditions are kept constant, the intensity of the emission of characteristic wavelengths is proportional to the concentration of the element.

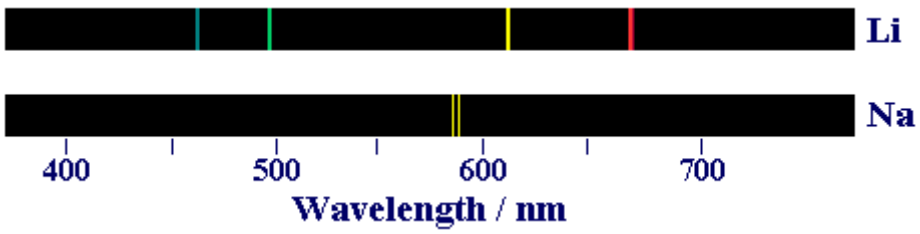

Figure 2.9 *Atomic line spectra for lithium and sodium (adapted from[36])*

Flame photometry instruments (Figure 2.10) usually consist of a nebuliser/flame unit which draws sample solutions from a reservoir and passes them through a mixing chamber to convert them to an aerosol, before spraying them into the flame. The emitted light is focused and passed through an element specific filter, after which it falls on a photodiode detector which produces an electric signal proportional to the radiation's intensity. This signal is then amplified and passed to a readout system. In this project, lithium and sodium ion exchanged species were dissolved in 0.1 M HNO_3 and measurements were taken using a Corning 400 flame photometer.

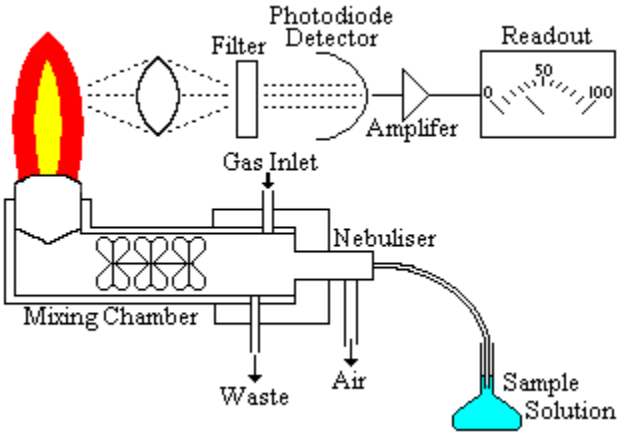

Figure 2.10 *Layout of a flame photometer*

2.11 HCN Elemental Analysis

HCN elemental analysis is a technique used to determine the amounts of hydrogen, carbon and nitrogen within an organic or inorganic sample. The technique combusts small amounts (5-20 mg) of a solid sample, at temperatures above 900 °C, under a flow of pure oxygen gas. This converts hydrogen, carbon and nitrogen to their respective oxides, which are passed into a gas chromatographer which analyses the amounts present, giving results as a percentage of the original sample.

The measurements in this project were performed upon a CE Instruments EA1110 elemental analyser and used to determine the amounts of organic molecules intercalated into AlTP phases.

2.12 Fourier Transform Infrared Spectroscopy

Infrared spectroscopy involves exposing a sample to a beam of infrared radiation, which has energy of the order of magnitude required to cause vibrations in chemical bonds. When the energy of an incident photon is equal to that of the energy gap between vibrational states, it may be absorbed causing the molecule to vibrate. For these vibrations to be infrared active they must cause a change in the molecular dipole moment of the molecule (Figure 2.11).

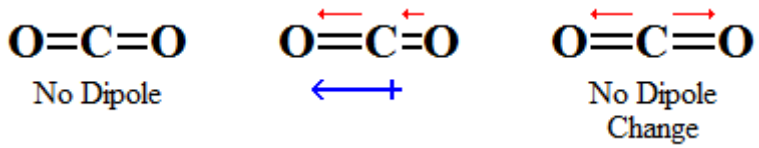

Figure 2.11 *Different vibrations affecting the molecules dipole moment*

The absorption of IR is measured in reciprocal centimetres (cm^{-1}), with typical IR spectra recorded over a region of 400 to 4000 cm^{-1}. The IR spectrum is affected by several factors such as molecular symmetry which can render some vibrations forbidden, whereas others are caused to be degenerate. The frequency vibrations occur at, relates to the strength of the absorbing bond and the mass of the atoms forming it, which allows these absorptions to be assigned to specific chemical groups.

Fourier transform infrared (FTIR) spectroscopy involves exposing a sample to all wavelengths of infrared radiation simultaneously. Fourier transform calculations are then performed upon the resulting waveform, separating it into its component wavelengths to provide a spectrum.

FTIR measurements in this project were recorded using a Varian 660-IR FTIR spectrometer fitted with a Pike MIRacle attenuated total reflectance (ATR) attachment. This spectrometer uses a ceramic Mid-IR source, capable of delivering a spectral range of 7900 – 375 cm^{-1}, and is fitted with a KBr beam splitter and a DLaTGS (deuterated L-alanine doped triglycene sulphate) detector. The IR beam is passed through a diamond prism in the ATR unit, where it is reflected to penetrate a small distance into the sample clamped to the prism's surface. Absorption of IR radiation occurring in this arrangement is equivalent to a transmission arrangement.

References

1. S. K. Rishi, B. M. Kariuki, N. J. Checker, J. Godber and A. J. Wright, *Chem Comm*, 2006, 747.
2. S. K. Rishi, Ph.D thesis, University of Birmingham, 2006.
3. G. Burns and A. M. Glazer, *Space Groups for Solid State Scientists*, Academic Press, 1978.
4. P. A. Chater, Ph.D thesis, University of Birmingham, 2010.
5. T. Hahn (editor), *International Tables for Crystallography, Volume A: Space-group symmetry 5th Edition*, Springer, 2005.
6. W. L. Bragg, *Proce. Cambri. Philos. Soc.*, 1912, **17**, 43.
7. JCPDS, *International Centre for Diffraction Data*, P.1., Swathmore, Pensylvania, PA 19081, USA, 11990.
8. A. R. West, *Solid State Chemistry and it's Applications*, John Wiley Sons, 1985.
9. V. K. Pecharsky and P. Y. Zavalij, *Fundamentals of Powder Diffraction and Structural Characterisation of Matrials*, Springer, New York, 2005.
10. J. P. Glusker and K. N. Trueblood, *Crystal Structure Analysis: A Primer 2nd edition*, Oxford University Press, Oxford, 1985.
11. P. Scherrer, *Göttin. Nachri.*, 1918, 394.
12. J. I. Langford and A. J. C. Wilson, *J. Appl. Crystallogr.*, 1978, **11**, 102.
13. A. L. Patterson, *Phys. Rev.*, 1939, **56**, 978.
14. The University of Oklahoma, *Chemical Crystallography Lab*, http://xrayweb.chem.ou.edu/notes/crystallography.html.
15. C. G. Darwin, *Philosop. Mag.*, 1914, **27**, 315.
16. P. P. Ewald, *Zeitsch. Kristallogr.*, 1921, **56**, 129.
17. W. Marshall and R. D. Lowde, *Rep. Prog. Phys.*, 1968, **31**, 705.
18. Institut Laue Langevin, http://www.ill.eu.
19. H. M. Reitveld, *Acta Crystallogr.*, 1967, **22**, 151.
20. H. M. Reitveld, *J. Appl. Crystallogr.*, 1969, **2**, 65.
21. R. A. Young (editor), *The Reitveld Method*, Oxford University Press, Oxford, 1993.
22. R. B. Von Dreele and A. C. Larson, *General Structure Analysis System*.
23. J. Rodriguez-Carvajal and T. Roisnel, *FullProf.98 and WinPLOTR: New Windows 95/NT Applications for Diffraction Commission For Powder Diffraction*, International Union for Crystallography, Newsletter N20, 1998.
24. B. H. Toby and S. J. L. Billinge, *Acta Crystallogr. A*, 2004, **A60**, 315.
25. T. Egami and S. J. L. Billinge, *Underneath the Bragg-Peaks: Strucural Analysis of Complex Materials*, Plenum, Oxford, 2003.
26. S. J. L. Billinge and M. G. Kanatzidis, *Chem. Comm.*, 2004, 749.
27. R. L. McGreevy and L. Pusztai, *Molecul. Simul.*, 1988, **1**, 359.
28. A. K. Soper, *Chem Phys*, 1996, **202**, 295.
29. W. Schweika, *Disordered Alloys: Diffuse Scattering and Monte Carlo Simulations*, Springer Verlag, New York, 1998.
30. T. Proffen and S. J. L. Billinge, *J. Appl. Crystallogr.*, 1999, **32**, 572.
31. *UK Surface Analysis Forum*, http://www.uksaf.org/.
32. G. D. Danilatos, *Advan. Electronic. Electron Phys.*, 1988, **71**, 109.
33. G. D. Danilatos and G. C. Lewis, *US Pat. 4823006*, 1989.
34. L. Reiner, *Scanning Electron Microscopy, 2nd Edition*, Springer, 1998.
35. E. Pungor and R. A. Chalmers, *Flame photometry theory*, London; Princeton, N.J: Van Nostrand, 1967.
36. T. P. Softley, *Atomic Spectra*, Oxford Chemistry Press, Oxford, 1994.

Chapter 3

Monovalent Ion Exchange in $AlH_2P_3O_{10}\cdot 2H_2O$

3.1 Introduction

Ion exchange was discovered to occur in soils over 160 years ago by Thompson[1] and Way[2]. Later the active compounds were found to be zeolites, clays, glauconites and humic acids[3, 4]. For several decades it was believed to be a property limited to very few types of inorganic compounds. As work progressed in the area, it became apparent that many different compounds possess ion exchange properties[5], including a number of phosphates and layered phosphates. The property has led to or become important in a large number of technologies and technological research areas. These include water softeners and molecular sieves, ionic conductors for use in batteries and fuel cells, nuclear waste management and catalysis.

Of all the layered phosphates, α-ZrP has received the most attention with regard to its ion exchange properties[6-8]. As mentioned in Chapter 1.5.1.1, α-ZrP contains terminal hydroxide groups within its inter-lamellar region, which provide the potential for exchange, with the topology of the inter-lamellar region affecting the kinetics and properties[9, 10].

All of the alkali metals have been exchanged into α-ZrP to varying extents[11-14]. Sodium and potassium form two phases with half exchange and full exchange achieveable[15],

shown by the plateaus in the uptake curves (Figure 3.1). Rubidium and caesium show no significant exchange until higher pHs are reached, where they first form a three quarters exchanged form then a fully exchanged form at around pH 11. This difference in behaviour between the different ions is explained by the structure of α-ZrP. The passageway between oxygens in the inter-lamellar region is 2.62 Å[11], a space which is sufficient to readily allow sodium and potassium ions into the inter-lamellar region to facilitate exchange, but the larger rubidium and caesium ions ingression is limited. For rubidium and caesium to exchange, the phosphate layers must first spread apart, the energy for which is supplied by a base, increasing pH and neutralising the lattice protons[16].

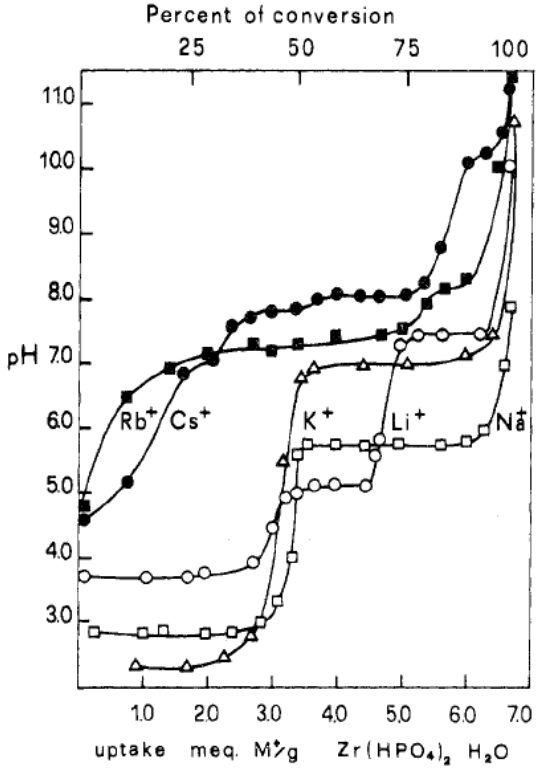

Figure 3.1 *Uptake curves with pH for the alkali metals in α-ZrP*[17]

Alberti also found the larger cations could be exchanged into α-ZrP at lower pH if small amounts of sodium salts were added to the exchanging solution[18]. He found sodium acted as a catalyst, by exchanging into the inter-lamellar region and expanding it making it easier for the larger cations to enter. These sodium ions are then replaced by the larger cations and return to the exchange solution.

Clearfield and Troup have studied lithium exchanged into α-ZrP[19] and found the uptake occurred in several steps (Figure 3.1) similar to the other alkali metal exchanges into α-ZrP. Unlike these other alkali metals, which can all form two phases of either half, three-quarter or full ion exchange, lithium exchange was able to form all three phases. Studies have also shown that lithium exchanged phases can be reversibly formed through exchange from other cation exchanged forms of α-ZrP[20, 21].

Clearfield and Cheng reported a silver exchanged α-ZrP phase[22]. They found reacting α-ZrP with $AgNO_3$ resulted only in a fully exchanged phase with no intermediate half exchanged phase. Bernasconi *et al* successfully isolated a half silver exchanged α-ZrP[23] by exchanging from $ZrNaH(PO_4)_2\cdot 5H_2O$.

As discussed previously (Chapter 1.6.1), AlTP shares a number of structural similarities to α-ZrP, most importantly, perhaps, the terminal hydroxide group in the inter-lamellar region. The presence of this gives AlTP similar ion exchange potential as seen in α-ZrP, with a capacity of 6.35 mmol g^{-1}, comparable to that of α-ZrP (6.71 mmol g^{-1}) and zeolites (3-7 mmol g^{-1}), and higher than a number of other types of ion exchangers such as smectic clays (0.5-1.5 mmol g^{-1}), ferrocyanides (1.1-6.1 mmol g^{-1}) or hydrous oxides (1-5 mmol g^{-1})[5].

A small number of studies have been undertaken into the ion exchange properties of AlTP. The original report of AlTP[24] made reference to two sodium exchanged phases, $AlNa_2P_3O_{10}\cdot 4H_2O$ and $AlNa_2P_3O_{10}\cdot 2H_2O$. These were again studied by Lyutsko in 1983[25], but details of how the ion exchange was achieved are unclear.

The ammonium ion has also been exchanged into AlTP. There have been two different phases reported with this ion, $AlNH_4HP_3O_{10}$[26] and $Al(NH_4)_2P_3O_{10}$[27]. The half exchanged form reported was formed directly with an acid flux using $(NH_4)_2HPO_4$, rather

than through ion exchange. This allowed Averbuch-Pouchot to obtain a single crystal large enough to provide a full crystal structure of this phase[26]. The fully exchanged form reported by Lyutsko was synthesised through ion exchange of the sodium phase and has no reported structural characterisation[27].

There have also been reports of silver exchanged AlTP. Hayashi *et al*[28] synthesised the phase with a view to intercalating small gaseous thiols and sulphides. They quantified the amount of Ag^+ exchanged by analysing the supernatant solution after equilibrium and determined up to 87% of the potential exchange had been achieved. They also concluded the amount exchanged was dependent on the concentration of the aqueous $AgNO_3$ exchange solution. No attempts were made in this study to provide any structural characterisation of the exchanged phase.

The silver exchanged AlTP phase has also been investigated by Rishi[29], who made no attempt to quantify the amount of silver exchanged, attempting instead to gain insight into the structural details of the phase. He assigned a possible monoclinic unit cell to the phase with parameters of a = 8.5679(8) Å, b = 4.9268(5) Å, c = 11.5048(12) Å and β = 96.14(1) °. This unit cell is consistent with that of the original AlTP[30] (a = 7.9381(3) Å, b = 4.9188(2) Å, c = 11.6286(4) Å and β = 95.739(2) °) but was unable to index a number of peaks in the XRD pattern, including a few of significant intensity. Rishi suggested this may be a result of the incomplete exchange resulting in the silver arranging in an incommensurate manner.

Rishi has also studied lithium exchange into AlTP[29], stirring AlTP in $LiNO_3$ solutions varying the Li:Al ratio and monitoring the lithium uptake using X-ray diffraction and flame photometry. After the exchange reactions he observed changes in the XRD patterns, most notably a shift in the d_{100} peak to lower 2θ values indicating the interlayer spacing had

increased. This peak occurred at different 2θ values for the exchanges performed at 5:1 and 25:1 $Li_{(aq)}$:$Al_{(s)}$ ratios, with the intermediate ratios displaying split peaks, Figure 3.2.

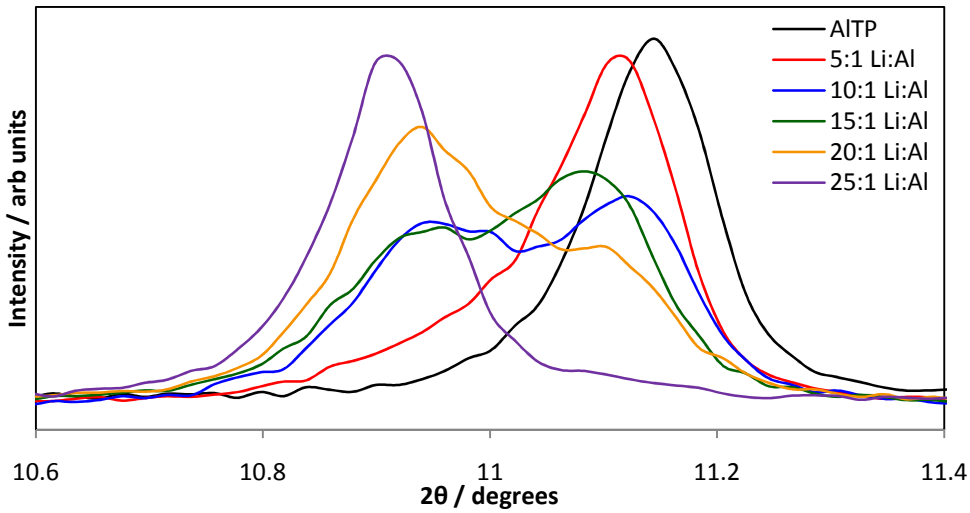

Figure 3.2 *XRD plots showing d_{100} peaks for AlTP and various Li:Al ratio exchanges (adapted from[29])*

Rishi concluded from this that the lithium exchange occurred via two steps, with the amount of lithium incorporated dependent upon the Li:Al giving a 'high loaded' and a 'low loaded' phase, with the intermediate ratios giving a mix of the two. This conclusion was validated by flame photometry which showed the 5:1 Li:Al ratio to give around 3.9% of the maximum possible exchange (6.35 mmol g^{-1}), whereas the 25:1 Li:Al and above ratios showed around 10% exchange. The observation of different levels of lithium loading is inconsistent with other exchanged cations in AlTP, but is consistent, albeit it at much lower loadings, with lithium exchange in α-ZrP[17].

Rishi indexed unit cells to the two different loaded phases, shown in Table 3.1. These showed an increase in the *a* parameter as would be expected from exchanging in a larger ion.

Table 3.1 *Unit cells for lithium exchanged AlTP phases[29]*

Phase	a / Å	b / Å	c / Å	β / °	Volume / $Å^3$
AlTP	7.9381(3)	4.9188(2)	11.6286(4)	95.739(2)	451.77(3)
Low loaded	7.968(3)	4.928(1)	11.656(4)	95.78(1)	455.45(3)
High loaded	8.1373(4)	4.9110(2)	11.5652(4)	96.44(2)	459.3(2)

This chapter initially focuses on a detailed study into the reported sodium exchanged AlTP phases to clarify their formation via exchange methods. Then the focus moves to the synthesis and characterisation of a wide range of monovalent exchanges in AlTP. This includes further studies on increasing the amount of lithium incorporated into AlTP. In all studied exchange reactions the products are indexed to provide unit cells in order to better understand the structural implications of the exchange.

3.2 Experimental

Sodium and potassium exchanges were achieved by stirring 0.5g of AlTP in 50ml of an aqueous solution of MCl and MOH containing a M:Al ratio of 25:1 with a 9:1 Cl:OH ratio. Rubidium, caesium and potassium exchanges were achieved by stirring 0.5g of AlTP in 50ml aqueous solutions of MCl and M_2CO_3 also with a M:Al ratio of 25:1 and 9:1 M:M ratio for the chloride and carbonate respectively. Silver exchange was affected by stirring 0.5g AlTP in a 50ml solution of $AgNO_3$ with a 25:1 Ag:Al ratio. The ratio of 25:1 is based on Rishi's findings with lithium showing this to be the lowest ratio to give the higher loading[29]. For all these systems it was found that reactions could be scaled to >5g of AlTP but required extra time (often several days) before complete exchange was achieved.

A number of different methods have been undertaken to exchange lithium into AlTP. These included adding base to the exchanging solution, refreshing the exchanging solution, increasing the concentration of the exchanging solution and varying the Li:Al ratio. The exact methods will be discussed alongside their resulting lithium uptake in Section 3.8. All experiments involved stirring 0.5g of AlTP in a 50ml exchanging solution, with 25:1 Li:Al, unless otherwise stated, for 24 hours.

3.3 Sodium Exchange

Initial attempts to obtain a sodium exchanged phase involved stirring AlTP in NaCl solutions, however this provided no evidence of exchange in resulting XRD patterns. Following success in α-ZrP, it was decided to add a base into the exchange solution, with the belief that a higher pH would facilitate the removal of H^+ from the layers, thus facilitating a more facile exchange reaction. The addition of NaOH to the solution had an immediate effect upon the XRD pattern (Figure 3.3) (see Appendix 1 for comparison to other exchanged phases), showing only the reported $AlNa_2P_3O_{10}\cdot 4H_2O$[24] (AlTP-Na·4) with no residual AlTP present.

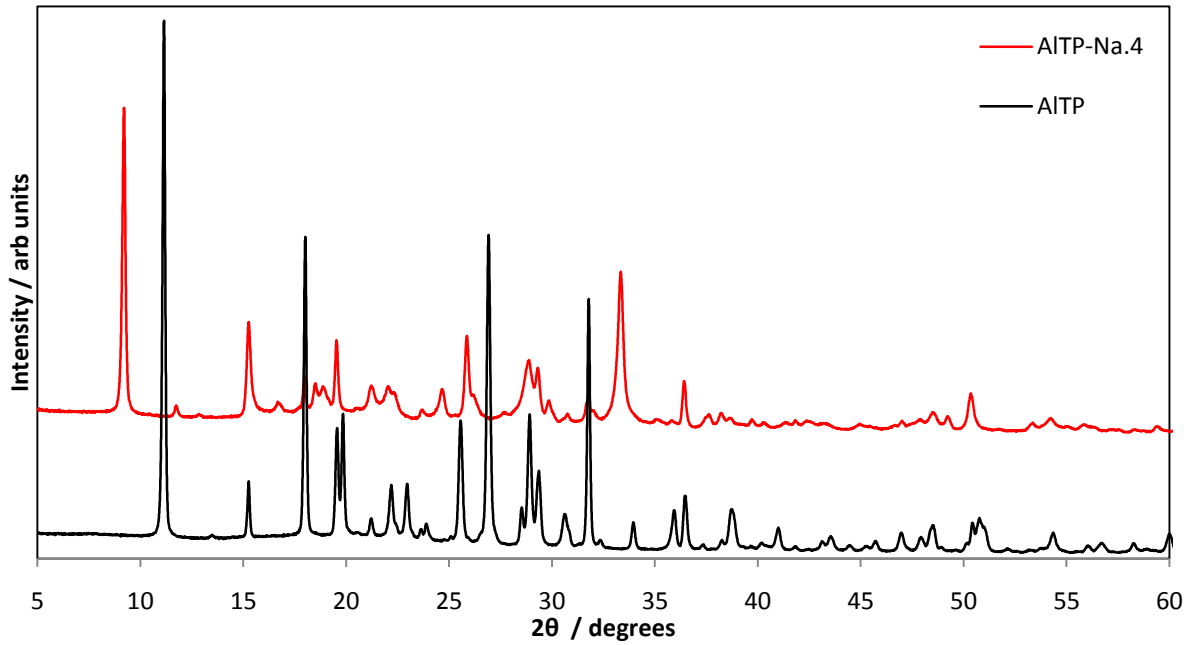

Figure 3.3 *XRD patterns of red) AlTP-Na·4 and black) AlTP*

To confirm the amount of sodium exchanged into the phase, flame photometry was undertaken. This confirmed that the phase had effectively undergone complete sodium exchange (for details see Appendix 2).

Attempts were made to index a unit cell to this phase with the aid of the computer programs Crysfire[31], DSPACE[32] and CELL[33]. Despite numerous attempts, these failed to provide a feasible unit cell for this phase.

Thermogravimetric Analysis (TGA) and Differential Thermal Analysis (DTA) were preformed to ascertain the water content of the phase (Figure 3.4). This showed the water loss occurs in two steps. The first, with an associated thermal event at around 70 °C, corresponds to the loss of two formula waters losing 8.7 wt% (9 wt% calculated for two waters per formula unit). The second at around 170 °C was also consistent with two formula waters losing 8.96 wt% (9.06 wt% calculated). This coupled with the flame photometry, confirmed the phase's stoichiometry to be $AlNa_2P_3O_{10}\cdot 4H_2O$.

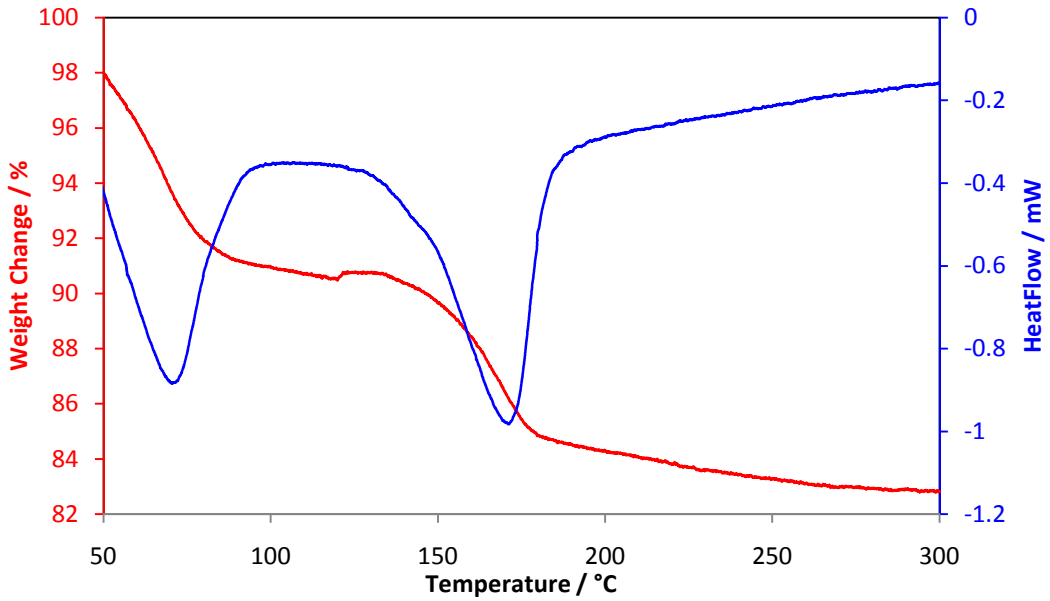

Figure 3.4 *TGA & DTA plot of AlTP-Na·4*

Given the earlier reports[24] of a second sodium phase with a different water content and the clear plateau between the two water loses in the TGA data, attempts were made to isolate the second phase. This was achieved by heating AlTP-Na·4 to 100 °C for 12 hours, the resulting product, with XRD pattern shown in Figure 3.5, being confirmed with TGA and flame photometry to be $AlNa_2P_3O_{10}\cdot 2H_2O$ (AlTP-Na).

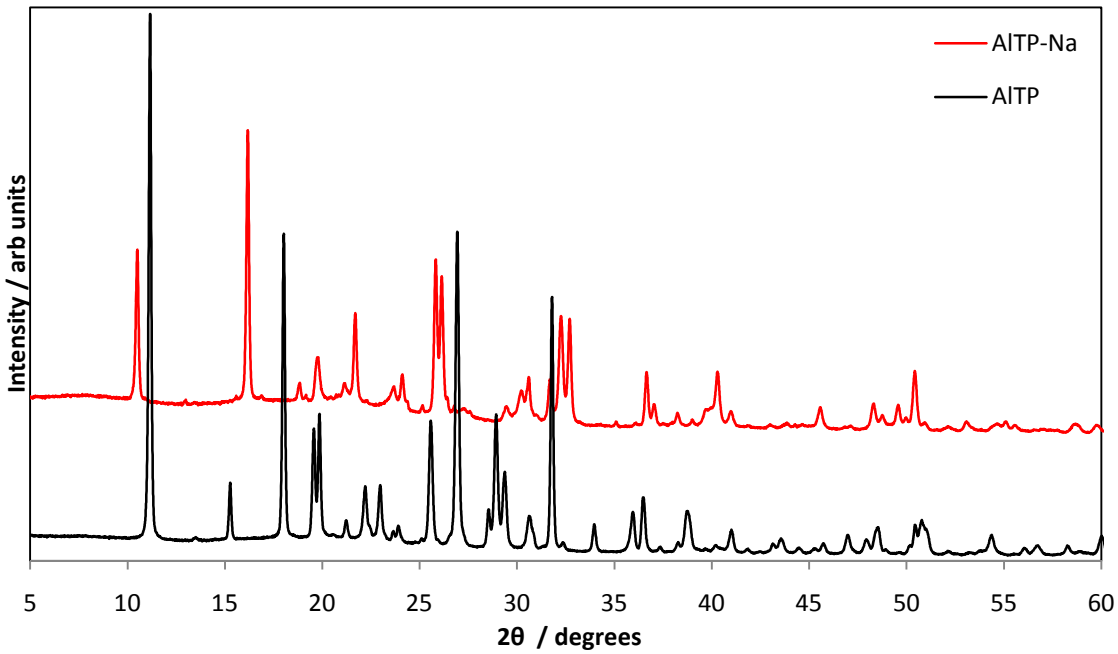

Figure 3.5 *XRD pattern of red) AlTP-Na and black) AlTP*

A sample of AlTP-Na was then dehydrated at 250 °C for 12 hours, giving a third phase with a different XRD pattern, and left exposed to the atmosphere. After 3 days this sample had completely rehydrated to the AlTP-Na phase. Prolonged exposure to the atmosphere did not result in the original four-watered AlTP-Na·4 phase being reformed, even after several months. In addition, submersion of AlTP-Na in water and refluxing for 7 days, failed to rehydrate to the level of four waters, confirming the initial loss of water is irreversible. This shows the AlTP-Na·4 phase to be metastable, with AlTP-Na being the favoured phase in the system. AlTP-Na·4 may provide a more readily exchangeable material for subsequent ion exchange reactions given the higher water content, increased inter-layer spacing and its limited stability.

Using the aforementioned methodology, a monoclinic unit cell, with parameters a =17.625(5) Å, b = 4.916(1) Å, c = 11.620(4) Å and β = 107.89(1) °, was indexed for the AlTP-Na phase (see Appendix 3-1 for full CELL refinement). Having indexed a unit cell, the program Checkcell[34] was used to suggest potential spacegroups for the phase. This suggested

C2, CM, C2/c or C2/M. This cell shares similar *b* and *c* parameters with the original AlTP cell, but the *a* parameter has been more than doubled. To ensure this larger cell was justified, and that cells similar in size to the parent AlTP were not viable, a study of significant peaks with odd values of *h* was undertaken. In essence, any odd value of *h* provide evidence of the more than doubling of the *a* parameter. Table 3.2 shows a list of reflections with odd *h* values and their intensity, confirming the validity of the enlarged unit cell along *a* as compared to AlTP.

Table 3.2 *XRD peaks with confirmed odd h values in the indexing of AlTP-Na. Intensity (%) is in comparison to the most intense peak*

Observed 2θ (°)	h k l	Intensity (%)
18.818	-1 1 0	18.9
23.649	-1 1 2	17.9
25.811	1 1 2	58.6
26.120	-3 1 2	53.2
30.580	-3 1 3	20.5
31.679	3 1 2	19.6
32.253	-5 1 0	40.0

Having successfully exchanged sodium into AlTP, attempts were made to determine if this could be reversed as is reported in α-ZrP with several different cations[10, 11]. Stirring AlTP-Na in 0.1M HCl for 24 hours proved to be an effective method to achieve this, resulting in the reformation of AlTP, albeit in a less crystalline form. The lack of any AlTP-Na present in the XRD patterns and the fact that flame photometry showed no evidence of sodium, indicated this reverse process resulted in complete exchange back to the parent AlTP.

ESEM images of AlTP-Na (Figure 3.6b) show it consists of flat blade-like crystals. These are similar to the needle/plate shaped crystals seen in the AlTP host (Figure 3.6a).

a)

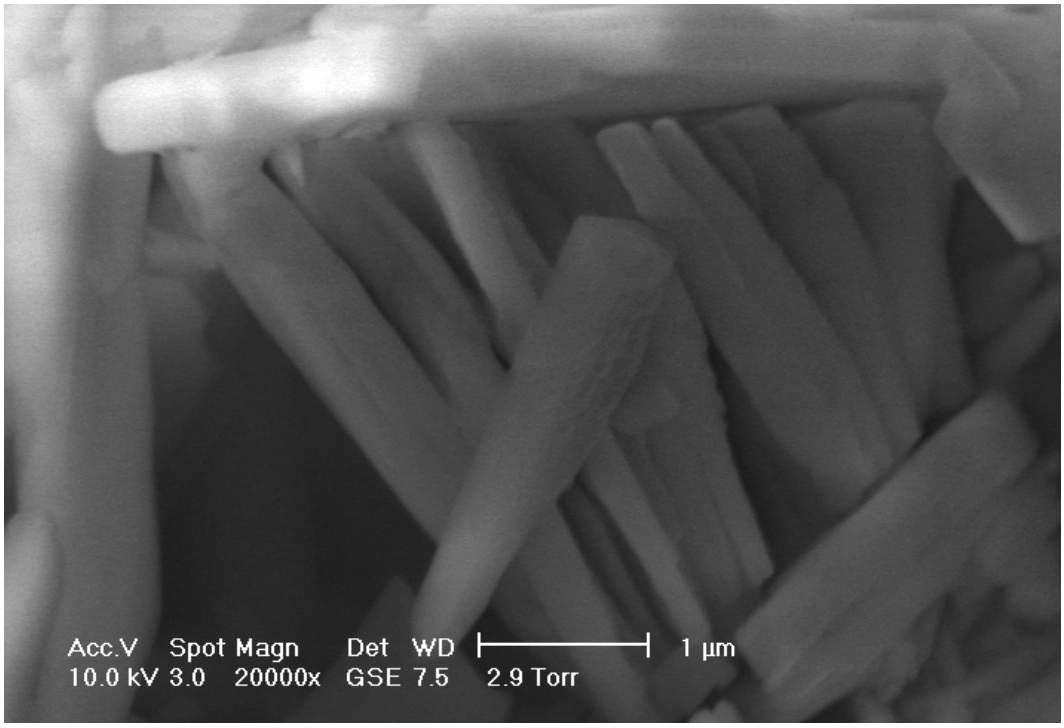

b)

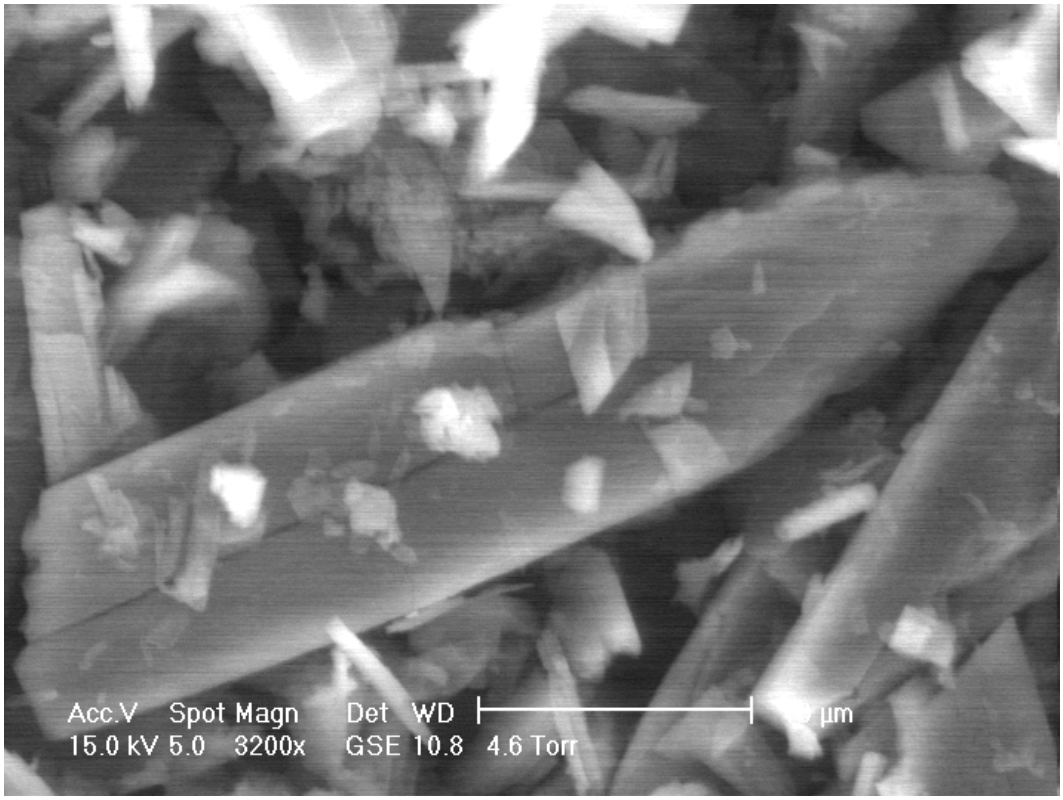

Figure 3.6 *ESEM images of a) AlTP[29] b) AlTP-Na*

As the thermal decomposition of AlTP directly involves the terminal hydrogen, it was decided to perform thermal studies on AlTP-Na to investigate how the replacement of the hydrogen affected the decomposition. The decomposition of this phase proceeds through the

dehydrated phase mentioned previously and begins to change again at around 450 °C (see Figure 3.7). Here a sodium detaches a phosphate unit to form $AlNaP_2O_7$ and $NaPO_3$. The pyrophosphate is stable until around 500 °C where it decomposes to give another $NaPO_3$ and $AlPO_4$. This gives a possible overall decomposition pathway:

$$AlNa_2P_3O_{10}\cdot 4H_2O \xrightarrow[-2H_2O]{\sim 70\,^{\circ}C} AlNa_2P_3O_{10}\cdot 2H_2O \xrightarrow[-2H_2O]{\sim 170\,^{\circ}C} AlNa_2P_3O_{10} \xrightarrow{\sim 450\,^{\circ}C} AlNaP_2O_7 + NaPO_3$$

$$\xrightarrow{\sim 500\,^{\circ}C} AlPO_4 + 2\ NaPO_3$$

This decomposition to pyrophosphate and orthophosphate is in complete contrast to the pathway observed in AlTP where water is ejected and the phosphates condense to infinite chains and form $Al(PO_3)_3$.

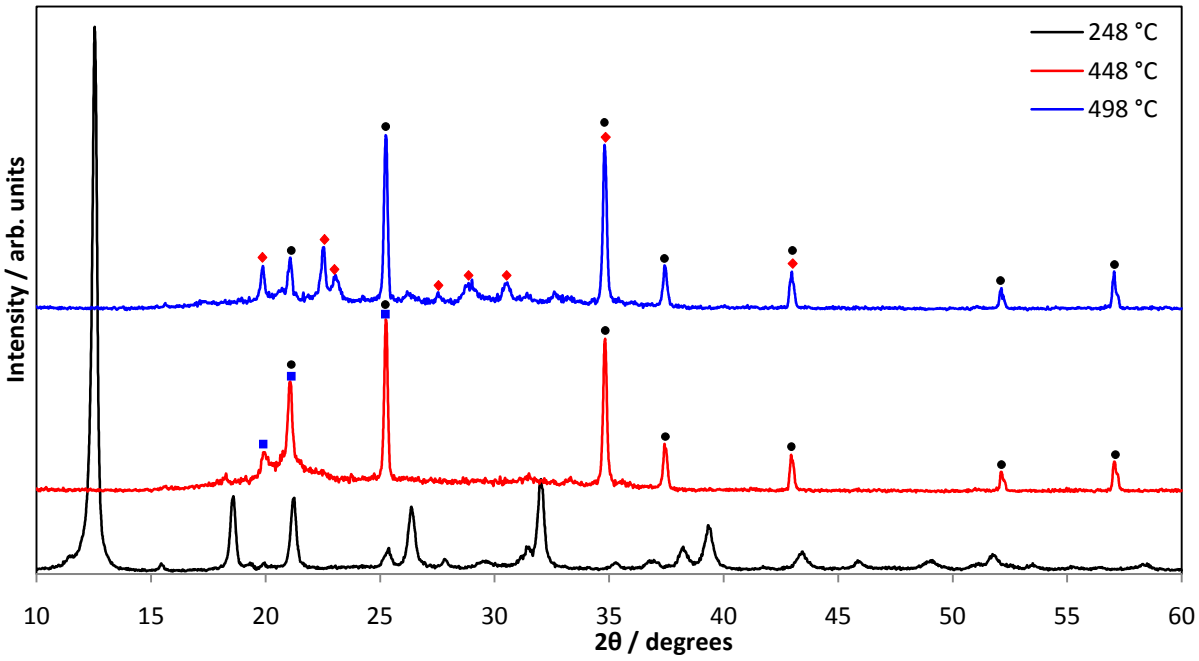

Figure 3.7 *XRD patterns showing thermal decomposition products of AlTP-Na at various temperatures.* ●*$NaPO_3$,* ■*$AlNaP_2O_7$ and* ◆*$AlPO_4$*

Finally attempts were made to produce a half exchanged phase as has been shown to be possible in α-ZrP[35] and suggested for ammonium in AlTP[26]. Reducing the amount of sodium in the exchange solution failed to produce a phase with a lower sodium content, instead the XRD patterns showed a mix of AlTP and AlTP-Na·4. This coupled with the lack

of exchange in the NaCl solutions suggests that once the activation barrier to exchange has been overcome, complete exchange is achieved with no intermediate partially exchanged phases.

3.4 Potassium Exchange

Following the success of the sodium exchange, attempts were made at potassium exchange using the same technique. This resulted in a new phase being obtained with a new XRD pattern shown in Figure 3.8.

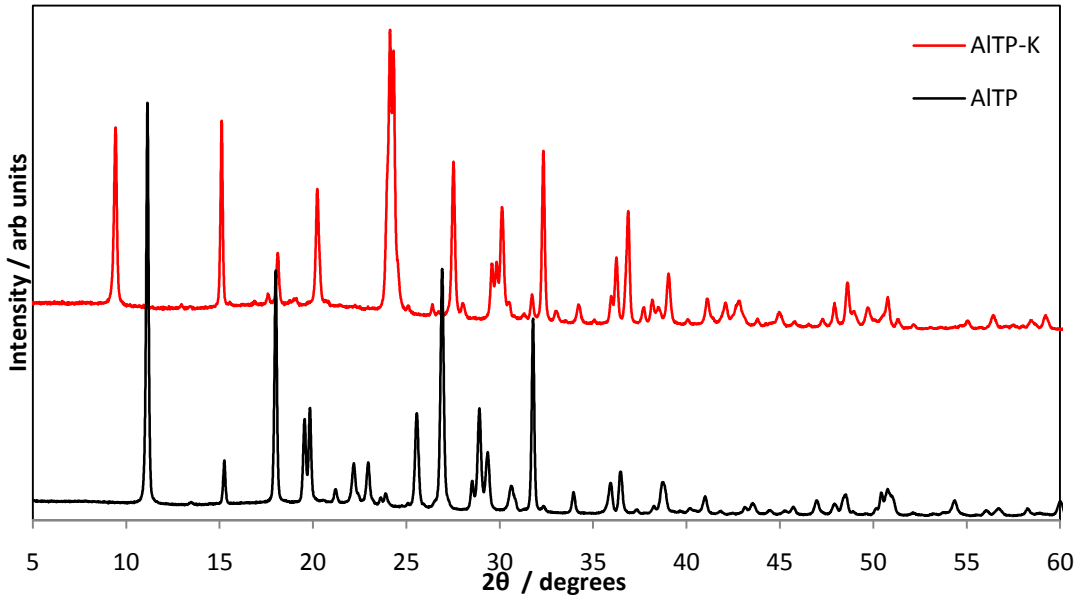

Figure 3.8 *XRD pattern of red) AlTP-K and black) AlTP*

Attempts were also undertaken to establish whether weaker bases were also able to achieve the same exchange result. K_2CO_3 instead of KOH also resulted in the same exchanged product being formed, implying while basic conditions are required for ion exchange into AlTP, less severe conditions are often sufficient and this lowers the risk of structural damage to AlTP framework from the exchange solution.

A third attempt at forming this phase was undertaken using AlTP-Na·4 as the exchangeable host. This resulted in exchange to an identical potassium phase as reported

above, with no residual AlTP-Na·4 as evidenced by XRD data. Analysis of the sodium content via flame photometry confirmed that no sodium remained in the host after potassium exchange, and therefore it may be assumed that the phase is fully potassium exchanged.

TGA and DTA were performed to determine the water content of the AlTP-K phase (Figure 3.9). This showed it to contain two moles of water per mole of triphosphate (9.24 wt% observed mass loss, 9.14 wt% calculated). The accuracy of the calculation also confirms the assumption of complete potassium exchange to be correct, giving the phase a stoichiometry of $AlK_2P_3O_{10}\cdot 2H_2O$ (AlTP-K).

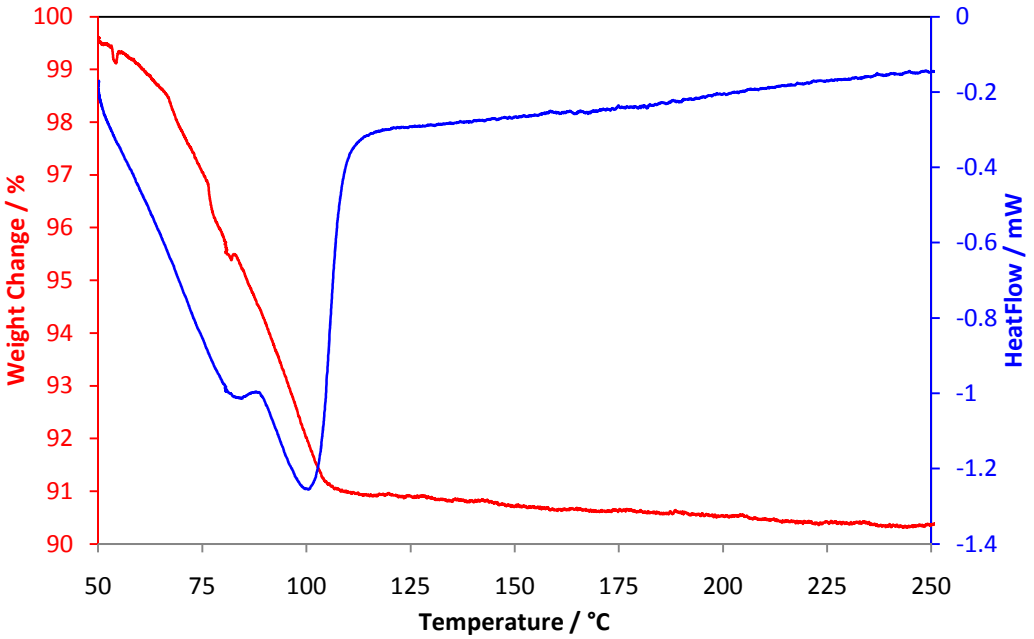

Figure 3.9 *TGA and DTA plot of AlTP-K*

A monoclinic unit cell with parameters a = 18.664(8) Å, b = 4.885(1) Å, c = 11.701(3) Å and β = 91.87(2) ° was assigned to this phase (see Appendix 3-2 for full CELL refinement). Once again Checkcell was used to identify potential space groups for the phase. This suggested that the cell may be either P2/c or $P2_1/c$, and therefore different to those suggested for the sodium cell, but consistent with the AlTP host. Importantly, the unit cell is fairly consistent with the AlTP-Na unit cell, with a greater than doubling of the a parameter evident and the b and c parameters being consistent with those of the AlTP host.

The main difference being the β angle is nearly 20 degrees smaller in AlTP-K. The reason for this is unclear, but may relate to the difference in size of the exchanged cation forcing the phosphate layers into slightly different relative orientations, also resulting in the different potential space groups between the sodium and potassium phases (see Chapter 4 for a more detailed discussion on structure following exchange).

The TGA plot (Figure 3.9) shows the water loss event is accompanied by two endotherms suggesting the presence of a second phase with lower water content. The close proximity and lack of a plateau in the mass loss data suggested this second phase may be difficult to isolate. To attempt isolation of the phase, a sample of AlTP-K was heated to 80 °C the suggested dehydration temperature from the TGA plot. Whilst a second sample was heated to 150 °C to dehydrate it completely then left exposed to the atmosphere for 3 days to monitor rehydration. Both routes produced the same product, with a typical XRD pattern shown in Figure 3.10.

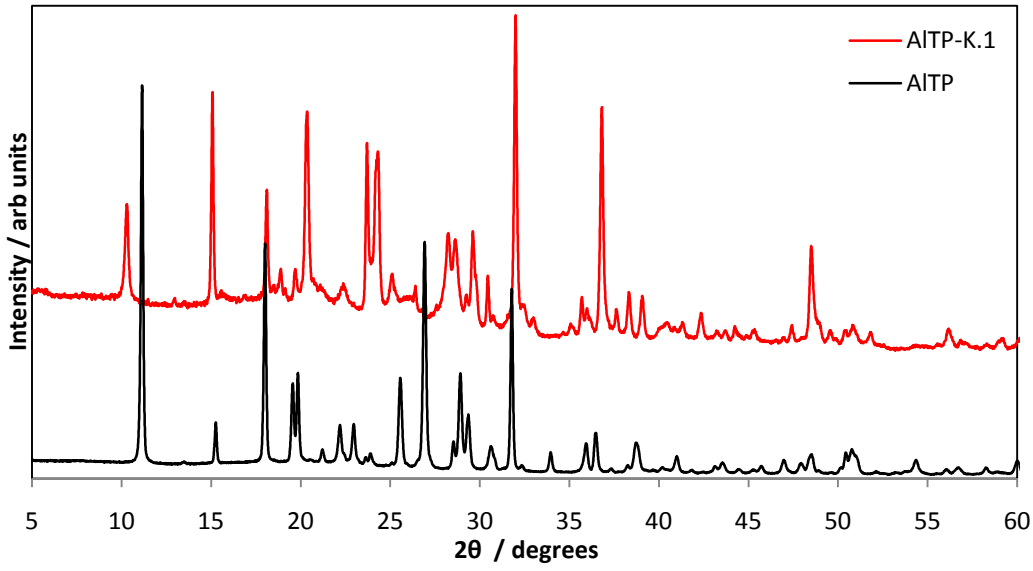

Figure 3.10 *XRD pattern of red) AlTP-K·1 and black) AlTP*

TGA and DTA result showed the phase to contain one mole of water per mole of triphosphate, giving the phase a stoichiometry of $AlK_2P_3O_{10}\cdot H_2O$ (AlTP-K·1). Leaving a sample of AlTP-K·1 exposed to the atmosphere for several weeks showed a rehydration to AlTP-K and therefore indicated that the loss of water between the two phases is reversible. This is contrary to the behaviour shown between the two sodium phases, where the initial loss of two waters is irreversible. This suggests that a phase with two waters of crystallisation is the thermodynamically favoured phase within the ion exchanged AlTPs and any other water content phases are only metastable and will relatively readily convert to phases containing two waters of crystallization.

AlTP-K·1 was indexed to a monoclinic unit cell with parameters a = 17.004(9) Å, b = 4.880(2) Å, c = 11.711(5) Å and β = 91.23 ° (see Appendix 3-3 for full CELL refinement). This is again consistent with the cell indexed for AlTP-K, the only difference being a reduced a parameter and slightly smaller β angle resulting from the loss of an inter-lamellar water.

ESEM showed AlTP-K to consist of long thin angular crystals (Figure 3.11), similar to those observed in AlTP-Na, implying a similar structural motif between the phases alongside the similarities in unit cell dimensions.

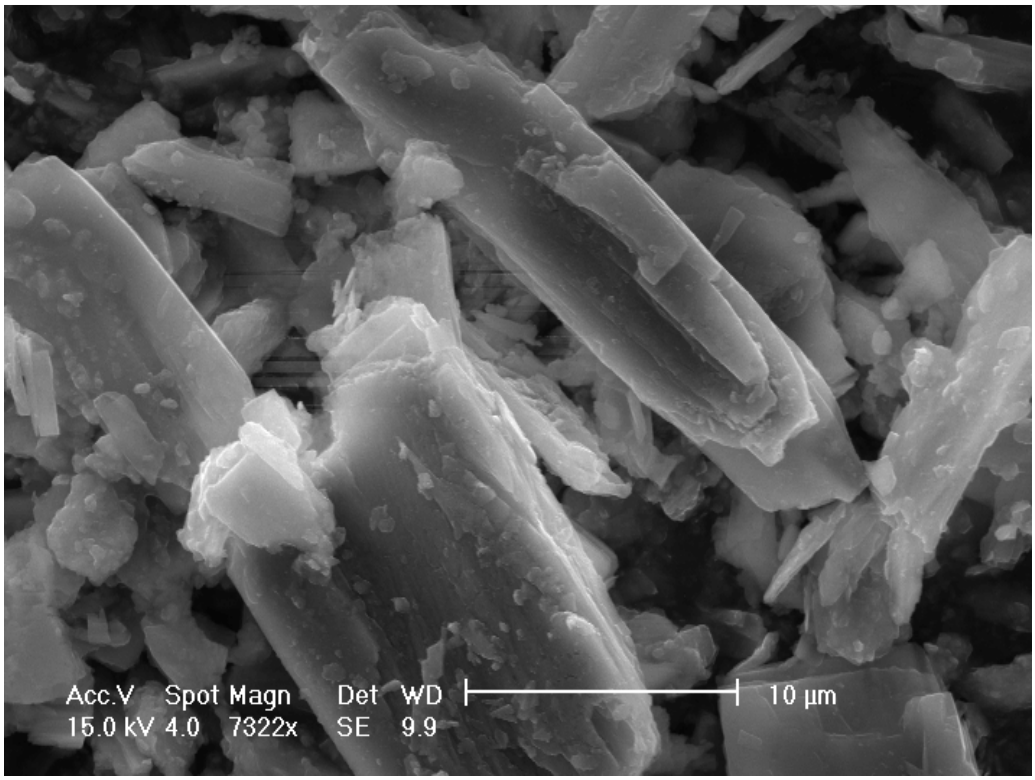

Figure 3.11 *ESEM image of AlTP-K*

The thermal decomposition pathway of AlTP-K was found to be similar to that observed in AlTP-Na. There was evidence of a dehydrated phase, resulting from the loss of all inter-lamellar water from around 100 °C. At around 550 °C, this begins to decompose to form $AlKP_2O_7$ and KPO_3 (see Figure 3.12). The pyrophosphate is then stable until around 750 °C where it decomposes to give more KPO_3 and $AlPO_4$. Thus a possible overall decomposition pathway is:

$$AlK_2P_3O_{10}{\cdot}2H_2O \xrightarrow[-H_2O]{\sim 80\,^{\circ}C} AlK_2P_3O_{10}{\cdot}H_2O \xrightarrow[-H_2O]{\sim 100\,^{\circ}C} AlK_2P_3O_{10} \xrightarrow{\sim 550\,^{\circ}C} AlKP_2O_7 + KPO_3$$

$$\xrightarrow{\sim 700\,^{\circ}C} AlPO_4 + 2\ KPO_3$$

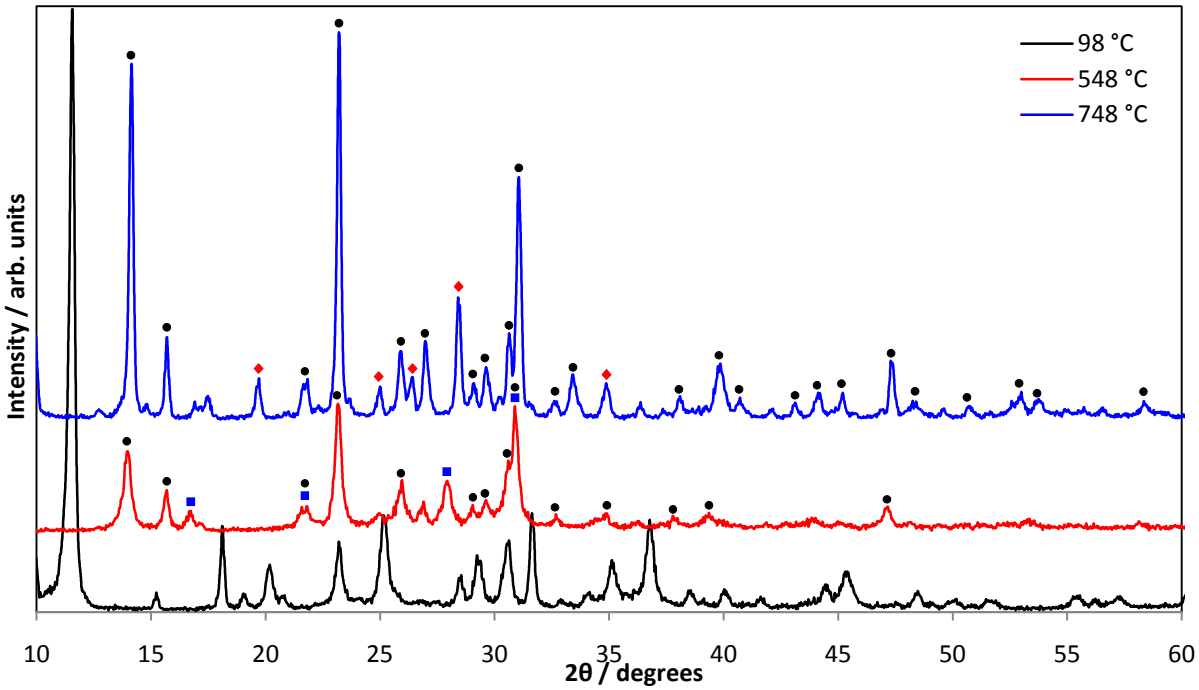

Figure 3.12 *XRD patterns showing thermal decomposition products of AlTP-K at various temperatures* •*KPO_3,* ▪*$AlKP_2O_7$ and* ◆*$AlPO_4$*

3.5 Rubidium Exchange

Attempts at rubidium exchange were undertaken with rubidium carbonate using the AlTP host and also exchanging from AlTP-Na·4, as with potassium in Section 3.4. Both methods were successful in providing a new phase with the associated XRD pattern shown in Figure 3.13. The lack of any sodium remaining after exchange from AlTP-Na·4, as determined by flame photometry (Appendix 2), implied complete exchange had occurred. This was subsequently supported by Rietveld analysis (see Chapter 4.4).

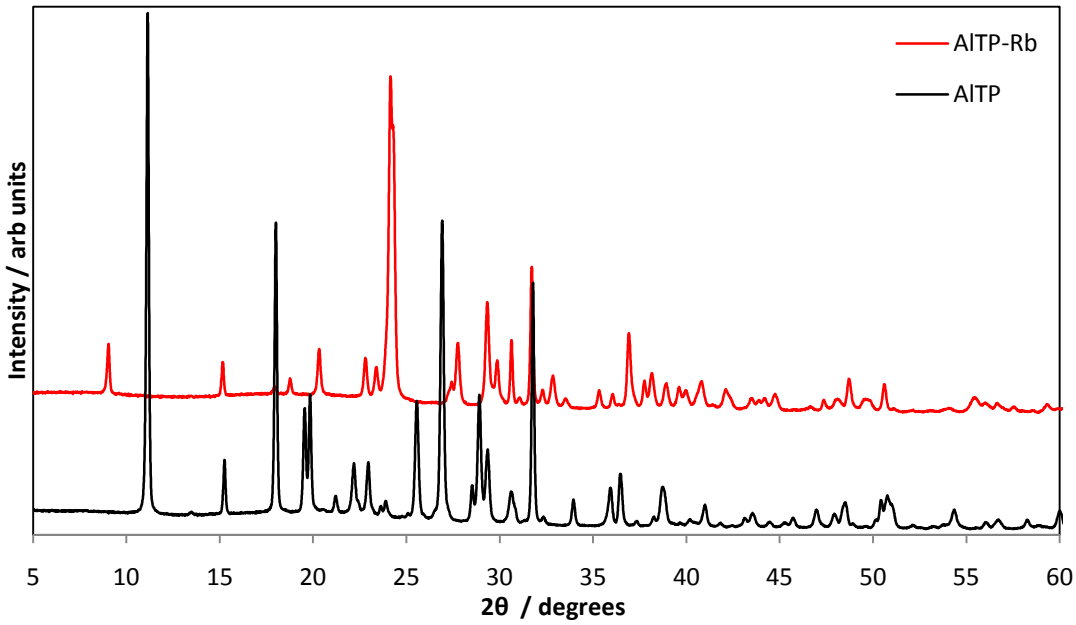

Figure 3.13 *XRD pattern of red) AlTP-Rb and black) AlTP*

TGA and DTA (Figure 3.14) show the phase to contain two formula units of water (7.66 wt% observed loss, 7.41 wt% calculated) giving the phase a stoichiometry of $AlRb_2P_3O_{10}\cdot 2H_2O$ (AlTP-Rb), consistent with the stoichiometry of the other exchanged phases.

The phase was indexed to a monoclinic unit cell with parameters of a = 19.506(15) Å, b = 4.872(3) Å, c = 11.799(8) Å and β = 91.73(4) °, with Checkcell suggesting possible space groups of P2/c or $P2_1/c$ (see Appendix 3-4 for full CELL refinement). The cell is consistent with those observed for sodium and potassium, with the β angle and potential space groups consistent with potassium, suggesting a difference to the sodium cell possibly as a result of sodium ion's smaller size.

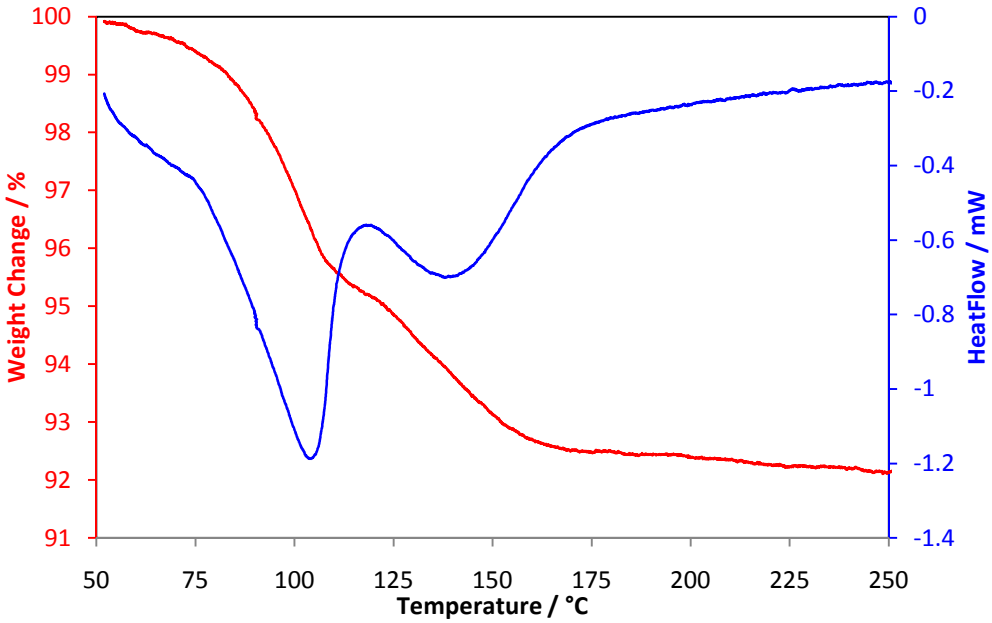

Figure 3.14 *TGA and DTA plot of AlTP-Rb*

Again there are two endothermic events accompanying the water loss process for AlTP-Rb, with a small plateau in the mass loss (Figure 3.14), implying the rubidium exchange also forms a second phase. This additional phase could not be isolated despite numerous attempts. XRD patterns collected, *ex situ*, very shortly after heating the sample at both 100 °C (the temperature of the first endotherm) and 200 °C, which should fully dehydrate the phase, showed only AlTP-Rb present. This suggests that the rate of rehydration is significantly faster than observed in both the sodium and potassium phases. There were a few extra peaks around 25° 2θ, indicating a second phase may exist but rehydration occurred too quickly to allow isolation. Therefore, variable temperature (*in situ*) XRD (VTXRD) was performed to study the phase in more detail (Figure 3.15).

The d_{200} reflection is a good indicator of the phases present at each temperature. The AlTP-Rb phase is present from room temp to around 71 °C and the dehydrated phase from 148 °C upwards. The temperature range between these two phases clearly shows an intermediate peak, showing $AlRb_2P_3O_{10}{\cdot}H_2O$ to exist, but is much less stable than AlTP-K·1, rehydrating almost immediately, and is hence only isolated *in situ*.

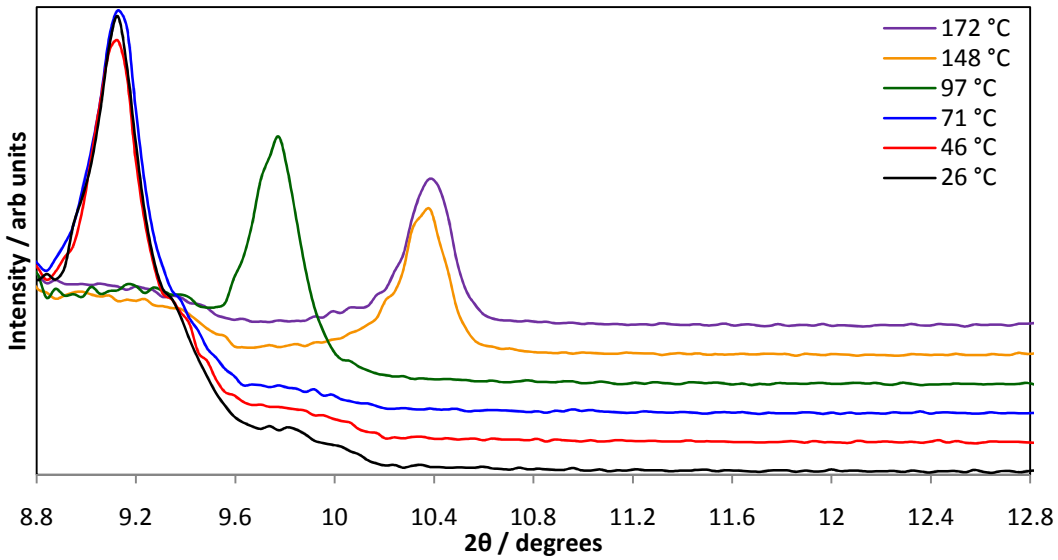

Figure 3.15 *VTXRD patterns of the d_{200} peak of AlTP-Rb*

As is the case with AlTP-Na and AlTP-K, ESEM showed AlTP-Rb to consist of long thin angular crystals (Figure 3.16).

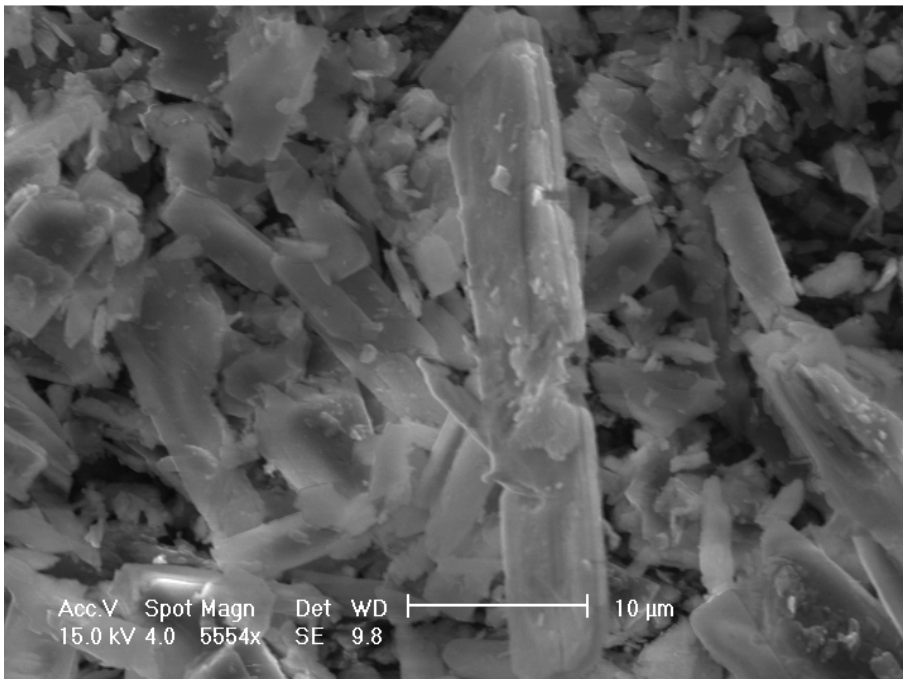

Figure 3.16 *ESEM image of AlTP-Rb*

The thermal decomposition of AlTP-Rb is also similar to those of the previously observed exchanged phases (see Figure 3.17). At around 550 °C the dehydrated phase decomposes to $RbPO_3$ and an unreported phase. This is believed to be $AlRbP_2O_7$, which is

not reported in either the JCPDS[36] or ICSD[37] databases, with this assumption based on its decomposition to form $AlPO_4$ and $RbPO_3$ at around 750 °C. This is consistent with both the sodium and potassium phases and gives an overall decomposition pathway of:

$$AlRb_2P_3O_{10}\cdot 2H_2O \xrightarrow[-H_2O]{\sim 100\,^{\circ}C} AlRb_2P_3O_{10}\cdot H_2O \xrightarrow[-H_2O]{\sim 150\,^{\circ}C} AlRb_2P_3O_{10} \xrightarrow{\sim 550\,^{\circ}C} AlRbP_2O_7 + RbPO_3$$

$$\xrightarrow{\sim 750\,^{\circ}C} AlPO_4 + 2\ RbPO_3$$

No further attempts were made to isolate or further characterise $AlRbP_2O_7$.

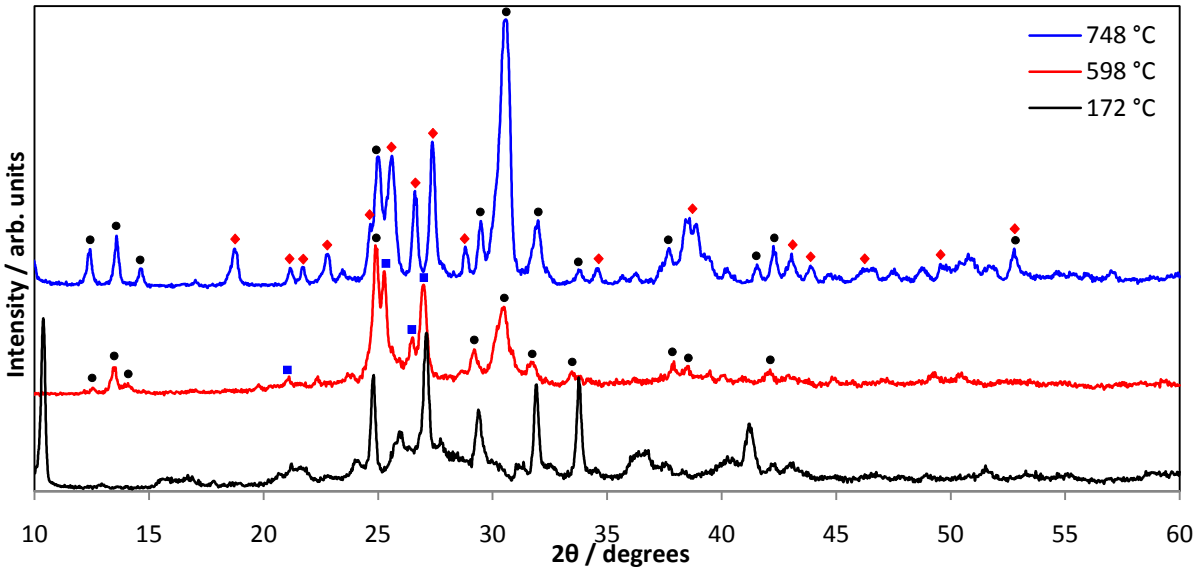

Figure 3.17 *XRD patterns showing thermal decomposition products of AlTP-Rb at various temperatures.* ●*$RbPO_3$,* ■*$AlRbP_2O_7$ and* ◆ *$AlPO_4$*

3.6 Caesium Exchange

Caesium is of added interest as an ion exchangeable cation due to the need to safely trap and remove it from nuclear waste[38, 39]. Caesium was exchanged into the AlTP structure successfully using the same two methods as described for rubidium (Section 3.5), producing a phase with the XRD pattern shown in Figure 3.18. Flame photometry again showed no sodium remaining after exchange from AlTP-Na·4 (see Appendix 2), implying complete exchange was achieved, supported by Rietveld analysis (Chapter 4.5).

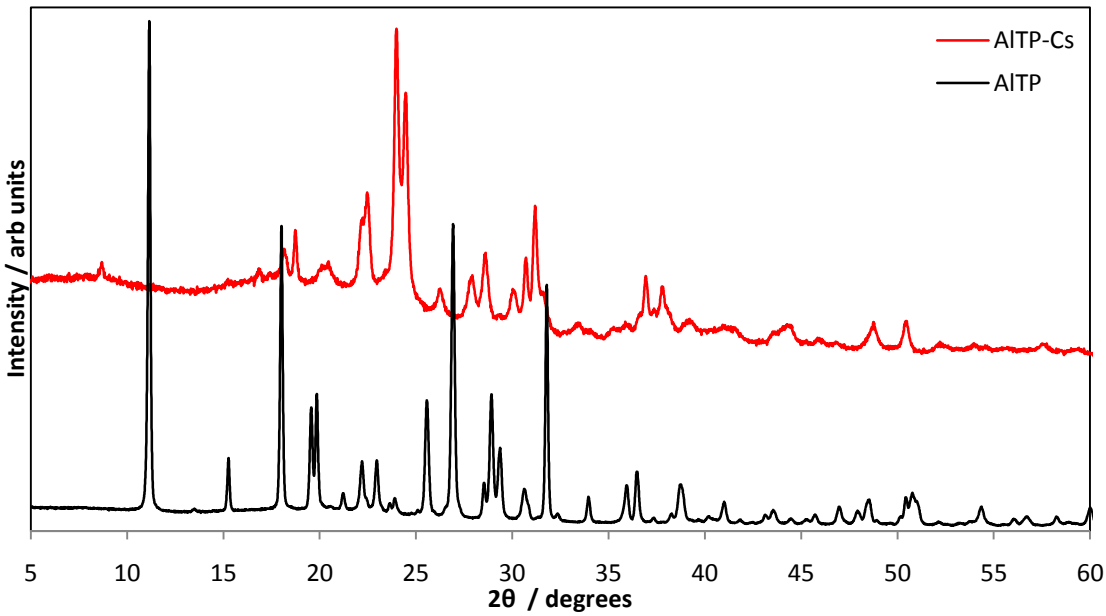

Figure 3.18 *XRD plot of red) AlTP-Cs and black) AlTP*

TGA and DTA (Figure 3.19) showed the phase to have two moles of water per triphosphate (6.3 wt% observed mass loss, 6.2 wt% calculated) giving the formula $AlCs_2P_3O_{10}{\cdot}2H_2O$ (AlTP-Cs).

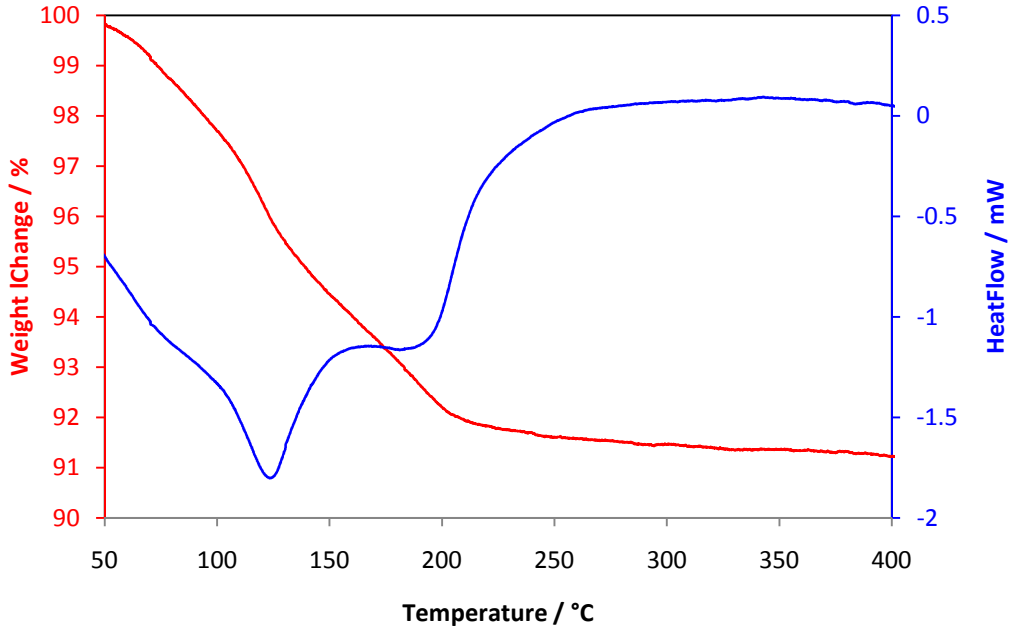

Figure 3.19 *TGA and DTA plot of AlTP-Cs*

The phase was indexed to a monoclinic unit cell with parameters a = 20.39(2) Å, b = 4.871(4) Å, c = 11.677(9) Å and β = 95.28(6) ° (see Appendix 3-5 for full CELL

refinement), consistent again with the other exchanged phases. There were too few peaks to assign potential spacegroups to the phase.

The DTA again shows two endotherms during the water loss process, with the TGA showing a slight change in gradient implying caesium also has a second phase. As with the rubidium phases, this second phase could not be isolated due to rapid rehydration back to AlTP-Cs, so VTXRD studies were undertaken (Figure 3.20).

Using the d_{200} peak as an indicator, the VTXRD patterns show the likely $AlCs_2P_3O_{10}\cdot H_2O$ present at 98 °C, with AlTP-Cs present below this temperature and the dehydrated phase present above 147 °C.

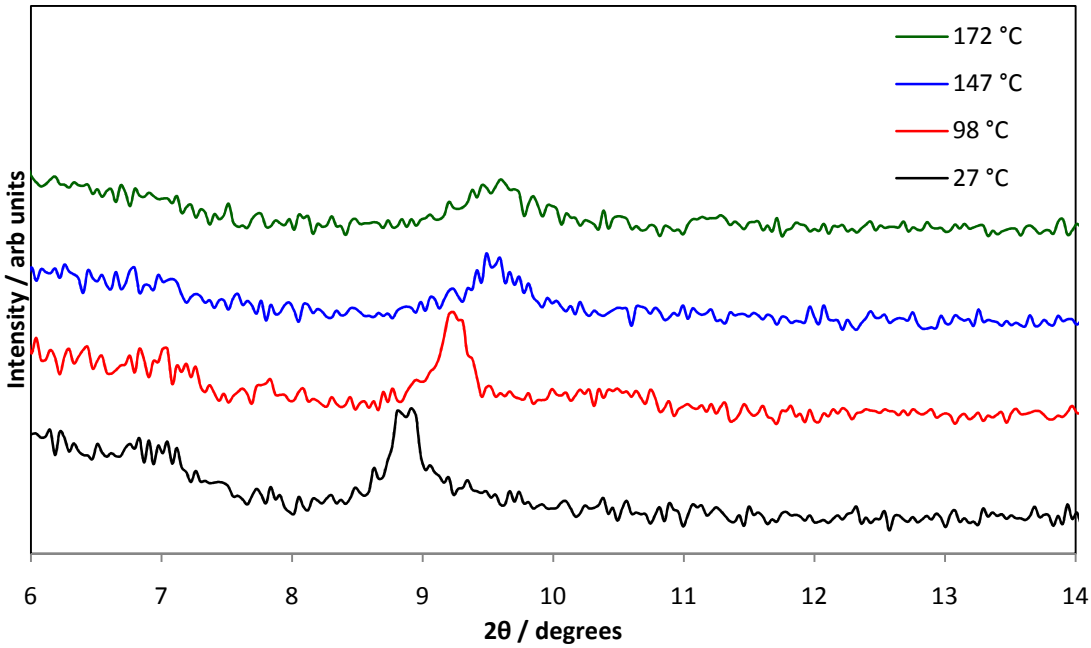

Figure 3.20 *VTXRD patterns of the d_{200} reflection in AlTP-Cs*

Taking the TGA and DTA data to higher temperatures showed the phase underwent a sharp exothermic event at 525 °C (Figure 3.21) rather than the broad endotherm observed in the other alkali metal phases. This thermal event was not accompanied by a mass loss event.

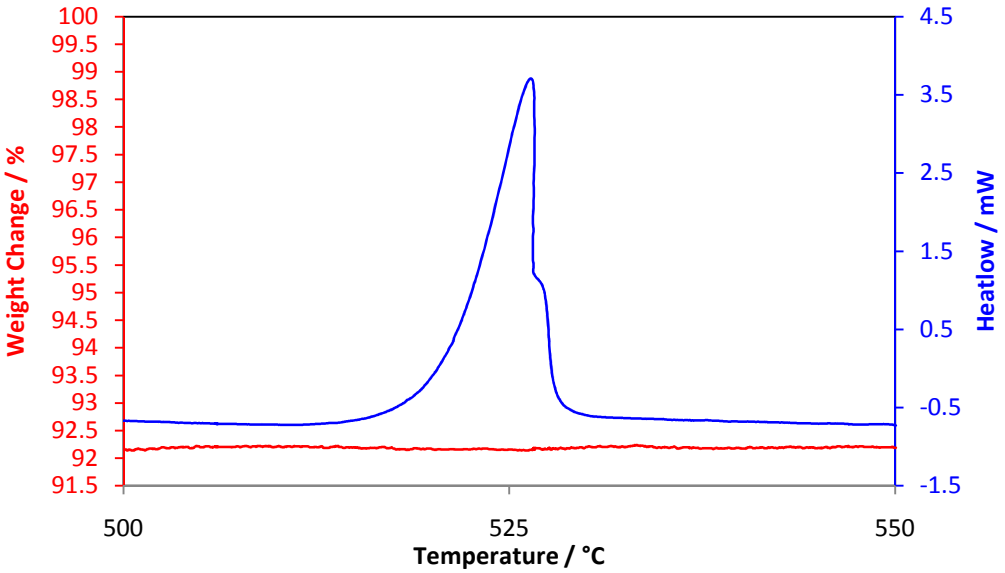

Figure 3.21 *Partial TGA and DTA of AlTP-Cs, showing large exotherm at 525 °C*

XRD patterns (Figure 3.22) taken after this event show that instead of decomposing to a pyrophosphate and an orthophosphate as in the previous systems, AlTP-Cs converts into another phase of stoichiometry $AlCs_2P_3O_{10}$. This phase has previously been reported[40, 41], but this route, *via* exchange reactions, is different to the direct synthesis *via* evacuated sealed silica tubes previously reported. Chapter 4.5 compares and contrasts the structural differences between these two phases.

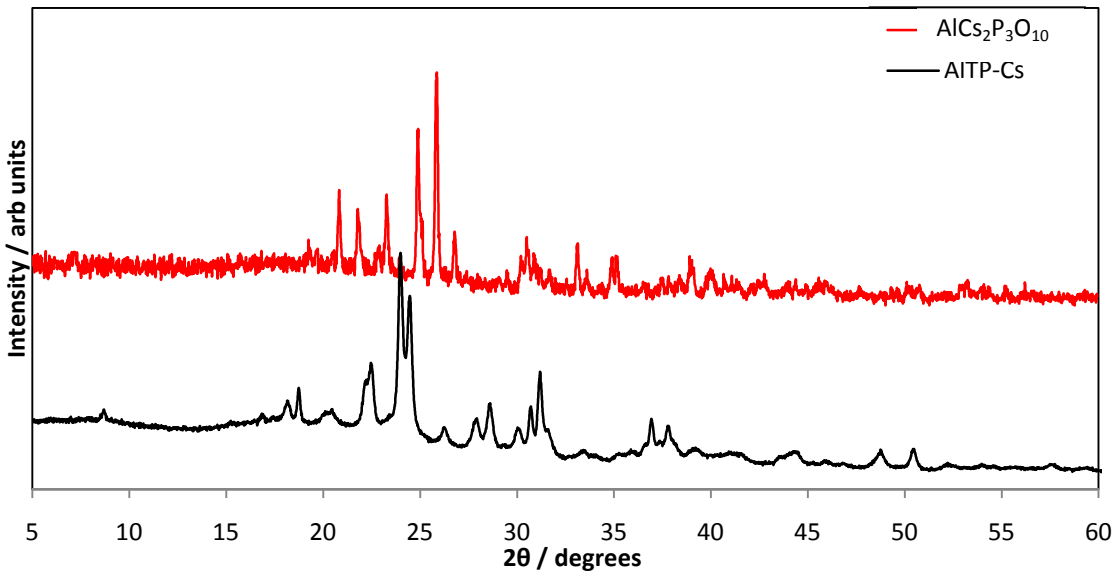

Figure 3.22 *XRD pattern of red) $AlCs_2P_3O_{10}$ and black) AlTP-Cs*

ESEM (Figure 3.23) shows AlTP-Cs, like the rest of the exchanged phases, consists of long angular crystals.

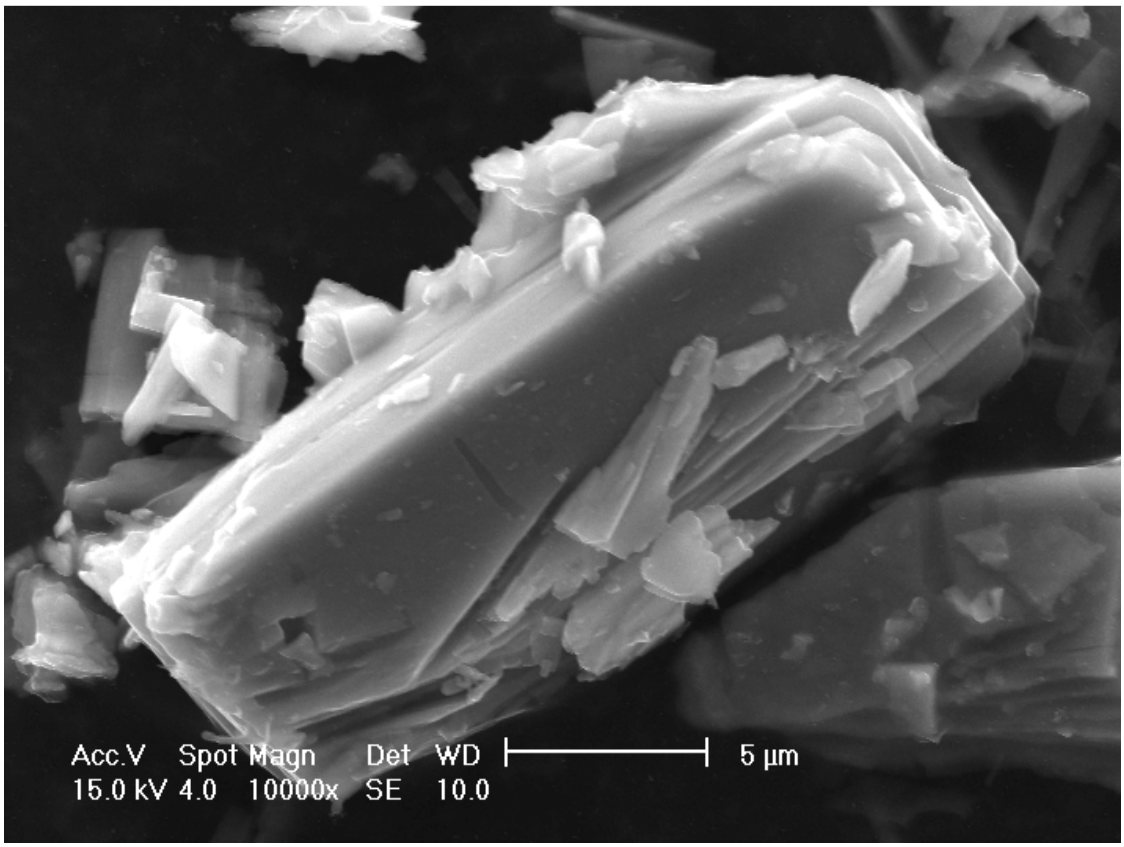

Figure 3.23 *ESEM image of AlTP-Cs*

3.7 Silver Exchange

Silver exchange was achieved using $AgNO_3$ as reported previously[28, 29], and by exchanging from AlTP-Na·4. This produced a phase with the XRD pattern shown in Figure 3.24. Full exchange is again assumed from flame photometry showing the removal of all the sodium when exchanging from AlTP-Na·4.

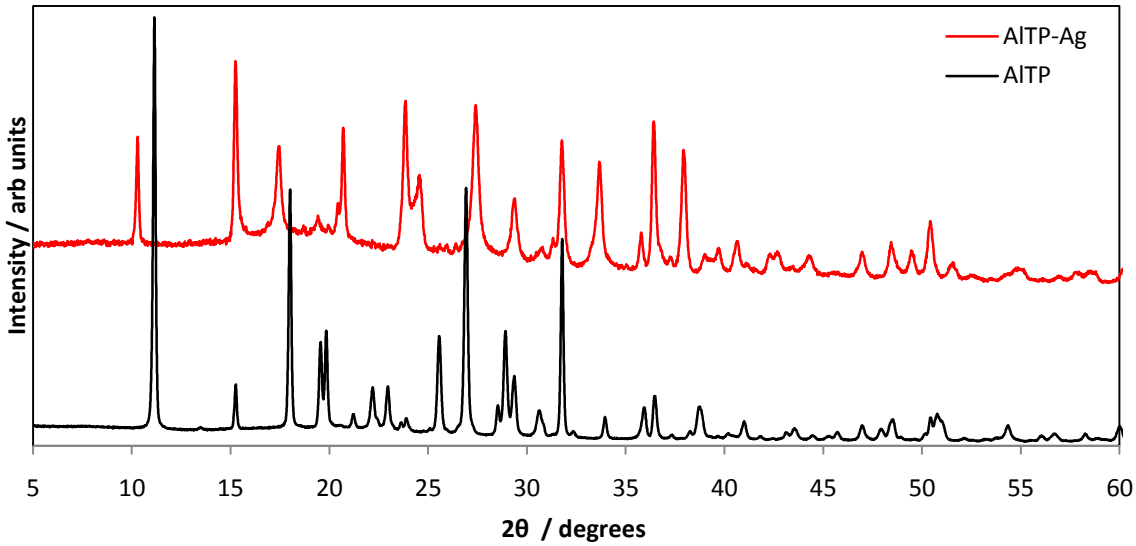

Figure 3.24 *XRD pattern of red) AlTP-Ag and black) AlTP*

DTA and TGA (Figure 3.25) have confirmed the stoichiometry of this phase as $AlAg_2P_3O_{10}\cdot 2H_2O$ (AlTP-Ag), with an observed mass loss of 6.48 wt%, compared to the calculated loss of 6.78 wt%.

The DTA plot shows a second small endotherm in this phase as with all the other phases produced. However unlike the others no evidence of a second phase with a lower water content has been observed, with VTXRD only showing the dehydrated phase.

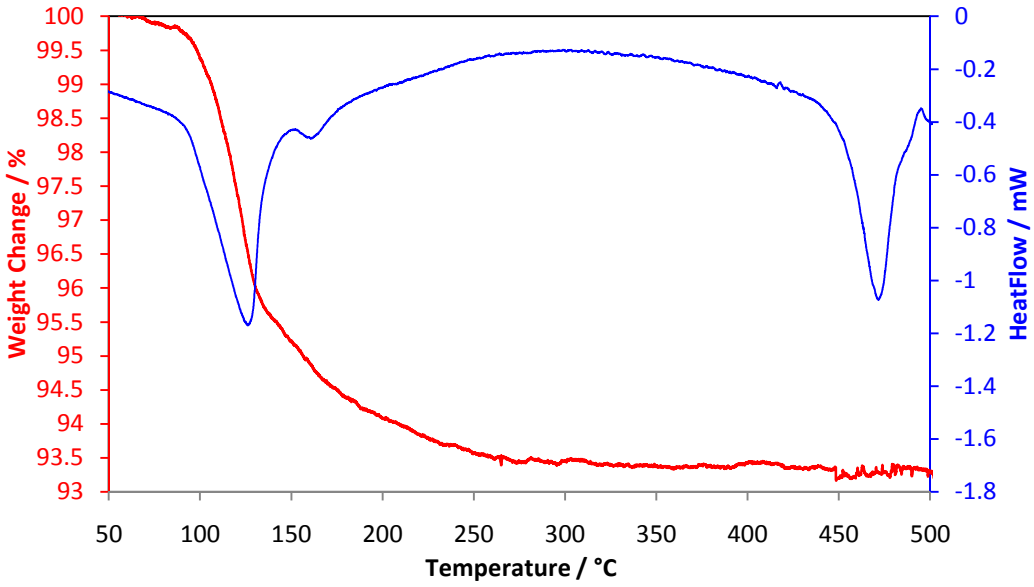

Figure 3.25 *TGA and DTA plots of AlTP-Ag*

A monoclinic unit cell was determined, with parameters a = 17.237(7) Å, b = 4.924(1) Å, c = 11.660(3) Å and β = 96.39(2) ° (see Appendix 3-6 for full CELL refinement), with Checkcell giving possible space groups of C2, CM, C2/c or C2/M.

Rishi had previously indexed a unit cell to AlTP-Ag[29] (a = 8.5679(8) Å, b = 4.9268(5) Å, c = 11.5048(12) Å and β = 96.14(1) °). The cells are almost identical except for the a parameter. The cell reported here has an a parameter double that of Rishi's, which is consistent with the other unit cells indexed for monovalent cation exchanged AlTP. It also indexes all of the observed peaks in the XRD pattern, unlike Rishi's cell.

Like the rest of the exchanged phases, ESEM shows AlTP-Ag consists of long thin angular crystals shown in Figure 3.26.

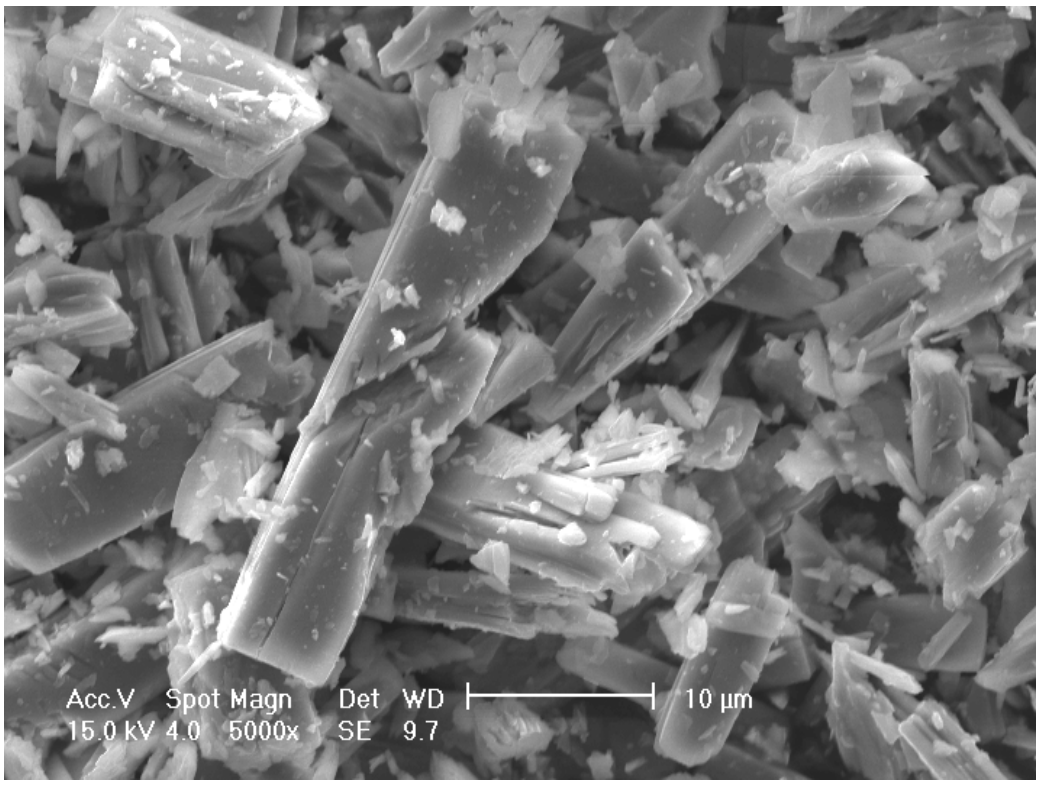

Figure 3.26 *ESEM image of AlTP-Ag*

The thermal decomposition pathway of AlTP-Ag remains unclear. After the dehydrated phase decomposes at around 420 °C it becomes amorphous and remains that way until much higher temperatures, even through the large endotherm at around 470 °C. It is possible that at these temperatures some silver may have vaporised out of the sample.

3.8 Lithium Exchange

The initial attempt at lithium exchange using a solution of LiCl concurred with Rishi's observations showing the same XRD pattern and level of lithium exchange. To attempt to increase the amount of lithium exchanged into the AlTP host, the pH of the exchanging solution was systematically increased by the addition of an increasing percentage of LiOH. The addition of LiOH to the exchanging solution had an immediate effect with a new phase observed with several differences apparent in its XRD pattern to that of the pure LiCl exchange phase (Figures 3.27 and 3.28).

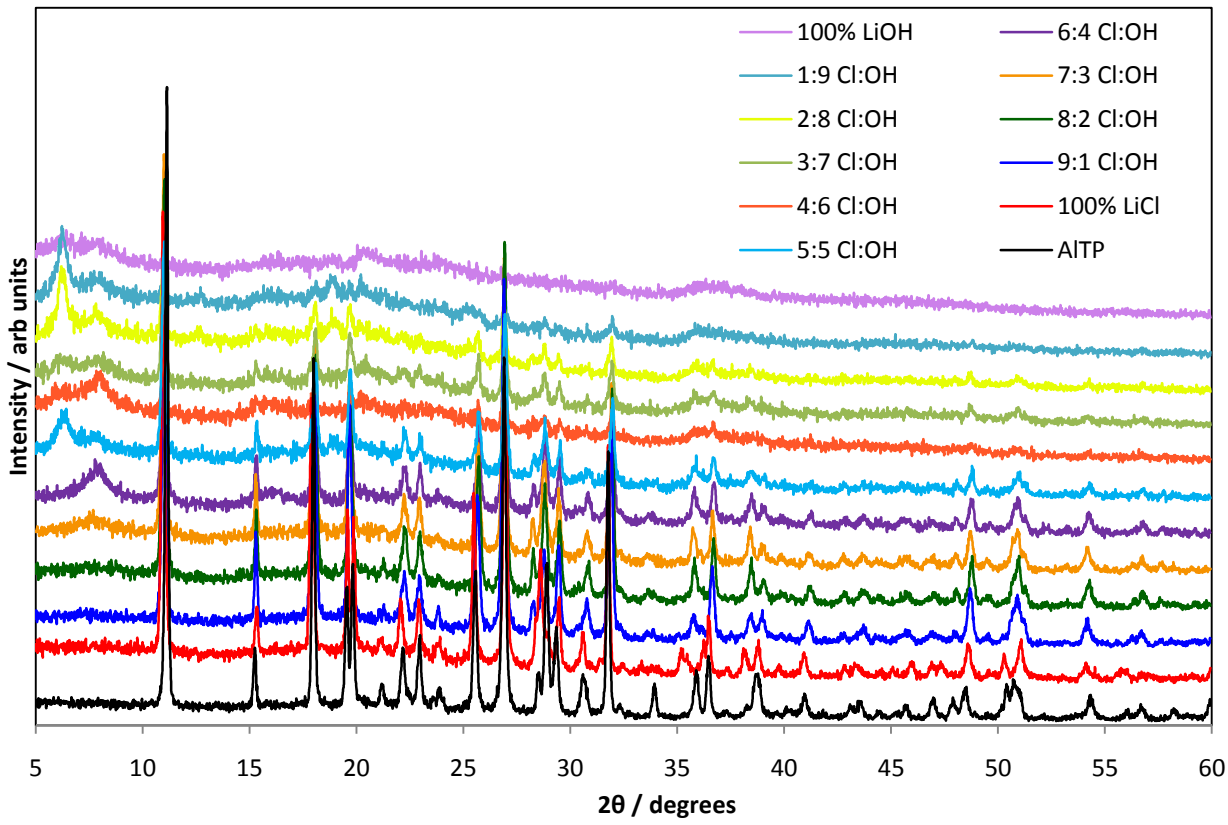

Figure 3.27 *XRD patterns for the LiCl:LiOH solution series for exchange of AlTP*

The most apparent change was the d_{100} peak shifting to an intermediate 2θ value of 8.03 Å, between those of AlTP (7.94 Å) and 8.07 Å in the pure LiCl solution (Figure 3.28a). This shows the interlayer spacing to have decreased as additional lithium has been inserted into the inter-lamellar region (see Table 3.3 and following discussion), which may result from lithium's high polarisation attracting oxygens from adjacent layers and pulling the layers together.

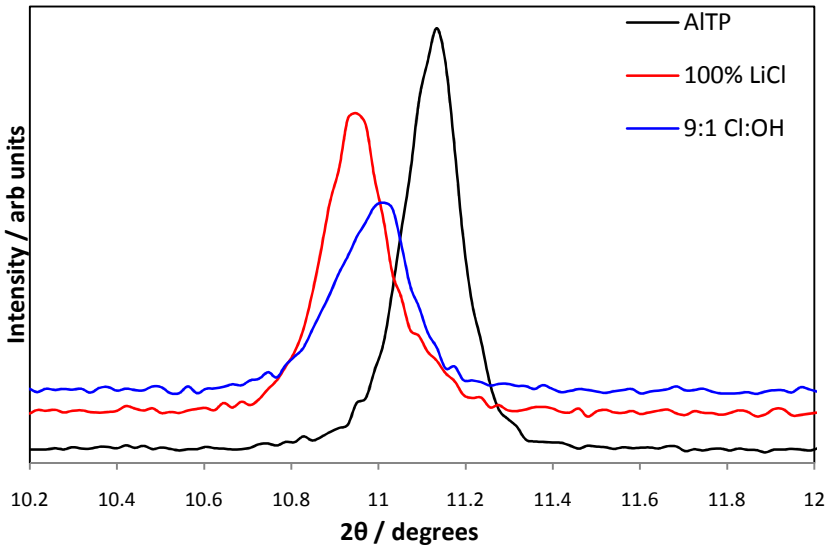

Figure 3.28 *Shifting of the d_{100} peak for different exchange solution*

A unit cell was indexed for this new phase with the parameters a = 8.015(6) Å, b = 4.890(3) Å, c = 11.586(6) Å and β = 95.24(3) °. It is notable that the a parameter has increased but not doubled as was seen with the other alkali metals exchanging into AlTP.

As the percentage of LiOH in the exchanging solution increases the crystallinity of the exchanged phases begins to reduce and other unidentified phases begin to form, with broad peaks appearing at lower values of 2θ from 40% hydroxide upward, until the phase becomes amorphous.

Flame photometry was performed on these phases to determine the lithium content with results shown in Table 3.3 (see Appendix 2 for raw results). The results show that the addition of hydroxide to the exchanging solution significantly increased the lithium loading by around 40%, to give 50% loading. This, with the different XRD pattern and unit cell, suggested there is a third phase with different lithium loading in this series.

Table 3.3 *Percentage lithium exchange of pH varied series. (% lithium exchange refers to the percentage of potential maximum exchange)*

Exchanging Solution	Lithium Exchanged (%)
100% LiCl	11(1)
90:10 LiCl : LiOH	50(1)
80:20 LiCl : LiOH	55(2)
70:30 LiCl : LiOH	60(2)
60:40 LiCl : LiOH	50(1)
50:50 LiCl : LiOH	77(1)
40:60 LiCl : LiOH	59(2)
30:70 LiCl : LiOH	84(2)
20:80 LiCl : LiOH	86(2)
10:90 LiCl : LiOH	95(3)
100% LiOH	73(2)

Above 40% hydroxide the XRD patterns show extra unidentified phases, so the much higher values of lithium content observed are likely to be unreliable, as the lithium cannot be assumed to have entered the AlTP host, possibly residing in unknown lithium containing phases.

To attempt to increase the lithium content further a process of solution refreshing was undertaken using the 100% LiCl and the 9:1 and 8:2 Li:Al solutions. This involved reacting AlTP in the solutions for 24 hours then draining off the solution and replacing it with a fresh solution, with the hope that removing the exchanged hydrogen ions would allow more lithium to enter the inter-lamellar region. The flame photometry results of this process are shown in Table 3.4.

Table 3.4 *Percentage lithium exchange from solution refreshing. (% lithium exchange refers to the percentage of potential maximum exchange)*

Exchanging Solution	Lithium Exchange (%)
100% LiCl	11(1)
1 solution refresh	31(2)
2 solution refreshes	39(1)
3 solution refreshes	59(3)
90:10 LiCl : LiOH	50(1)
1 solution refresh	64(1)
2 solution refreshes	62(1)
3 solution refreshes	69(1)
80:20 LiCl : LiOH	55(2)
3 solution refreshes	74(3)

The solution of pure lithium chloride showed an increase from the initial 10% to around 30-40% with 1-2 solution refreshes showing no alteration to its XRD pattern and therefore not indicating a change to the higher loaded phase. After the third refresh the higher loaded phase was formed with the lithium content sharply increasing to around 60%.

The hydroxide solutions increased the lithium content to around 60% after 2 refreshes and around 70% after a third. The XRD patterns for this process (Figure 3.29), however, showed an increase of amorphous background and decrease of crystallinity suggesting a breakdown of the host structure.

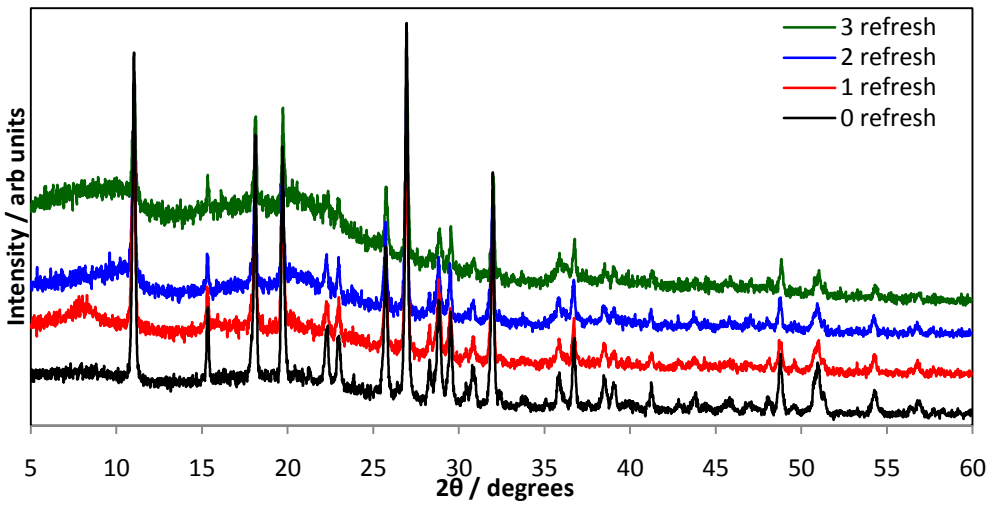

Figure 3.29 *XRD patterns of solution refreshing for the 80:20 LiCl : LiOH samples, showing a breakdown of the crystalline structure*

As Rishi had found that altering the lithium to aluminium ratio gave a higher percentage of exchange, studies were undertaken to use this method with the hydroxide solutions, specifically the 9:1 Cl:OH. The flame photometry, Table 3.5, shows an increase of lithium content as the lithium to aluminium ratio increased but this increase was coupled to a loss of crystallinity observed in the XRD patterns (Figure 3.30). The 50:1 Li:Al ratio showed the largest lithium content achieved to this point, at around 70% of the potential exchange, whilst remaining crystalline and showing no formation of other phases. The 100:1 Li:Al exchange solution caused an almost complete breakdown of the host structure, its XRD pattern being almost completely amorphous, therefore its value of 95% exchange is likely to be unreliable.

Table 3.5 *Percentage lithium exchange from varying Li:Al ratio. (% lithium exchange refers to the percentage of potential maximum exchange)*

Li:Al ratio	Lithium Exchange (%)
10:1	32(5)
25:1	50(1)
50:1	69(1)
100:1	95(4)

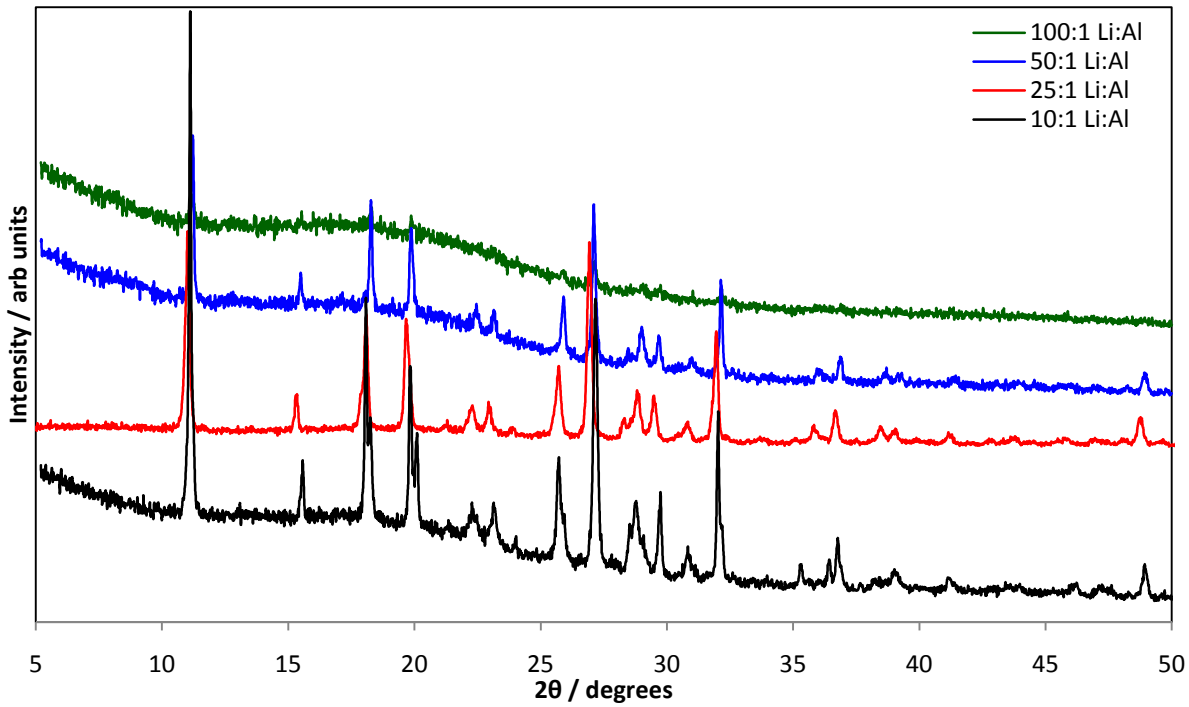

Figure 3.30 *XRD patterns of differing Li:Al ratio phases*

3.9 Mixed Cation Exchanges

It has been observed in Sections 3.4-3.7 that AlTP-Na·4 can be used as an exchanging host to produce any of the other ion exchanged phases, excluding lithium. With this knowledge, experiments were preformed to investigate if this was a common trait in all the exchanged AlTP phases and to discover if any selectivity of AlTP towards the exchangeable cations existed.

Initially, attempts were made to reverse all of the exchanges with hydrogen, using the method discussed in Section 3.3. This showed that all the exchanges could be reversed and proves the aluminium phosphate layers remain intact and no irreversible structural rearrangement occurs when ion exchange takes place.

It was found that, given an excess of another ion in an exchanging solution, all the fully exchanged AlTP phases could be interchanged, with a loss of crystallinity each time the process was undertaken. No phases containing more than one cation type were isolated, with all exchanges going to completion. This is different to reports of cation-cation exchange in α-ZrP. Alberti *et al*[42] reported being able to form $ZrNaK(PO_4)_2$, a half and half sodium potassium zirconium phosphate, when exchanging potassium into the sodium form of α-ZrP.

AlTP appears to show no selectivity towards any one cation when two or more cations were present in the exchange solution, with the XRD patterns showing the presence of several exchanged phases. This has implications for any potential application requiring selective uptake of one particular cation, for instance caesium removal from nuclear waste. This is again different to α-ZrP which shows a preference to smaller cations in its pure form and a preference to larger cations when exchanging from the sodium exchanged form[18].

As other monovalent cation exchange forms of AlTP have been shown to be able to exchange cations readily, and lithium is able to reversibly exchange with other cations in

α-ZrP[43], it was decided to attempt to exchange lithium into AlTP-Na·4. This showed that unlike in α-ZrP, or the other exchanged forms of AlTP, lithium is not able to readily exchange fully with other cations, with its XRD pattern (Figure 3.31) instead showing a mix of poorly crystalline AlTP-Na·4 and partially lithium exchanged AlTP.

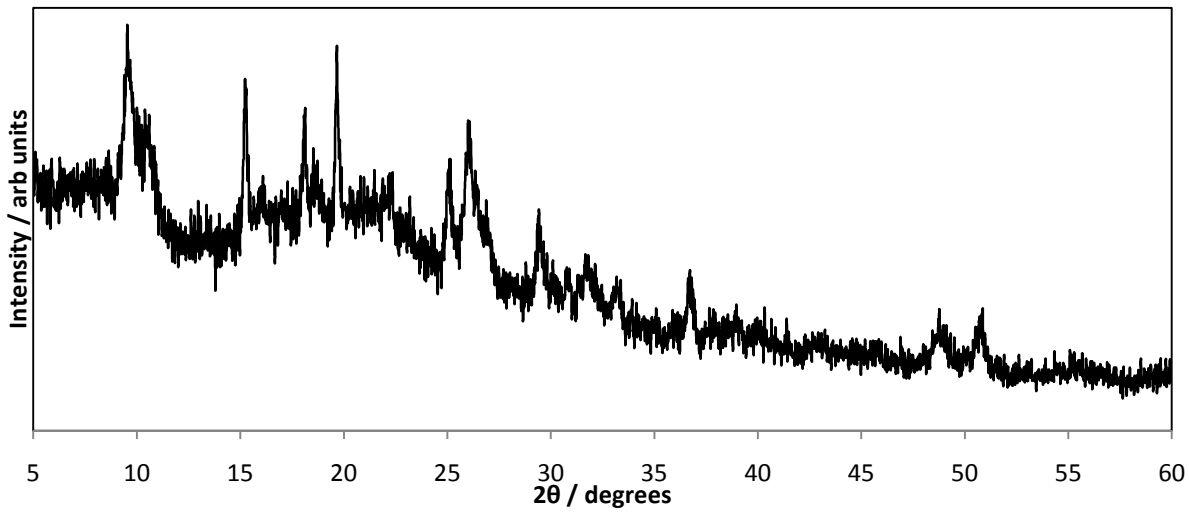

Figure 3.31 *XRD pattern of attempt to exchange lithium into AlTP-Na·4*

3.10 Structural Comparison of Exchanged phases

Table 3.6 shows the indexed unit cells and d-spacing of the d_{200} peak for all the fully exchange phases with comparable water content (2 formula units of water).

Table 3.6 *Unit cells and d-spacing of d_{200} peak for exchanged AlTP phases.*

Phase	a / Å	b / Å	c / Å	β / °	Volume / Å^3	d_{200} / Å
AlTP	7.9381(3)	4.9188(2)	11.6286(4)	95.739(2)	451.77(3)	7.94*
AlTP-Na	17.625(5)	4.916(1)	11.620(4)	107.89(1)	958.1(5)	8.42
AlTP-K	18.664(8)	4.855(1)	11.701(3)	91.87(2)	1059.7(6)	9.36
AlTP-Rb	19.506(15)	4.872(3)	11.799(8)	91.73(4)	1121(1)	9.77
AlTP-Cs	20.390(21)	4.871(4)	11.677(9)	95.28(6)	1154(2)	10.18
AlTP-Ag	17.237(7)	4.924(1)	11.660(3)	96.39(2)	983.5(5)	8.58

*This is the d_{100} peak in the case of AlTP

All the exchanged phases show a general similarity to the AlTP phase with respect to their *b* and *c* parameters but no apparent correlation in β angle. A general trend is apparent with the *a* parameter, it having slightly more than doubled in all the fully exchanged phases.

The doubling of the unit cell along *a* is not a result of the inter-lamellar region doubling in size (as the d-spacing of the d_{200} peak, which is directly related to the interlayer spacing, increases but does not double) but is likely the result of adjacent phosphate layers somehow becoming crystallographically distinct. This may result from either the exchanged cations ordering in a way which requires two AlTP layers before a suitable unit cell is formed or if neighbouring phosphate layers are shifted with respect to each other. As this more than doubling of the *a* parameter occurs for every exchanged phase except lithium, it suggests the probable structural shift observed is dependent upon the size of the cation exchanged and lithium is too small to effect such a change on the structure.

It appears that the d-spacing of the d_{200} peak is directly correlated to the radii of the cation exchanged (Figure 3.32). The interlayer spacing relates to the size of the *a* parameter, but the linear relationship does not extend to *a* (Figure 3.33). This is likely due to the minor difference in *b* and *c* and major differences in β, so the unit cell volume is likely a more reliable comparison. This shows a clear linear relationship with the cationic radii (Figure 3.34), implying all the exchanged phases are either isostructural or have similar cation sites in the inter-lamellar region.

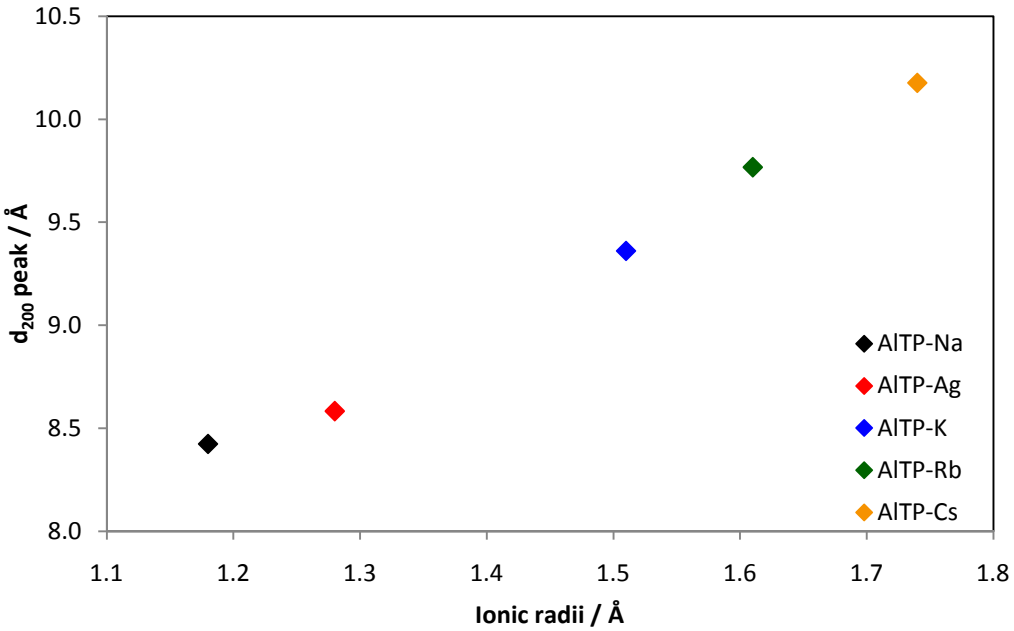

Figure 3.32 *d-spacing of d_{200} peak against ionic radii of exchanged cation[44] (Ionic radii for 8 coordinate cation used)*

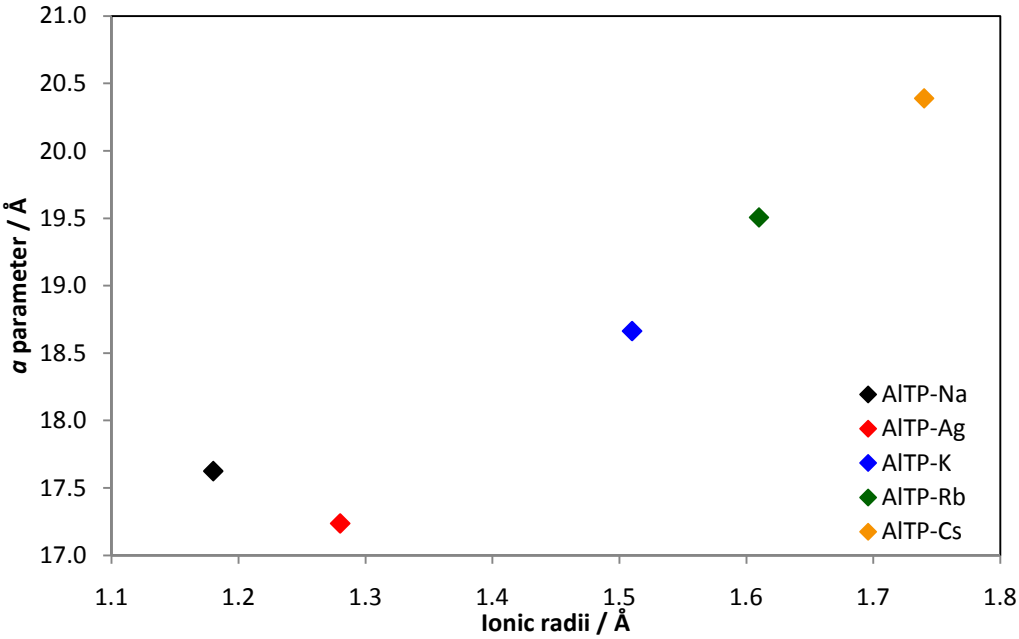

Figure 3.33 *a parameter against ionic radii of exchanged cation[44] (Ionic radii for 8 coordinate cation used)*

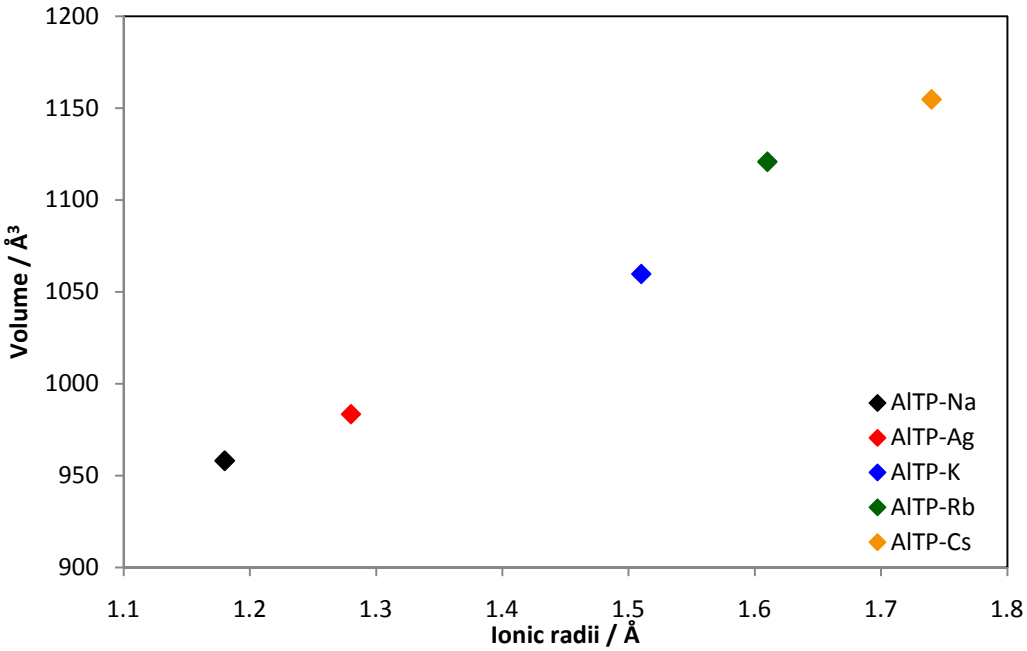

Figure 3.34 *Unit cell volume against ionic radii of exchanged cation[44] (Ionic radii for 8 coordinate cation used)*

3.11 Conclusions

Alkali metals (Na, K, Rb and Cs) and Ag have been successfully ion exchanged into AlTP, with complete exchange being achieved. Exchanges were only possible with raising the pH by the addition of a base to the exchanging solution. Unlike α-ZrP a strong base is not required for exchange, often a carbonate is sufficient; So the AlTP host is therefore a more readily exchanged material than α-ZrP.

TGA and DTA data show all the alkali metal exchanged phases contain a thermodynamically stable phase with two waters of crystallisation and a metastable phase with a different number of waters. Potassium, rubidium and caesium have a monohydrate phase reversibly formed from heating the more stable dihydrate, with only the potassium phase isolable at room temperature. In sodium's case the second phase is formed first with four waters and irreversibly forms the two water phase upon heating. The sodium, potassium and rubidium all decompose between 500-550 °C to form MPO_3 and $AlMP_2O_7$ which further

decompose to another MPO_3 and $AlPO_4$. The caesium phase transforms into another previously reported layered phase with the same stoichiometry.

Unit cells have been indexed for most of the fully exchanged phases synthesised. All show *b* and *c* parameters similar to the AlTP unit cell and have an *a* parameter more than double that of the original unit cell. This is likely to be a result of adjacent phosphate layers becoming crystallographically inequivalent. Also there is a linear relationship between the d-spacing of the d_{200} peak and cationic radii, and the unit cell volume and cationic radii, suggesting the different exchanged phases are either isostructural or have similar cation sites.

Lithium has shown very different ion exchange properties to other monovalent cations with respect to AlTP. It shows 3 different phases of differing lithium loading, two previously reported and a third reported here. Unlike the other monovalent cations lithium has not yet been fully exchanged into the structure. The third loading phase reported here was obtained by adding hydroxide to the exchanging solution with LiCl:LiOH ratios of 9:1 or 8:1 and has a unit cell of a = 8.015(6) Å, b = 4.890(3) Å, c = 11.586(6) Å and β = 95.24(3) ° and a content of around 50% of the potential maximum exchange. The lithium content can be increased by altering the ratio of lithium to aluminium to 50:1 or by refreshing the exchanging solution. Increasing the ratio any higher or refreshing solutions containing hydroxide results in a significant breakdown in the crystallinity of the phase and formation of other unidentified phases. Refreshing the pure lithium chloride solution pushes the resulting products into the highest loading phase and increases its exchange to around 60%.

References

1. H. S. Thompson and Roy, *J. Agric. Soc. Engl.*, 1850, **11**, 68.
2. J. T. Way and Roy, *J. Agric. Soc. Engl.*, 1850, **11**, 313.
3. J. Z. Lemberg, *Dtsch. Geol. Ges.*, 1870, **22**, 355.
4. G. J. Wiegner, *Landwirtsch*, 1912, **60**, 197.
5. A. Clearfield, *Chem. Rev.*, 1988, **88**, 125.
6. A. Clearfield, R. H. Blessing and J. A. Stynes, *J. Inorg. & Nucl. Chem.*, 1968, **30**, 2249.
7. G. Alberti, M. Casciola and U. Costantino, *J. Memb. Sci.*, 1983, **16**, 137.
8. Y. Hasegawa and I. Tomita, *Bull. Chem. Soc. Jpn.*, 1970, **43**, 3011.
9. G. Alberti, M. G. Bernasconi, M. Casciola and U. Costantino, *J. Inorg. & Nucl. Chem.*, 1980, **42**, 1631.
10. G. Alberti, U. Costantino, S. Allulli and M. A. Massucci, *J. Inorg. & Nucl. Chem.*, 1975, **37**, 1779.
11. A. Clearfield, W. L. Duax, A. S. Medina, G. D. Smith and J. R. Thomas, *J. Phys. Chem.*, 1969, **73**, 3423.
12. A. Clearfield, A. S. Medina, W. L. Duax and J. M. Garces, *J. Inorg. & Nucl. Chem.*, 1972, **34**, 329.
13. A. Clearfield and A. Oskarsson, *Ion Exch. Membr.*, 1974, **1**, 205.
14. L. Kullberg and A. Clearfield, *J. Phys. Chem.*, 1980, **84**, 165.
15. A. Clearfield, *Annu. Rev. Mater. Sci.*, 1984, **14**, 205.
16. J. Albertsson, A. Oskarsson, R. Tellgren and J. O. Thomas, *J. Phys. Chem.*, 1977, **81**, 1574.
17. G. Alberti, *Acc. of Chem. Res.*, 1978, **11**, 163.
18. G. Alberti, U. Costanti and J. P. Gupta, *J. Inorg. & Nucl. Chem.*, 1974, **36**, 2103.
19. A. Clearfield and J. Troup, *J. Phys. Chem.*, 1970, **74**, 314.
20. Y. Hasegawa and Y. Komiyama, *Bull. Chem. Soc. Jpn.*, 1978, **51**, 2302.
21. S. Allulli, A. Laginest and N. Tomassin, *J. Inorg. & Nucl. Chem.*, 1974, **36**, 3839.
22. A. Clearfield and S. Cheng, *J. Inorg. & Nucl. Chem.*, 1980, **42**, 1341.
23. M. G. Bernasconi, M. Casciola, U. Costantino and M. L. L. Giovagnotti, *Ann. Chim.*, 1979, **69**, 9.
24. F. D'Yvoire, *Bull. Soc. Chim. Fr*, 1962, **6**, 1224.
25. V. A. Lyutsko, M. V. Nikanovich, K. N. Lapko and V. F. Tikavyi, *Z. Neorg. Khim.*, 1983, **28**, 1949.
26. M. T. Averbuch-Pouchot, A. Durif and J. C. Guitel, *Acta Crystallogr. Sect. B-Struct. Commun.*, 1977, **33**, 1436.
27. V. A. Lyutsko and A. F. Selevich, *Z. Neorg. Khim.*, 1985, **30**, 1800.
28. A. Hayashi, H. Saimen, N. Watanabe, H. Kimura, A. Kobayashi, H. Nakayama and M. Tsuhako, *Langmuir*, 2005, **21**, 7238.
29. S. K. Rishi, Ph.D thesis, University of Birmingham, 2006.
30. S. K. Rishi, B. M. Kariuki, N. J. Checker, J. Godber and A. J. Wright, *Chem Comm*, 2006, 747.
31. R. Shirely, *The CRYSFIRE System for Automatic Powder Indexing: User's Manual*, The Lattice Press, 41 Guilford Park Avenue, Guilford, Surry, GU42 47NL, England, 2000.
32. C. Greaves, *DSPACE*, The School of Chemistry, The University of Birmingham, 1982.
33. CELL, based on original code by M.F. Pye, I.C.L., Oxford.

34. J. Laugier and B. Bochy, *LMGP Suite of Programs*, Grenoble, France, 2000, http://www.ccp2014.ac.uk/tutorial/lmgp/.
35. P. R. Rudolf and A. Clearfield, *Inorg. Chem.*, 1989, **28**, 1706.
36. JCPDS, *International Centre for Diffraction Data*, P.1., Swathmore, Pensylvania, PA 19081, USA, 11990.
37. ICSD, *Inorganic Crystal Structure Database*, http://www.cds.dl.ac.uk/datasets/crys/icsd/llicsd.html.
38. W. R. Wilmarth, G. J. Lumetta, M. E. Johnson, M. R. Poirier, M. C. Thompson, P. C. Suggs and N. P. Machara, *Solv. Extract. Ion Exch.*, 2011, **29**, 1.
39. S. Chitra, S. Viswanathan, S. V. S. Rao and P. K. Sinha, *J. Radioanal. & Nucl. Chem.*, **287**, 955.
40. R. N. Devi and K. Vidyasagar, *J. Chem. Soc. - Dalt. Trans.*, 2000, 1605.
41. A. Guesdon, E. Daguts and B. Raveau, *J. Sol. Stat. Chem.*, 2002, **167**, 258.
42. G. Alberti, U. Costanti, S. Allulli and M. A. Massucci, *J. Inorg. & Nucl. Chem.*, 1973, **35**, 1339.
43. G. Alberti, U. Costanti, S. Allulli, M. A. Massucci and N. Tomassin, *J. Inorg. & Nucl. Chem.*, 1974, **36**, 653.
44. R. D. Shannon, *Acta Crystallogr. Sec. A*, 1976, **32**, 751.

Chapter 4

Structural Determinations of Ion Exchanged $AlH_2P_3O_{10}\cdot 2H_2O$

4.1 Introduction

Solving the crystal structure of a newly synthesised phase can often be more challenging than the synthesis itself. The host AlTP material for example was first synthesised by D'Yvoire in 1962[1] but the structure remained unknown until 44 years later, finally being solved by Rishi in 2006[2].

Several routes are potentially available to determine the crystal structure of a material. The first and often preferred method is *via* single crystal X-ray diffraction. This method is able to produce an XRD pattern where spots of intensity can usually be related to a single *hkl* value, rather than in powder patterns where a given peak may contain several overlapping *hkl* reflections. The location and intensity of these spots can then be used to identify a structural model for the crystal by direct methods or other methods such as Patterson methods. If necessary, this model can be used to generate a powder XRD pattern to confirm that a crystal is representative of the whole sample. One significant drawback to single crystal methods is the need for suitably sized crystals of the materials of interest, which are often difficult to produce.

In powder data, the presence of overlapping peaks provide a significant challenge to structure determination. The most common method to overcome this detail is Rietveld analysis. As discussed in greater detail in Chapter 2.5, this technique requires an initial model, the identification of which is often difficult, but may be found in one of several structural databases[3, 4]. Once obtained the model can then be refined to better match observed diffraction data, and techniques such as Fourier-difference and Patterson mapping applied to locate missing or misplaced atoms within the model.

Ab initio methods are also possible; generally for phases with few overlapping peaks, often possessing higher symmetry and small unit cells. A number of computational techniques also exist, using global optimisation algorithms, for example the Differential Evolution algorithm[5], which can use suitable fragments or molecules, such as an AlTP layer for instance, if present, to build and refine potential models. In recent years these computational methods have found increasing use in modelling and simulating layered materials[6-8].

This chapter describes attempts undertaken to solve the crystal structures of the ion exchanged AlTP phases synthesised in Chapter 3 using X-ray and neutron diffraction data, Rietveld refinement and Pair Distribution Function analysis methods.

4.2 Experimental

Ion exchanged samples were prepared as described in Chapter 3. To deuterate samples for neutron diffraction studies, 6g of ion exchange AlTP were refluxed in D_2O for 48 hours under flowing nitrogen gas. After 24 hours the D_2O was replaced with a fresh solution, while minimising contact with the atmosphere. Samples were then collected *via* vacuum filtration and dried over several hours under vacuum on a schlenk line.

4.3 Structural Determination

Several observations and assumptions about the structure of the ion exchanged AlTP phases have so far been made in Chapter 3.10. Firstly the exchanged cations likely sit in a similar site in all the exchanged phases and secondly that the phosphate layers remain intact. This second observation has been supported by Pair Distribution Function analysis (PDF), shown in Figure 4.1. The short range order section of the PDF patterns, showing local structure, shows the presence of a number of peaks corresponding to atom to atom distances from within the phosphate layer. Utilising this and the knowledge that the unit cell now contains two intact phosphate layers, several possible models for the layered framework were constructed. These models were then analysed using the Rietveld refinement method through the GSAS suite of programs[9], with a view to determine their accuracy as framework models and to use difference fourier mapping to attempt to locate cationic and inter-lamellar water sites in the inter–lamellar region. The following section will outline each of these models and the analysis they underwent.

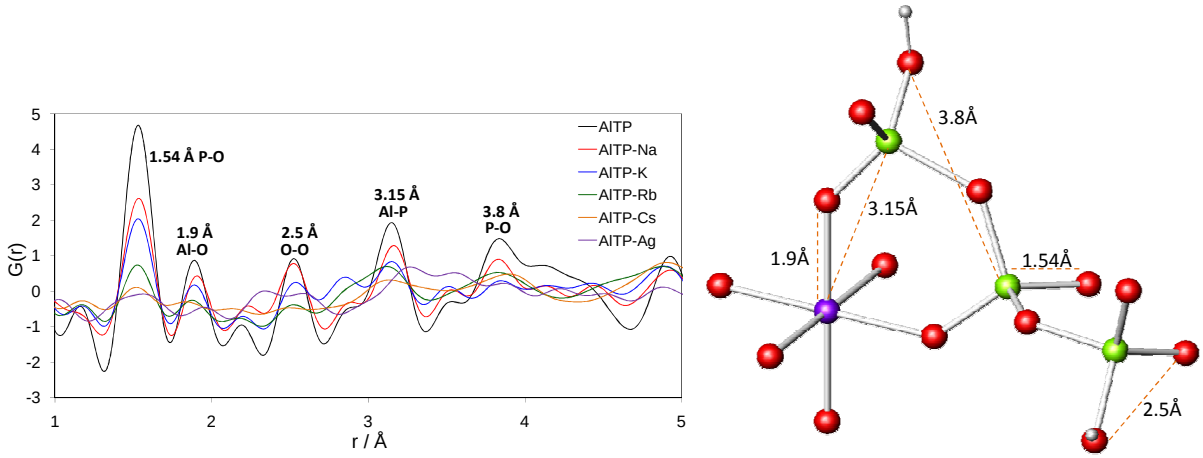

Figure 4.1 *PDF plots for AlTP and ion exchanged phases and layer fragment showing inter-atom distances. Purple spheres aluminium, green phosphorus and red oxygen.*

4.3.1 Framework Models

The AlTP-Rb system was chosen for initial studies as the X-ray diffraction scattering from the Rb cations would dominate the scattering from the phosphate framework, making them easier to locate using fourier mapping. In contrast, the neutron diffraction data collected should give a more equal scattering intensity between phosphate layer and cation, helping to more accurately confirm P and O positions. This approach was viewed as giving a sensible route to determining how the host AlTP structure had been altered by the ion exchange process. The AlTP-K phase displays a more equal scattering between host and cation in both X-ray and neutron and the AlTP-Cs displays lower crystallinity. In addition Chekcell[10] results of the initial CELL[11] refinements suggested that AlTP-Rb may adopt the same space group (P2/c) as the host material, which makes altering the host structure to produce new framework models initially easier.

4.3.1.1 Model 1: Ordered Ion Exchanged Cations

The first model attempted assumed that there was no change in the relative orientation of the phosphate layers and that the doubling of the unit cell resulted from the inter-lamellar cations ordering in alternate sites within the inter-lamellar regions.

To create the model, the original AlTP structure[12] was placed into the expanded AlTP-Rb unit cell and all the *x* co-ordinates modified to keep the layer thickness identical to that of the original AlTP. The Al site was then moved to the origin for convenience, and a second layer added at half a unit cell along [100] (model shown in Figure 4.2).

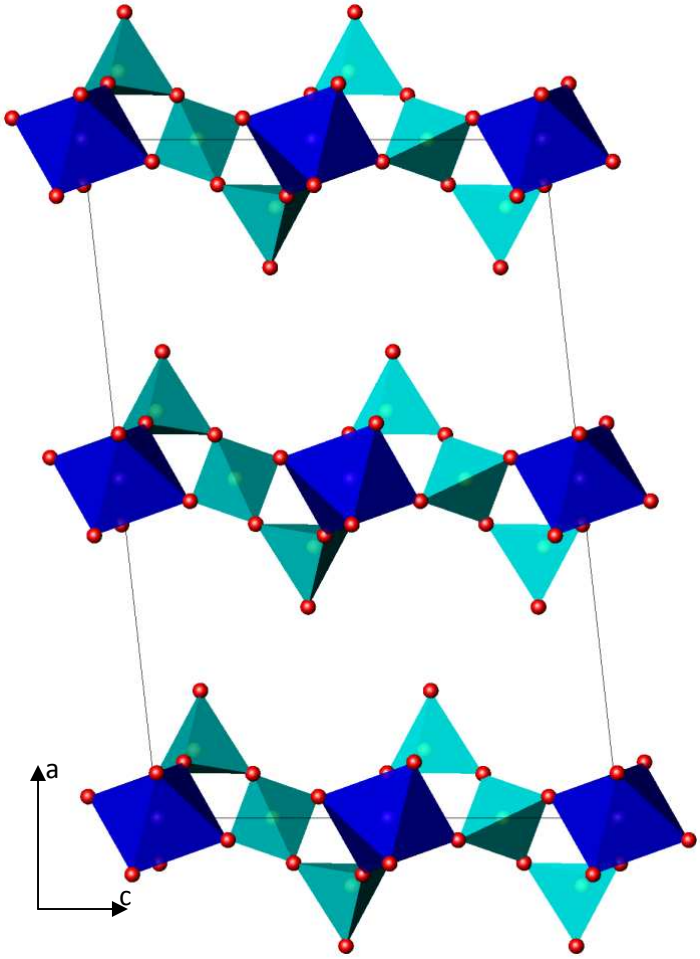

Figure 4.2 *Framework model containing no inter-layer displacement. Dark blue octahedra AlO_6, light blue tetrahedral PO_4 and red spheres are oxygen, unit cell shown*

The Rietveld refinement of this model resulted in poor fits for both X-ray (χ^2 = 285.0, R_{wp} = 42.47% and R_p = 30.75%) and neutron diffraction (χ^2 = 82.99, R_{wp} = 10.57% and R_p = 6.52%), Figures 4.3 and 4.4. Although reflection markers matched all the observed peaks, substantial intensity mismatches, especially in the X-ray refinement were evident. Given the model was missing the strongest X-ray scattering ion, this was not unexpected and numerous fourier maps were produced to search the inter-lamellar region for the cations and water molecules. However, these failed to provide any potential suitable sites for the exchanged cations so this model was rejected.

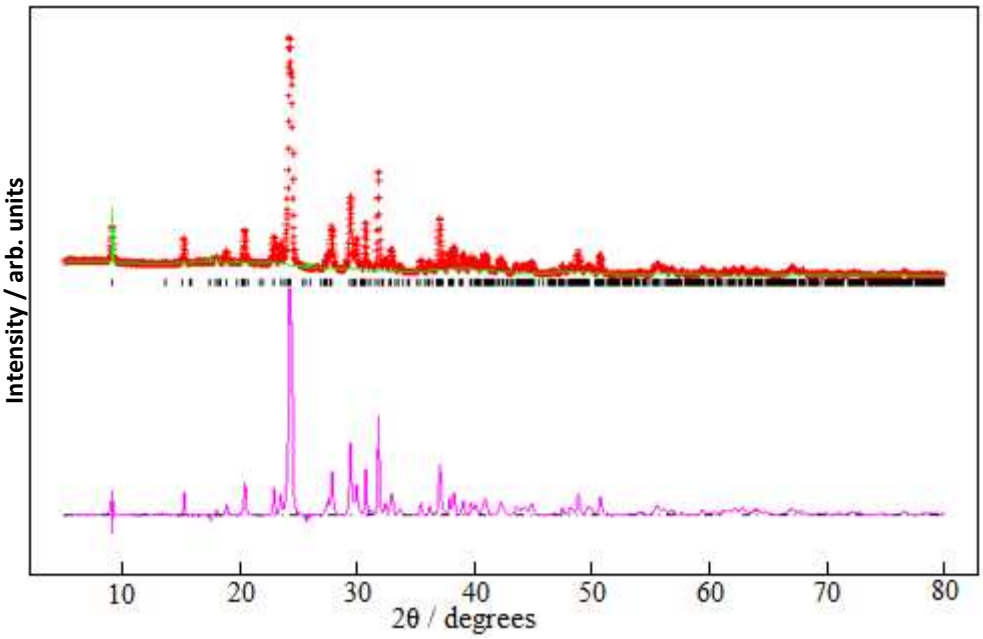

Figure 4.3 *Observed (+), calculated (-) and difference (-) X-ray powder diffraction refinement of framework model containing no inter-layer displacement. Reflection positions are also marked (***|***)*

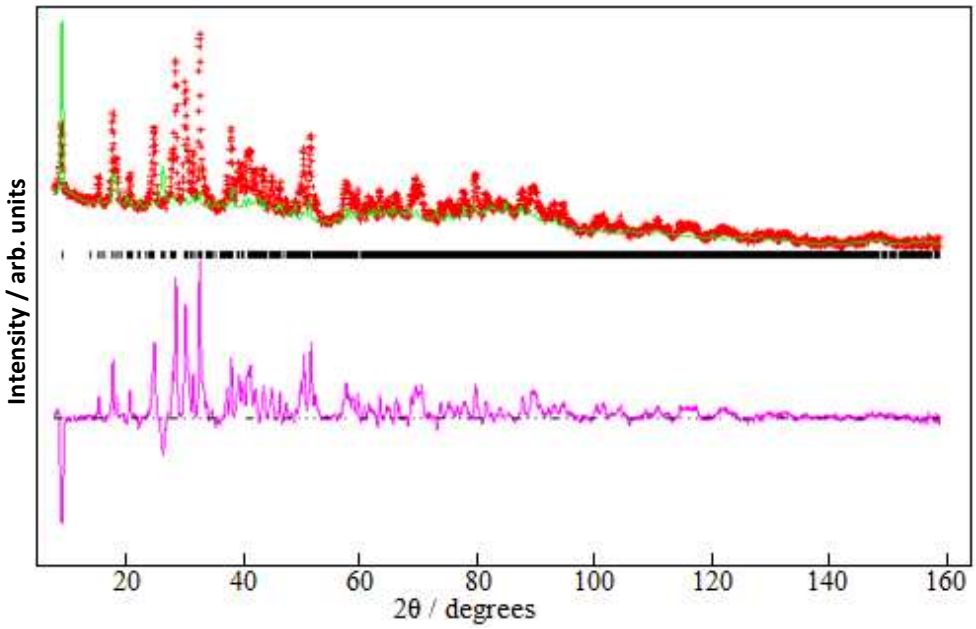

Figure 4.4 *Observed (+), calculated (-) and difference (-) neutron powder diffraction refinement of framework model containing no inter-layer displacement. Reflection positions are also marked (***|***)*

4.3.1.2 Model 2: Layer displaced half unit cell along [001]

The second model attempted, involved displacing alternative AlTP layers along the *c* axis direction by half a unit cell; the model is shown in Figure 4.5. This movement creates no topographic movement with respect to the orientation of terminal oxygens group of

adjacent layers, but changes the orientation of the AlO_6 octahedra in every other layer. This creates two crystographically distinct layers within the unit cell, justifying the doubling along the *a* axis.

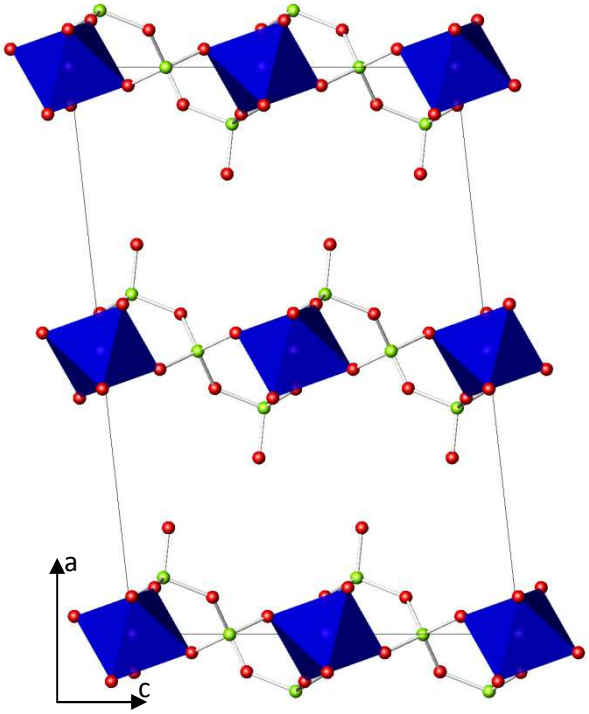

Figure 4.5 *Unit cell of the framework model containing a layer displacement half a unit cell along [001], showing the different tilt orientation of the blue AlO_6 octahedra. Green spheres phosphorus and red oxygen*

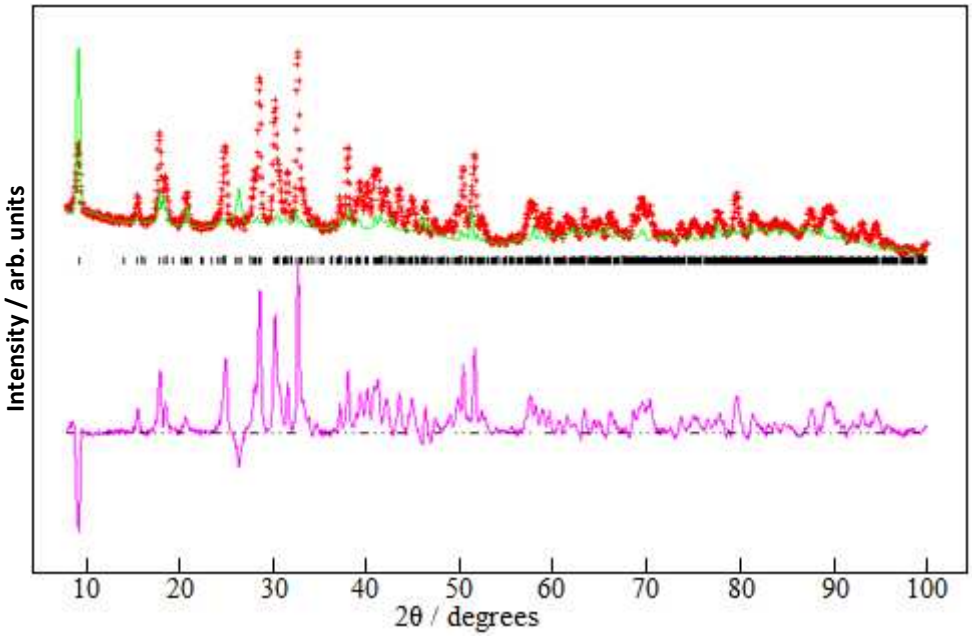

Figure 4.6 *Observed (+), calculated (-) and difference (-) neutron powder diffraction refinement of framework model containing a layer displacement half a unit cell along [001]. Reflection positions are also marked* **(ı)**

A Rietveld refinement using this model gave very similar results as model 1, (χ^2 = 92.75, R_{wp} = 11.16% and R_p = 7.22%) (Figure 4.6). All peaks were successfully indexed and therefore fourier mapping was performed. However as with model 1, no cationic positions were located, resulting in this model also being discarded.

4.3.1.3 Model 3: Layer displaced half unit cell along [010]

The next model developed involved displacing alternate AlTP layers in a direction half a unit cell along the *b* axis. This gave a noticeable framework change as now the terminal oxygens protruding into the interlayer region are now staggered in the *bc* plane as well as the *ac* plane, Figure 4.7. This model gave similar results following Rietveld refinements as had the previous models (χ^2 = 87.54, R_{wp} = 10.85% and R_p = 6.98%) and no cationic sites were established after fourier mapping was attempted. This model was therefore also rejected.

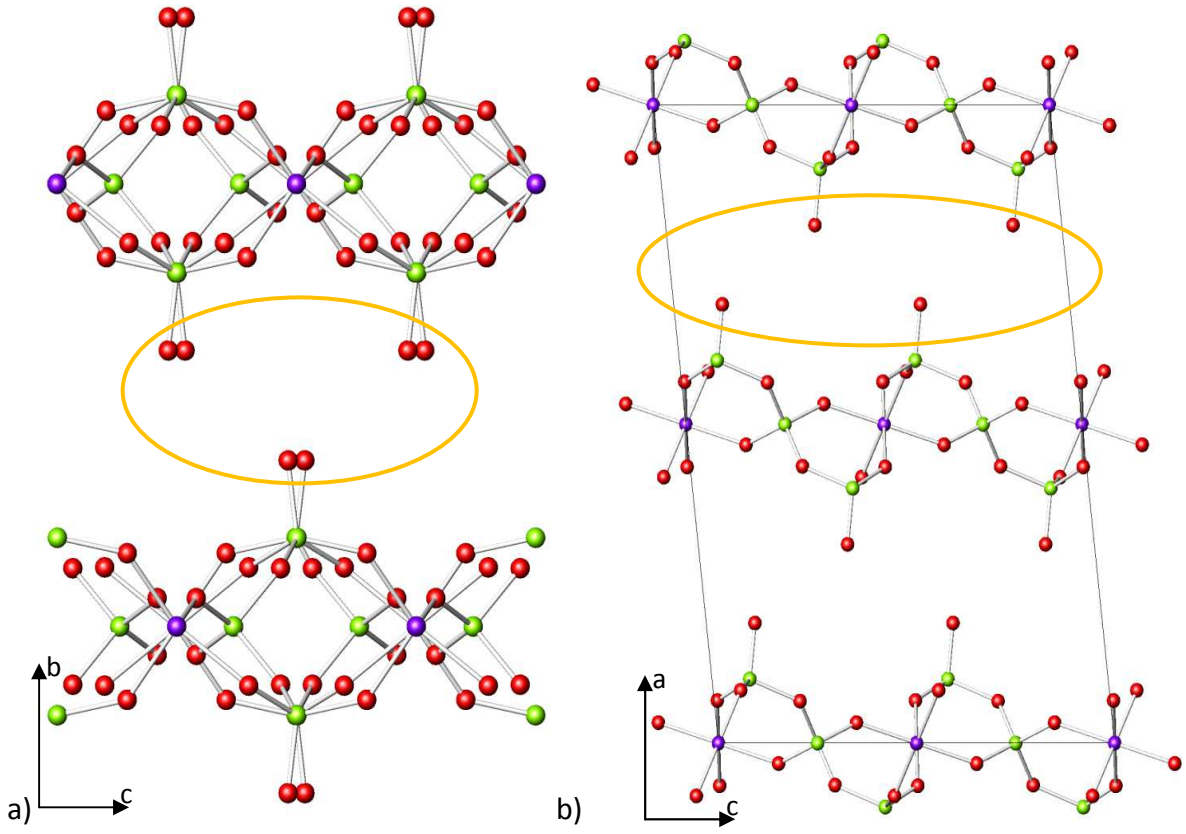

Figure 4.7 *Framework of model containing half unit cell displacement along* [010]*, highlighted area showing staggering of terminal oxygens in both a) ac plane and b)bc plane. Purple spheres aluminium, green phosphorus and red oxygen*

4.3.1.4 Model 4: Layer displaced half unit cell along [011]

The previous two models were then combined to create another model containing both alternating AlTP layers with alternating AlO_6 tilt angles and also staggered oxygens. Unfortunately, this model also failed to provide an acceptable fit following Rietveld analysis (χ^2 = 88.64, R_{wp} = 10.92% and R_p = 7.05%) and was therefore rejected.

4.3.1.5 Model 5: Layer displaced quarter unit cell along [001]

This model displaced alternate AlTP layers by a quarter of a unit cell along the *c* axis. This alters the framework so the terminal oxygens are eclipsed in both the *ac* and *bc* planes, Figure 4.8. The Rietveld refinement and attempted fourier maps, similar to the other models, failed to provide an acceptable fit (χ^2 = 98.48, R_{wp} = 11.5% and R_p = 7.55%) or cation positions, and was therefore also rejected.

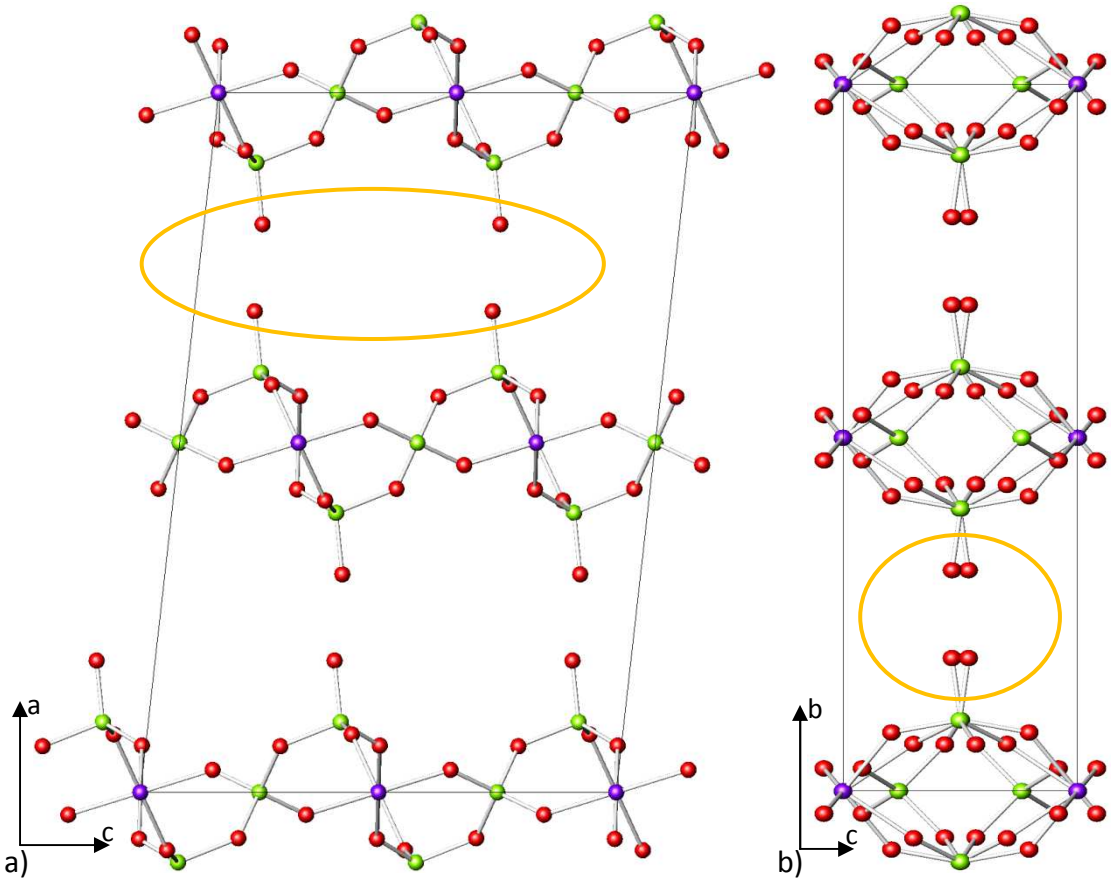

Figure 4.8 *Framework of model containing quarter unit cell displacement along c axis, highlighted eclipsed formation of terminal oxygens in a) the ac plane, b) the bc plane. Purple spheres aluminium, green phosphorus and red oxygen*

4.3.1.6 Model 6: Layer displaced quarter unit cell along [001] and half along [010]

The next model attempted for the AlTP-Rb phase moved alternate AlTP layers by half a unit cell along the *b* axis and quarter of a unit cell along the *c* axis. This moved the terminal oxygens into an eclipsed formation in the *ac* plane but a staggered formation in the bc plane. Again the Rietveld refinement and fourier maps were unable to provide an acceptable fit (χ^2 = 100.4, R_{wp} = 11.61% and R_p = 7.66%) with the diffraction data and so this model too was rejected.

4.3.2 Alternate space group models

Having been unsuccessful with models based on P2/c, the space group used to generate models was reconsidered. In revisiting the unit cell determination from Chapter 3, it was noted that C2 was a possible space group for AlTP-Na and AlTP-Ag. As C2 possesses lower symmetry than space group P2/c it was deemed a reasonable starting point for building framework models for the phase.

4.3.2.1 Model 7: C2 AlTP-Rb Model

Moving the origin and taking careful account of the presence of C-centring allowed the building of a model equivalent to P2/c with alternate layers displaced half a unit cell along the *b* axis. Rietveld refinement of this model showed the model was clearly not complete yet, but was a significant improvement upon those attempted with P2/c. Possible cationic sites within the inter-lamellar region were identified using fourier mapping, followed by possible sites for the inter-lamellar waters (Figure 4.9).

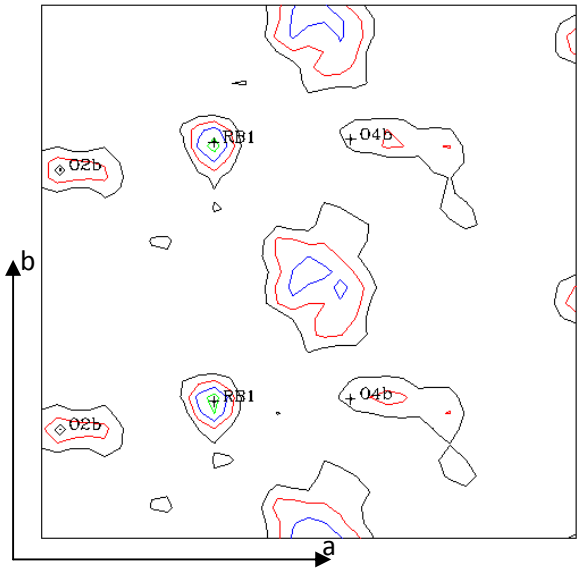

Figure 4.9 *Fourier map of C2 AlTP-Rb model, showing potential site for inter-lamellar water positions*

Adding the oxygens to the model allowed it to be refined further (Figure 4.10), giving values, for the neutron refinement, of χ^2 = 16.27, R_{wp} = 4.67% and R_p = 3.5%. This was a clear improvement on those of models 1-6. Despite further attempts no significant improvements were possible.

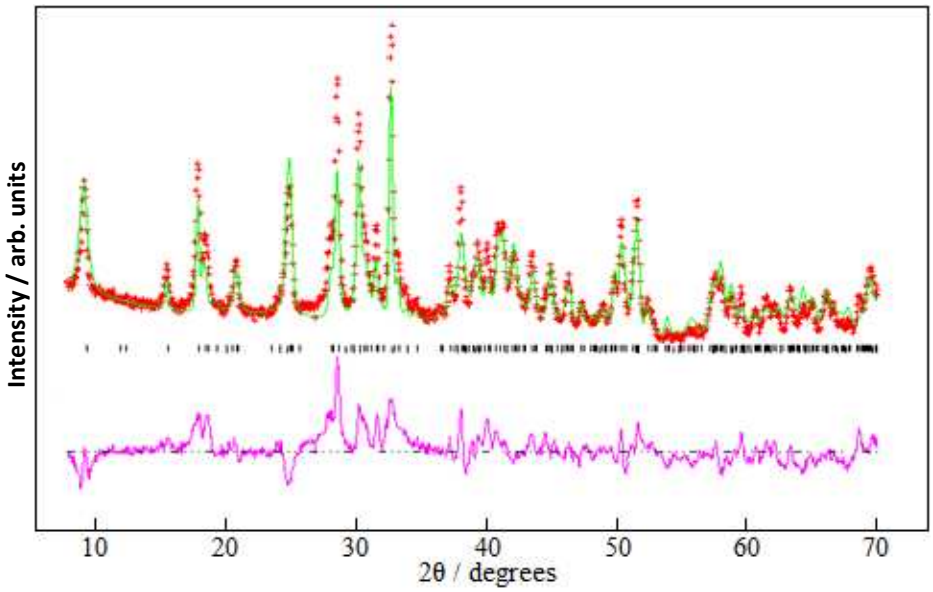

Figure 4.10 *Observed (+), calculated (-) and difference (-) neutron powder diffraction refinement of C2 AlTP-Rb model containing inter-lamellar oxygens. Reflection positions are also marked* **(|)**

4.3.2.2 Model 8: C2/c AlTP-Rb Model

On reconsidering the host structure, it was noted that each AlTP layer possessed a *c* glide plane as an integral part of its symmetry. If we consider that each AlTP layer was still intact after the exchange, it is a reasonable assumption that it may have retained the *c* glide plane symmetry. In view of this it was decided to combine the *c* glide with the *C* centring of the C2 model and create a new model for the phase in the space group C2/c.

The model involved moving the aluminium site to the inversion centre of the *c* plane at the origin of the unit cell. Application of this model improved the Rietveld refinement fit of the neutron diffraction data and facilitated the locating of the inter-lamellar water deuterium positions. Adding these to the model and refining the amount of deuteration gave the refinement fit shown in Figure 4.11 with values of χ^2 = 3.288, R_{wp} = 2.09% and R_p = 1.62%, and the final structure for the AlTP-Rb phase, with refined unit cell values of *a* = 19.482(1) Å, *b* = 4.8639(4) Å, *c* = 11.6594(8) and β = 91.899(6) °, which is discussed in Section 4.4.

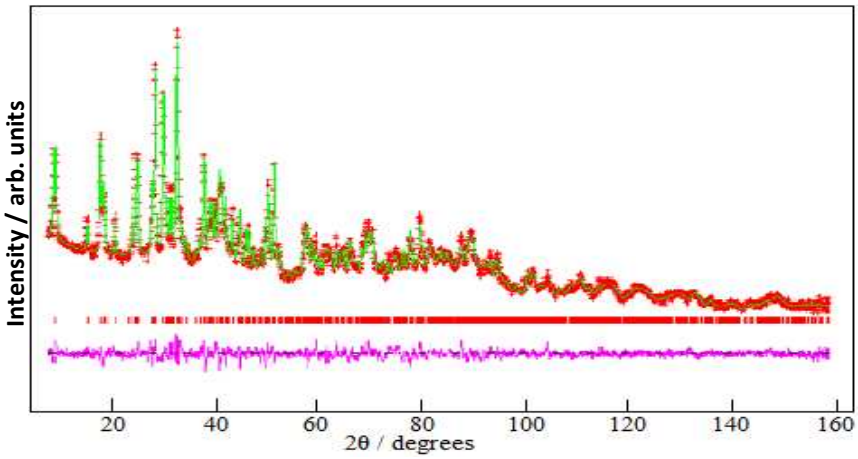

Figure 4.11 *Final observed (+), calculated (-) and difference (-) neutron powder diffraction refinement of AlTP-Rb structure. Reflection positions are also marked (I)*

4.4 AlTP-Rb Structure

Atomic coordinates for the AlTP-Rb structure are given in Table 4.1, Figure 4.12 shows the crystal structure and selected bond distances and angles are shown in Table 4.2.

Table 4.1 *Atomic coordinates for AlTP-Rb and equivalent isotropic displacement parameters ($Å^2 \times 10^2$). Space group C2/c, a = 19.482(1) Å, b = 4.8639(4) Å, c = 11.6594(8) and β = 91.899(6) °*

Atom	*x*	*y*	*z*	*U(eq) /* $Å^2 \times 10^2$	*Occupancy*	*Multiplicity*
Al	0	0	0	0.012(8)	1	4
P1	0.0905(3)	0.504(1)	0.5860(5)	0.2(1)	1	8
P2	0	0.255(2)	0.75	1.6(2)	1	4
O1	0.0555(3)	0.307(1)	0.4997(5)	0.69(7)	1	8
O2	0.9709(3)	0.083(1)	0.6512(5)	0.69(7)	1	8
O3	0.0745(3)	0.805(1)	0.5603(5)	0.7(1)	1	8
O4	0.1636(3)	0.452(1)	0.6039(5)	2.1(1)	1	8
O5	0.0597(4)	0.430(2)	0.7131(6)	4.4(2)	1	8
Rb	0.1746(3)	0.054(2)	0.3710(6)	6.1(2)	1	8
Ow	0.7378(5)	0.448(2)	0.6364(9)	5.8(3)	1	8
D1	0.6959(9)	0.283(3)	0.605(1)	6.3(5)	0.664(4)	8
H1	0.6959(9)	0.283(3)	0.605(1)	6.3(5)	0.336(4)	8
D2	0.7047(8)	0.580(4)	0.635(2)	6.3(5)	0.664(4)	8
H2	0.7047(8)	0.580(4)	0.635(2)	6.3(5)	0.336(4)	8

Table 4.2 *Selected bond lengths (Å) and angles (°) for AlTP-Rb*

Bond Lengths (Å)		*Bond Angels (°)*	
Al-O1	1.847(5)	O1-Al-O3	87.9(3)
Al-O2	1.913(6)	O2-Al-O3	90.6(2)
Al-O3	1.853(6)	O1-P1-O4	113.6(6)
P1-O1	1.531(7)	O1-P1-O5	106.6(5)
P1-O3	1.525(8)	O4-P1-O5	102.5(5)
P1-O4	1.454(7)	O2-P2-O5	104.7(3)
P1-O5	1.656(8)	O5-P2-O5	111.7(9)
P2-O2	1.517(7)	O1-Rb-O2	52.1(2)
P2-O5	1.516(9)	O1-Rb-O3	48.1(2)
Rb-O1	3.06(1)	O1-Rb-O4	136.9(3)
Rb-O2	2.919(9)	O1-Rb-Ow	141.8(4)
Rb-O3	3.23(1)	O2-Rb-O3	50.7(2)
Rb-O4	3.154(9)	O2-Rb-O4	166.0(4)
Rb-O4	3.35(1)	O2-Rb-Ow	111.2(4)
Rb-O4	3.93(1)	O2-Rb-Ow	138.1(4)
Rb-O4	3.97(1)	O3-Rb-O4	66.8(2)
Rb-O4	4.01(1)	O3-Rb-O4	123.8(3)
Rb-O5	3.70(1)	O3-Rb-Ow	152.3(4)
Rb-O5	3.79(1)	O4-Rb-O4	91.3(3)
Rb-Ow	2.99(1)	O4-Rb-Ow	50.8(2)
Rb-Ow	3.33(1)	O4-Rb-Ow	140.6(4)
Rb-Ow	3.04(1)	Ow-Rb-Ow	72.9(4)
Rb-Rb	4.80(1)	Ow-Rb-Ow	133.4(4)
Rb-Rb	5.854(2)	Rb-Ow-Rb	88.7(3)
Ow-H1/D1	1.19(2)	Rb-Ow-Rb	133.6(4)
Ow-H2/D2	0.91(2)	H1/D1-Ow-H2/D2	89.7(2)

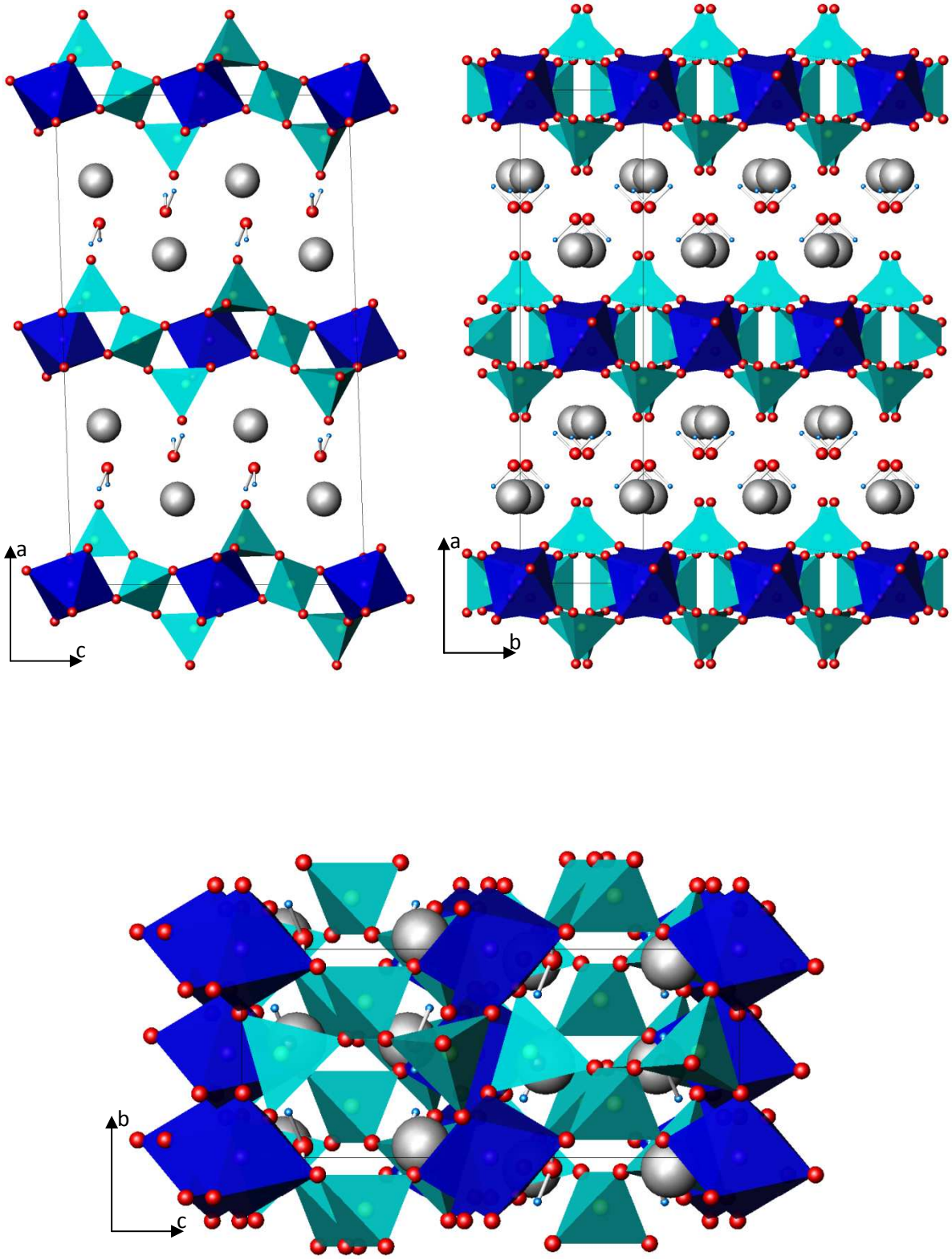

Figure 4.12 *Structure of AlTP-Rb. Dark blue octahedra AlO_6, light blue tetrahedra PO_4, red spheres oxygen, light blue spheres hydrogen/deuterium and grey spheres rubidium*

4.4.1 AlTP layers

The overall connectivity and structure of individual phosphate layers remains intact and equal to that seen in AlTP. There are differences in bond lengths and angles, but this is not unexpected due to the addition of rubidium cations to the structure.

The AlO_6 octahedra was found to be distorted by Rishi[12], containing 2 shorter Al-O bonds and 4 longer ones, with the ideal 90° angles distorted by up to 1.5° in AlTP. The AlO_6 octahedra in AlTP-Rb now contains 4 shorter bonds (2 × 1.847(5) Å and 2 × 1.853(6) Å) and 2 longer ones (2 × 1.913(6) Å) with distortions of up to 2° from the ideal O-Al-O angle of 90°.

The range of P-O bond lengths was found to be 1.454(7) Å to 1.656(8) Å and is unchanged from that of AlTP. The distribution differs slightly with the terminal P1-O4 now being the shortest length, as opposed to the P to O1 and O2 which are now intermediate lengths (Table 4.2). The bridging O5 still has the longest P-O bond lengths but, opposite to that in AlTP, the P1-O5 length is now greatest at over 1.6 Å. This change is consistent with other triphosphates, where those with hydrogen ions remaining on the triphosphate, such as $YbH_2P_3O_{10}$[13], have longer P-O bonds on the central phosphorus, whilst those without hydrogen ions, such as $LiNi_2P_3O_{10}$[14], have longer P-O bonds on the terminal phosphorus group. The O-P-O angles range from 102.5(5)° to 113.6(6)° (109.5° is ideal tetrahedral angle) which is ~5° narrower than the range observed in AlTP. Finally the P-P distances, P-O-P angles and P-P-P angles are 2.907(8) Å, 132.8(5)° and 130.84° respectively. These are consistent with AlTP with values of 2.901(4) Å, 132.0(5)° and 127.0(5)°, and other known triphosphates such as $Al(NH_4)HP_3O_{10}$[15] with values of 2.919 Å, 132.2° and 127.7°.

Where the phosphate layer structure in AlTP and AlTP-Rb differs significantly is the orientation of adjacent layers. AlTP possesses crystographically identical phosphate layers,

whereas AlTP-Rb has an alternating arrangement of identical layers but displaced with respect to each other. This means for the host, the *bc* plane has an eclipsed arrangement of terminal oxygens. In contrast, AlTP-Rb has layers displaced by half a unit cell along the *b* axis creating a staggered formation of the terminal oxygens in the *bc* plane (see Figure 4.12). The terminal oxygens are also arranged in a staggered arrangement in the *ac* plane, as is the case in AlTP.

4.4.2 Inter-lamellar region

The inter-lamellar region has three elements; the P_3O_{10} terminal oxygens, discussed in Section 4.4.1, the inter-lamellar water molecules and the exchanged rubidium cations. Both the water molecules and rubidium ions exist in zig-zag positions running along the *c* axis. The water molecules are located in close proximity to a given phosphate layer between two adjacent terminal oxygens (O4) in the *ab* plane with Ow-O4 bond distances of 2.8306 Å and an O4-Ow-O4 angle of 117.26°. The hydrogen/deuteriums of the water molecules are directed towards each of the terminal oxygens on the same phosphate layer, implying the inter-lamellar water molecules now have intra-layer hydrogen bonding across the face of layers (Figure 4.13) rather than inter-layer hydrogen bonding that exists in the AlTP host structure.

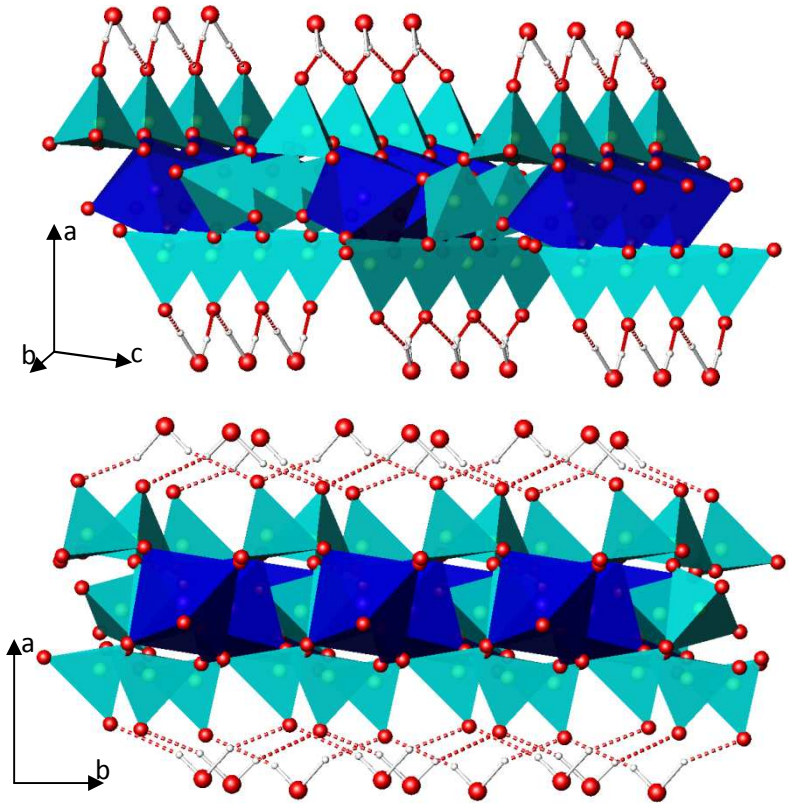

Figure 4.13 *Hydrogen bonding arrangement in AlTP-Rb (rubidiums omitted for clarity)*

The single rubidium site is described in detail in Section 4.4.3. The rubidium ions are located in chains along *b* and in alternate positions with the water molecules along *c*. In this way the large rubidium ions are positioned within the ridges of the AlTP layers in both the *b* and *c* directions.

Both the rubidium ions and water molecules have large temperature factors, suggesting some disorder on their sites. This is not unexpected given that their positions result from a room temperature exchange process.

4.4.3 Rubidium site

Figure 4.14 shows a fragment of the structure containing the local structure of the rubidium cation. The rubidium has a large coordination number of 14, supported by bond valence sum calculations (see Appendix 4). It forms a distorted square based pyramid with four terminal oxygens from one layer and a fifth from the adjacent layer. The rubidium sits

off-centre in this arrangement giving a number of differing bond lengths (3.35(1) Å to 4.01(1) Å) the shortest being that to the adjacent layer oxygen at 3.154(9) Å. The bond angles O4-Rb-O4 in this arrangement range from 75.97(3)° to 96.23(2)°. An oxygen 'well' is created above the four terminal oxygens by bridging oxygens attached to the terminal phosphorus atoms and topped by the O2 bridging between an aluminium and P2. The rubidium sits to one side of this well, having shorter bond distances to O1 and O3 (3.06(1) Å and 3.23(1) Å) than to the two O5 sites (3.70(1) Å and 3.79(1) Å). The O2 is closest to rubidium in this well, with a bond distance of 2.919(9) Å and O2-Rb-O4(adjacent layer) angle of 165.99(4)°. Finally the rubidium bonds to the four surrounding inter-lamellar waters with a narrow range of bond lengths of 2.96(1) Å to 3.33(1) Å.

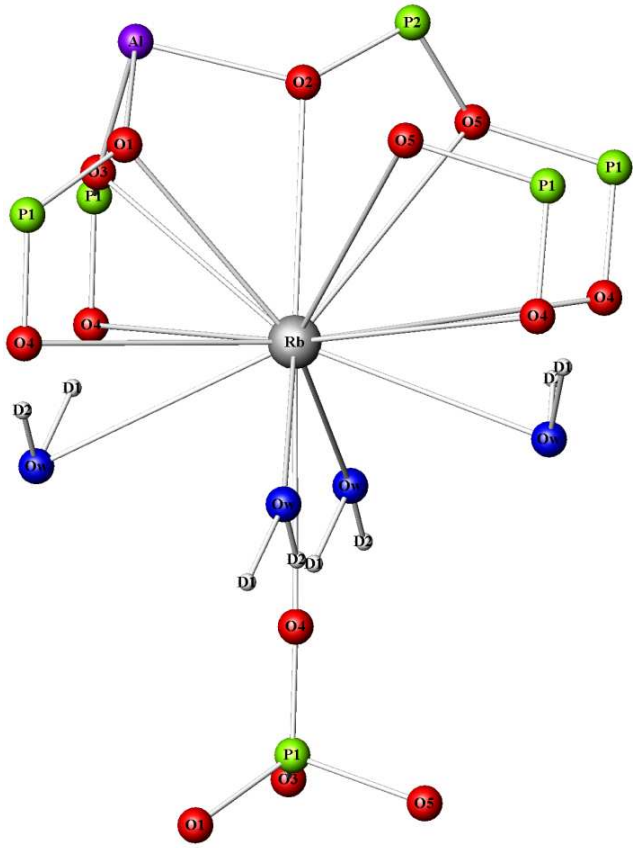

Figure 4.14 *Local structure around rubidium site. Grey spheres rubidium, purple aluminium, green phosphorus, red oxygen, blue inter-lamellar oxygen and white deuterium*

4.5 AlTP-Cs Structure

It was suggested in Chapter 3 that given the similar unit cells, the cationic site is likely similar in all of the ion exchanged AlTP phases. Utilising this assumption, the structural model of AlTP-Rb was used as a basis for the AlTP-Cs phase. This resulted in the refinement fit shown in Figure 4.15 with χ^2 = 3.124, R_{wp} = 2.53% and R_p = 2.03%, and the structure of AlTP-Cs with refined unit cell parameters of *a* = 20.450(2) Å, *b* = 4.8546(6) Å, *c* = 11.701(1) Å and β = 94.893(7)°. Atomic coordinates are shown in Table 4.3 and selected bond lengths and angles in Table 4.4.

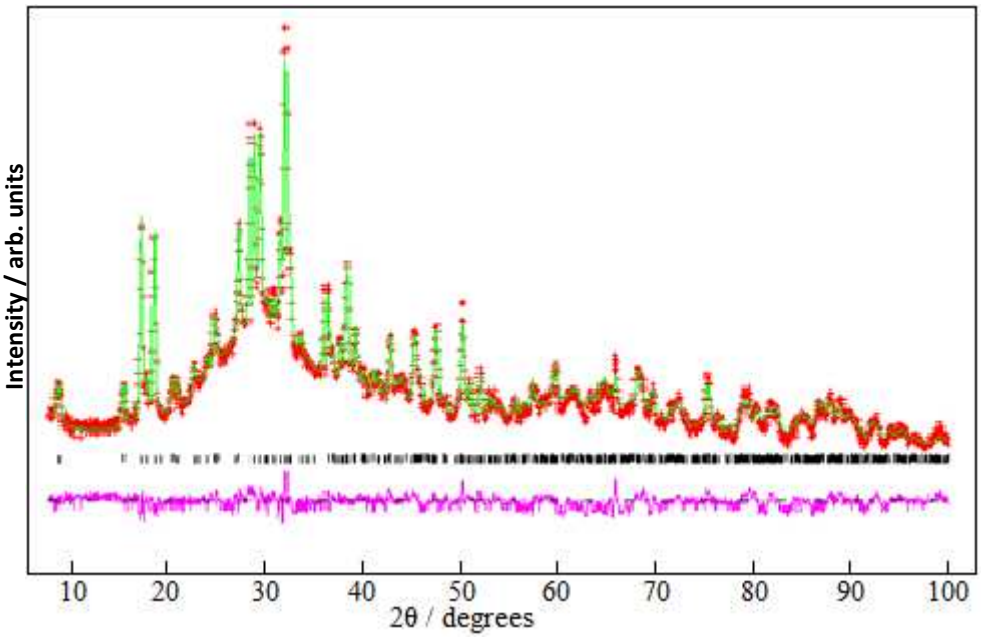

Figure 4.15 *Final observed (+), calculated (-) and difference (-) neutron powder diffraction refinement of AlTP-Cs structure. Reflection positions are also marked* **(**|**)**

Table 4.3 *Atomic coordinates for AlTP-Cs and equivalent isotropic displacement parameters ($Å^2 \times 10^2$). Space group C2/C, a = 20.450(2) Å, b = 4.8546(6) Å, c = 11.701(1) Å and β = 94.893(7)°*

Atom	*x*	*Y*	*z*	*U(eq) / $Å^2 \times 10^2$*	*Occupancy*	*Multiplicity*
Al	0	0	0	2.9(8)	1	4
P1	0.0862(6)	0.483(3)	0.592(1)	1.8(3)	1	8
P2	0	0.257(3)	0.75	1.3(4)	1	4
O1	0.0555(6)	0.328(3)	0.507(1)	3.6(3)	1	8
O2	0.9718(4)	0.071(2)	0.6440(8)	0.8(2)	1	8
O3	0.0744(5)	0.794(2)	0.5674(9)	2.1(3)	1	8
O4	0.1622(7)	0.458(3)	0.613(1)	4.3(4)	1	8
O5	0.0603(6)	0.429(3)	0.717(1)	4.3(3)	1	8
Cs	0.1709(6)	0.072(3)	0.355(1)	5.3(5)	1	8
Ow	0.7294(7)	0.454(4)	0.613(1)	5.8(5)	1	8
D1	0.7021(9)	0.300(4)	0.610(2)	7.4(7)	0.895(7)	8
H1	0.7021(9)	0.300(4)	0.610(2)	7.4(7)	0.105(7)	8
D2	0.6951(7)	0.607(3)	0.614(1)	3.7(4)	0.895(7)	8
H2	0.6951(7)	0.607(3)	0.614(1)	3.7(4)	0.105(7)	8

Table 4.4 *Selected bond lengths (Å) and angles (°) for AlTP-Cs*

Bond Lengths (Å)		*Bond Angels (°)*	
Al-O1	1.95(1)	O1-Al-O2	88.2(4)
Al-O2	1.86(1)	O1-Al-O3	91.8(6)
Al-O3	1.93(1)	O1-P1-O3	110.5(1)
P1-O1	1.35(2)	O1-P1-O4	117.8(1)
P1-O3	1.55(2)	O3-P1-O4	104.1(9)
P1-O4	1.56(1)	O4-P1-O5	104.2(9)
P1-O5	1.62(2)	O2-P2-O2	111.4(1)
P2-O2	1.60(1)	O2-P2-O5	110.3(5)
P2-O5	1.56(1)	O2-P2-O5	104.7(5)
Cs-O1	3.32(2)	O1-Cs-O3	46.1(4)
Cs-O2	3.00(2)	O1-Cs-O4	135.2(5)
Cs-O3	3.57(2)	O1-Cs-O5	92.6(4)
Cs-O4	3.57(2)	O2-Cs-O5	43.3(3)
Cs-O4	3.63(2)	O2-Cs-Ow	144.0(6)
Cs-O4	3.41(2)	O3-Cs-O4	121.1(5)
Cs-O5	3.61(2)	O3-Cs-O5	72.2(4)
Cs-O5	3.60(2)	O4-Cs-O4	92.9(5)
Cs-Ow	3.27(2)	O4-Cs-O5	87.3(4)
Cs-Ow	3.07(2)	O4-Cs-Ow	48.6(4)
Cs-Ow	3.20(2)	O5-Cs-O5	84.6(4)
Cs-Ow	3.17(2)	O5-Cs-Ow	160.3(5)
Cs-Cs	4.855(6)	Ow-Cs-Ow	99.8(6)
Cs-Cs	4.88(3)	Ow-Cs-Ow	134.1(6)
Cs-Cs	5.47(3)	Cs-Ow-Cs	102.8(6)
Ow-H1/D1	0.93(2)	Cs-Ow-Cs	135.3(6)
Ow-H2/D2	1.02(2)	H1/D1-Ow-H2/D2	99.9(2)

The AlTP-Cs phase is clearly isostructural to AlTP-Rb, as shown in Figure 4.17a and 4.17b. There are a few changes in bond lengths and angles due to accommodating the larger caesium ions. The AlO_6 octahedra now have four longer and two shorter bonds (2 ×1.95(1), Å 2 × 1.93(1) Å and 2 × 1.86(1) Å) as opposed to two longer and four shorter bonds. The P-O bond length range is larger for the caesium phase ranging from 1.35(2) Å to 1.62(2) Å, with the P1-O1 bond becoming the shortest and the P1-O5 remaining the longest. The range of O-P-O angles also increases to 104.1(9)° to 117.8(1)° in the caesium phase. The P-P bond lengths and P-O-P and P-P-P angles also slightly alter to 2.88 Å, 129.6° and 135.2° respectively, but remain consistent with the rubidium phase.

As mentioned in Chapter 3, the AlTP-Cs phase undergoes a transformation following the loss of the inter-lamellar water at around 525° to the previously reported $AlCs_2P_3O_{10}$[16, 17]. Figures 4.17 and 4.18 shows a comparison of the two structures. It is clear that the caesium phase undergoes a major rearrangement to form the anhydrous phase as an apparent buckling of the AlTP layers appears to occur. This results from a change in the connectivity of the AlO_6 and P_3O_{10} chains; from the terminal phosphate groups attaching to two adjacent AlO_6 octahedra with the central phosphate connecting to both in AlTP-Cs (Figure 4.16a); to the P_3O_{10} coordinating along one face of an AlO_6 octahedra, with each phosphate sharing one of its oxygens with the aluminium, and the remaining shared with neighbouring AlO_6 octahedra in the anhydrous form (Figure 4.16b).

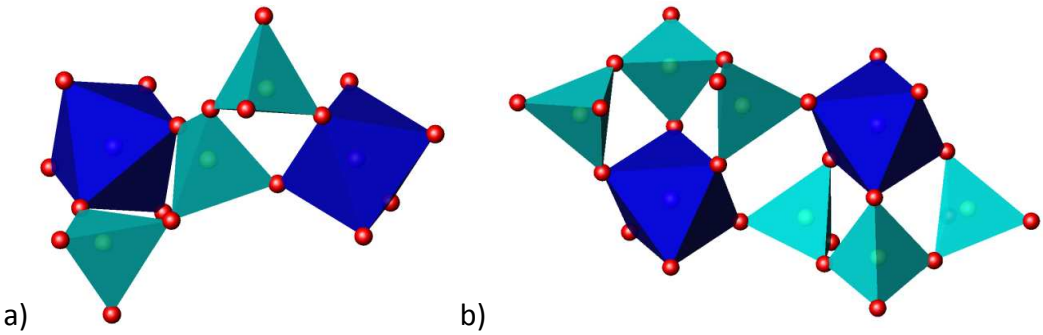

Figure 4.16 *Connectivity of AlO_6 and P_3O_{10} in a) $AlCs_2P_3O_{10}\cdot 2H_2O$ and b) $AlCs_2P_3O_{10}$. Dark blue octahedra AlO_6, light blue tetrahedral PO_4, red spheres oxygen*

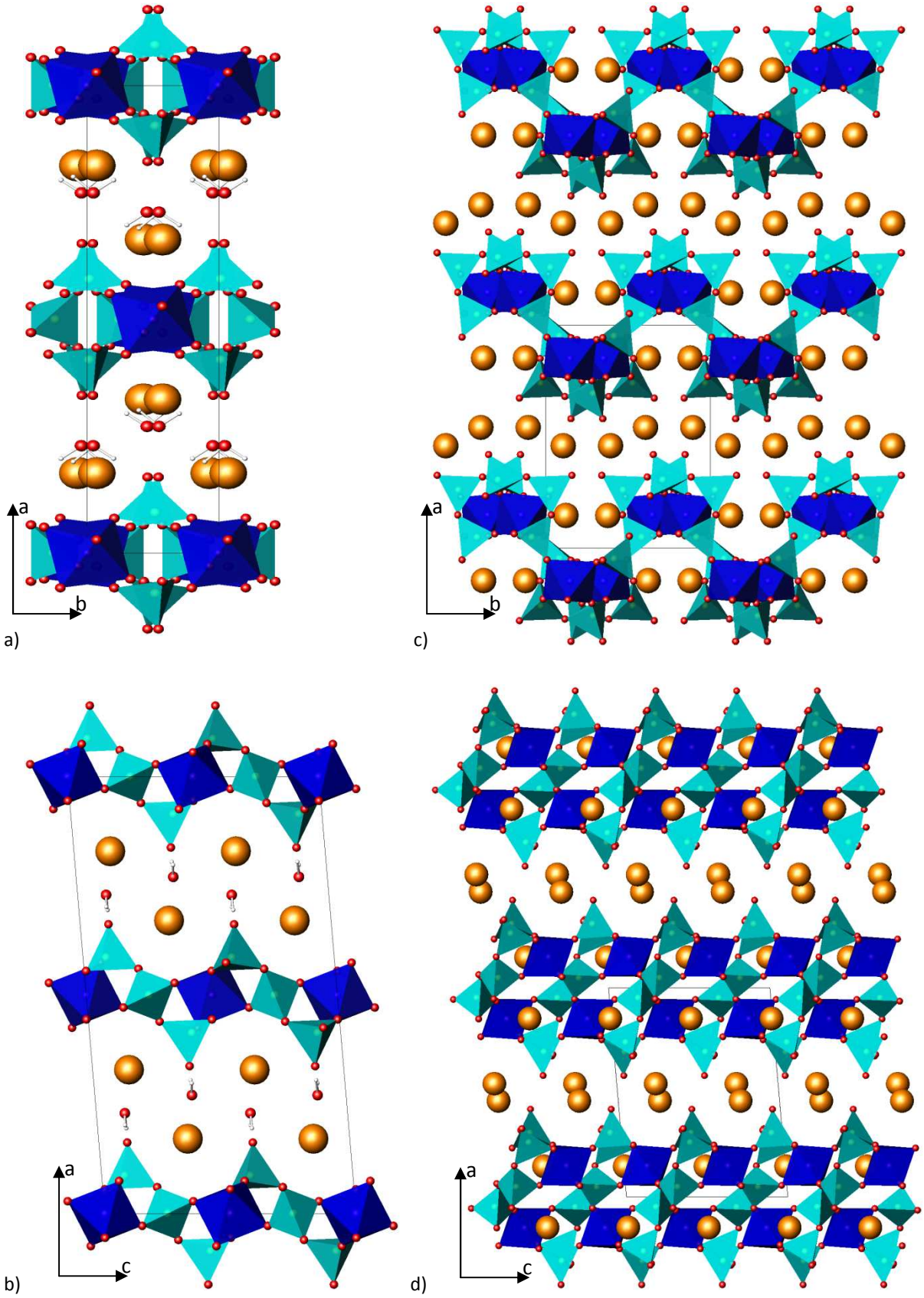

Figure 4.17 *a & b) AlTP-Cs, c & d) $AlCs_2P_3O_{10}$. Dark blue octahedra AlO_6, light blue tetrahedral PO_4, red spheres oxygen and orange spheres caesium*

The alteration in the AlO_6-P_3O_{10} connectivity modifies the layer structure significantly. $[AlP_3O_{10}]_\infty$ chains now run along the *bc* plane in a zig-zag formation (Figure 4.18b), whereas the original AlTP-Cs has pseudo-chain regions of AlO_6 and P_3O_{10} running along the *b* axis (Figure 4.18a). Along the *ab* plane the phosphate layers have become 'buckled' doubling the thickness of the layer compared with AlTP-Cs. This buckling also creates channels running along the *c* axis inside the layers which house caesium cations in the anhydrous phase. This gives two different caesium environments, one ten-fold coordinated between the phosphate layers, similar to the fourteen-fold site in AlTP-Cs, and a seven-fold site in the channels.

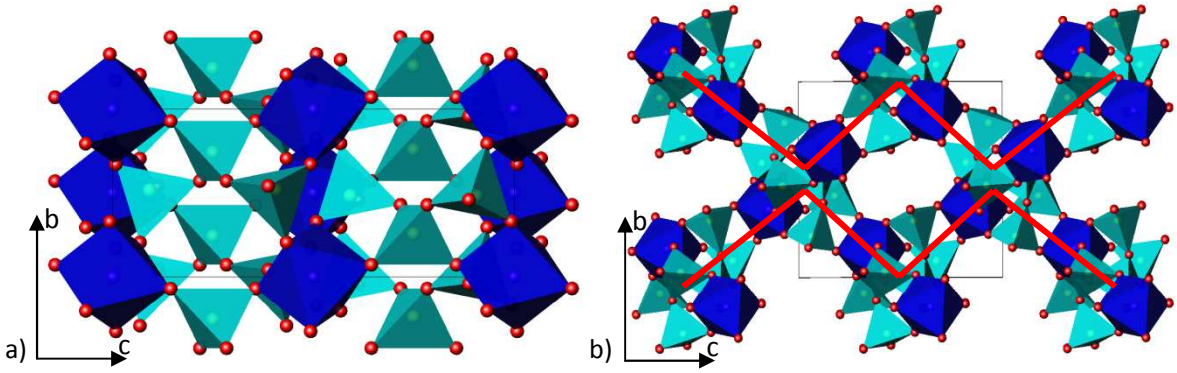

Figure 4.18 *a) AlTP-Cs viewed along bc plane b) $AlCs_2P_3O_{10}$ showing $[AlP_3O_{10}]_\infty$ chains running along bc plane. Dark blue octahedra AlO_6, light blue tetrahedral PO_4, caesiums omitted for clarity*

4.6 AlTP-Na, AlTP-K and AlTP-Ag

Following success with rubidium and caesium, this structural model was used to model sodium, potassium and silver exchanged phases. Unfortunately to date in all three phases this has failed to give a satisfactory Rietveld refinement (e.g. AlTP-K fit shown in Figure 4.19).

Despite the inability to gain a fit in the C2/c space group it was still believed that all the phases have similar structures. With this in mind the structural model was adjusted into the space group C2 as this had shown early promise in the work towards solving the AlTP-Rb

structure. This did not improve the Rietveld fits (fit for AlTP-Ag shown in Figure 4.20). It is clear that more work is required to complete the structure determination in these systems.

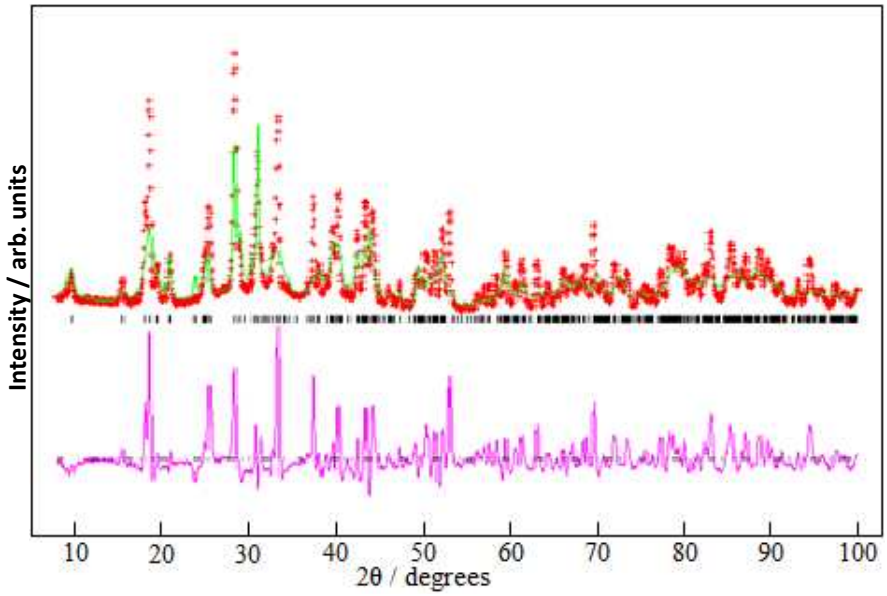

Figure 4.19 *Observed (+), calculated (-) and difference (-) neutron powder diffraction refinement of AlTP-K structure. Reflection positions are also marked (|). χ^2 = 87.54, R_{wp} = 9.62% and R_p = 6.72%*

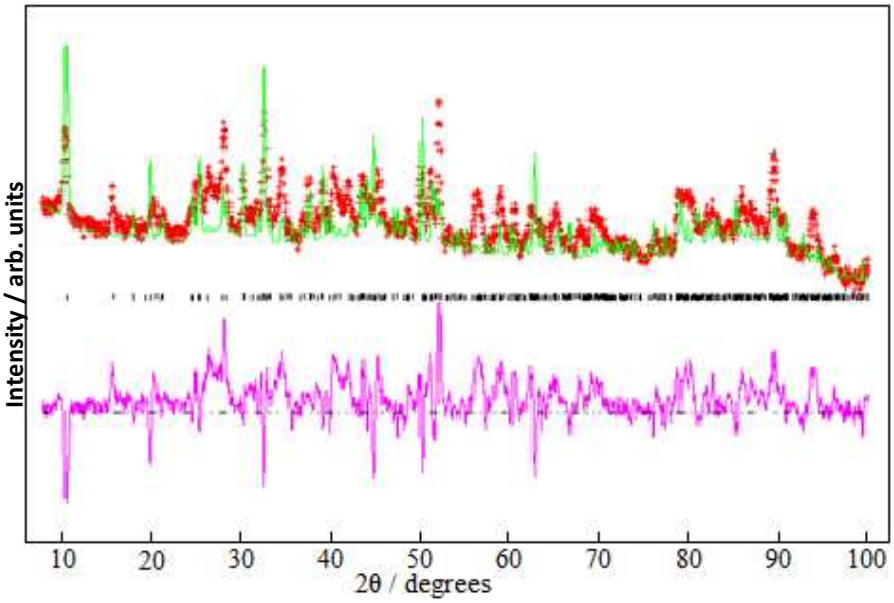

Figure 4.20 *Observed (+), calculated (-) and difference (-) neutron powder diffraction refinement of AlTP-Ag structure. Reflection positions are also marked (|). χ^2 = 20.58, R_{wp} = 5.63% and R_p = 4.29%*

4.7 Conclusions

A series of models were developed in the structural determination of these ion exchange phases (refinement statistics summarised in Table 4.5). Eventually, these resulted in the successful determination of isostructural crystal structures of AlTP-Rb and AlTP-Cs. The structures adopted the space group C2/c, with phosphate layers staggered half a unit cell along [010] with respect to each other. The inter-lamellar waters were located and are positioned along the face of each layer, hydrogen bonding occurring between terminal oxygens on the same layer rather than to terminal oxygens on adjacent layers. The cations were found to occupy 14 coordinate sites bonding to four terminal oxygens and five bridging oxygens from one layer, forming an 'oxygen well', and a terminal oxygen from the adjacent layer and four inter-lamellar water molecules.

Table 4.5 *Refinement statistics for attempted models and final crystal structures*

Model	χ^2	R_{wp} / %	R_p / %
1	82.99	10.57	6.52
2	92.75	11.16	7.22
3	87.54	10.85	6.98
4	88.69	10.92	7.05
5	98.48	11.5	7.55
6	100.4	11.61	7.66
7	16.27	4.67	3.5
AlTP-Rb	2.288	2.09	1.62
AlTP-Cs	3.124	2.53	2.03

α-ZrP is by far the most studied of the layered phosphates and to our knowledge only has 3 reported structures for its ion exchanged phases[18-20]. Having identified numerous phases and solved two structures for monovalent ion exchanged, AlTP has been shown to have just as much potential as α-ZrP as an ion exchange material.

References

1. F. D'Yvoire, *Bull. Soc. Chim. Fr*, 1962, **6**, 1224.
2. S. K. Rishi, B. M. Kariuki, N. J. Checker, J. Godber and A. J. Wright, *Chem Comm*, 2006, 747.
3. CDIF, Crystal Data Identification File from the US National Institute of Standards and Technology, http://www.cds.dl.ac.uk/cds/datasets/crys/cdif/llcdif.html.
4. ICSD, *Inorganic Crystal Structure Database*, http://www.cds.dl.ac.uk/datasets/crys/icsd/llicsd.html.
5. K. V. Price, D. Corne, M. Dorigo and F. Glover, *New Ideas in Optimization*, McGraw-Hill, London, UK, 1997.
6. R. T. Cygan, J. A. Greathouse, H. Heinz and A. G. Kalinichev, *J. Mater. Chem.*, 2009, **19**, 2470.
7. B. J. Teppen, K. Rasmussen, P. M. Bertsch, D. M. Miller and L. Schafer, *J. Phys. Chem. B*, 1997, **101**, 1579.
8. N. T. Skipper, K. Refson and J. D. C. McConnell, *J. Chem. Phys.*, 1991, **94**, 7434.
9. R. B. Von Dreele and A. C. Larson, *General Structure Analysis System*, Los Alamos National Laboratory: Los Alamos, NM, 1994.
10. J. Laugier and B. Bochy, *LMGP Suite of Programs*, Grenoble, France, 2000, http://www.ccp2014.ac.uk/tutorial/lmgp/.
11. CELL, based on original code by M.F. Pye, I.C.L., Oxford.
12. S. K. Rishi, Ph.D thesis, University of Birmingham, 2006.
13. K. K. Palkina, S. I. Maksimova and V. G. Kuznetsov, *Inorg. Mater.*, 1979, **15**, 1704.
14. F. Erragh, A. Boukhari and E. M. Holt, *Acta Crystallogr. Sec. C-Cryst. Struct. Comm.*, 1996, **52**, 1867.
15. M. T. Averbuch-Pouchot, A. Durif and J. C. Guitel, *Acta Crystallogr. Sect. B-Struct. Commun.*, 1977, **33**, 1436.
16. R. N. Devi and K. Vidyasagar, *J. Chem. Soc. - Dalt. Trans.*, 2000, 1605.
17. A. Guesdon, E. Daguts and B. Raveau, *J. Sol. Stat. Chem.*, 2002, **167**, 258.
18. D. M. Poojary and A. Clearfield, *Inorg. Chem.*, 1994, **33**, 3685.
19. P. Rudolf and A. Clearfield, *Acta Crystallogr. Sec. B-Struct. Sci.*, 1985, **41**, 418.
20. A. Clearfield, L. B. McCusker and P. R. Rudolf, *Inorg. Chem.*, 1984, **23**, 4679.

Chapter 5

Divalent Ion Exchange in $AlH_2P_3O_{10}\cdot 2H_2O$

5.1 Introduction

Many of the transition block metals form divalent or higher cations and have a wealth of properties associated with them, such as magnetism[1], electronic properties[2] or even catalysis[3]. Ion exchanging these into a structure may transfer some of these properties into the exchanged product. The alkaline earth metals are also of interest due to their potential use in biomaterial applications. Calcium phosphates, particularly hydroxyapatite, are widely studied as bone cements and bone replacement materials, while magnesium and strontium have proved to provide beneficial properties, such as increased replication of preostoblastic cells[4], after being incorporated into these materials[5, 6]. As with caesium, strontium is also of interest in nuclear waste remediation.

The divalent ion exchange chemistry of α-ZrP has again received much interest[7-9]. Alberti *et al.* studied the uptake of alkaline earth metals into α-ZrP[10] and found crystalline α-ZrP was capable of complete exchange of barium and could uptake 70% and 80% of the maximum potential exchange for calcium and strontium respectively. No exchange was reported for magnesium and Alberti concluded this to be the result of steric hindrance caused by its large hydrated radius.

Clearfield and Hagiwara further studied the exchange of alkaline earth metals with respect to the crystallinity of α-ZrP[11]. They found that crystallinity decreases with increasing exchange. Like Alberti, they reported full exchange of barium, but found full exchange of magnesium was possible in less crystalline α-ZrP, but the exchange required a long time at elevated temperatures to proceed. Finally they reported calcium and strontium both form two phases, one with half exchange achieved and one with complete exchange.

Aberti found adding small amounts of sodium hydroxide to the exchanging solution enabled sodium to act as a catalyst and 'spread apart' the layers allowing alkaline earth metal cations to be exchanged[12]. Clearfield also showed that starting with the fully sodium exchanged phase allowed the alkaline earth metals to be exchanged into α-ZrP[13]. He also noted that unlike with monovalent ion exchange, the exchange of divalent cations was irreversible[14].

The uptake of a range of transition metals (Mn, Co, Ni and Zn) into α-ZrP has been studied by Clearfield and Kalnins[15]. Clearfield found that for most of these metals 90-100% of exchange could be achieved, with the notable exception of nickel where only 22% was observed. He concluded that this was due to the exchange occurring *via* insertion of the dehydrated cation into the host, then rehydration of the cations and host, and nickel has a larger hydration energy than the other ions making the process energetically unfavourable, thus reducing the nickel uptake. Arhland *et al.*[16] found similar results and also noted that α-ZrP showed an increased affinity for the trivalent cation Cr(III). He also observed an extremely high affinity towards Fe(III), though noted this was being incorporated into the α-ZrP matrix, so this was not simple ion exchange.

Unlike the monovalent exchanges, there have been no previous reports of the ion exchange of divalent cations into AlTP. This chapter discusses the attempts made to

exchange a range of divalent cations into AlTP, using a variety of methods including several adapted from those successfully used in exchanging into α-ZrP.

5.2 Experimental

Taking Alberti's findings on using sodium as a catalyst for divalent exchange into α-ZrP[12], and Clearfield's use of a fully sodium exchanged α-ZrP as a divalent exchange precusor[13] into account, initial attempts at divalent ion exchange into AlTP involved the use of sodium. AlTP-Na·4 or AlTP with NaCl (10:1 Al:Na ratio) were stirred in 50 ml solutions of MCl_2 (M = Mg, Ca, Sr, Fe, Mn, Zn) or $M(NO_3)_2$ (M = Cu), with a M:Al ratio of 25:1, for 24 hours.

Further attempts involved expanding upon Alberti's idea of 'spreading apart' the host layers[12], by attempting the exchange using the same method, but with AlTP that had previously been intercalated with 1,6-diaminohexane, which increases the interlayer spacing to ~14.7 Å. AlTP was intercalated with 1,6-diaminohexane, by stirring 0.5g of AlTP in molten 1,6-diaminohexane at 70 °C for 24 hours[17].

5.3 Copper Exchange

The initial exchanges using a sodium catalyst or AlTP-Na·4 failed to give any evidence of copper exchange resulting in AlTP and AlTP-Na·4 or just AlTP-Na·4 being present in the resulting XRD patterns. When the exchange with Cu(II) was attempted with intercalated AlTP, however, the resulting product was found to have changed colour from white to a light blue, a good indication that copper had been exchanged into the material. The XRD pattern of this product (Figure 5.1) was not matched in the JCPDS database[18] and suggested that a new phase had been formed. This phase, labelled AlTP-Cu herein, was poorly crystalline, showing very broad peaks in its XRD, indicating a loss of order within the crystal structure. We can only surmise that the replacement of two hydrogen atoms with a

single Cu^{2+} has disrupted the structural order. The nature of the XRD pattern prevented the determination of a unit cell and hence confirmation of a single phase ion exchanged product.

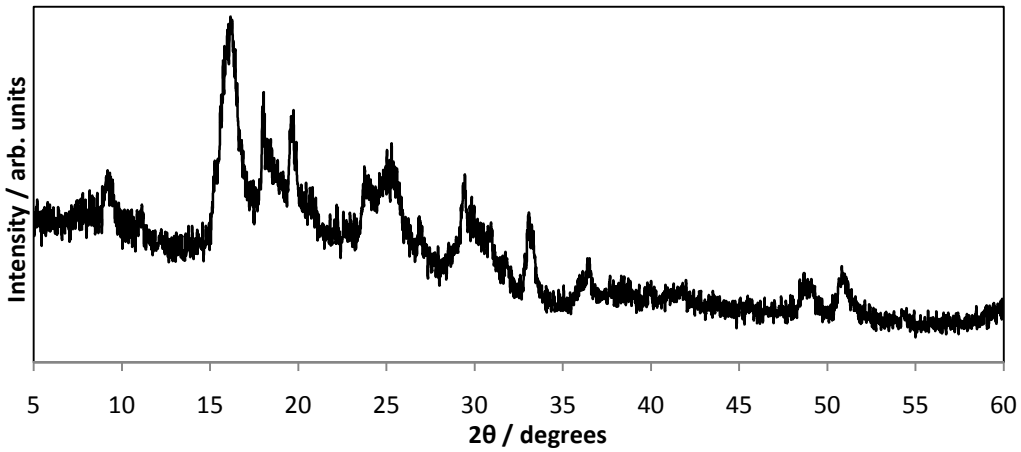

Figure 5.1 *XRD pattern of AlTP-Cu*

To attempt to quantify the copper content, thermal studies were performed. These indicated that the phase became amorphous above 100 °C. It is likely that this change to an amorphous material is linked to the loss of water. This is supported by Thermogravimetric Analysis (TGA) and Differential Thermal Analysis (DTA) (Figure 5.2) which show the phase to have a mass loss beginning at around 100 °C, with an associate thermal event evident in the DTA. The mass loss of 14.6 wt% suggested the phase had a water content of 3.25 (14.5 wt% calculated for 3.25 waters per formula unit) giving the phase a stoichiometry of $AlCuP_3O_{10}\cdot 3.25H_2O$.

The phase remained amorphous until new crystalline phases began to form above 600 °C. XRD analysis of heated samples (Figure 5.3) shows these phases to be $Cu_2P_2O_7$, $Al(PO_3)_3$ and $AlPO_4$. These decomposition products, while not a direct measure of the copper content of the phase, are stoichiometrically equivalent to fully exchanged AlTP, and suggest a probable decomposition pathway for the phase of:

$$2\ AlCuP_3O_{10}\cdot 3.25H_2O \xrightarrow[-3.25H_2O]{\sim 100\ ^\circ C} 2\ AlCuP_3O_{10} \xrightarrow{\sim 600\ ^\circ C} Cu_2P_2O_7 + Al(PO_3)_3 + AlPO_4$$

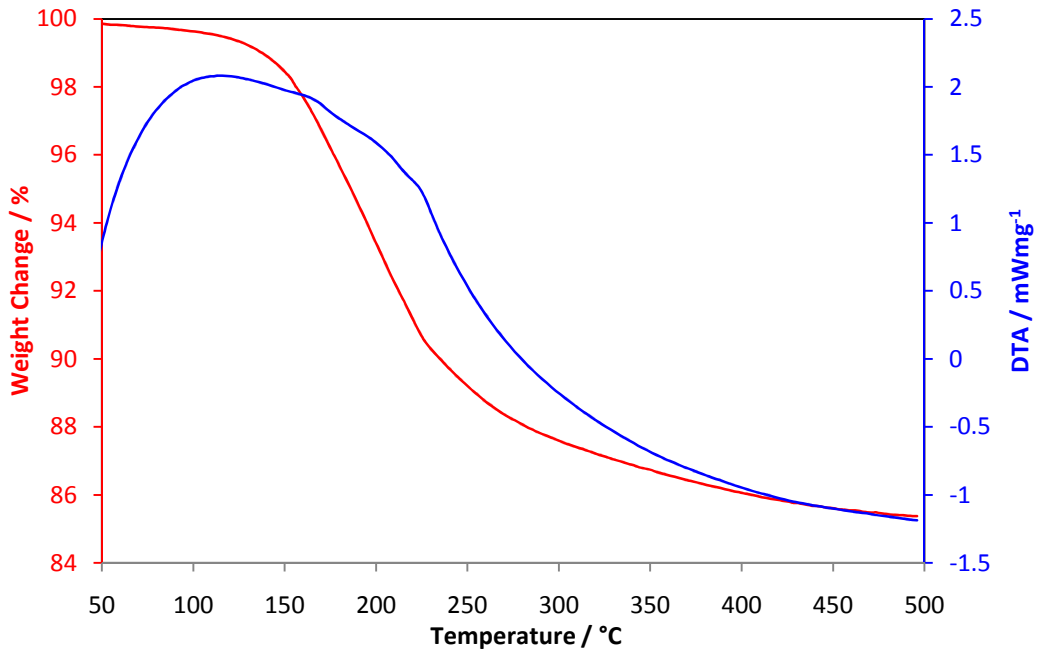

Figure 5.2 *TGA plot of AlTP-Cu*

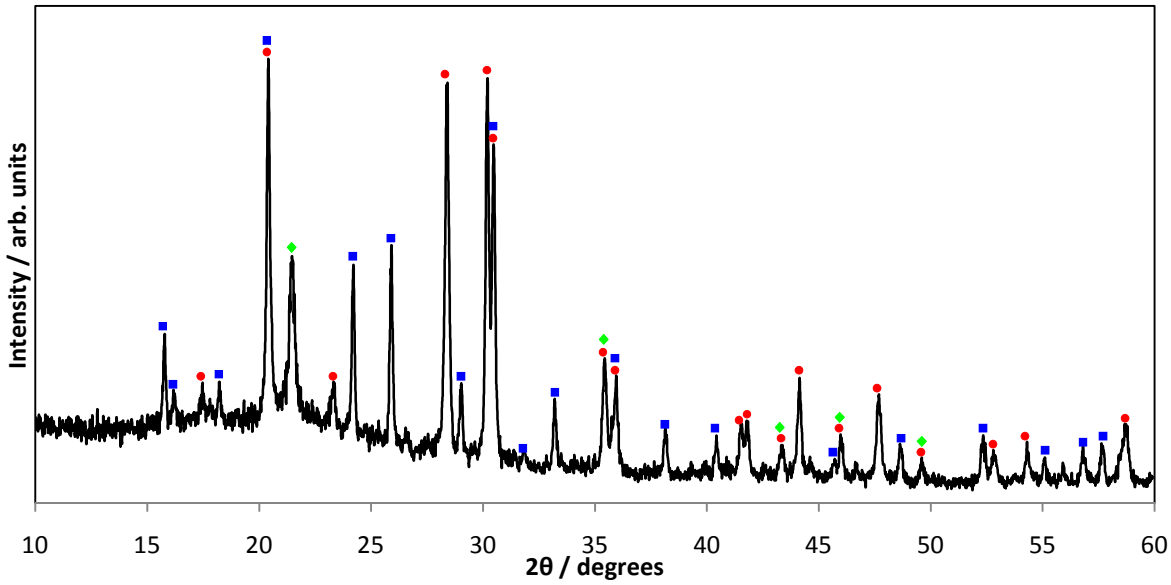

Figure 5.3 *XRD pattern showing AlTP-Cu after heating to 700 °C becoming* ● $Cu_2P_2O_7$, ■ $Al(PO_3)_3$ *and* ♦ $AlPO_4$

ESEM showed the phase to consist of flat angular plates (Figure 5.4), similar to those observed following monovalent exchange (see Chapter 3).

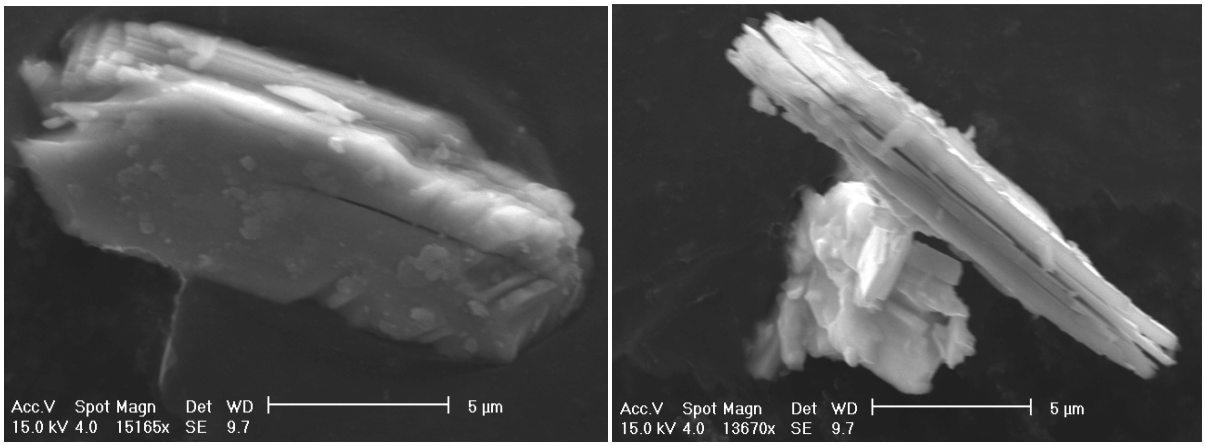

Figure 5.4 *ESEM images of AlTP-Cu*

Energy-dispersive X-ray spectroscopy (EDX), see Appendix 5, suggested that copper had fully exchanged into the structure showing an aluminium to copper ratio of around 1:1. Multiple scans were taken from several different areas of the sample, showing the phase appeared to have a homogeneous composition throughout.

Attempts at reversing the ion exchange with 0.1M HCl failed to recreate AlTP. This inability to exchange back to the original host from a divalent exchanged form is consistent with α-ZrP[14].

5.4 Iron Exchange

Iron (II) exchange was also attempted into AlTP *via* an intercalated host. The XRD pattern for this exchange (Figure 5.5) is mostly amorphous with evidence of the intercalated host material still present, but having lost crystallinity. This alone provides no evidence of exchange having occurred but does not preclude the possibility of an amorphous exchanged product. Indeed the few peaks that can be discerned from the background are similar in position to those seen in other M^{2+} exchanged systems. Thermal studies on the product of the exchange at 700 °C showed only $AlPO_4$ is present in the XRD pattern. $AlPO_4$ is not the expected thermal decomposition of AlTP, but is consistent with the copper exchanged phase's decomposition route, indicating some iron may have exchanged into the structure.

There is no evidence of any iron containing phases following decomposition which suggests that if iron is present it is in an amorphous form. The relatively high amorphous background of the sample supports this. The high background may also be a good indication of the presence of iron, as iron has a high fluorescence with copper radiation. Further studies are required to determine if iron has been exchanged into the structure.

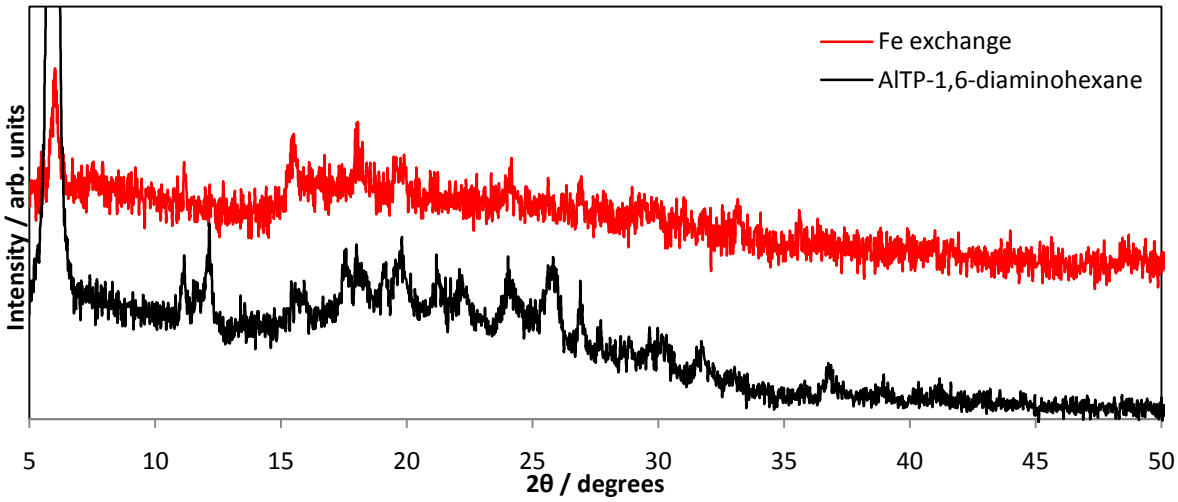

Figure 5.5 *XRD patterns of (black) intercalated AlTP and (red) attempted Fe exchange*

5.5 Manganese Exchange

Manganese (II) exchange resulted in an XRD pattern (Figure 5.6) displaying poor crystallinity, but possessing similar features to those of the copper system, with no evidence of the intercalated AlTP precursor. As with the copper system, we can tentatively suggest an exchange product, AlTP-Mn, has been formed.

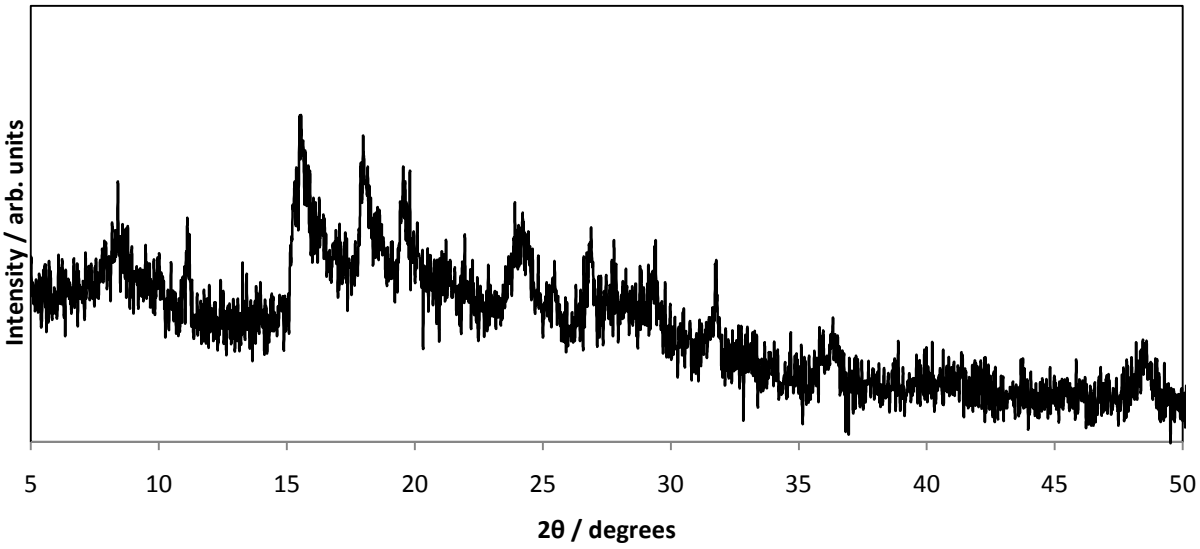

Figure 5.6 *XRD pattern of AlTP-Mn*

This is supported by thermal treatment showing a decomposition similar to AlTP-Cu with products of $AlPO_4$, $Al(PO_3)_3$ and $Mn_2P_2O_7$ observed in the XRD pattern (Figure 5.7) at 600 °C. These are stoichiometrically equivalent to fully exchanged AlTP and may therefore indicate that full exchange has been achieved. These products show a probable decomposition pathway for the phase of:

$$2\ AlMnP_3O_{10}{\cdot}\,nH_2O \xrightarrow[-nH_2O]{\sim 100\ ^\circ C} 2\ AlMnP_3O_{10} \xrightarrow{\sim 600\ ^\circ C} Mn_2P_2O_7 + Al(PO_3)_3 + AlPO_4$$

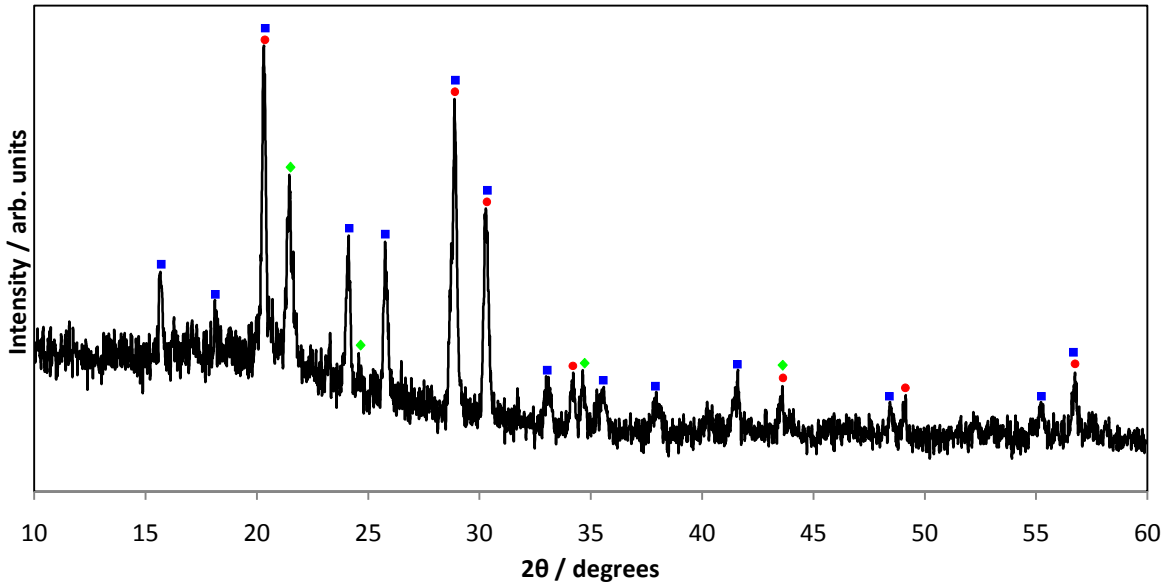

Figure 5.7 *XRD pattern at 700 °C, showing ● $Mn_2P_2O_7$, ■ $Al(PO_3)_3$ and ◆ $AlPO_4$*

5.6 Zinc Exchange

The attempted exchange of zinc into AlTP resulted in the XRD pattern shown in Figure 5.8. Analysis of this data suggested the presence of both intercalated AlTP and AlTP itself, both of reduced crystallinity, but no definitive evidence of a new phase. However after being heated to 700 °C for 12 hours the XRD pattern (Figure 5.9) shows $Zn_2P_2O_7$, $Al(PO_3)_3$and $AlPO_4$ products equivalent to decomposition of both AlTP-Cu and AlTP-Mn, suggesting some exchange may have been achieved.

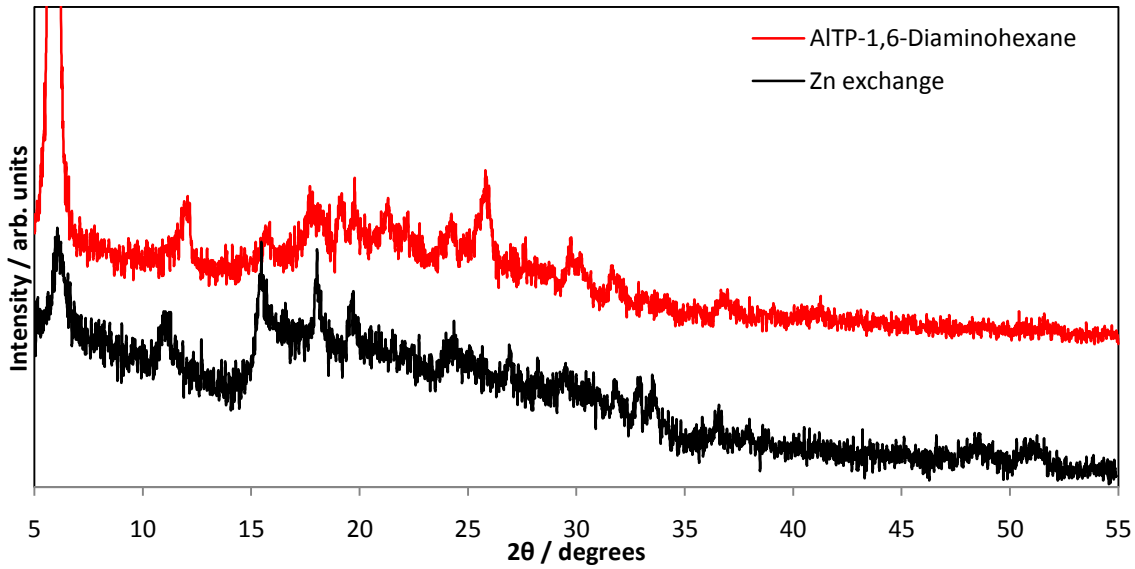

Figure 5.8 *XRD patterns of: red intercalated AlTP and black attempt at Zn exchange in AlTP*

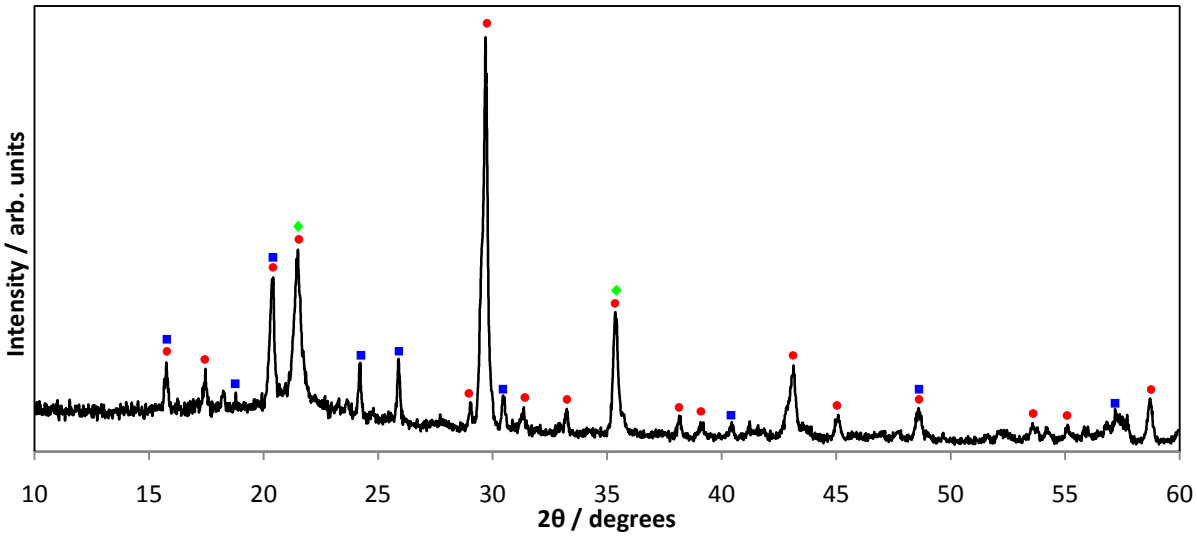

Figure 5.9 *XRD pattern of attempted zinc exchange heated to 700 °C showing ● $Zn_2P_2O_7$, ■ $Al(PO_3)_3$ and ◆ $AlPO_4$*

5.7 Magnesium Exchange

Alkaline earth metals were also attempted to be exchanged into AlTP, with attempts being made to ion exchange magnesium. The XRD pattern (Figure 5.10) shows a reduction in the amount of intercalated AlTP and evidence of a low crystallinity phase similar to those of copper and manganese. Thermal studies on this exchange product are similar to those of the iron phase showing only $AlPO_4$ present in the XRD pattern (Figure 5.11) above 700 °C, which is a product consistent with other exchanged phases and contrary to that seen for the decomposition of pure AlTP. Note also the background suggests amorphous materials are also present.

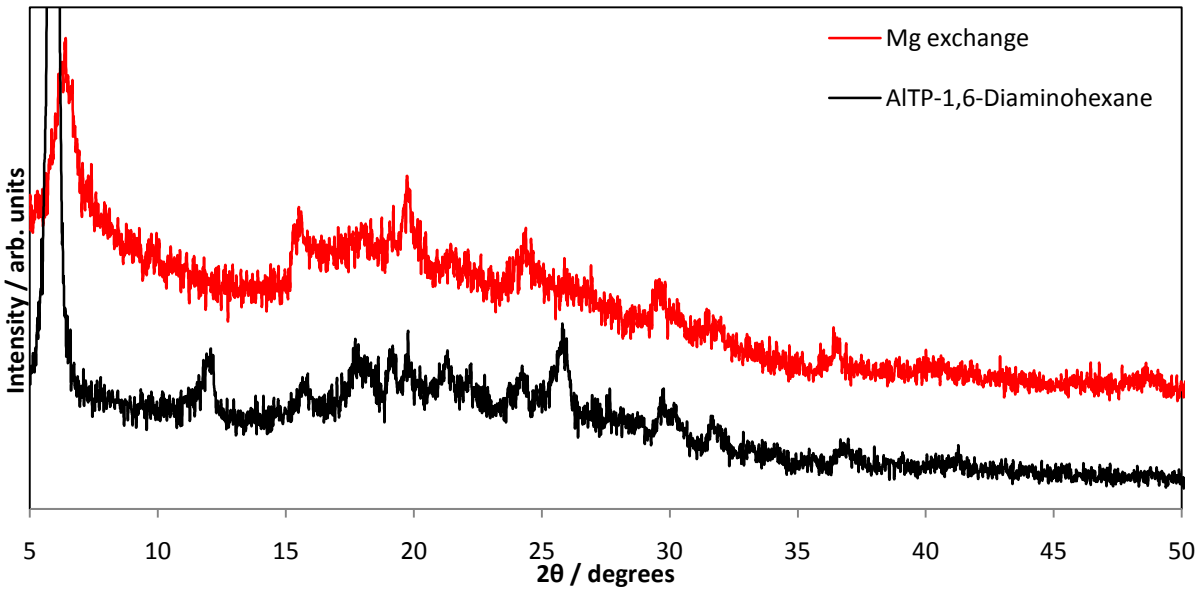

Figure 5.10 *XRD pattern of: red attempt at magnesium exchange and black AlTP-1,6-diaminohexane*

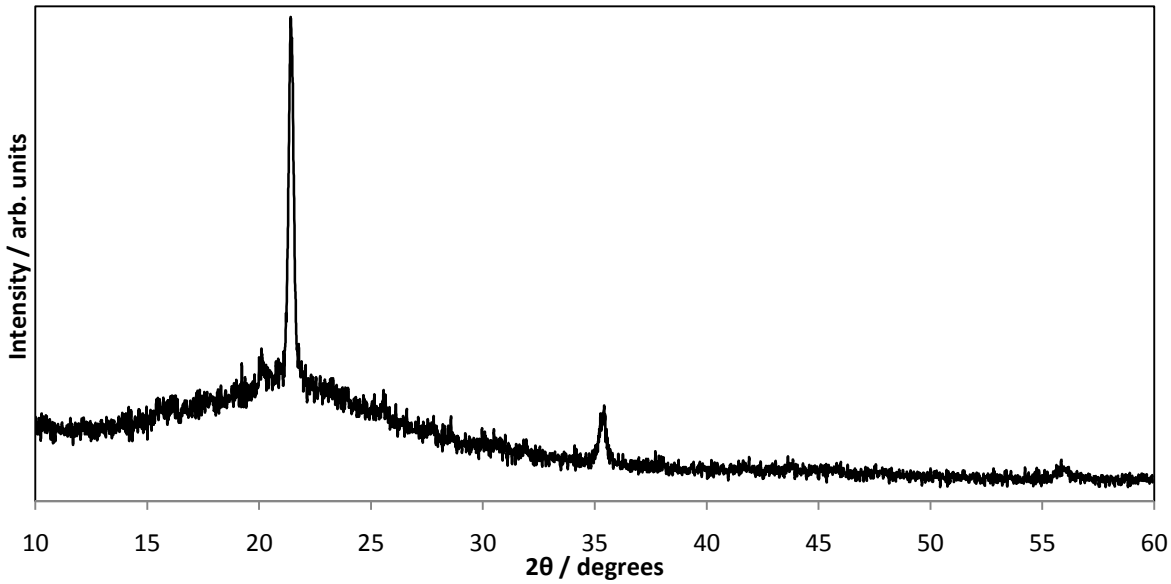

Figure 5.11 *XRD pattern of Mg exchanged AlTP heated to 700 °C showing $AlPO_4$*

5.8 Calcium Exchange

Calcium exchange resulted in a new phase being observed through XRD (Figure 5.12), labelled AlTP-Ca. In comparison to the other divalent exchanged phases AlTP-Ca is relatively crystalline, with somewhat sharper peaks indicating a more ordered system. This may be a result of calcium being larger than all the exchanged divalent cations thus far, and may provide for a more ordered inter-lamellar region.

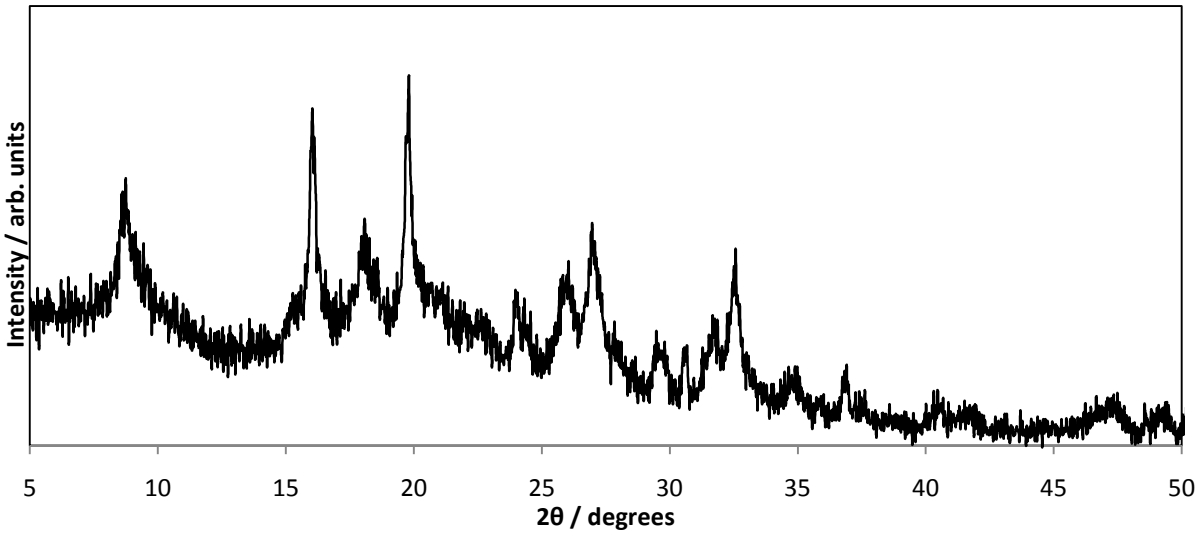

Figure 5.12 *XRD pattern of AlTP-Ca*

The phase follows the trend of other divalent exchanged phases of being amorphous between around 100 °C to 600 °C. At 700 °C a different set of products is formed, β-$Ca(PO_3)_2$ and $AlPO_4$ (Figure 5.13). These products suggest full exchange has been achieved with their stoichiometry, suggesting a possible thermal decomposition pathway of:

$$AlCaP_3O_{10}{\cdot}nH_2O \xrightarrow[-nH_2O]{\sim 600\,^{\circ}C} AlCaP_3O_{10} \xrightarrow{\sim 600\,^{\circ}C} \beta\text{-}Ca(PO_3)_2 + AlPO_4$$

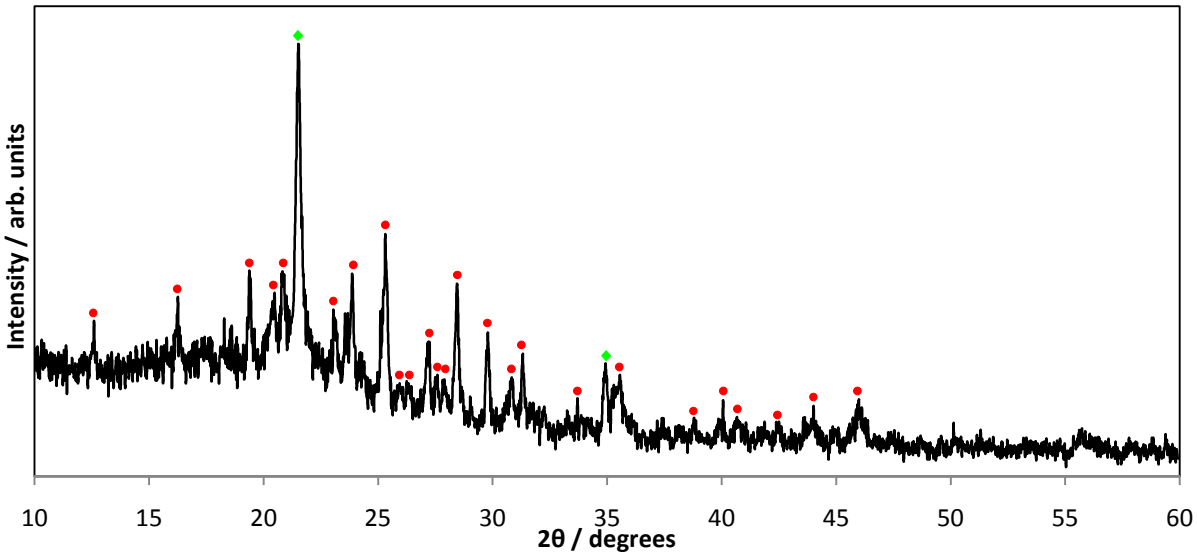

Figure 5.13 *XRD pattern of calcium exchanged AlTP showing ● β-$Ca(PO_3)_2$ and ◆ $AlPO_4$*

5.9 Strontium Exchange

The final divalent cation attempted to exchange into AlTP was strontium. The XRD pattern (Figure 5.14) shows substantial amounts intercalated AlTP still present, but the rest of the pattern is similar to AlTP-Ca, albeit less crystalline with the exception of the peak at around 15.3 ° 2θ. Thermal treatment of the phase produces amorphous phases between 100 °C and 600 °C with the XRD pattern at 700 °C showing $Sr(PO_3)_2$ and $AlPO_4$ (Figure 5.15). These products are equivalent to the calcium phase and the stoichiometry of a fully exchanged AlTP, giving a possible thermal decomposition pathway of:

$$AlSrP_3O_{10}{\cdot}nH_2O \xrightarrow[-nH_2O]{\sim 100\,^{\circ}C} AlSrP_3O_{10} \xrightarrow{\sim 600\,^{\circ}C} Sr(PO_3)_2 + AlPO_4$$

This indicates an exchanged phase may be formed (AlTP-Sr), which as for the monovalent cations forms a completely exchanged phase with no intermediates (see Chapter 3), but the exchange reaction seems to take longer than the other divalent exchanges leaving the residual intercalated AlTP observed in the XRD pattern. Further studies are required to confirm if this is indeed the case.

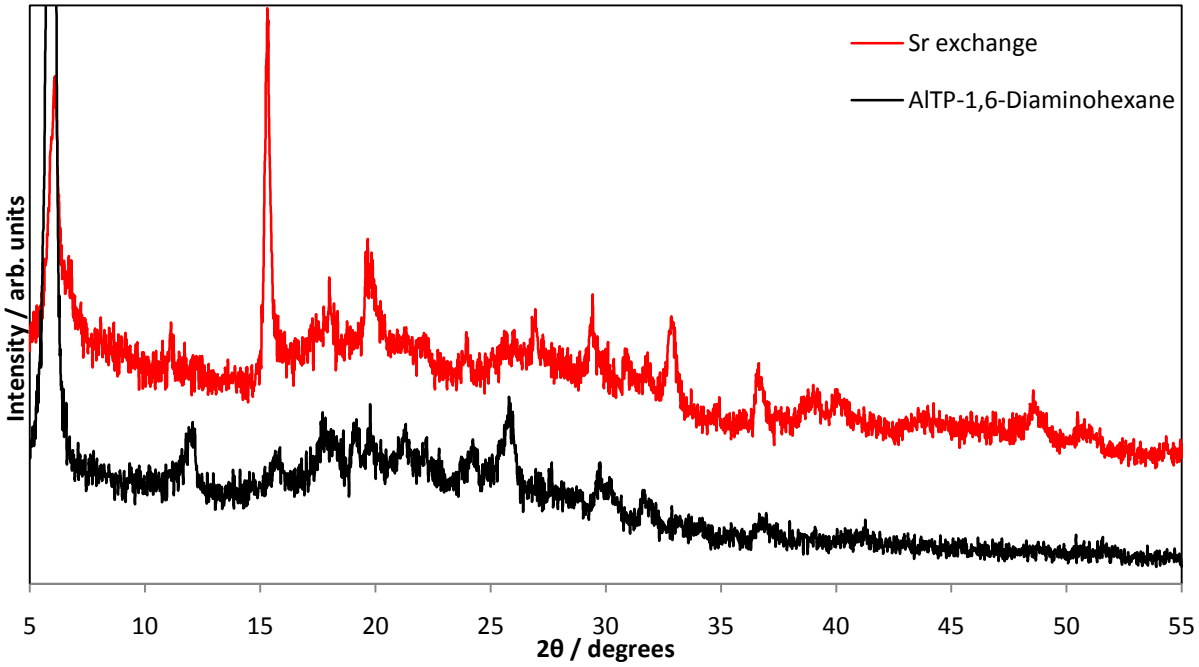

Figure 5.14 *XRD pattern of AlTP-Sr with residual intercalated AlTP still apparent*

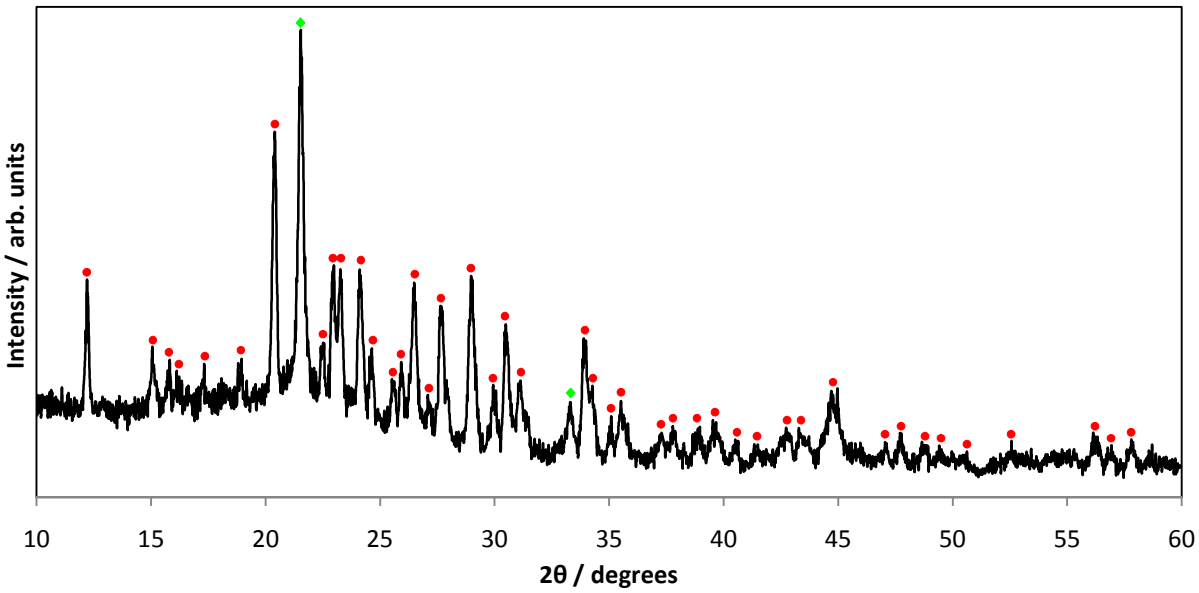

Figure 5.15 *XRD pattern of calcium exchanged AlTP showing • $Sr(PO_3)_2$ and ◆ $AlPO_4$*

5.10 Exchange Comparison

A comparison of the XRD patterns of all the attempted exchanges (Figure 5.16) shows similarities between them, notably the three peaks between 15-21 ° 2θ. While not in itself strong direct evidence that ion exchange is occurring in all these phases, it is not unfeasible that exchange has occurred given the similar size of ions involved and their similar X-ray scattering powers which would result in phases with similar XRD patterns.

Several of the attempted exchanges show residual intercalated AlTP remaining in their XRD patterns implying, unlike with the monovalent ion exchanges described in Chapter 3, a standard time of 24 hours is not enough for all divalent ions to exchange into AlTP. As the 'slower' ions range in size from the smallest to largest attempted and come from both the s-block and p-block metals it is unclear at present as to what affects the reaction kinetics.

The reasons for the apparent increased crystallinity of the calcium and strontium phases is unclear but may be a result of the increased size of the cations and differences in coordination preferences which may more readily facilitate order in the inter-lamellar region. It is likely that some distortion of the AlTP layers may be necessary to stabilise the replacement of two protons by one cation. Certain cations may achieve this by locating in a limited number of sites (hence more order), whereas others may be present in a more disordered manner within the inter-lamellar region.

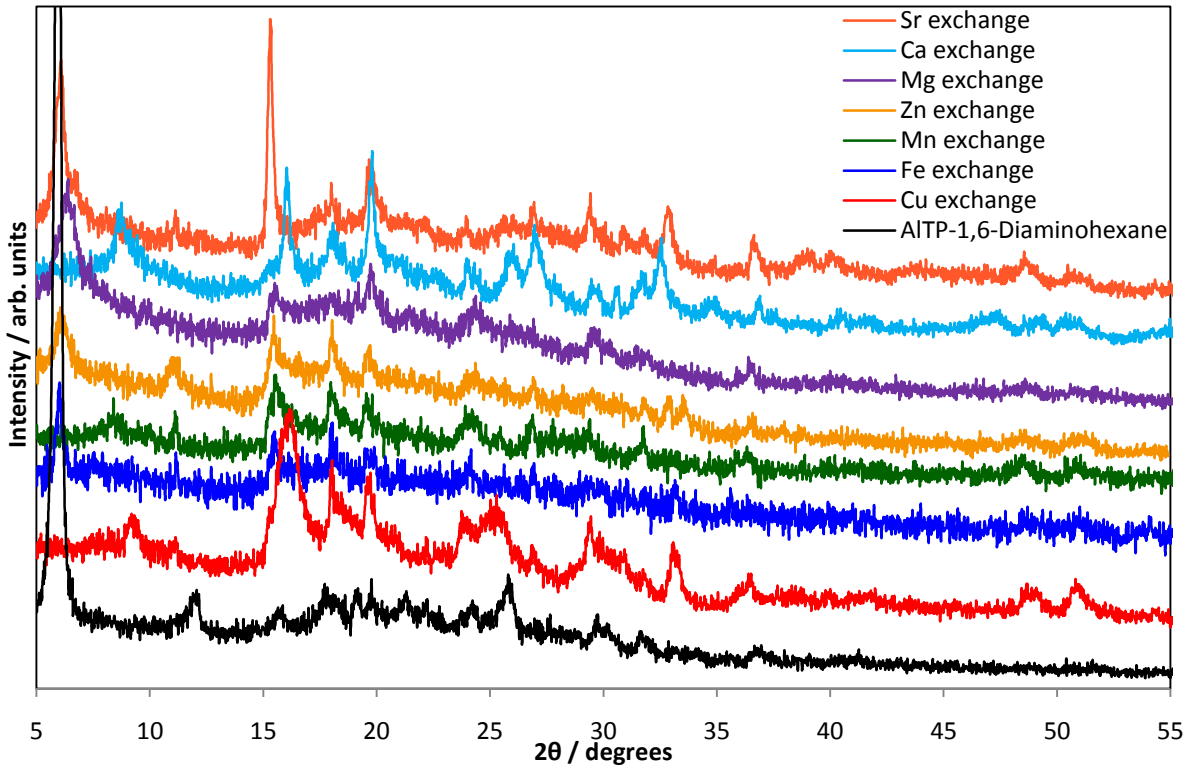

Figure 5.16 *XRD patterns of attempts at divalent ion exchange in AlTP*

Several exchange routes utilising monovalent ions as catalysts or precursors have been reported for α-ZrP[12, 13]. This is not the case with AlTP, where the use of small amounts of sodium hydroxide as a catalyst in the exchanging solution resulted in small amounts of AlTP-Na·4 being formed but no divalent exchange being achieved. Similarly starting with AlTP-Na·4 and attempting to exchange out the sodium yielded no exchange from the sodium phase. This suggests the stability of monovalent exchanged phases is higher than that of divalent exchanged phases.

5.11 Conclusions

Ion exchange of Cu^{2+}, Mn^{2+} and Ca^{2+} directly into AlTP displayed the most convincing evidence of a successful ion exchange. Unlike α-ZrP, exchange cannot be achieved using small amounts of sodium as a catalyst as AlTP has a preference for monovalent cations and forms AlTP-Na·4 instead. The M^{2+} exchanged phases display decomposition products that appear to indicate significant exchange has occurred and suggest

that, as with the monovalent exchange, full exchange is achieved with no partly exchanged phases being formed. ESEM shows AlTP-Cu to consist of crystallites similar to those of the monovalent ion exchanged form of AlTP, with EDX showing the phase to have a homogenous aluminium to copper ratio of around 1:1.

Strontium and zinc exchanges both show evidence of ion exchange in their XRD patterns and decomposition products, but the residual intercalated AlTP suggests that the exchanges are slower than with the other successful divalent exchanges. Iron and magnesium may have been exchanged into AlTP, with both their XRD patterns showing similarities to those of the successful exchanges, and thermal decomposition products differing from those of AlTP. However, further work is required to provide more conclusive evidence of successful exchange in these phases.

References

1. H. A. Salama and G. A. Stewart, *J. Phys.-Condens. Matt.*, 2009, **21**.
2. V. Hinkov, C. T. Lin, M. Raichle, B. Keimer, Y. Sidis, P. Bourges, S. Pailhes and A. Ivanov, *Euro. Phys. J.-Spec. Top.*, 2010, **188**, 113.
3. D. Rochu, N. Viguie, F. Renault, D. Crouzier, M. T. Froment and P. Masson, *Biochem. J.*, 2004, **380**, 627.
4. E. Canalis, M. Hott, P. Deloffre, Y. Tsouderous and P. J. Marie, *Bone*, 1996, **18**, 176.
5. J. Buehler, P. Chappuis, J. L. Saffar, Y. Tsouderos and A. Vignery, *Bone*, 2001, **29**, 176.
6. M. Hott, P. Deloffre, Y. Tsouderos and P. J. Marie, *Bone*, 2003, **33**, 115.
7. C. H. Kim and H. S. Kim, *Synth. Metals*, 1995, **71**, 2051.
8. A. Dyer, T. Shaheen and M. Zamin, *J. Mater. Chem.*, 1997, **7**, 1895.
9. G. Alberti, U. Costanti, S. Allulli, M. A. Massucci and M. Pellicci, *J. Inorg. & Nucl. Chem.*, 1973, **35**, 1347.
10. G. Alberti, U. Costanti and M. Pellicci, *J. Inorg. & Nucl. Chem.*, 1973, **35**, 1327.
11. A. Clearfield and H. Hagiwara, *J. Inorg. & Nucl. Chem.*, 1978, **40**, 907.
12. G. Alberti, R. Bertrami and U. Costantino, *J. Inorg. & Nucl. Chem.*, 1976, **38**, 1729.
13. A. Clearfield, W. L. Duax, A. S. Medina, G. D. Smith and J. R. Thomas, *J. Phys. Chem.*, 1969, **73**, 3423.
14. A. Clearfield and Z. Djuric, *J. Inorg. & Nucl. Chem.*, 1979, **41**, 885.
15. A. Clearfield and J. M. Kalnins, *J. Inorg. & Nucl. Chem.*, 1976, **38**, 849.
16. S. Ahrland, J. Albertss, A. Oskarsso and A. Niklasso, *J. Inorg. & Nucl. Chem.*, 1970, **32**, 2069.
17. N. J. Checker, Ph.D thesis, University of Birmingham, 2006.
18. JCPDS, *International Centre for Diffraction Data*, P.1., Swathmore, Pensylvania, PA 19081, USA, 11990.

Chapter 6

Intercalation in $AlH_2P_3O_{10}·2H_2O$ Phases

6.1 Introduction

Modifying existing structures by intercalation offers the opportunity to create many new materials with potentially important properties. Intercalation is the process of inserting a guest species into a one-, two- or three- dimensional host structure[1]. In this thesis, the system of interest involves AlTP as a host for inserting organic molecules. Intercalation has been observed in many different materials such as layered double hydroxides[2-4], many layered phosphates[5, 6], perovskites[7] and even in simple compounds such as $Zn(OH)_2$ [8, 9]. In layered phosphates such as AlTP and α-ZrP, amines are the predominant subject of intercalation studies[10-12], though a wealth of studies into the intercalation of other organic molecules such as alcohols[12, 13], acetates[14], organometallics[15] and even anticancer agents[16] exist.

There has been much interest in intercalating amino acids, and other bio-active molecules, into layered phases as a possible mechanism in therapeutic molecular delivery[16]. L-amino acids have been intercalated into α-ZrP and γ-ZrP[17, 18]. With α-ZrP it was found only basic amino acids such as histidine, lysine and arginine could be intercalated[19]. 6-Aminohexanoic acid is another amino acid to have been intercalated into α-ZrP[20] and clays[21, 22]. It forms both monolayers in α-ZrP and clays (Figure 6.1a) and bilayers in clays

(Figure 6.1b). The intercalation in α-ZrP and the bilayer in vermiculite both form parallel to the host layers, rather than at an angle to them as seen in most other intercalations. They also form a head to tail arrangement with the amine group positioning next to the carboxylic acid; Ding *et al.* [20] showed that this allows the formation of nylon within the inter-lamellar region following heating to 260 °.

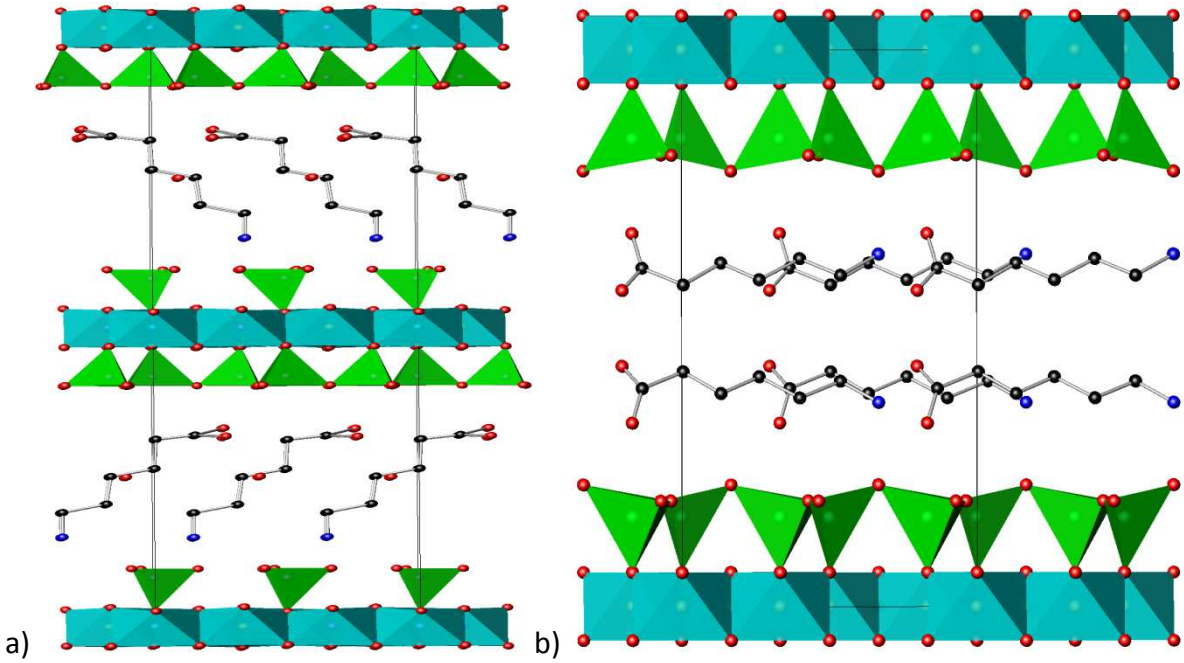

Figure 6.1 *6-Aminohexanoic acid intercalated in clays forming a) monolayers in* $(Mg_{2.628}Fe_{0.309}Ti_{0.06}Mn_{0.003})(Al_{1.04}Si_{2.883}Fe_{0.076})O_{10}(OH)_2Ca_{0.343}·xH_2O$[21] *b) bilayers in* $(Mg_{2.36}Fe_{0.48}Al_{0.16})(Al_{1.28}Si_{2.72})O_{10}(OH)_2Mg_{0.32}·xH_2O$[22]

Simple monoamines of the general formula $CH_3(CH_2)_xNH_2$ have been intercalated into a range of layered phosphates[5, 10, 23-25]. In the α type metal phosphates (see Chapter 1.5.1), complete intercalation occurs, where each P-OH present coordinates to an amine moiety. This results in the amine molecules forming a bilayer in the inter-lamellar region. Alberti's investigation of monoamine intercalation into α-ZrP[26] found the amine to have Lewis acid – Lewis base interactions with the terminal hydroxide group, becoming NH_3^+ and $P\text{-}O^-$. He suggested the amine then forms three $P\text{-}O^-$ - HN^+ bonds to three oxygen atoms on one face of the phosphate group (Figure 6.2). Assuming the amine's alkyl chain

adopts a trans-trans orientation this would give a theoretical intercalation angle of 55 °, very closely matching the angle of 54 ° observed experimentally for intercalation of monoamine into α-ZrP[24].

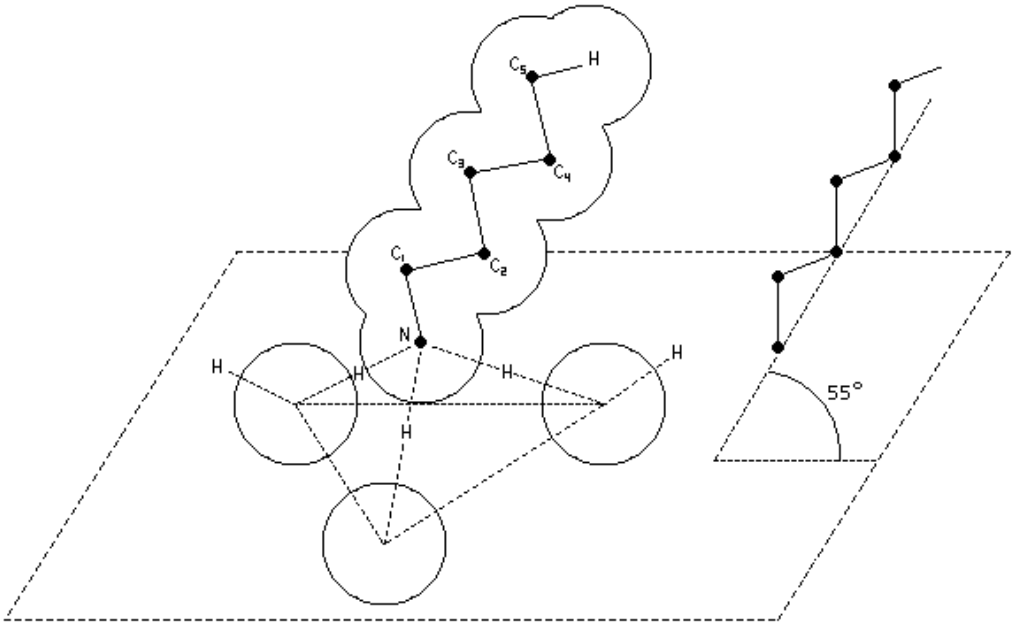

Figure 6.2 *Schematic representation of amine bonding in intercalated α-ZrP (adapted from[26])*

The apparent intercalation angle of intercalated phases can be calculated by plotting the d-spacing of the d_{100} peaks (a direct measure of interlayer spacing) against the number of atoms in the carbon chain, with the gradient showing the increase in inter-layer spacing per carbon. Adding one extra carbon to a chain should increase the chain length of a perpendicular monolayer by 1.27 Å (Figure 6.3a) or a perpendicular bilayer by 2.54 Å (assuming a C – C bond of 1.54 Å and an angle of 112°). Using trigonometry allows the calculation of an intercalation angle (Figure 6.3b). In bilayers this linear relationship between interlayer spacing and number of carbons relies on the bilayers forming in an ordered manner as seen in Figure 6.4.

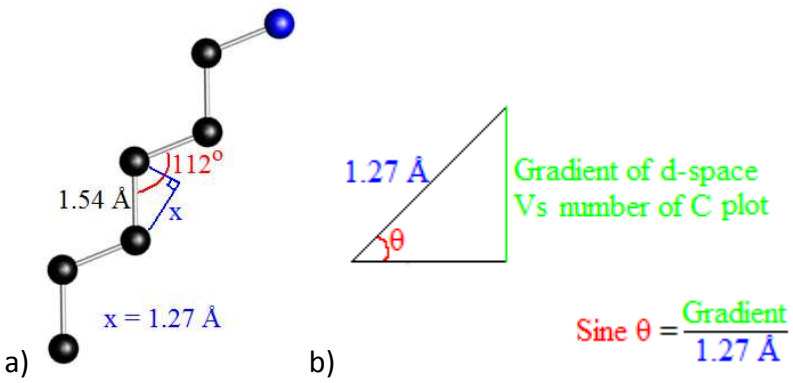

Figure 6.3 *a) Increase of amine chain length with additional carbon b) Intercalation angle calculation*

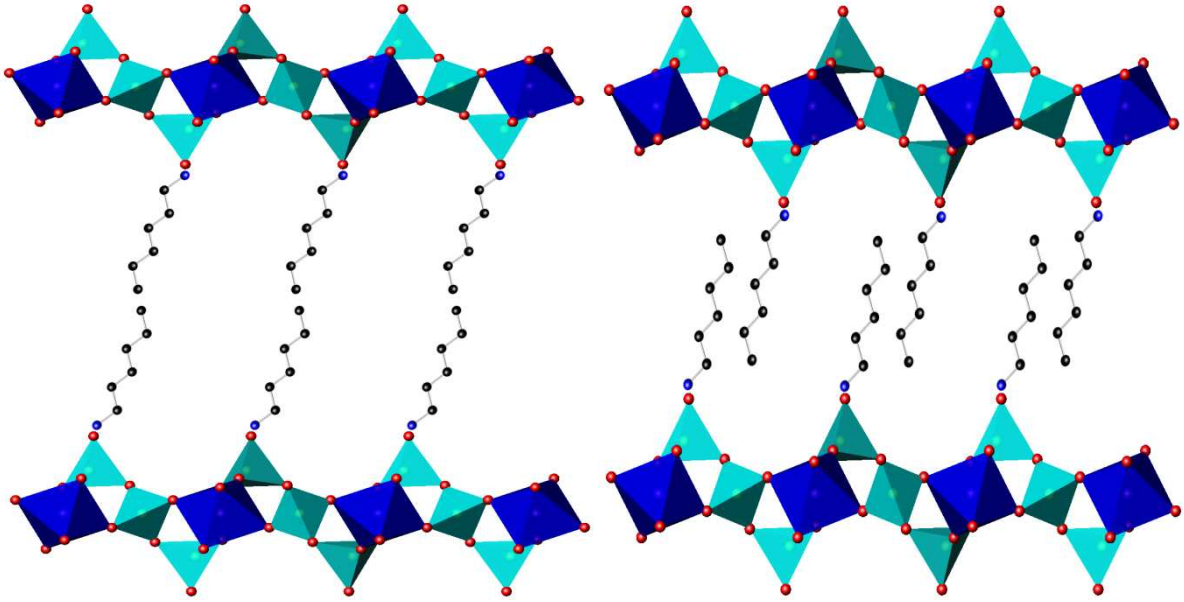

Figure 6.4 *Ordered bonding arrangements for monoamine intercalation*

As with ion exchange, the structural similarities of α-ZrP and AlTP suggest AlTP is a worthy candidate for study of its intercalation properties. There have already been some studies into AlTPs intercalation properties[27-29]. Checker[27] and Hayashi *et al*[28] have studied intercalation of α,ω-diamines into AlTP. These are similar to the monoamines mentioned previously but possess a second amine group at the tail end of the molecule. Both Checker and Hayashi found this additional amine group facilitated the formation of monolayers within the inter-lamellar region, with the two amines bonding to both adjacent layers, with an

intercalation angle of ~57 ° similar to the angles for monoamine intercalation in other layered phases[10, 23, 24].

Tagaya *et al.* has successfully intercalated a small number of azo compounds (for example 4-Phenylazoaniline) into AlTP[29]. Despite the study occurring before the crystal structure of AlTP was known, Tagaya was interested in modifying the inorganic surface by covalently attaching the amine group in place of the terminal hydroxide. He reported success in his attempts between the temperatures of 200 and 300 °C, after which the organic molecules were lost from the system.

A large number of ion exchanged layered phosphates have been reported[30-34] that may also act as intercalating hosts. However, there are surprisingly few reports of attempts to intercalate organic molecules into these ion exchanged phases. Hayashi *et al.* have performed the only real study into intercalation in an ion exchanged phase[35]. They intercalated several small short chain gaseous thiols and sulphides into AlTP-Ag. They found thiols with one mercapto group intercalated at a 1:1 ratio with the amount of silver in the phase, while thiols with two mercapto groups only intercalated at a ratio of 1:2 and concluded that the gaseous monothiols formed bilayer in the inter-lamellar region while the dithiols formed monolayers. This is consistent with observations with amines intercalating in layered phosphates where diamines form monolayers[27] and monoamines form bilayers[10].

Chapter 1.6.1 described how the d_{100} reflection in AlTP is a direct measure of the interlayer spacing of the AlTP host. The process of intercalation into AlTP, or other layered materials, causes an expansion of the inter-lamellar region, thus expanding the interlayer spacing and moving the d_{100} reflection to lower values of 2θ. This is often coupled with a loss of almost all other peaks within the XRD pattern as the intercalation has disrupted order within the material leaving just the reflections determined from the interlayer spacing

dominating the pattern. As a result XRD patterns which show a large peak at low values of 2θ after intercalation reactions are therefore a strong indication that the intercalation has been successful.

This chapter discusses work undertaken to investigate the intercalation potential of AlTP, starting with monoamines, investigating the amount intercalated and method of intercalation, then increasing the complexity of organic molecules intercalated. It also describes investigations into the effect basicity of a molecule has on its ability to intercalate, using a range of amino acids. It finally investigates the intercalation of 6-aminohexanoic acid into AlTP, comparing it to the intercalation in α-ZrP and clays. The chapter also discusses studies undertaken to investigate the intercalation potential of ion exchanged AlTP phases, particularly the AlTP-Ag phase, focusing on the intercalation reactions found to be successful in AlTP and attempts at the intercalation of several thiols.

6.2 Experimental

Intercalation reactions were achieved by stirring 0.5g of AlTP or AlTP-M, for 24 hours, in 50 ml solutions of pure amine or thiol, where the amine or thiol were liquid at room temperature, or 0.5M solutions, where the amine or thiol was a solid at room temperature.

6.3 Monoamine Intercalation into AlTP

Intercalation of AlTP was successfully attempted with a range of simple monoamines, with carbon chain lengths ranging from 3-12. XRD patterns (Figures 6.5 and 6.6) for these phases showed a significant shift in the d-spacing of the d_{100} peak of theses phases from 7.94(1) Å in the AlTP host up to 33.5(5) Å in longer chained amines, Table 6.1.

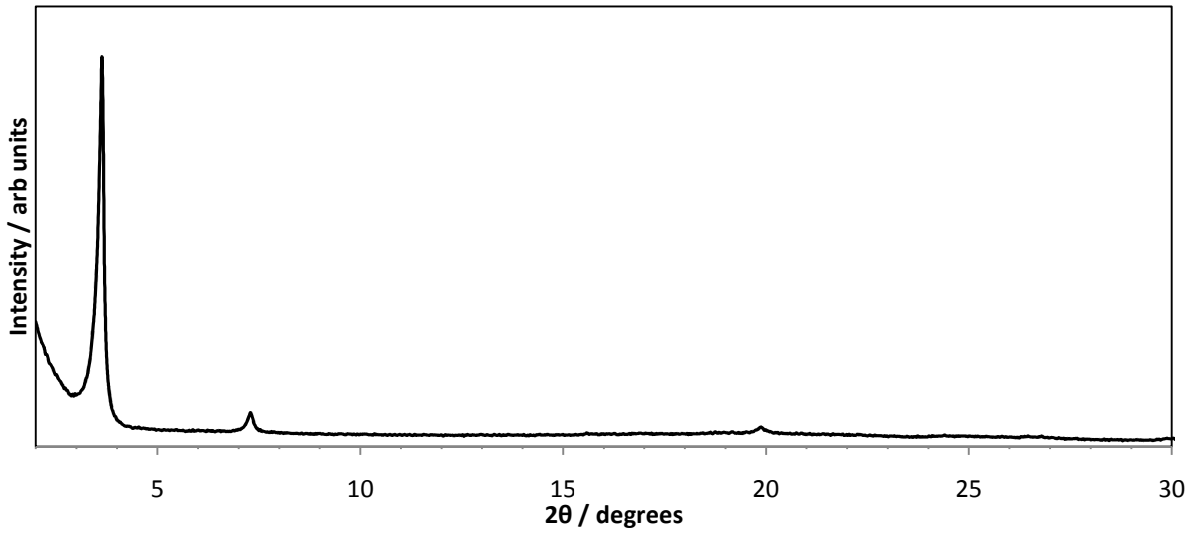

Figure 6.5 *XRD pattern of heptylamine intercalated AlTP*

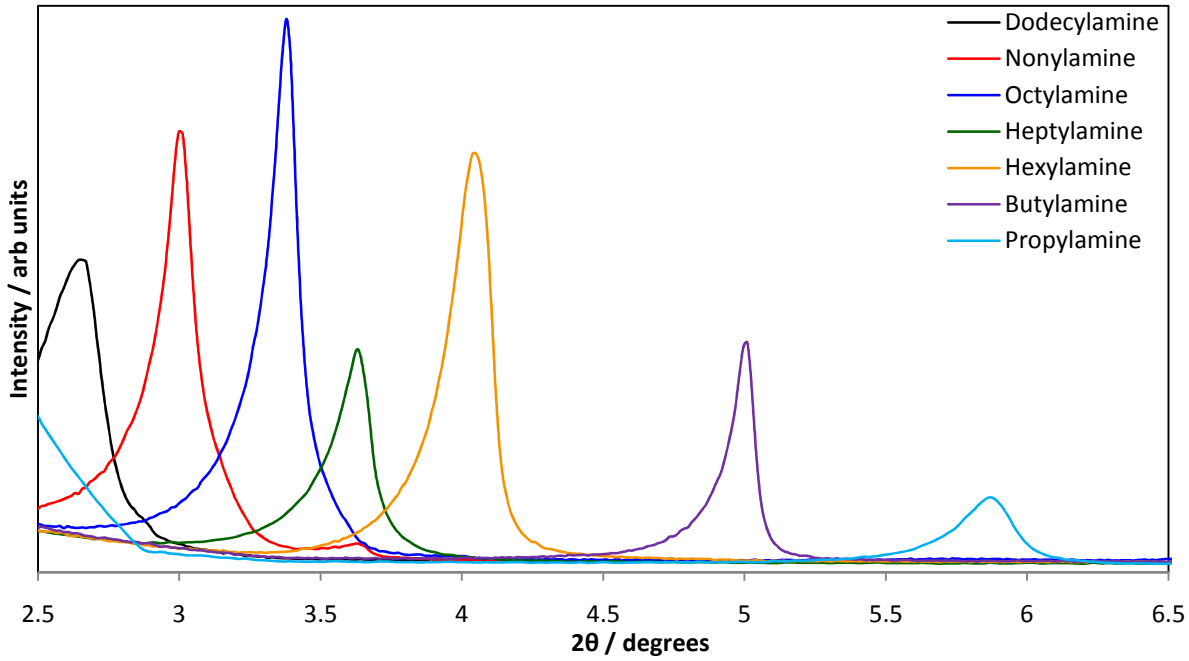

Figure 6.6 *d_{100} peaks for intercalated AlTP phases*

Table 6.1 *d_{100} peak spacings for mono- and di- amine intercalated phases*

Number of Carbons in Chain	d-spacing / Å	
	Monoamines	Diamines[27]
3	15.0 (4)	11.1 (3)
4	17.6 (3)	12.1 (2)
6	21.8 (1)	14.7 (2)
7	24.3 (1)	16.9 (3)
8	26.1 (1)	-
9	29.4 (2)	-
12	33.5 (5)	-

Evidence for bilayer formation in the monoamine intercalations comes from a comparison of the d-spacing of the d_{100} peak, with carbon chain lengths of the amines, shown in Table 6.1. As diamines are known to form monolayers in AlTP, their d-spacing forms a good basis for establishing a baseline of monolayer size and any d-spacing of an equivalent monoamine significantly larger than the diamine would be evidence of the formation of bilayers. All comparable monoamines showed a significant increase in the d-spacing in comparison to their equivalent diamines, suggesting a bilayer had been formed.

This comparison, however, relies on a consistent intercalation angle, as steeper angles of intercalation will give larger increases in the inter-layer spacing than shallower angles. A plot of d-spacing against number of carbons (Figure 6.7) shows an increase of ~2.10 Å for every carbon added to the amines carbon chain. This is much larger than the maximum possible of 1.27 Å allowed for a monolayer (see Section 6.1) and thus providing further evidence of bilayer formation. These data also equate to an intercalation angle of 56(2) °, consistent with that of 57 ° observed in diamines in AlTP[27, 28] and angles of 60 °, 54 ° and 59 ° observed in monoamine intercalation in $VOHPO_4\cdot 0.5H_2O$[23], α-ZrP[24] and α-TiP[10] respectively.

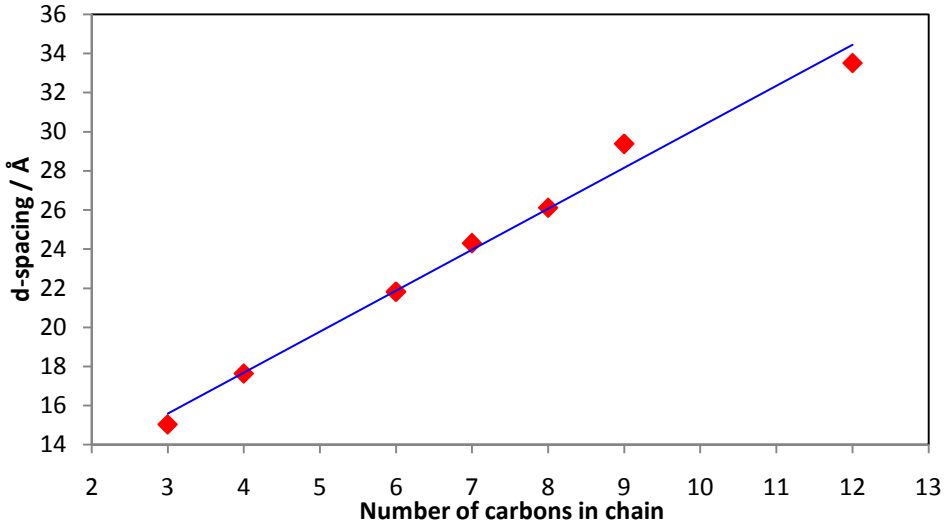

Figure 6.7 *d-spacing of d_{100} against number of carbons in chain for intercalation of monoamines (best fit line shown)*

The monoamines are believed to bond to the AlTP host in a similar fashion to that observed in α-ZrP[26], where the amine gains the terminal hydrogen to become NH_3^+ and bonds to all the oxygens on one face of the PO_4 tetrahedra through lewis acid – lewis base interactions.

HCN elemental analysis (see Appendix 6) showed these phases had intercalated to around 95-100% of their maximum intercalation potential of 2 moles of amine per mole of AlTP. The hydrogen results also indicated that the intercalation process has driven out the inter-lamellar waters, replacing them solely with the amines, rather than the two coexisting.

6.4 Secondary Amine Intercalation into AlTP

To increase the complexity of amine intercalation secondary amines with the general formula $(CH_3(CH_2)_x)_2NH$ (where x = 1-3) were attempted to be intercalated into AlTP. XRD patterns (Figure 6.8) showed evidence of intercalation with the d_{100} peak shifting to lower values of 2θ. Diethylamine only partially intercalated into AlTP with the XRD pattern still showing the host present, Figure 6.9. Attempts to fully intercalate this with higher temperatures and longer reaction times proved unsuccessful with host material always still present. This is consistent with previous observations that diaminoethane could not be intercalated into AlTP[27].

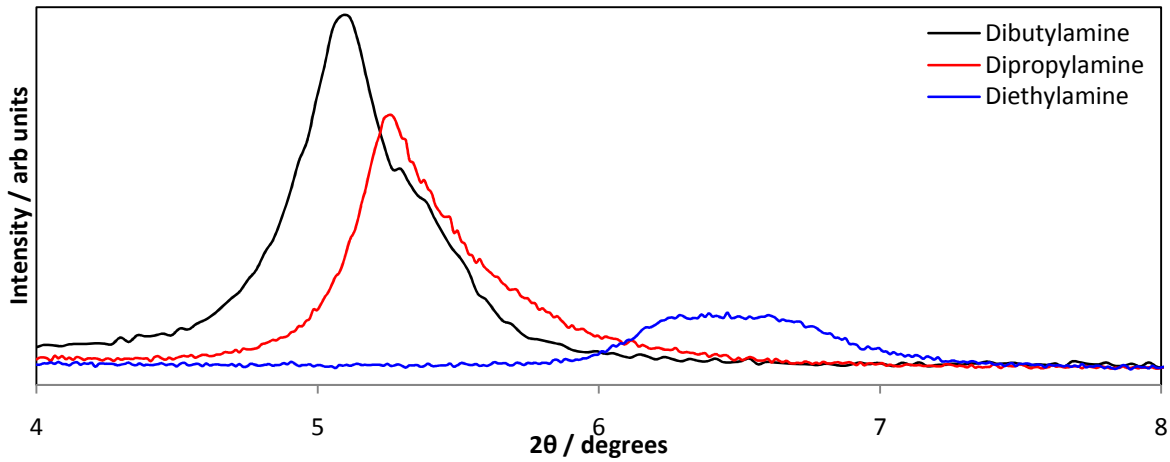

Figure 6.8 *XRD patterns of secondary amine intercalated AlTP phases*

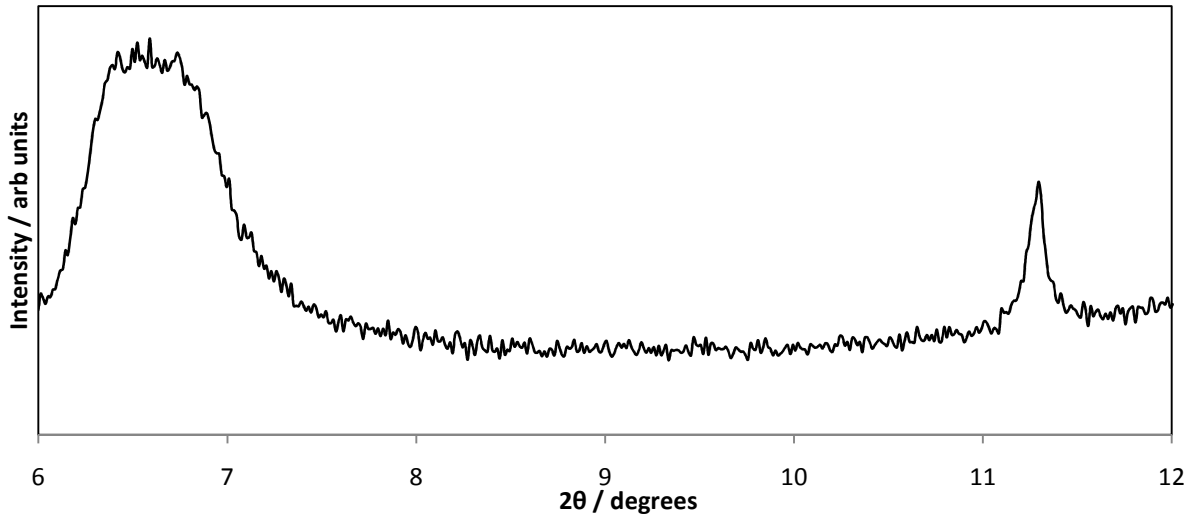

Figure 6.9 *XRD patterns of diethylamine intercalated AlTP, peak at 11.2 ° is AlTP host*

The d-spacings of the d_{100} peak for these phases, 13.7(7) Å, 16.8(4) Å and 17.3(4) Å for diethyl-, dipropyl- and dibutylamine respectively, are substantially larger than the equivalent chain length diamine, suggesting the secondary amines intercalate in bilayers. HCN elemental analysis (see Appendix 6) showed around 50-55% intercalation had been achieved, much less than seen with the primary monoamines. This may be a result of the amine's carbon chain 'arms' now branching outwards and blocking the adjacent terminal hydroxide groups (Figure 6.10) and hindering complete amine intercalation. For example if we consider dipropylamine as possessing an 'arm-span' of around 4.5 Å (given a trans-trans arrangement of the carbon chains), this contrasts with the host's terminal oxygens which are 4.9 Å and 5.9 Å apart along *b* and *c* respectively. This also explains the increased broadness of the d_{100} peaks compared with their primary monoamine equivalents, as this mode of intercalation is likely to increase disorder within the inter-lamellar region.

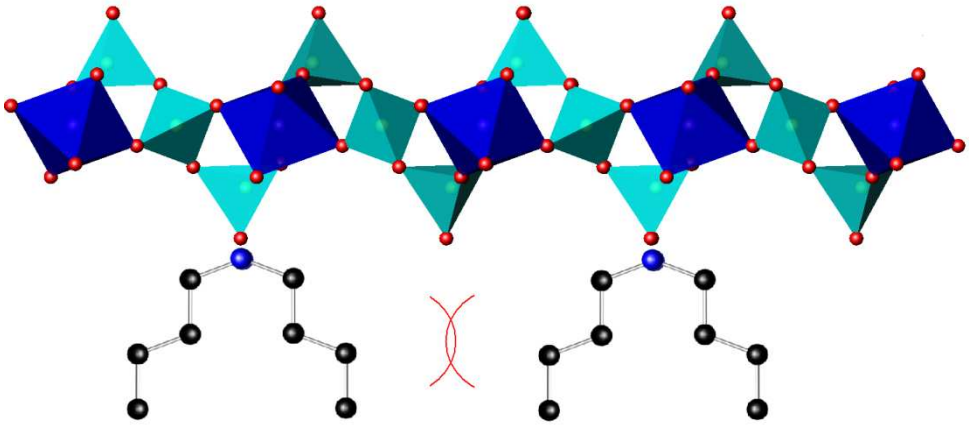

Figure 6.10 *Proposed intercalation of secondary amines showing steric blockage of adjacent sites*

ESEM images are consistent with the layered nature of these phases, Figure 6.11.

Figure 6.11 *ESEM image of dibutylamine intercalated AlTP*

6.5 Tertiary Amine Intercalation into AlTP

Increasing the complexity of the intercalating amine further, tertiary amines, with the general formula $(CH_3(CH_2)_x)_3N$ (where x = 1-3) were next intercalated into AlTP. These all intercalated successfully giving the XRD patterns shown in Figure 6.12. The triethylamine

showed consistent problems as with diethylamine and diaminoethane, only partially intercalating into the phase, with host AlTP still evident in the XRD pattern after intercalation.

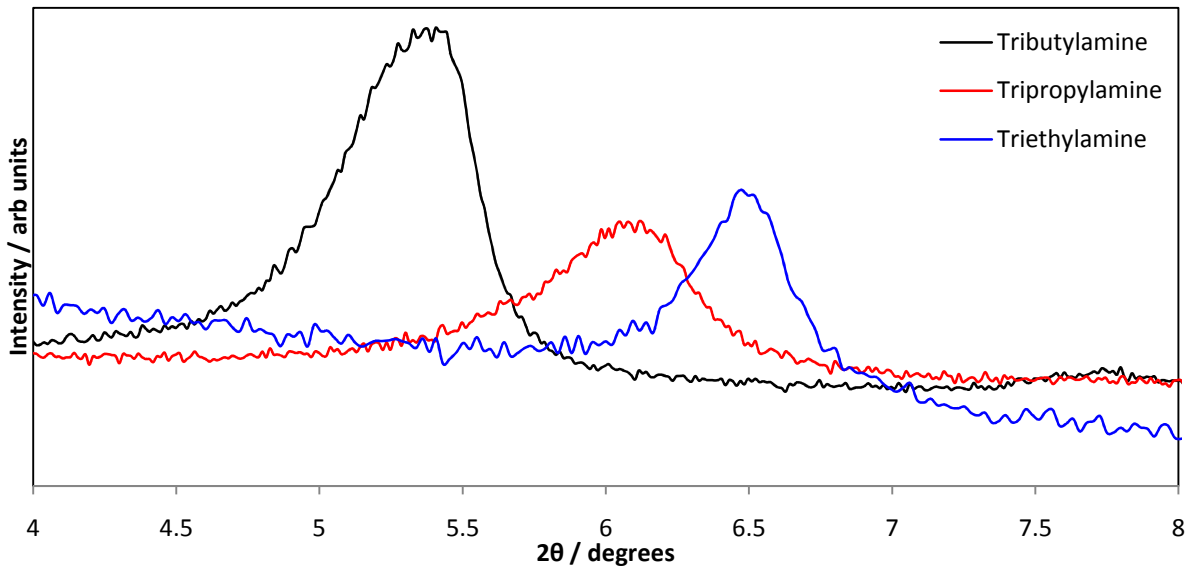

Figure 6.12 *XRD patterns of tertiary amine intercalated AlTP*

Also, as with secondary amine intercalation, the d-spacing of the d_{100} peak for tertiary amine intercalation (14.1(4) Å and 16.6(4) Å for tripropyl- and tributylamine respectively) was significantly larger than the equivalent diamine, indicative of bilayer formation. HCN elemental analysis showed around 40-50% intercalation was achieved in these phases. This is again similar to secondary amine intercalationand may be explained by steric factors causing a blocking of neighbouring hydroxide groups.

ESEM images (Figure 6.13) of the tertiary amine intercalation products show no noticeable difference in morphology to secondary amine intercalation phases.

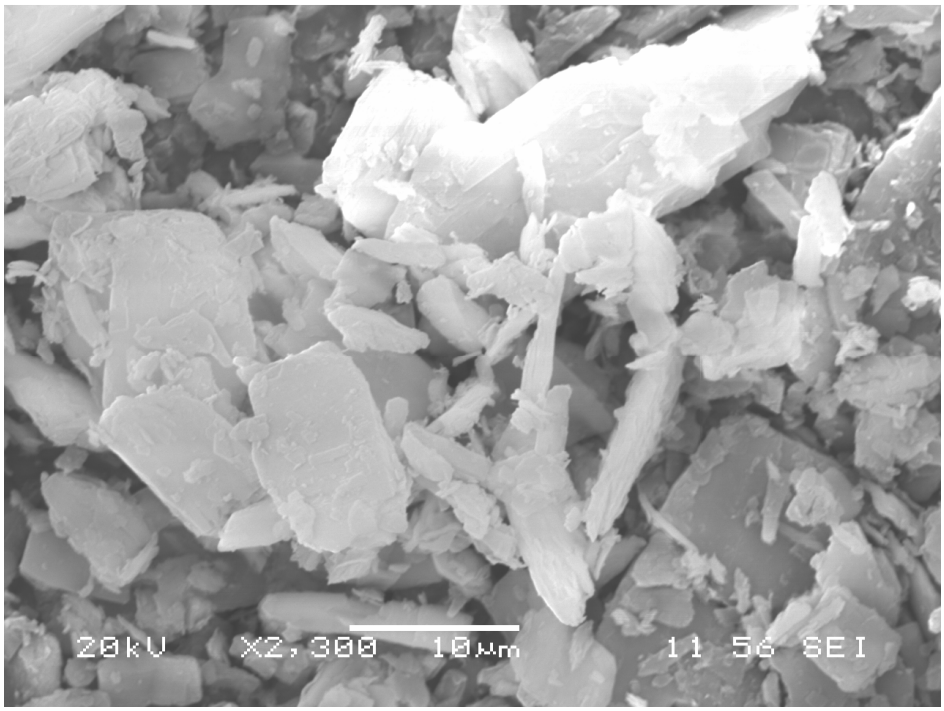

Figure 6.13 *ESEM image of tributylamine intercalated AlTP*

6.5.1 N,N-Diethylaminoethanol

In a further increase to the complexity of intercalating molecules, N,N-diethylaminoethanol was also attempted to be intercalated into AlTP; this is similar to the triethylamine molecule but has gained a hydroxyl group on the terminal carbon of one of its carbon chains. Analysis of the XRD data (Figure 6.14) suggests that some intercalation has been successful given the small peak at 6.5 ° (13.6(5) Å). This is at a similar position to the peak described for triethylamine and suggests a similar ability to intercalate and stacking arrangement. The ability to intercalate such multifunctional molecules in AlTP is significant, although the limited level of intercalation is evident from the presence of significant host material in the products XRD pattern.

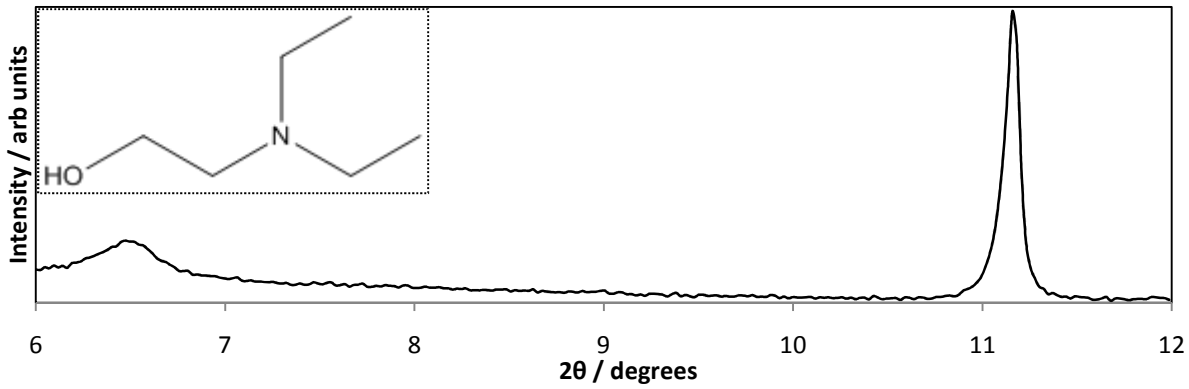

Figure 6.14 *XRD pattern of N,N-diethylaminoethanol (molecule inset) intercalated AlTP, peak at 11.2 ° is the AlTP host*

6.6 Trans-1,4-Diamino Cyclohexane Intercalation into AlTP

Previously reported intercalations in AlTP have involved diamines[27] or amines with cyclic rings[29]. As an extension to this, attempts were made to intercalate trans-1,4-diamino cyclohexane (T-1,4), which is essentially a cyclic diamine. XRD data (Figure 6.15) suggested the intercalation was successful showing a peak at around 6.25° 2θ, around the region expected for the interlayer reflection of intercalated AlTP phases. The d-spacing of the d_{100} peak for this phase is 14.1(3) Å, which is consistent with the value observed of 14.7(2) Å for diaminohexane intercalation into AlTP. However, this is a somewhat surprising as although this is consistent with a monolayer, we might expect a smaller d_{100} with the cyclic T-1,4 as it is closer in length to diaminobutane (d-spacing value of 12.1(2) Å for intercalation peak). We can only surmise that the intercalation angle of the T-1,4 is much higher than those seen in simple alkyl diamines

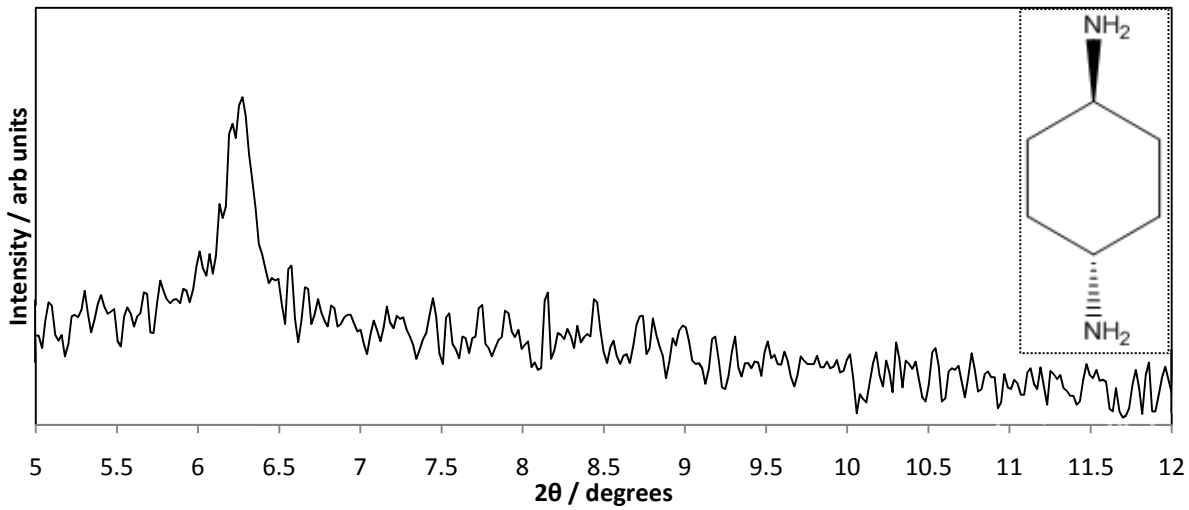

Figure 6.15 *XRD pattern of AlTP intercalated with trans-1,4-diaminocyclohexane (molecule inset)*

6.7 pK_b Dependence of Intercalation

Previous reports have shown that the basicity of an organic molecule influences its ability to intercalate into α-ZrP[19]. Given the similarities between α-ZrP and AlTP it would seem sensible to investigate how an organic molecules basicity affects its ability to intercalate into AlTP. Knowing the factors affecting intercalation success would greatly aid future studies as it would enable simple predictions to be made as to a molecules intercalation capability, or even aid in designing molecules to be intercalated.

6.7.1 Amines Unable to Intercalate in AlTP

A number of aromatic amine intercalation reactions have been attempted in AlTP which have proved unsuccessful, with XRD patterns of the resulting phases showing no changes to the AlTP host. The first of these was 2,6-lutidine (Figure 6.16a) containing methyl groups on the ortho positions adjacent to the nitrogen. It was initially thought that these methyl groups may be sterically hindering the amines ability to bind to the phosphate layer, so intercalation was attempted with 3,4-lutidine (Figure 6.16b) which has no such steric issues, but this also failed to intercalate. Following this, a further range of amines (Figure 6.16) were found to be unsuccessful in attempted intercalation. Importantly, these

were all less basic than the amines that have been intercalated into AlTP thus far, indicating as with α-ZrP[19], the basicity and pK_b of the intercalating molecule has a strong influence on the intercalation potential of a molecule.

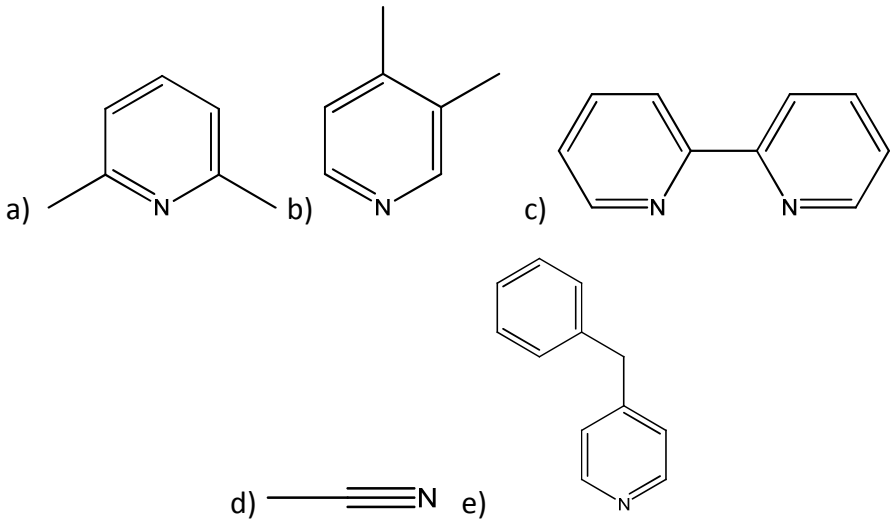

Figure 6.16 *Molecules unable to intercalate in AlTP a) 2,6-lutidine b)3,4-lutidine c)2,2'-dipyridyl d) acetonitrile e) 4-benzyl pyridine*

6.7.2 Amino Acid Intercalations in AlTP

As mentioned in Section 6.1, there is much interest in the intercalation of biomolecules such as amino acids, which also display a wide range of pK_b values. This makes them a good series of molecules to use during an investigation of the effects of pK_b upon intercalation potential into AlTP. Intercalation reactions for a range of amino acids (see Figure 6.17 and Section 6.8) were attempted and results could be grouped into three different intercalation behaviours. The first were those that failed to show any evidence of intercalation and these included alanine, cysteine and glycine (Figure 6.17a-c). These are all weaker bases, with pK_b values above 9.5 (10.08, 10.28 and 9.58 for alanine, cysteine and glysine respectively) and their failure to intercalate is consistent with observations made in Section 6.7.1 and previous reports with α-ZrP[17].

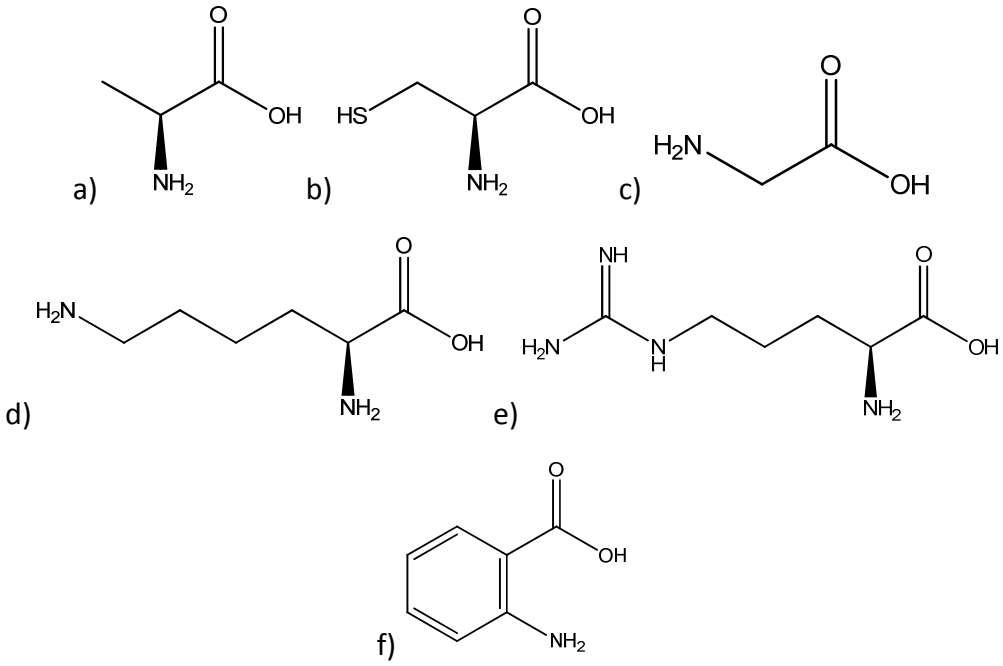

Figure 6.17 *Amino acids attempted to be intercalated into AlTP a) alanine b) cysteine c) glycine d) lysine e) arginine f) anthranlic acid*

The second group of amino acids were observed to intercalate into AlTP. These included lysine and arginine (Figure 6.17d & e), giving the XRD patterns shown in Figure 6.18, and are also consistent with observations in α-ZrP[19]. These have lower pK_b values of around 9 (9.16 and 9 for lysine and arginine respectively) implying a limit to intercalations in AlTP, for organic molecules with a pK_b of below 9.5.

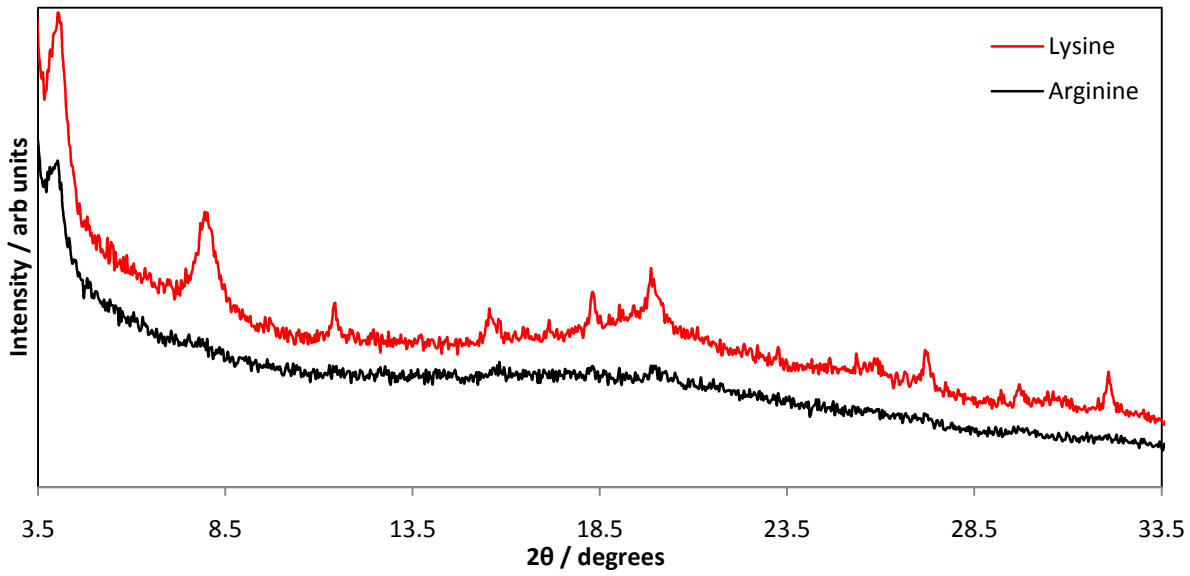

Figure 6.18 *XRD patterns of lysine and arginine intercalated AlTP*

We may also define a third group of amino acids, which possess the apparent basicity but steric factors limit their intercalation. These include Anthranilic acid (Figure 6.17f) which has a pK_b value of 4.95, much lower than the perceived limit of around 9.5, but no intercalation is observed into AlTP. It is believed that steric hindrance is created by the positioning of the carboxylic acid group next to the amino group on the aromatic ring, which prevents interaction between the amine group and the host phosphate layers. As we might expect, this implies that sterics, as well as pK_b, play an important role in a molecule's intercalation potential with AlTP.

6.7.3 Altering Basicity to affect intercalation

To further confirm the influence of basicity on the intercalation reactions, a study of previously intercalated molecules with modified basicity was undertaken. Carbonyl groups were added on the carbons bonded to the amine groups in butylamine and 1,6-diaminohexane to give butyramide and adipamide respectively, Figure 6.19. Carbonyl groups are electron withdrawing and lower the basicity and thus raise the pK_b of neighbouring functional groups, so the addition of these to previously intercalated molecules should prevent intercalation on basicity grounds. This was indeed the case with no intercalation observed into AlTP with either of these molecules. Although this supports the trend in basicity, we must also consider whether the presence of the carbonyl group imparts any steric barrier to intercalation. This is difficult to assess without some detailed modelling of the guest-host binding in these materials. Clearly designing and modifying organic molecules to optimise their intercalation capabilities is needed to guide future studies, but this is likely to be increasingly challenging as the complexity of intercalating molecules in AlTP increases.

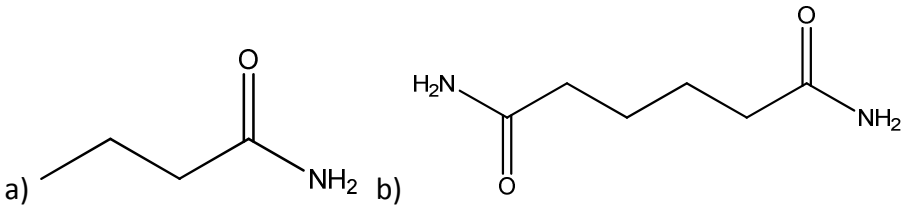

Figure 6.19 *a) butyramide b) adipamide*

6.8 6-Aminohexanoic Acid Intercalation into AlTP

Attempts at the intercalation of 6-Aminohexanoic acid (6AHA) have proven successful in AlTP, producing a phase (labelled AlTP-6AHA) with the XRD pattern shown in Figure 6.20. The XRD pattern is still dominated by the d_{100} peak but is much more complex than the intercalation patterns seen thus far, with numerous peaks, suggesting increased order within the inter-lamellar region. It was hoped that the presence of greater order would allow a unit cell to be indexed to the phase, but attempts to do this have proved unsuccessful.

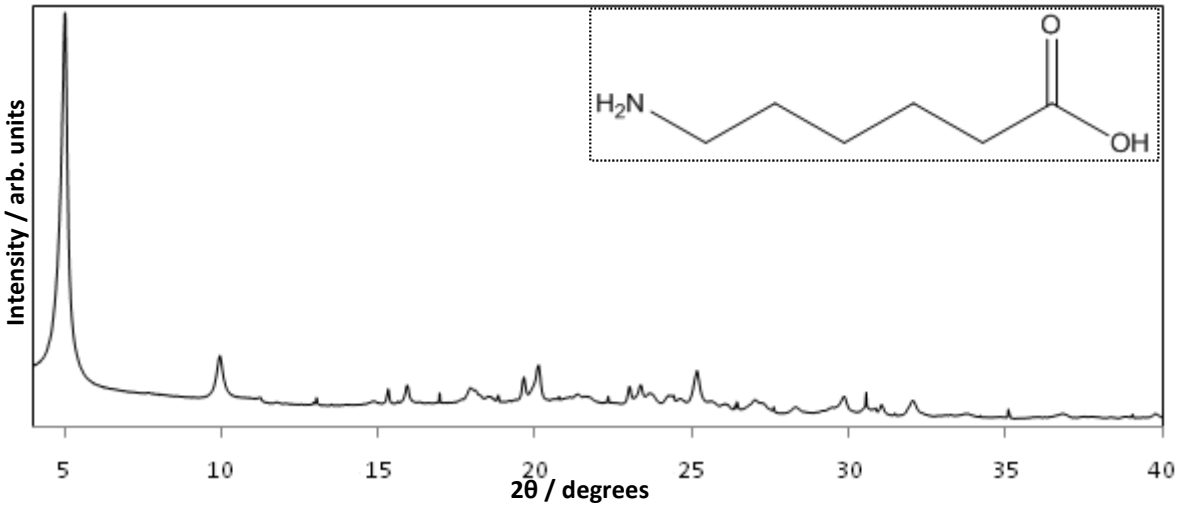

Figure 6.20 *XRD pattern of AlTP-6AHA (6AHA molecule inset)*

Unlike in α-ZrP, the intercalation of 6AHA into AlTP appears to form bilayers with HCN elemental analysis (see Appendix 6) confirming around 72% of the potential intercalation was achieved. The d-spacing of the d_{100} peak has been reduced from 21.8(1) Å in hexylamine to 18.1(1) Å for 6AHA. Previous studies on the intercalation of 6AHA into layered materials have suggested either the formation of bilayers parallel to the phosphate

layers (as seen previously in clays[22]) or the formation of an angled bilayer (as seen with monoamines in AlTP). The value of 18.1(1) Å would appear to support the latter of these scenarios and this is supported by studies on 4-aminobutanoic acid (Section 6.8.1). The potential for interactions between the 6AHA molecules in the inter-lamellar region may explain the reduced d_{100} compared to hexylamine as it may result in the layers becoming closer together. These interactions may be zwitterions forming in a head to tail arrangement of 6AHA molecules (Figure 6.21a) seen previously in other phases[20-22] or a head to head arrangement of 6AHA molecules with the carboxylic acids hydrogen bonding with each other (Figure 6.21b).

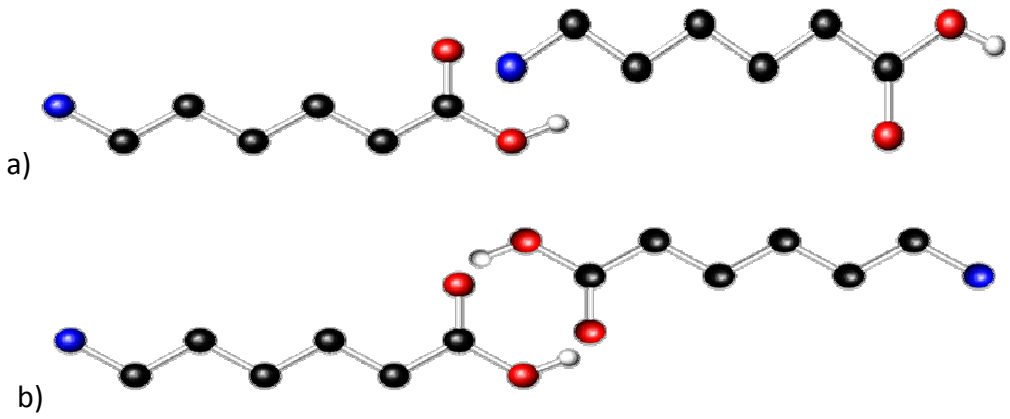

Figure 6.21 *Possible 6AHA interactions a) head to tail b) head to head*

In an angled bilayer intercalation arrangement, as seen with monoamines in AlTP, the head to head arrangement would seem more favourable, freeing the amine groups to bond to both adjacent phosphate layers. The head to tail arrangement would require a carboxylic acid binding to the phosphate layers. Such interactions have been reported in α-ZrP[14, 36], but there have been no reports in the literature of carboxylic acids intercalating into AlTP in a similar manner. Despite numerous studies, we have been unable to intercalate carboxylic acids or alcohols into AlTP, without the presence of an amine group, suggesting the interactions between P-OH and CO_nH (n = 1 for alcohol, 2 for carboxylic acid) are not favourable in

AlTP. This therefore indicates the head to head arrangement, seen in Figure 6.21b, is more likely for 6AHA intercalating into AlTP. To support this, FTIR spectroscopy (Figure 6.22) showed an expansion of the OH stretch of the carboxylic acid to higher wavenumbers from around 2300-3000 cm^{-1} to around 2300-3600 cm^{-1}. This is consistent with hydrogen bonding, which effectively lowers the reduced mass of the O-H bond and increases the wavenumber of its stretch, typically extending the OH stretch from 2500-3000 cm^{-1} to 2500-3500 cm^{-1} in carboxylic acid dimers. This supports the assertion that 6AHA is intercalating in angled bilayers in a head to head fashion.

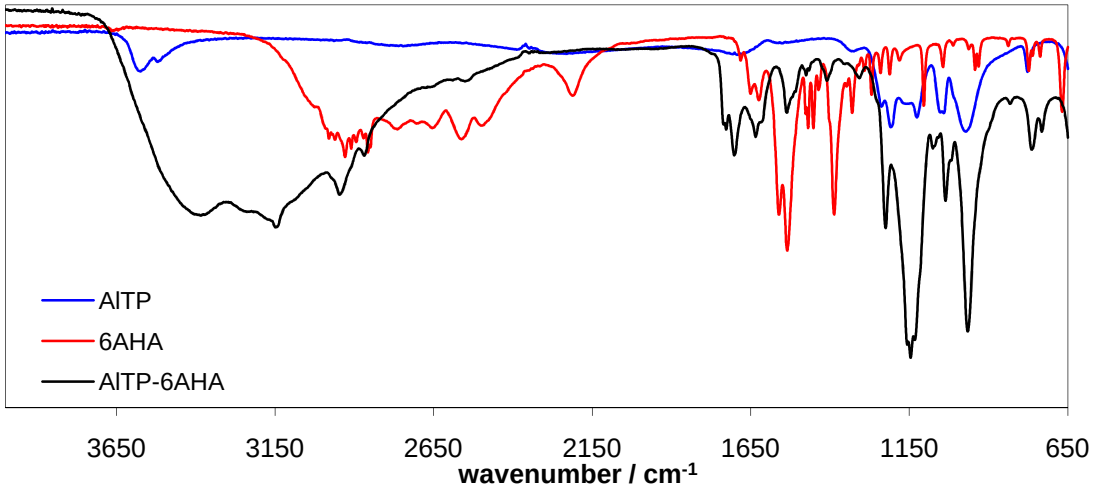

Figure 6.22 *FTIR spectra of AlTP, AlTP-6AHA and 6AHA*

ESEM images of AlTP-6AHA (Figure 6.23) were similar to the other intercalation phases, and showed a morphology consistent with the layered nature of the phase.

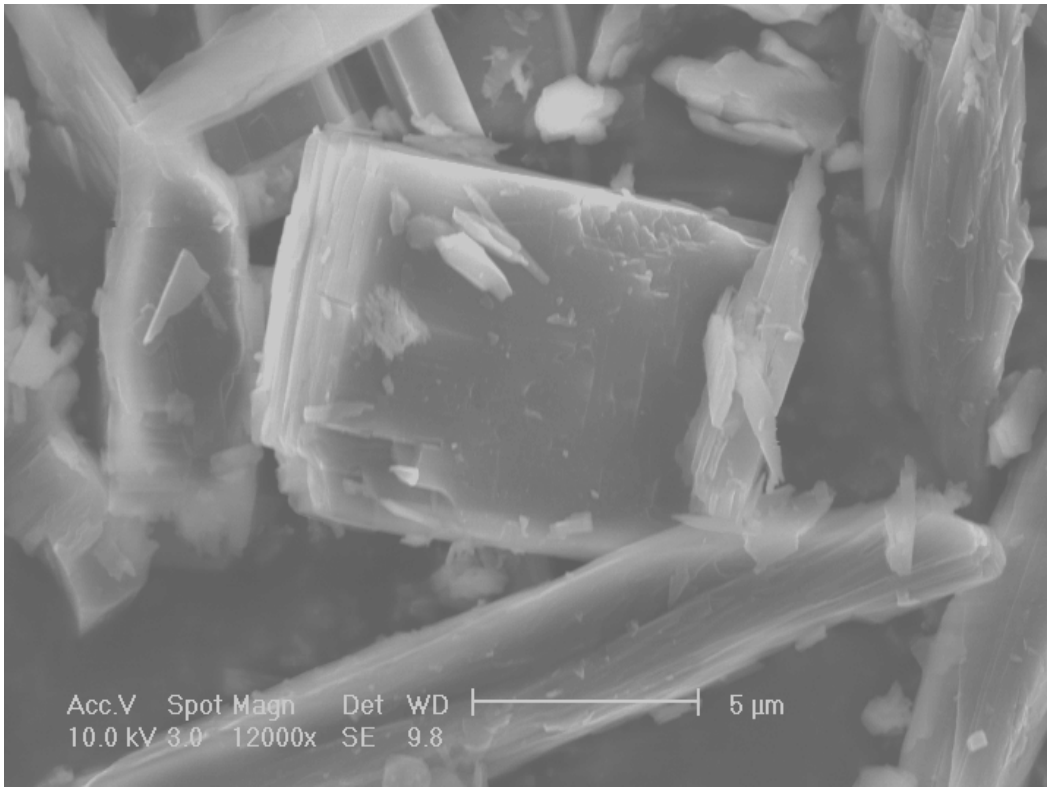

Figure 6.23 *ESEM image of AlTP-6AHA*

Attempts at repeating the production of nylon in the inter-lamellar region, as reported in 6AHA intercalated α-ZrP[20], proved unsuccessful in AlTP-6AHA, with the amino acid being decomposed rather than polymerising. This appears to further support a model where the 6AHA molecules are arranged head to head, rather than head to tail motif, thus limiting chemical reactivity.

6.8.1 4-Aminobutanoic Acid

In a continuation of related amino acids, 4-Aminobutanoic acid (4ABA) has also been intercalated into AlTP, giving the XRD pattern shown in Figure 6.24. As with the 6AHA phase, the resulting XRD pattern is more complex than those of simpler amines previously intercalated, indicating increased order within the layers and the potential for identification of a unit cell which has not yet been achieved.

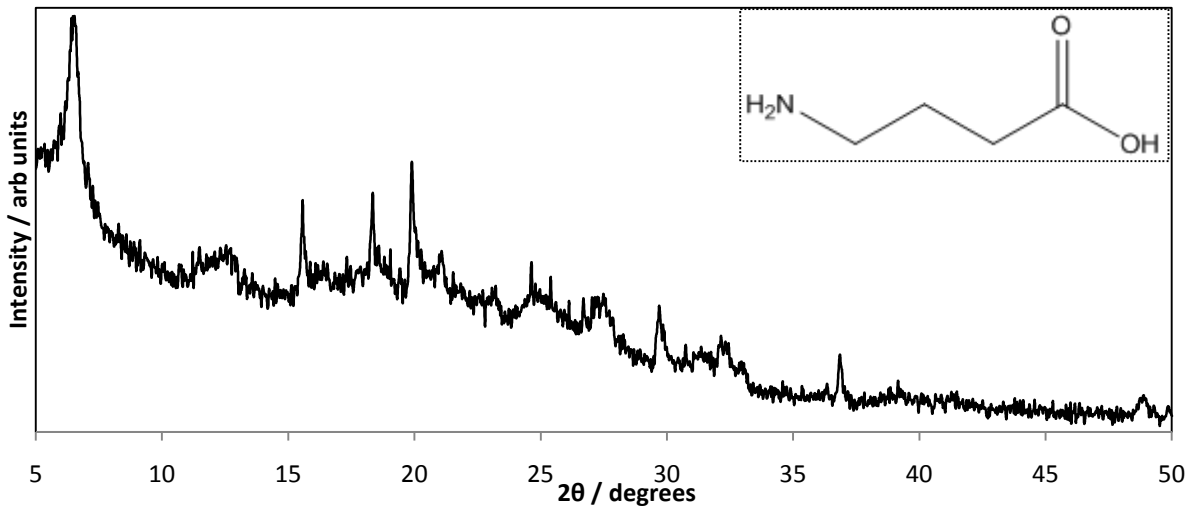

Figure 6.24 *XRD pattern of 4ABA intercalated AlTP*

The d-spacing of the d_{100} peak for this phase is 14.2(3) Å and is much smaller than that of 18.1(1) Å observed in AlTP-6AHA. We would expect these two amino acids to exhibit similar dimensions perpendicular to the chain direction. Therefore intercalation in bilayers parallel to the phosphate layers, as seen in clays[22], would result in the same interlayer spacing for both phases. The fact that the interlayer separations are different shows further evidence that these amino acids are intercalating in an angled fashion similar to that of monoamines. With only two of these amino acids intercalated there are not enough data to calculate an accurate intercalation angle for these phases.

It is conceivable that having the acid groups, from both 6AHA and 4ABA, arranged in a head to head manner may open the possibility of chelating cations or other species between the acid groups. Due to time constraints this was not pursued during this project, but this additional binding potential could allow for an expanded range of intercalation and ion exchange species in AlTP. The formation of metal oxide layers in the inter-lamellar region has been reported in α-ZrP[14, 36], and such hybrid phases would be of great interest in the MTP family given the ability to replace Al for other cations (e.g. catalytic or magnetic ions).

6.9AlTP-M Intercalation

All intercalation reactions so far presented appear to rely on the interaction of the guest molecule with the acidic proton available on the metal phosphate surface. The synthesis of a range of ion exchanged AlTP materials, where these protons have been replaced by mono- and divalent metals, offers an opportunity to determine whether these protons are integral to intercalation behaviour. A series of intercalation reactions with amines, alcohols and thiols was undertaken with the alkali metal exchanged phases and the divalent exchanged phases reported in Chapters 3 and 5. In all cases no evidence of intercalation was seen. The alkali metal AlTP phases displayed an unchanged XRD pattern after reaction and the divalent AlTP phases became amorphous. However, there was one exception. The AlTP-Ag phase which, as mentioned in Section 6.1, had previously been shown to intercalate with small gaseous thiol and sulphide molecules[35], was now also shown to intercalate amines.

6.10 Monoamine Intercalation into AlTP-Ag

In a similar manner to AlTP (see Section 6.3), a range of monoamines were successfully intercalated into AlTP-Ag. XRD patterns (Figures 6.25 and 2.26) for these phases, as with their AlTP counterparts (Section 6.3), showed a significant shift in the d-spacing of the d_{100} peak from 8.58(1) Å in the AlTP-Ag host up to 32.4(8) Å for longer chained amines, Table 6.2.

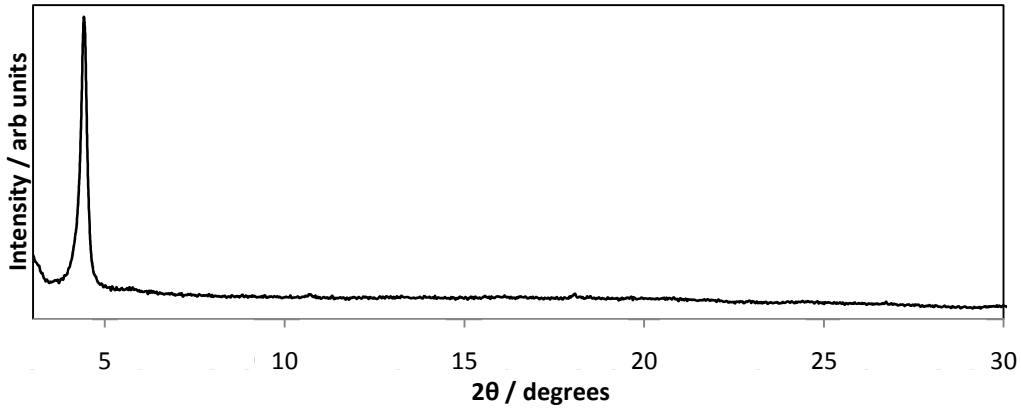

Figure 6.25 *XRD pattern of butylamine intercalated AlTP*

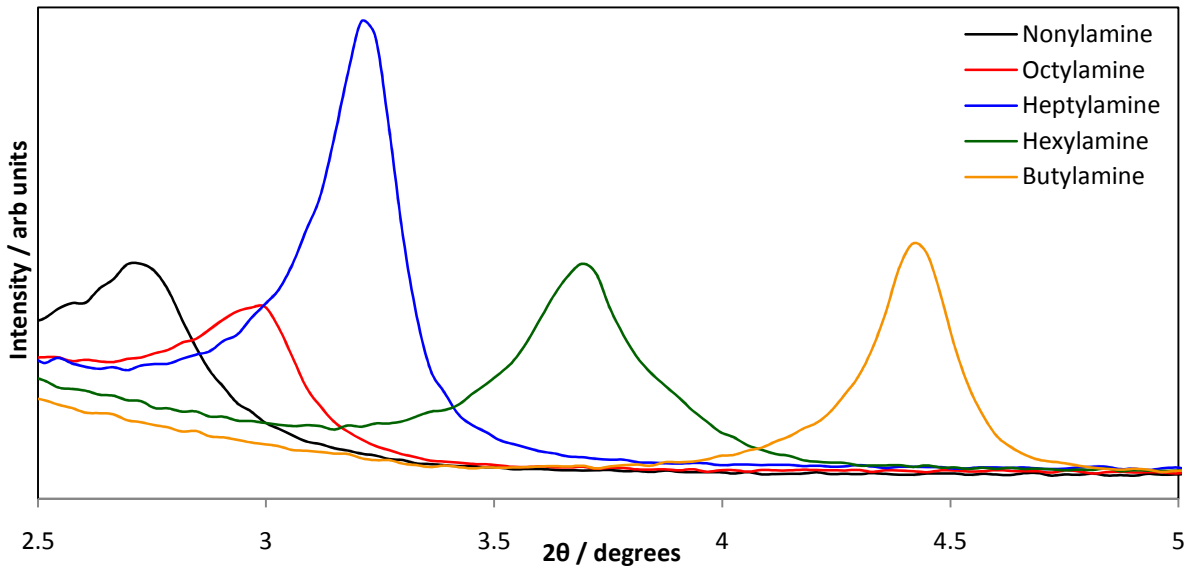

Figure 6.26 *d_{100} peaks for intercalated AlTP phases*

Table 6.2 *d_{100} peak spacings for monoamine intercalated AlTP-Ag phases*

Number of Carbons in Chain	d-spacing / Å
4	20.0 (2)
6	23.9 (2)
7	27.5 (3)
8	29.6 (6)
9	32.4 (8)

The plot of d-spacing against number of carbons (Figure 6.27) showed an increase of ~2.51 Å for every carbon added, giving an intercalation angle of ~81(7) °. This angle is much higher than any reported for intercalation in any other layered phosphate. The still unsolved crystal structure of AlTP-Ag means we are unable to rationalise this observation at present.

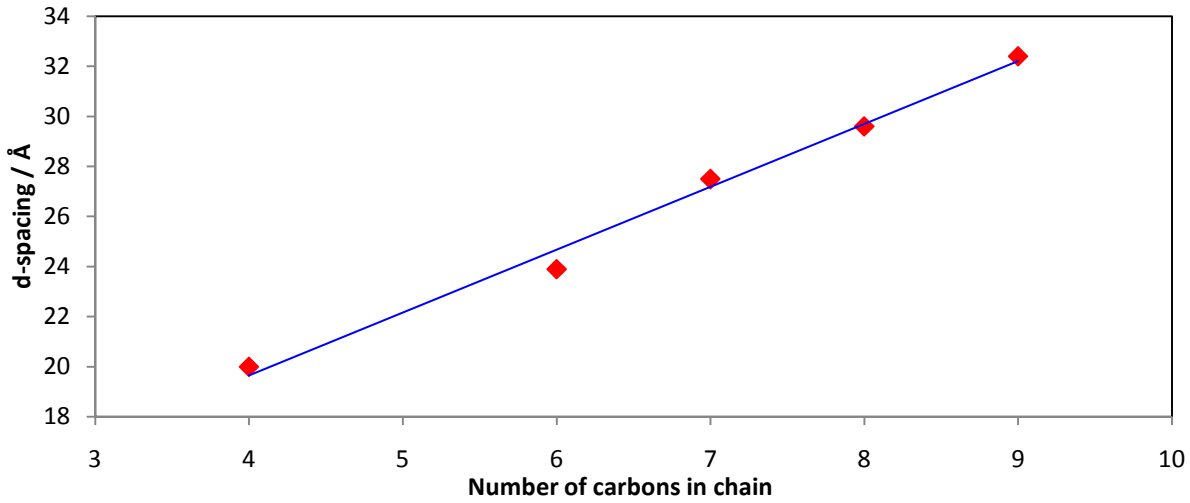

Figure 6.27 *d-spacing of d_{100} against number of carbons in chain (best fit line shown)*

HCN elemental analysis (see Appendix 6) showed the AlTP-Ag monoamine intercalated phases reached effectively 100% of their potential intercalation maximum of two moles of amine per mole of AlTP-Ag host. This amount is consistent with the amount exchanged into the AlTP-monoamine phases, with the hydrogen analysis showing the intercalation to exclude the inter-lamellar waters from the phase in favour of solely organic guests, again consistent with AlTP.

6.11 Thiol Intercalation into AlTP-Ag

Given silver's affinity for sulphur and previous reports of the intercalation of small gaseous thiols into AlTP-Ag[35], attempts were made to intercalate a range of monothiols into AlTP-Ag. These were successful with XRD patterns (Figure 6.28) showing the products followed a similar trend to the monoamines, exhibiting a linear relationship between the number of carbons in the alkyl chain and the position of the d_{100} peak. The appearance of the XRD patterns for these phases suggested more order than those of the AlTP-Ag monoamine intercalated phases. The XRD data contain a number of extra peaks at a regular spacing, suggesting increased order as thiols intercalate, while the monoamines XRD data only contain one or two much smaller additional peaks. These extra peaks are all evenly spaced in

multiples of the main peaks d-spacing indicating that they are all peaks from an h00 reflection.

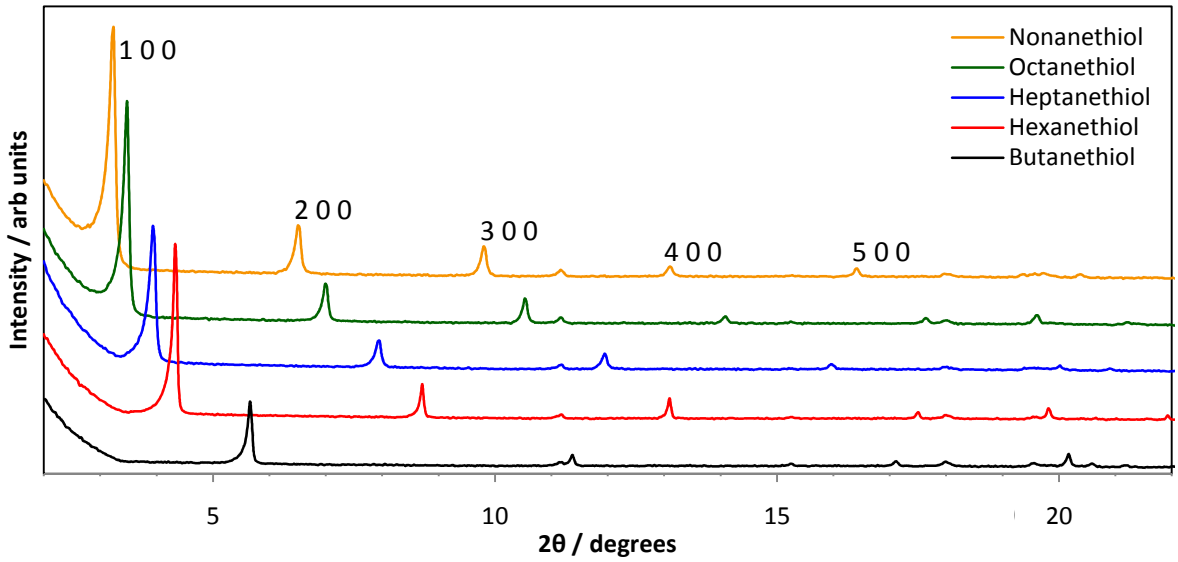

Figure 6.28 *XRD patterns of thiol intercalated AlTP-Ag*

The d-spacings of the d_{100} peak in these phases, whilst being large enough to suggest the formation of bilayers, are significantly smaller than their equivalent monoamines intercalated in both AlTP and AlTP-Ag, Table 6.3. A larger expansion would be expected from a silver ion and sulphur, compared to a silver and nitrogen and especially more than a hydrogen and nitrogen, suggesting a very different bonding arrangement between the layered host and organic guest for the thiol compared to the amines. This may be the loss of the thiols hydrogen and the formation of a covalent bond between sulphur and silver, a bonding method commonly observed when attaching thiol molecules to silver nanosurfaces[37].

Table 6.3 *d-spacings of d_{100} peak for intercalated phases*

Number of carbons in chain	d-spacing / Å		
	AlTP Monoamines	AlTP-Ag Monoamines	AlTP-Ag Monothiols
4	17.6 (3)	20.0 (2)	15.6 (2)
6	21.8 (1)	23.9 (2)	20.4 (2)
7	24.3 (1)	27.5 (3)	22.4 (3)
8	26.1 (1)	29.6 (6)	25.4 (2)
9	29.4 (2)	32.4 (8)	27.3 (3)

The plot of d-spacing against chain length (Figure 6.29) shows an increase of 2.37 Å per carbon added to the alkyl chain, proving bilayer formation, and gives an angle of intercalation for these phases of ~69(2)°. This angle falls between those observed in intercalating monoamines into AlTP-Ag and AlTP (81(7) ° and 56(2) ° respectively) and is consistent with 66 ° observed intercalating monoamines into α-SnP[25].

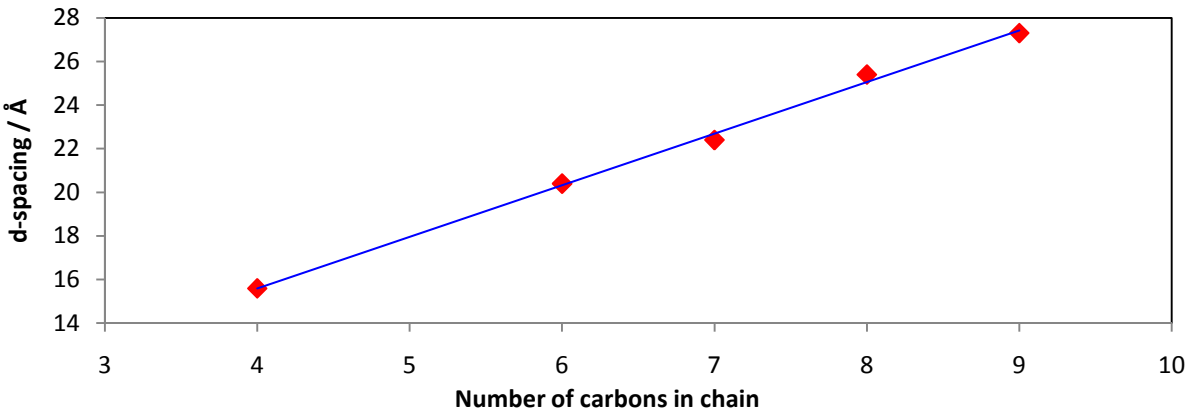

Figure 6.29 *d-spacing of d_{100} against number of carbons in chain (best fit line shown)*

Similar to the monoamines, these phases were shown to achieve around 90% of their potential amount of intercalation by HCN elemental analysis (see Appendix 6).

Thiol intercalation was also attempted in AlTP in view of these results but no intercalation was observed. This shows that the presence of silver in AlTP-Ag expands the intercalation potential of the MTP family, opening up new avenues for intercalation chemistry.

6.12 Secondary and Tertiary Amine Intercalation into AlTP-Ag

Intercalation of secondary and tertiary amines into AlTP-Ag were also attempted but were only partly successful. The XRD patterns (Figure 6.30) show a small broad d_{100} peak resulting from intercalation, but the remainder of the pattern was that of the AlTP-Ag host. Numerous attempts were made to induce full intercalation with higher temperatures and longer reaction times, but all resulted in a mix of intercalated and unintercalated host

AlTP-Ag. It is possible that the amines intercalate around the crystal edges, and so block the inter-lamellar region thus preventing any more intercalation and creating two crystallographically distinct regions.

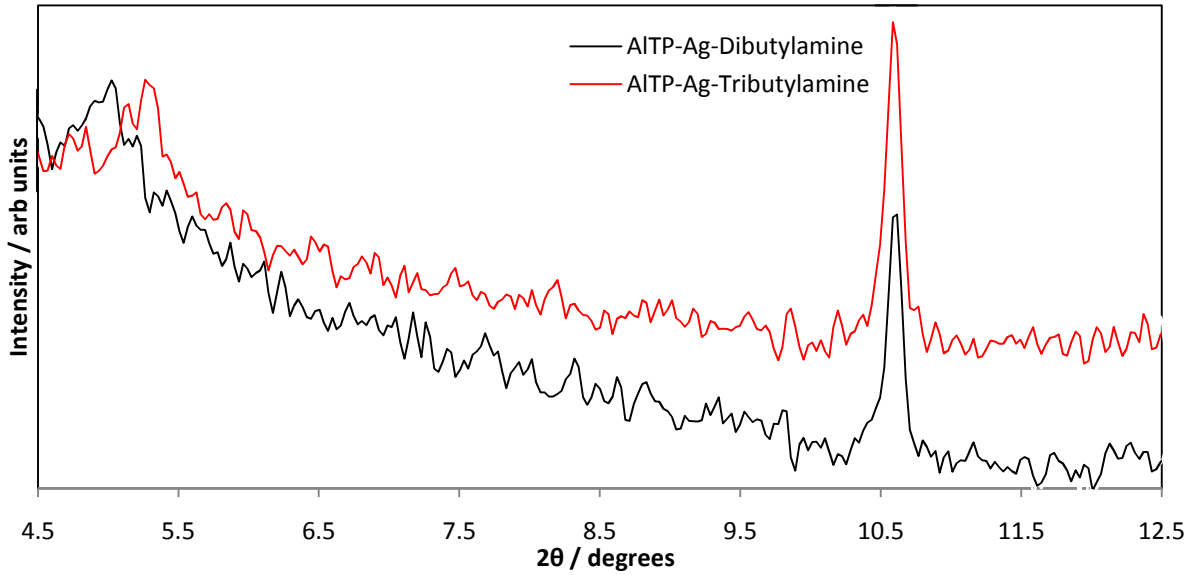

Figure 6.30 *Partial XRD patterns of AlTP-Ag intercalated with di- and tributylamine*

The d-spacings of the observed intercalation peaks, 18.7(7) Å for dibutylamine and 17.9(7) Å for tributylamine, are similar to those observed in AlTP (17.3(4) Å and 16.6(4) Å for di- and tributylamine respectively) with the increased size of the additional silver ion taken into account, implying that the small amount of amine that is able to intercalate forms bilayers as seen with AlTP.

6.13 Amino Acid Intercalation into AlTP-Ag

All of the amino acids attempted in intercalation reactions into AlTP (Sections 6.7.2 and 6.8) were also attempted with AlTP-Ag. With the notable exception of cysteine, which itself cannot intercalate into AlTP, all of these failed to intercalate, including 6-aminohexanoic acid. As we might expect, this implies the dependence upon pK_b of intercalation is markedly different between AlTP and AlTP-Ag and this must be related to the change in change in bonding of the intercalated molecule to the host.

6.13.1 Cysteine Intercalation into AlTP-Ag

Cysteine was unable to be intercalated into pure AlTP, but the incorporation of silver allowed for an intercalation reaction. The intercalation produced a green phase with the XRD pattern shown in Figure 6.31.

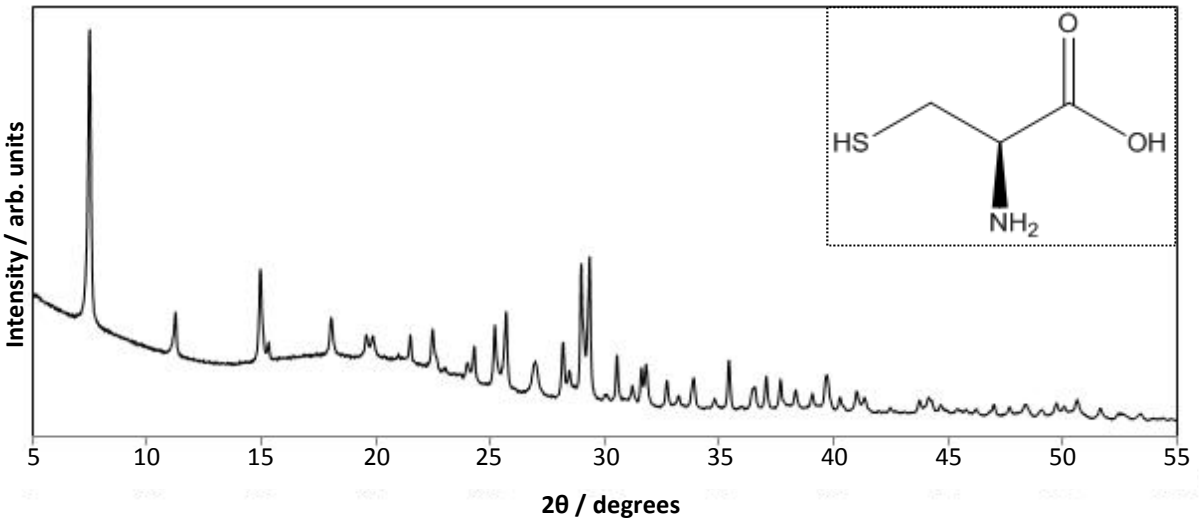

Figure 6.31 *XRD pattern of cysteine intercalated AlTP-Ag*

Like the AlTP-6AHA phase, the silver-cysteine phase showed a much more complex XRD pattern implying an increased level of order within the inter-lamellar region. With this extra complexity it may be possible to assign a unit cell to the phase, although initial attempts in this project have been unsuccessful.

With both a thiol and amine group on cysteine it has two possible methods of binding to silver. It is likely that the bonding to AlTP-Ag host is through the thiol group, rather than the amine, as cysteine is unable to intercalate in AlTP and intercalations involving amine groups in molecules with greater complexity than simple monoamines have not proved as successful in AlTP-Ag as AlTP.

The d-spacing of the d_{100} peak for this phase is 11.8(2) Å. This is very similar to the value of 11.1(3) Å observed in diaminopropane[27], a similar length molecule which bonds in monolayers. The HCN elemental analysis (see Appendix 6), however, shows around 90% of

the intercalation potential is achieved for a silver to cysteine ratio of 1:1, which is usually an indicator of bilayers. The increase in d-space for the d_{100} peak in this phase is only 3.22 Å, which is less than the length of cysteine (around 4 Å), which suggests that cysteine may intercalate into AlTP-Ag in overlapping bilayers running parallel to the phosphate layers similar to the intercalation of 6-aminohexanic acid in some vermiculite clays[22]. Cysteine cannot be intercalated into α-ZrP[20] and there have been no reports of attempting to intercalate it into the silver ion exchanged α-ZrP.

6.14 Conclusions

AlTP has been shown to be an excellent host for the intercalation of organic molecules. Monoamines are intercalated into AlTP in bilayers with 95-100% of the potential intercalation achieved, confirmed by HCN analysis, and an intercalation angle of 56(2) °, consistent with the intercalation angle seen in other layered phosphates [10, 23, 24].

Secondary and tertiary amines are also able to intercalate into AlTP, with d-spacings of their d_{100} peaks suggesting bilayer formation. However, only around 50% of the potential intercalation is achieved and this is believed to be a result of steric blockage of bonding sites by the 'arms' of the secondary and tertiary amines.

The basicity of an organic molecule has been shown to affect its intercalation potential in AlTP. A 'cut-off' point of pK_b above 9.5 has been found with amino acids above this value unable to intercalate, whilst those below are able to. Steric effects have also been found to play a significant role in the intercalation potential of organic molecules in AlTP, with molecules with pK_b values much lower than the cut off point being unable to intercalate on steric grounds.

6-Aminohexanoic acid and 4-aminobutanoic acid have been successfully intercalated into AlTP. These form bilayers within the inter-lamellar region and the intercalated acids are

believed to interact through hydrogen bonding between two adjacent acid groups. This may allow chelation of metal ions between the acids in future work.

AlTP-Ag has also been shown to be an excellent host for the intercalation of organic molecules, displaying its own distinct intercalation properties to its precursor AlTP. There are no reports in the literature of intercalation into ion exchanged forms of the other layered phosphates, so the ability to do so, with its own distinct properties, means AlTP-Ag offers a new branch of intercalation chemistry for layered phosphates.

Monoamines intercalate into AlTP-Ag in bilayers with around 93-100% of the potential maximum intercalation achieved, similar to the amounts observed in AlTP. The intercalation angle of 81(7) ° is, however, much higher than reported for monoamine intercalation in other layered phosphates, the reason for which remains unclear until the structure of AlTP-Ag is determined.

The addition of silver altered the intercalation properties to allow the intercalation of thiols into AlTP-Ag. Monothiols intercalate into AlTP-Ag in a similar fashion to monoamines and possess an intercalation angle of 69(2) °. D-spacings of the d_{100} peaks are considerably smaller than those of their amine equivalents suggesting a different method of bonding to the thiols, potentially involving the formation of a covalent bond between silver and sulphur.

In addition, AlTP-Ag was able to intercalate cysteine due to its thiol group. The intercalated phase had a complex XRD pattern suggesting increased order within the inter-lamellar region. HCN elemental analysis suggested 90% intercalation of a silver to cysteine ratio of 1:1, with the d_{100} peak only showing a small increase on intercalation suggesting therefore bilayers forming parallel to the phosphate layers. The incorporation of cysteine into AlTP-Ag shows that despite the lack of research into the MTP phases, they have

intercalation potential almost equal to and sometimes surpassing those of the α type metal phosphates.

References

1. *IUPAC Gold Book*, http://goldbook.iupac.org/.
2. M. Silion, D. Hritcu and M. I. Popa, *J. Optoelectron. Adv. Mater.*, 2010, **12**, 2151.
3. M. Y. Ghotbi and M. Z. bin Hussein, *J. Phys. Chem. Solids*, 2010, **71**, 1565.
4. T. Itoh, T. Shichi, T. Yui and K. Takagi, *Langmuir*, 2005, **21**, 3217.
5. L. Peng, J. H. Yu, J. Y. Li, Y. Li and R. R. Xu, *Chem. Mater.*, 2005, **17**, 2101.
6. W. L. Hemme, W. Fujita, K. Awaga and H. Eckert, *J. Sol. Stat. Chem.*, 2009, **182**, 3330.
7. M. Darder, A. I. Ruiz, P. Aranda, H. Van Damme and E. Ruiz-Hitzky, *Curr. Nanosci.*, 2006, **2**, 231.
8. S. Ogata, I. Miyazaki, Y. Tasaka, H. Tagaya, J. Kadokawa and K. Chiba, *J. Mater. Chem.*, 1998, **8**, 2813.
9. S. Ogata, Y. Tasaka, H. Tagaya, J. Kadokawa and K. Chiba, *Chem. Letts.*, 1998, 237.
10. F. Menendez, A. Espina, C. Trobajo and J. Rodriguez, *Mater. Res. Bull.*, 1990, **25**, 1531.
11. A. Hayashi, Y. Nakabayashi, J. Yasutomi, H. Nakayama and M. Tsuhako, *Bull. Chem. Soc. Jpn.*, 2006, **79**, 262.
12. A. Clearfield and U. Costantino, *Compre. Supramol. Chem.*, Volume 7, 1996.
13. U. Costantino, *J. Chem. Soc. - Dalt. Trans.*, 1979, 402.
14. B. G. Shpeizer, P. Sylvester, R. A. Cahill and A. Clearfield, *Chem. Mater.*, 1999, **11**, 1201.
15. R. C. Yeates, S. M. Kuznicki, L. B. Lloyd and E. M. Eyring, *J. Inorg. & Nucl. Chem.*, 1981, **43**, 2355.
16. M. Danjo, Y. Mizuguchi, Y. Yagita, K. Kakiguchi, T. Yanagida and M. Tsuhako, *Bull. Chem. Soc. Jpn.*, 1997, **70**, 3011.
17. T. Kijima, Y. Sekikawa and S. Ueno, *J. Inorg. & Nucl. Chem.*, 1981, **43**, 849.
18. T. Kijima and S. Ueno, *J. Chem. Soc. - Dalt. Trans.*, 1986, 61.
19. T. Kijima, S. Ueno and M. Goto, *J. Chem. Soc. - Dalt. Trans.*, 1982, 2499.
20. Y. Ding, D. J. Jones, P. Maireles-Torres and J. Roziere, *Chem Mater.*, 1995, **7**, 562.
21. P. G. Slade, M. I. Telleria and E. W. Radoslovich, *Clays & Clay Miner.*, 1976, **24**, 134.
22. F. Kanamaru and V. Vand, *Am. Mineralog.*, 1970, **55**, 1550.
23. V. V. Guliants, J. B. Benziger and S. Sundaresan, *Chem. Mater.*, 1994, **6**, 353.
24. R. M. Tindwa, D. K. Ellis, G. Z. Peng and A. Clearfield, *J. Chem. Soc.-Farad. Trans. I*, 1985, **81**, 545.
25. E. Rodriguez-castellon, S. Bruque and A. Rodriguez-garcia, *J. Chem. Soc. - Dalt. Trans.*, 1985, 213.
26. G. Alberti and U. Costantino, *Intercal. Chem.*, 1982, 147.
27. N. J. Checker, Ph.D thesis, University of Birmingham, 2006.
28. A. Hayashi, H. Nakayama, M. Tsuhako, T. Eguchi and N. Nakamura, *J. Inclus. Phenom. Macrocyc. Chem.*, 1999, **34**, 401.
29. H. Tagaya, S. Ogata, S. Nakano, J. I. Kadokawa, M. Karasu and K. Chiba, *J. Incl. Phenom. Mol. Recogn. Chem.*, 1998, **31**, 231.
30. G. Alberti, *Acc. of Chem. Res.*, 1978, **11**, 163.
31. A. Clearfield and S. Cheng, *J. Inorg. & Nucl. Chem.*, 1980, **42**, 1341.
32. G. Alberti, U. Costanti and M. Pellicci, *J. Inorg. & Nucl. Chem.*, 1973, **35**, 1327.
33. A. Clearfield and J. M. Kalnins, *J. Inorg. & Nucl. Chem.*, 1976, **38**, 849.
34. S. Ahrland, J. Albertss, A. Oskarsso and A. Niklasso, *J. Inorg. & Nucl. Chem.*, 1970, **32**, 2069.

35. A. Hayashi, H. Saimen, N. Watanabe, H. Kimura, A. Kobayashi, H. Nakayama and M. Tsuhako, *Langmuir*, 2005, **21**, 7238.
36. B. Shpeizer, D. M. Poojary, K. Ahn, C. E. Runyan and A. Clearfield, *Science*, 1994, **266**, 1357.
37. A. Kudelski, *J. Raman Spectrosc.*, 2003, **34**, 853.

Chapter 7

Conclusions and Further Work

The studies presented throughout this thesis have shown AlTP to be an excellent host for both ion exchange and intercalation, often with properties superior to those of the much studied α-ZrP phases.

Chapter three describes how the alkali metals Na, K, Rb and Cs and silver all readily formed fully exchanged phases with AlTP without the need for high pHs as with α-ZrP. TGA showed the alkali metal exchange phases formed thermodynamically stable phases with two waters of crystallisation and metastable phases with differing numbers of waters, one in the cases of potassium, rubidium and caesium and four in the case of sodium. Unit cells were identified for these phases and showed *b* and *c* values consistent with the AlTP host, but with the *a* parameter more than doubled as adjacent layers became crystallographically distinct from each other. A linear relationship was found to exist between the cationic radii and the d-spacing of the d_{200} peak and unit cell volume suggested the different exchanged phases are either isostructural or have similar cation sites. The sodium, potassium and rubidium phases all decompose between 500-550 °C to form MPO_3 and $AlMP_2O_7$ which further decomposes to MPO_3 and $AlPO_4$, whilst the caesium phase transforms into another previously reported layered phase of the same stoichiometry[1, 2], giving a new synthetic route for this phase.

Chapter three also describes that lithium exchange into AlTP possessed a third level of lithium loading with a greater lithium content than the two previously reported phases[3]. This third loading level, formed through the addition of hydroxide to the exchanging solution, has around 50% of the maximum possible exchange, which is around 40% higher than previously reported. The amount of lithium could be increased to around 70% by increasing the lithium to aluminium ratio to 50:1, or by refreshing the exchange solution. Increasing the ratio higher and the solution refreshing method caused significant breakdown of the crystallinity of the system. This higher loading level could be achieved with around 60% exchange by refreshing an exchanging solution of LiCl and does not breakdown the phase's crystallinity.

Chapter four determined the crystal structure of two of the fully ion exchanged phases, rubidium and caesium, through Rietveld and fourier difference analysis of X-ray and neutron diffraction data. The two phases were found to be isostructural to one another, with the structure now having the space group C2/c as a result of the phosphate layers being staggered half a unit cell along [010] with respect to each other. The inter-lamellar waters were found to run along the face of each layer, hydrogen bonding between terminal oxygens on the same layer rather than to terminal oxygens on adjacent layers as in the AlTP host. The cations were found to sit in 14 coordinate sites, bonding to four terminal oxygens and five bridging oxygens from one layer, forming an 'oxygen well', and a terminal oxygen from the adjacent layer and four inter-lamellar water molecules. The cations now appear to hold the adjacent phosphate layers together electrostatically.

The crystal structures of the sodium, potassium and silver exchanged phases remain unsolved. These are believed to be similar to the rubidium and caesium crystal structures, but further studies are required to elucidate the individual structures. These studies may include

further Rietveld studies using joint neutron XRD/synchrotron refinements, supplemented by pair distribution function analysis.

Chapter five showed that the ion exchange of divalent cations into AlTP was possible, with copper, manganese and calcium showing the most evidence of exchange. Decomposition products of $M_2P_2O_7$, $Al(PO_3)_3$ and $AlPO_4$ for the transition metal phases and β-$Ca(PO_3)_2$ and $AlPO_4$ for calcium, suggest significant exchange had occurred. To further support this EDX showed the AlTP with copper was found to have an aluminium to copper ratio of around 1:1. Further studies to investigate the composition of these phases using techniques such as X-ray fluorescence spectroscopy or flame photometry/atomic absorbance spectroscopy are necessary.

Strontium and zinc also showed evidence of ion exchange in their XRD patterns and decomposition products, but residual intercalated AlTP suggests that the exchange is slower than with the other successful divalent exchanges. Further studies are required to determine optimal conditions to push this exchange towards completion. Iron and magnesium show little evidence of exchange in their XRD patterns, but their decomposition products were consistent with those of the other divalent exchanged phases. Further investigations into whether these ions have exchanged or not is required.

Chapter 6 demonstrated the excellent intercalation behaviour of AlTP. Monoamines were readily intercalated into AlTP, at around the theoretical maximum amount, with an intercalation angle of 56(2) °. This angle is consistent with monoamine intercalation in numerous other layered phosphates[4-6]. Secondary and tertiary amines are also able to intercalate into AlTP, forming bilayers with around 50% of the intercalation potential achieved. This lower level of insertion is believed to be a result of steric blockage of binding sites by the ‘arms’ of the secondary and tertiary amines.

Studies have also shown the basicity of the organic molecule affects its intercalation potential with a cut off point of pK_b ~ 9.5 above which intercalation does not occur in AlTP, similar to α-ZrP. Sterics effects also have also been shown to play a major role in the intercalation potential of organic molecules in AlTP, with molecules with pK_b values much lower than the cut off point being unable to intercalate on steric grounds.

The amino acids, 6-Aminohexanoic and 4-aminobutanoic acid, have been successfully intercalated into AlTP. These products possess more complex XRD patterns than other intercalated phases, suggesting increased inter-lamellar ordering, which appears to result from the formation of bilayers with hydrogen bonding interactions between the acid groups of the molecules in the inter-lamellar region. Future studies are required to investigate the possibility of utilising the acid to acid region for the chelation of cations between these intercalated organic molecules. This may have the potential to form metal oxide layers in between the phosphate layers, through thermal decomposition of the organic components. Such nano-composite structures offer immense potential for various properties. To date such a structure has been suggested in one α-ZrP study but AlTP may offer more potential given the flexibility in metals which form the AlTP structure.

In an extra dimension to the intercalation studies, AlTP-Ag has also shown to be an excellent host for the intercalation of organic molecules, displaying its own distinct intercalation properties compared to its precursor AlTP. To our knowledge there are no reports in the literature of intercalation into ion exchanged forms of the other layered phosphates, so the ability to do so, with its own distinct properties, suggests an overlooked branch of intercalation chemistry for layered phosphates exists.

Monoamines intercalate into AlTP-Ag in similar amounts to AlTP. The intercalation angle for the AlTP-Ag phase, however, is much greater (81(7) °) than previously observed in other layered phosphates. AlTP-Ag also has the ability to intercalate monothiols, a property

the original AlTP host does not possess. These intercalate in a similar fashion to monoamines and have an intercalation angle of 69(2) °. D-spacings of the d_{100} peaks are considerably smaller than those of their amine equivalents suggesting a different method of bonding to the thiols, potentially involving the formation of a covalent bond between silver and sulphur.

Secondary and tertiary amines only partially intercalate into AlTP-Ag, with significant amounts of the parent material remaining after the reaction. This may be be a result of intercalation occurring around the crystal edges, which then blocks the inter-lamellar region, creating two crystallographically distinct regions.

Interestingly, cysteine was able to intercalate into AlTP-Ag, an intercalation not possible in the pure AlTP host. As with other amino acids, the XRD pattern showed evidence of increased order within the inter-lamellar region. HCN elemental analysis suggests 90% intercalation is achieved, assuming a maximum with a silver to cysteine ratio of 1:1. The d_{100} peak only showed a small increase on intercalation which suggests bilayers being formed parallel to the phosphate layers. The incorporation of cysteine into AlTP-Ag shows despite the previous lack of research into the MTP phases, they have intercalation potentials almost equal to and often surpassing those of the α type metal phosphates.

An area of further work is to expand these findings to the other members of the $M^{III}P_3O_{10}\cdot 2H_2O$ family to ascertain if the ion exchange and intercalation properties shown by AlTP are family-wide. For the members of the family which show magnetic properties (Fe and Mn), it would be interesting to observe if these are altered by ion exchange or intercalation. Ion exchanging of cations with variable oxidation states into some of the transition metal phases themselves with potential for variable oxidation states may also prove interesting.

References

1. R. N. Devi and K. Vidyasagar, *J. Chem. Soc. - Dalt. Trans.*, 2000, 1605.
2. A. Guesdon, E. Daguts and B. Raveau, *J. Sol. Stat. Chem.*, 2002, **167**, 258.
3. S. K. Rishi, Ph.D thesis, University of Birmingham, 2006.
4. V. V. Guliants, J. B. Benziger and S. Sundaresan, *Chem. Mater.*, 1994, **6**, 353.
5. R. M. Tindwa, D. K. Ellis, G. Z. Peng and A. Clearfield, *J. Chem. Soc.-Farad. Trans. I*, 1985, **81**, 545.
6. F. Menendez, A. Espina, C. Trobajo and J. Rodriguez, *Mater. Res. Bull.*, 1990, **25**, 1531.

Appendix 1: XRD Patterns of Monovalent Cation Exchanged AlTP

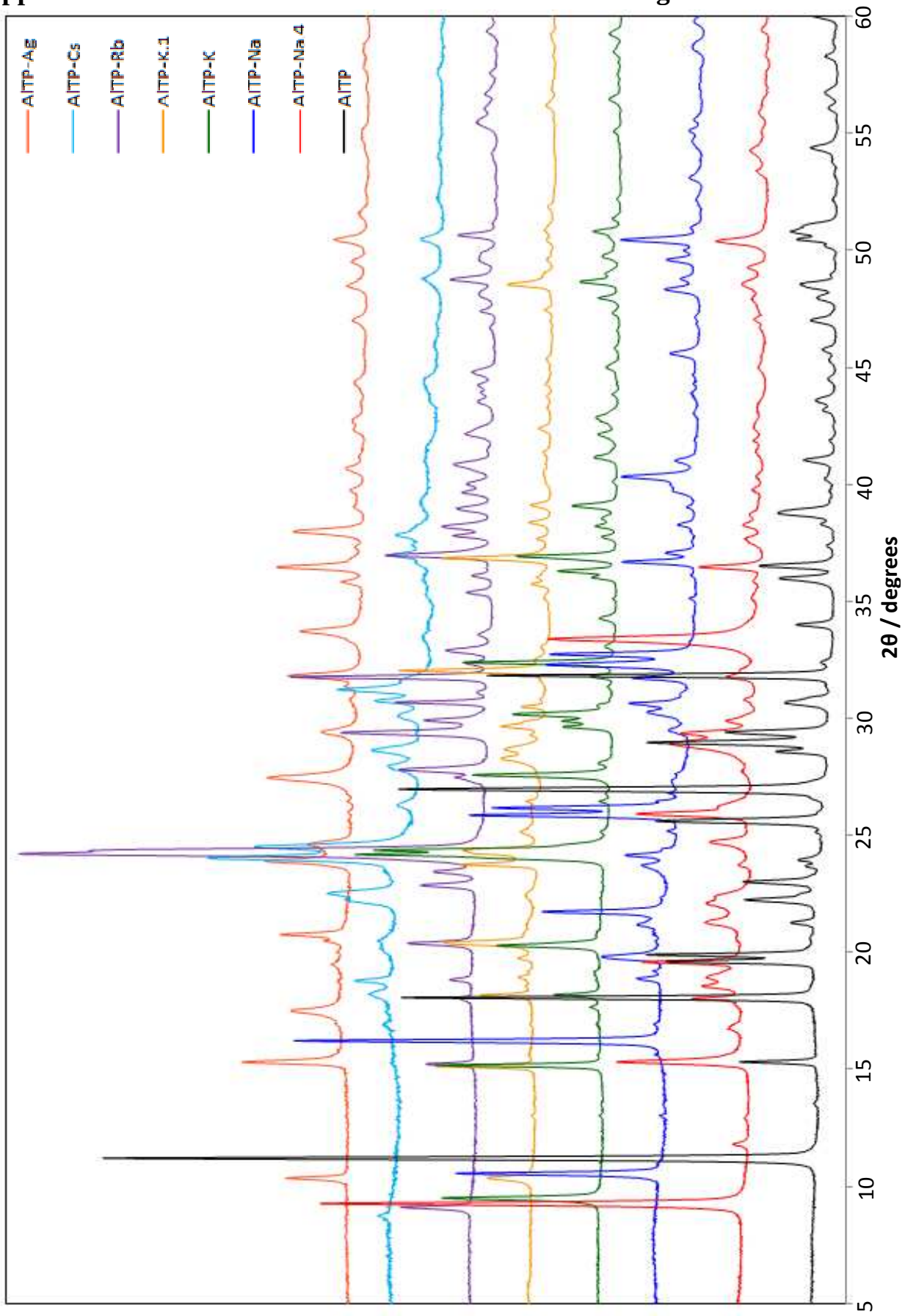

Appendix 2: Flame Photometry Data

A2.1 Sodium Data

A2.1.1 Raw Data

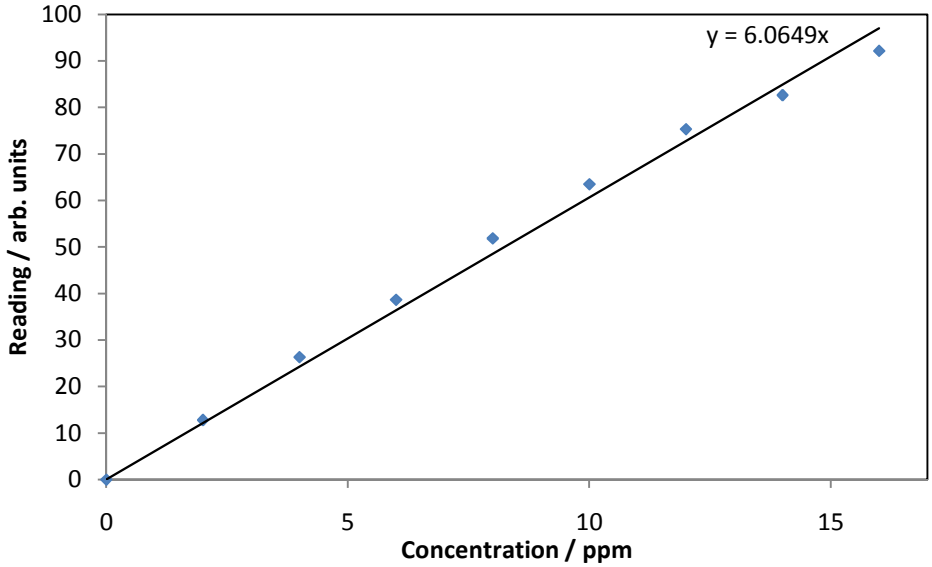

Sample	Reading				Concentration / ppm
	1	2	3	Average	
AlTP-Na	85	84	84	13.9	13.91
AlTP-Na·4	75	75	74.5	12.4	12.34
AlTP-K	1	1	0	0.2	0.11
AlTP-Rb	0	0	0	0.0	0.00
AlTP-Cs	0	1	0	0.2	0.05
AlTP-Ag	0	0	0	0.0	0.00

A2.1.2 Calculations

Sample	Mass / mg	Concentration / ppm	Mass Na / mg	Moles Na	Moles Na, Full Exchange*	Percentage Exchange
AlTP-Na	10.9	13.91	1.39	6.05×10^{-5}	6.02×10^{-5}	100(1)
AlTP-Na·4	10.1	12.34	1.23	5.37×10^{-5}	5.08×10^{-5}	105(2)
AlTP-K	11.1	0.11	0.01	4.78×10^{-7}	6.13×10^{-5}	1(1)
AlTP-Rb	10.5	0.00	0.00	0	5.8×10^{-5}	0
AlTP-Cs	10.2	0.05	0.01	2.39×10^{-7}	5.64×10^{-5}	0.4(1)
AlTP-Ag	10.6	0.00	0.00	0	5.86×10^{-5}	0

*This is the moles of sodium if the fully exchanged form of $AlNa_2P_3O_{10}\cdot nH_2O$ was achieved

A2.2 Lithium Data

A.2.2.1 Raw Data

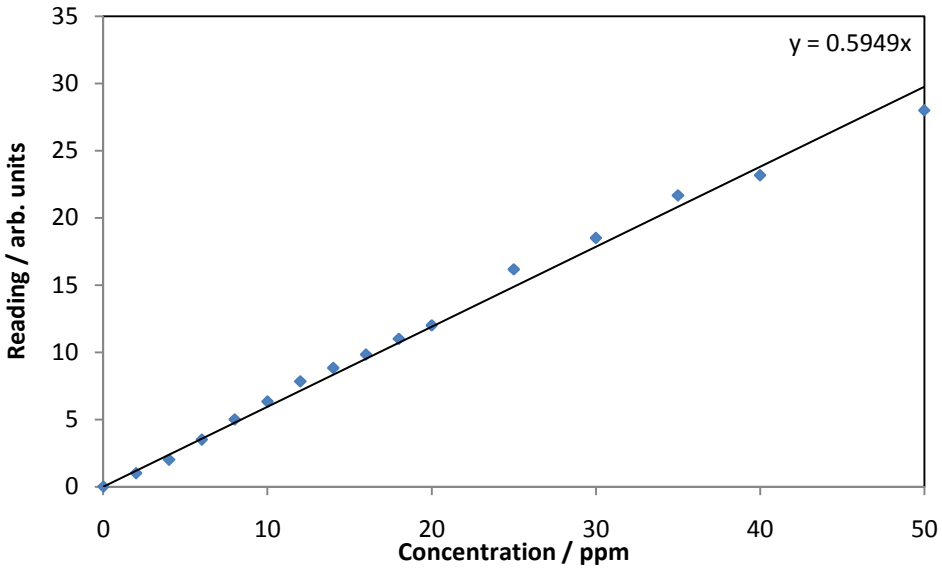

Sample	Reading				Concentration / ppm
	1	2	3	Average	
100%LiCl	3.0	3.0	3.0	3.0	5.04
90:10 LiCl:LiOH	13.0	13.0	13.0	13.0	21.85
80:20 LiCl:LiOH	14.5	14.0	14.0	14.2	23.81
70:30 LiCl:LiOH	15.5	16.0	15.5	15.7	26.33
60:40 LiCl:LiOH	13.0	13.0	13.0	13.0	21.85
50:50 LiCl:LiOH	20.0	20.0	20.0	20.0	33.62
40:60 LiCl:LiOH	15.5	15.0	15.0	15.2	25.49
30:70 LiCl:LiOH	22.5	22.5	22.0	22.3	37.54
20:80 LiCl:LiOH	22.5	22.5	22.0	22.3	37.54
10:90 LiCl:LiOH	24.0	24.0	23.0	23.7	39.78
100% LiOH	19.0	19.5	19.0	19.2	32.22

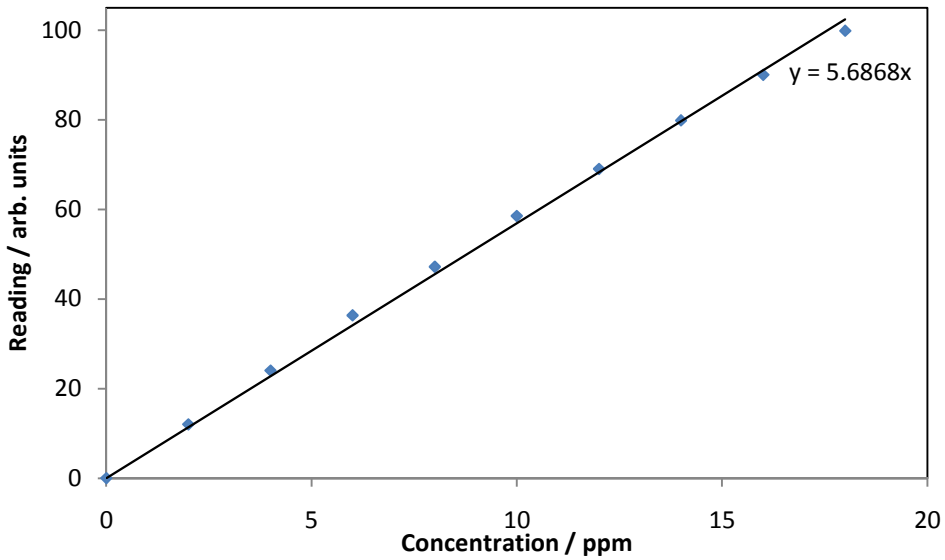

Sample	Reading				Concentration / ppm
	1	2	3	Average	
100%LiCl					
1 refresh	29.5	29	28.5	29	5.10
2 refresh	39.5	39.5	39.5	39.5	6.95
3 refresh	58	57	57.5	57.5	10.11
80:20 LiCl:LiOH					
3 refresh	71	71.5	71.5	71.3	71

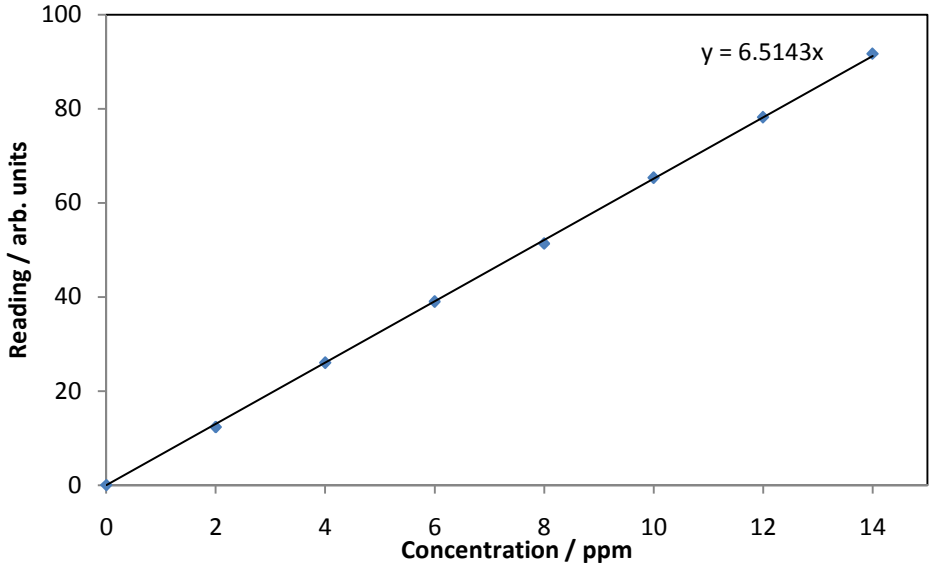

Sample	Reading				Concentration / ppm
	1	2	3	Average	
90:10 LiCl:LiOH					
1 refresh	72	73	74	73.0	11.21
2 refresh	70	69	69	69.3	10.64
3 refresh	79	79	79	79.0	12.13

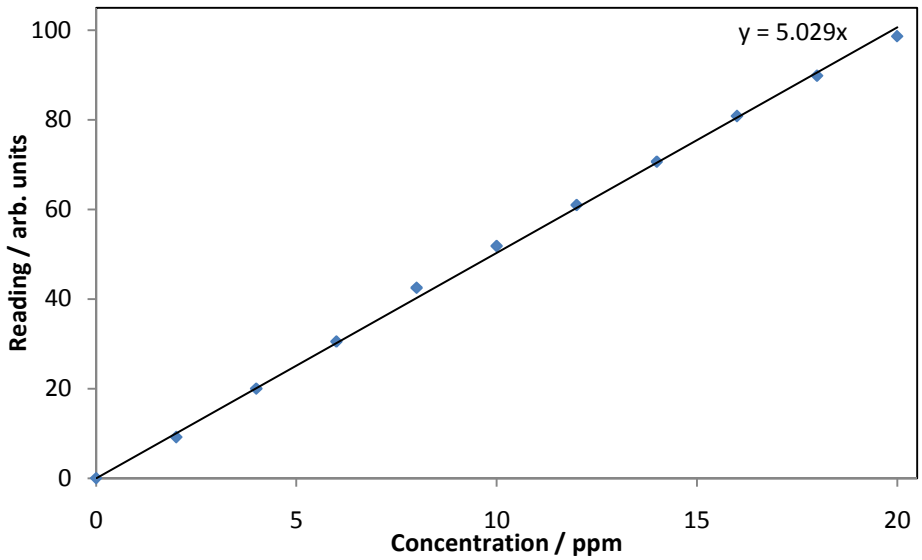

Sample	Reading				Concentration / ppm
	1	2	3	Average	
10:1 Li:Al	16	16	16	16.0	3.18
50:1 Li:Al	34.5	34.5	34.5	34.5	6.86
100:1 Li:Al	47	47.5	47.5	47.3	9.41

A.2.2.2 Calculations

Sample	Mass / mg	Concentration / ppm	Mass Li / mg	Moles Li	Moles Li, Full Exchange*	Percentage Exchange
100% LiCl	108.9	5.04	0.50	7.27×10^{-5}	1.37×10^{-3}	11(1)
1 refresh	39.5	5.10	0.51	7.35×10^{-5}	4.79×10^{-4}	31(2)
2 refresh	43	6.95	0.69	1.00×10^{-4}	5.22×10^{-4}	38(1)
3 refresh	40.4	10.11	1.01	1.46×10^{-4}	4.90×10^{-4}	59(3)
90:10 LiCl:LiOH	100.2	21.85	2.19	3.15×10^{-4}	1.26×10^{-3}	50(1)
1 refresh	40.3	11.21	1.12	1.61×10^{-4}	5.07×10^{-4}	64(1)
2 refresh	39.5	10.64	1.06	1.53×10^{-4}	4.97×10^{-4}	62(1)
3 refresh	40.4	12.13	1.21	1.75×10^{-4}	5.08×10^{-4}	69(1)
80:20 LiCl:LiOH	99.5	23.81	2.38	3.43×10^{-4}	1.25×10^{-3}	55(2)
3 refresh	40.2	12.54	1.25	1.81×10^{-4}	4.88×10^{-4}	74(3)
70:30 LiCl:LiOH	100.3	26.33	2.63	3.79×10^{-4}	1.26×10^{-3}	60(2)
60:40 LiCl:LiOH	99.4	21.85	2.19	3.15×10^{-4}	1.25×10^{-3}	50(1)
50:50 LiCl:LiOH	99.6	33.62	3.36	4.84×10^{-4}	1.25×10^{-3}	77(1)
40:60 LiCl:LiOH	99.6	25.49	2.55	3.67×10^{-4}	1.25×10^{-3}	59(2)
30:70 LiCl:LiOH	102	37.54	3.75	5.41×10^{-4}	1.28×10^{-3}	84(2)

20:80 LiCl:LiOH	99.6	37.54	3.75	5.41×10^{-4}	1.25×10^{-3}	86(2)
10:90 LiCl:LiOH	96	39.78	3.98	5.73×10^{-4}	1.21×10^{-3}	95(3)
100% LiOH	101.5	32.22	3.22	4.64×10^{-4}	1.28×10^{-3}	73(2)
10:1 Li:Al	23.9	3.18	0.32	4.58×10^{-5}	1.45×10^{-4}	32(5)
50:1 Li:Al	23.5	6.86	0.69	9.89×10^{-5}	1.43×10^{-4}	69(1)
100:1 Li:Al	23.5	9.41	0.94	1.36×10^{-4}	1.43×10^{-4}	95(4)

*This is the moles of lithium if the fully exchanged form of $AlLi_2P_3O_{10}\cdot 2H_2O$ was achieved

Appendix 3-1: CELL Refinement of AlTP-Na

Cell parameters: a = 17.621(5) Å, b = 4.915(1) Å, c = 11.619(3) Å, β = 107.89(1) °.

Observed 2-θ (°)	Calculated 2-θ (°)	h k l	Observed d-spacing	Calculated d-spacing	Difference	Weight	Sin^2 (obs – calc)
10.493	10.519	2 0 0	8.424	8.403	-0.021	1	-0.00004
16.160	16.232	-2 0 2	5.480	5.456	-0.024	1	-0.00018
18.818	18.776	-1 1 0	4.712	4.722	0.011	1	0.00012
19.745	19.728	0 1 1	4.493	4.497	0.004	1	0.00005
21.136	21.152	-4 0 0	4.200	4.197	-0.003	1	-0.00005
21.677	21.765	2 0 2	4.096	4.080	-0.016	1	-0.00028
23.649	23.672	-1 1 2	3.759	3.755	-0.004	1	-0.00008
24.104	24.104	0 0 3	3.689	3.689	0.000	1	0.00000
25.811	25.823	1 1 2	3.449	3.447	-0.002	1	-0.00005
26.120	26.124	-3 1 2	3.409	3.408	-0.001	1	-0.00002
27.261	27.182	-4 1 1	3.269	3.278	0.009	1	0.00032
29.449	29.391	-1 1 3	3.031	3.037	0.006	1	0.00025
30.212	30.263	0 1 3	2.956	2.951	-0.005	1	-0.00022
30.580	30.556	-3 1 3	2.921	2.923	0.002	1	0.00011
31.679	31.713	3 1 2	2.822	2.819	-0.003	1	-0.00016
32.253	32.265	-5 1 0	2.773	2.772	-0.001	1	-0.00005
32.696	32.827	-4 0 4	2.737	2.726	-0.011	1	-0.00062
36.650	36.511	0 2 0	2.450	2.459	0.009	1	0.00072
37.032	37.044	4 0 3	2.426	2.425	-0.001	1	-0.00006
38.242	38.196	1 2 1	2.352	2.354	0.003	1	0.00025
39.702	39.708	2 2 1	2.268	2.268	0.000	1	-0.00003
40.289	40.330	6 0 2	2.237	2.235	-0.002	1	-0.00023
40.968	41.038	-8 0 2	2.201	2.198	-0.004	1	-0.00040
41.868	41.895	-7 1 0	2.156	2.155	-0.001	1	-0.00016
45.559	45.539	1 2 3	1.989	1.990	0.001	1	0.00012
47.122	47.071	-8 1 0	1.927	1.929	0.002	1	0.00033
48.295	48.284	4 1 4	1.883	1.883	0.000	1	0.00007
48.752	48.699	-1 2 4	1.866	1.868	0.002	1	0.00035
49.565	49.570	0 2 4	1.838	1.837	0.000	1	-0.00004
49.960	49.978	3 2 3	1.824	1.823	-0.001	1	-0.00012
50.419	50.556	6 2 -3	1.809	1.804	-0.005	1	-0.00092
50.931	51.052	4 1 -6	1.792	1.788	-0.004	1	-0.00082
52.142	52.104	-5 1 6	1.753	1.754	0.001	1	0.00026
53.068	53.003	0 1 6	1.724	1.726	0.002	1	0.00045
54.652	54.667	10 0 0	1.678	1.678	0.000	1	-0.00011
55.089	55.089	-4 2 5	1.666	1.666	0.000	1	0.00000
55.559	55.535	6 2 2	1.653	1.653	0.001	1	0.00017
58.645	58.637	-8 1 6	1.573	1.573	0.000	1	0.00006
59.764	59.788	7 2 2	1.546	1.546	-0.001	1	-0.00018
61.178	61.117	-11 1 3	1.514	1.515	0.001	1	0.00046
61.619	61.600	0 1 7	1.504	1.504	0.000	1	0.00014
62.888	62.943	1 3 3	1.477	1.475	-0.001	1	-0.00043
64.420	64.402	8 2 2	1.445	1.446	0.000	1	0.00014
65.617	65.618	-7 2 6	1.422	1.422	0.000	1	-0.00001

67.273	67.267	-3 1 8	1.391	1.391	0.000	1	0.00005
67.995	67.999	5 3 2	1.378	1.378	0.000	1	-0.00004
68.511	68.503	-2 2 7	1.368	1.369	0.000	1	0.00006
71.550	71.522	-11 0 7	1.318	1.318	0.000	1	0.00023
72.231	72.164	-7 3 4	1.307	1.308	0.001	1	0.00056
75.392	75.364	8 2 4	1.260	1.260	0.000	1	0.00024
76.021	76.016	-3 3 6	1.251	1.251	0.000	1	0.00005
77.078	77.084	11 1 3	1.236	1.236	0.000	1	-0.00005
77.936	77.945	0 3 6	1.225	1.225	0.000	1	-0.00007
78.532	78.551	-6 3 6	1.217	1.217	0.000	1	-0.00016
79.188	79.253	8 3 2	1.209	1.208	-0.001	1	-0.00056
80.236	80.241	-14 1 1	1.195	1.195	0.000	1	-0.00004
81.119	81.133	-13 2 2	1.185	1.184	0.000	1	-0.00012
82.061	82.052	-10 3 4	1.173	1.174	0.000	1	0.00008
84.371	84.362	-7 0 10	1.147	1.147	0.000	1	0.00008
85.394	85.379	-5 4 3	1.136	1.136	0.000	1	0.00013
85.961	85.962	-4 1 10	1.130	1.130	0.000	1	-0.00001
87.103	87.114	3 2 8	1.118	1.118	0.000	1	-0.00009
90.180	90.150	13 1 3	1.088	1.088	0.000	1	0.00027
90.462	90.458	-16 0 5	1.085	1.085	0.000	1	0.00004
93.435	93.494	-15 1 7	1.058	1.058	-0.001	1	-0.00051
94.098	94.089	4 4 4	1.052	1.052	0.000	1	0.00008
94.278	94.336	-5 2 10	1.051	1.050	0.000	1	-0.00051
95.575	95.588	-7 4 5	1.040	1.040	0.000	1	-0.00011
96.039	96.025	-2 2 10	1.036	1.036	0.000	1	0.00012
99.401	99.411	-10 0 11	1.010	1.010	0.000	1	-0.00008

R FACTOR 0.00000565

Appendix 3-2: CELL Refinement of AlTP-K

Cell parameters: a = 18.664(8) Å, b = 4.885(1) Å, c = 11.701(3) Å and β = 91.87(2) °.

Observed 2-θ (°)	Calculated 2-θ (°)	h k l	Observed d-spacing	Calculated d-spacing	Difference	Weight	Sin^2 (obs – calc)
9.440	9.461	2 0 0	9.361	9.340	-0.021	1	-0.00003
15.122	15.126	0 0 2	5.854	5.853	-0.001	1	-0.00001
17.604	17.609	-2 0 2	5.034	5.033	-0.001	1	-0.00001
18.122	18.139	2 0 2	4.891	4.887	-0.004	1	-0.00005
20.244	20.239	-4 0 1	4.383	4.384	0.001	1	0.00002
24.139	24.169	-1 1 2	3.684	3.679	-0.004	1	-0.00011
24.315	24.294	-3 1 1	3.658	3.661	0.003	1	0.00007
26.392	26.467	-4 1 0	3.374	3.365	-0.009	1	-0.00029
27.538	27.564	-3 1 2	3.236	3.233	-0.003	1	-0.00011
29.594	29.618	-1 1 3	3.016	3.014	-0.002	1	-0.00011
29.842	29.864	1 1 3	2.992	2.989	-0.002	1	-0.00010
30.137	30.173	-5 1 0	2.963	2.960	-0.003	1	-0.00016
30.498	30.538	0 0 4	2.929	2.925	-0.004	1	-0.00018
31.742	31.734	-2 0 4	2.817	2.817	0.001	1	0.00004
32.340	32.347	2 0 4	2.766	2.765	-0.001	1	-0.00003
33.025	33.030	6 0 2	2.710	2.710	0.000	1	-0.00002
34.241	34.225	-7 0 1	2.617	2.618	0.001	1	0.00008
35.978	36.004	-1 1 4	2.494	2.492	-0.002	1	-0.00013
36.249	36.280	1 1 4	2.476	2.474	-0.002	1	-0.00016
36.886	36.854	-2 1 4	2.435	2.437	0.002	1	0.00017
37.712	37.648	-5 1 3	2.383	2.387	0.004	1	0.00034
38.184	38.158	1 2 1	2.355	2.357	0.002	1	0.00014
38.505	38.492	-7 1 0	2.336	2.337	0.001	1	0.00007
39.042	39.059	-7 1 1	2.305	2.304	-0.001	1	-0.00009
41.118	41.152	-7 1 2	2.194	2.192	-0.002	1	-0.00020
42.089	42.050	6 1 3	2.145	2.147	0.002	1	0.00023
42.814	42.768	4 2 1	2.110	2.113	0.002	1	0.00027
43.799	43.814	4 0 5	2.065	2.065	-0.001	1	-0.00009
44.969	44.965	-3 1 5	2.014	2.014	0.000	1	0.00003
45.778	45.800	7 1 3	1.980	1.980	-0.001	1	-0.00013
46.553	46.542	0 0 6	1.949	1.950	0.000	1	0.00007
47.294	47.278	-2 0 6	1.920	1.921	0.001	1	0.00010
47.933	47.939	2 0 6	1.896	1.896	0.000	1	-0.00004
48.625	48.557	4 2 3	1.871	1.873	0.002	1	0.00045
48.966	48.964	-5 1 5	1.859	1.859	0.000	1	0.00002
49.717	49.691	10 0 1	1.832	1.833	0.001	1	0.00018
50.774	50.765	9 1 2	1.797	1.797	0.000	1	0.00006
51.317	51.316	3 2 4	1.779	1.779	0.000	1	0.00000
55.052	55.086	9 0 4	1.667	1.666	-0.001	1	-0.00024
56.424	56.399	7 1 5	1.629	1.630	0.001	1	0.00018
58.460	58.464	-9 0 5	1.577	1.577	0.000	1	-0.00003
59.226	59.271	-8 2 3	1.559	1.558	-0.001	1	-0.00033
60.902	60.891	0 2 6	1.520	1.520	0.000	1	0.00008
63.804	63.800	-3 3 3	1.458	1.458	0.000	1	0.00003
64.846	64.827	-7 0 7	1.437	1.437	0.000	1	0.00015
65.873	65.904	0 3 4	1.417	1.416	-0.001	1	-0.00024
67.134	67.149	1 1 8	1.393	1.393	0.000	1	-0.00012

R FACTOR 0.00000117

Appendix 3-3: CELL Refinement of AlTP-K·1

Cell parameters: a = 17.004(9) Å, b = 4.880(2) Å, c = 11.711(5) Å and β = 91.23 °.

Observed 2-θ (°)	Calculated 2-θ (°)	h k l	Observed d-spacing	Calculated d-spacing	Difference	Weight	Sin^2 (obs – calc)
10.342	10.348	2 0 0	8.547	8.542	-0.005	1	-0.00001
15.065	15.070	0 0 2	5.876	5.874	-0.002	1	-0.00001
18.100	18.112	0 1 0	4.897	4.894	-0.003	1	-0.00003
18.894	18.852	-1 1 0	4.693	4.703	0.010	1	0.00012
19.689	19.641	0 1 1	4.505	4.516	0.011	1	0.00014
20.324	20.286	-1 1 1	4.366	4.374	0.008	1	0.00012
20.383	20.370	1 1 1	4.353	4.356	0.003	1	0.00004
22.292	22.337	4 0 1	3.985	3.977	-0.008	1	-0.00015
23.699	23.665	0 1 2	3.751	3.757	0.005	1	0.00012
24.209	24.173	-1 1 2	3.673	3.679	0.005	1	0.00013
24.336	24.315	1 1 2	3.655	3.658	0.003	1	0.00008
25.106	25.082	-3 1 1	3.544	3.548	0.003	1	0.00009
28.266	28.292	-3 1 2	3.155	3.152	-0.003	1	-0.00011
28.675	28.660	3 1 2	3.111	3.112	0.002	1	0.00006
29.592	29.615	-1 1 3	3.016	3.014	-0.002	1	-0.00010
30.469	30.464	0 0 4	2.931	2.932	0.000	1	0.00002
31.992	32.006	-5 1 0	2.795	2.794	-0.001	1	-0.00007
32.979	33.063	5 1 1	2.714	2.707	-0.007	1	-0.00040
35.663	35.690	0 1 4	2.516	2.514	-0.002	1	-0.00014
36.805	36.830	-4 0 4	2.440	2.438	-0.002	1	-0.00013
37.641	37.603	4 0 4	2.388	2.390	0.002	1	0.00020
38.313	38.297	-2 2 0	2.347	2.348	0.001	1	0.00009
39.076	39.043	-2 2 1	2.303	2.305	0.002	1	0.00018
42.346	42.343	7 1 1	2.133	2.133	0.000	1	0.00001
44.263	44.263	7 0 3	2.045	2.045	0.000	1	0.00000
47.387	47.384	-7 1 3	1.917	1.917	0.000	1	0.00002
48.464	48.483	0 2 4	1.877	1.876	-0.001	1	-0.00012
49.524	49.573	-2 2 4	1.839	1.837	-0.002	1	-0.00033
51.803	51.807	-7 1 4	1.763	1.763	0.000	1	-0.00003
56.200	56.181	2 0 7	1.635	1.636	0.001	1	0.00014
56.828	56.818	-9 1 3	1.619	1.619	0.000	1	0.00007
59.138	59.132	1 3 2	1.561	1.561	0.000	1	0.00004

R FACTOR 0.0000005

Appendix 3-4: CELL Refinement of AlTP-Rb

Cell parameters: a = 19.506(15) Å, b = 4.872(3) Å, c = 11.799(8) Å and β = 91.73(4) °.

Observed 2-θ (°)	Calculated 2-θ (°)	h k l	Observed d-spacing	Calculated d-spacing	Difference	Weight	Sin^2 (obs – calc)
9.047	9.140	2 0 0	9.767	9.668	-0.099	1	-0.00013
15.164	15.087	0 0 2	5.838	5.867	0.029	1	0.00017
17.949	17.875	2 0 2	4.938	4.958	0.020	1	0.00020
18.782	18.834	-1 1 0	4.721	4.708	-0.013	1	-0.00015
20.340	20.351	1 1 1	4.363	4.360	-0.002	1	-0.00003
22.817	22.862	5 0 0	3.894	3.887	-0.008	1	-0.00015
23.392	23.378	-4 0 2	3.800	3.802	0.002	1	0.00005
24.153	24.231	3 1 1	3.682	3.670	-0.012	1	-0.00028
24.294	24.274	1 1 2	3.661	3.664	0.003	1	0.00007
27.433	27.500	6 0 0	3.249	3.241	-0.008	1	-0.00027
27.763	27.861	5 0 2	3.211	3.200	-0.011	1	-0.00040
29.336	29.388	-5 1 0	3.042	3.037	-0.005	1	-0.00022
29.863	29.798	-4 1 2	2.990	2.996	0.006	1	0.00028
30.643	30.549	5 1 1	2.915	2.924	0.009	1	0.00042
31.067	31.067	-6 0 2	2.876	2.876	0.000	1	0.00000
31.726	31.893	6 0 2	2.818	2.804	-0.014	1	-0.00077
32.303	32.185	7 0 0	2.769	2.779	0.010	1	0.00055
32.851	32.833	-5 1 2	2.724	2.726	0.001	1	0.00008
33.529	33.491	5 1 2	2.671	2.674	0.003	1	0.00018
35.333	35.261	-7 0 2	2.538	2.543	0.005	1	0.00036
36.056	36.066	1 1 4	2.489	2.488	-0.001	1	-0.00005
36.928	36.958	-5 1 3	2.432	2.430	-0.002	1	-0.00016
37.763	37.751	0 2 1	2.380	2.381	0.001	1	0.00006
38.154	38.120	-2 2 0	2.357	2.359	0.002	1	0.00018
38.915	38.964	2 2 1	2.312	2.310	-0.003	1	-0.00027
39.619	39.624	-8 0 2	2.273	2.273	0.000	1	-0.00003
39.973	39.964	-7 1 2	2.254	2.254	0.000	1	0.00005
40.808	40.741	7 1 2	2.209	2.213	0.003	1	0.00038
42.119	42.106	-4 2 1	2.144	2.144	0.001	1	0.00008
43.496	43.454	-7 1 3	2.079	2.081	0.002	1	0.00025
43.892	43.931	2 1 5	2.061	2.059	-0.002	1	-0.00024
44.191	44.149	-4 2 2	2.048	2.050	0.002	1	0.00025
44.745	44.753	8 1 2	2.024	2.023	0.000	1	-0.00005
47.361	47.449	6 2 1	1.918	1.915	-0.003	1	-0.00056
48.092	48.112	-9 1 2	1.890	1.890	-0.001	1	-0.00013
48.724	48.779	-10 0 2	1.867	1.865	-0.002	1	-0.00036
49.587	49.553	6 2 2	1.837	1.838	0.001	1	0.00023
50.611	50.627	4 0 6	1.802	1.802	-0.001	1	-0.00011
53.878	53.796	-5 2 4	1.700	1.703	0.002	1	0.00058
54.129	54.151	0 2 5	1.693	1.692	-0.001	1	-0.00016
55.441	55.381	6 0 6	1.656	1.658	0.002	1	0.00043
56.015	55.999	11 1 1	1.640	1.641	0.000	1	0.00011
56.664	56.676	12 0 0	1.623	1.623	0.000	1	-0.00009
57.534	57.523	1 3 1	1.601	1.601	0.000	1	0.00008
58.576	58.613	-3 3 0	1.575	1.574	-0.001	1	-0.00028
59.347	59.384	-3 1 7	1.556	1.555	-0.001	1	-0.00027

R FACTOR 0.00000354

Appendix 3-5: CELL Refinement of AlTP-Cs

Cell parameters: a = 20.390(21) Å, b = 4.871(4) Å, c = 11.677(9) Å and β = 95.28(6) °.

Observed 2-θ (°)	Calculated 2-θ (°)	h k l	Observed d-spacing	Calculated d-spacing	Difference	Weight	Sin^2 (obs – calc)
8.682	8.712	2 0 0	10.177	10.142	-0.035	1	-0.00004
16.875	16.857	-2 0 2	5.250	5.255	0.006	1	0.00005
18.168	18.208	0 1 0	4.879	4.868	-0.011	1	-0.00011
18.739	18.729	-1 1 0	4.732	4.734	0.002	1	0.00003
20.444	20.390	1 1 1	4.341	4.352	0.011	1	0.00016
22.206	22.153	-4 0 2	4.000	4.009	0.009	1	0.00017
22.467	22.481	-3 1 0	3.954	3.952	-0.002	1	-0.00005
23.988	23.968	-1 1 2	3.707	3.710	0.003	1	0.00007
24.456	24.485	1 1 2	3.637	3.633	-0.004	1	-0.00010
26.248	26.324	6 0 0	3.393	3.383	-0.010	1	-0.00029
27.902	27.920	5 0 2	3.195	3.193	-0.002	1	-0.00008
28.593	28.606	-5 1 0	3.119	3.118	-0.001	1	-0.00005
30.059	30.089	1 1 3	2.971	2.968	-0.003	1	-0.00013
30.698	30.649	-1 0 4	2.910	2.915	0.005	1	0.00022
31.182	31.199	-2 0 4	2.866	2.864	-0.002	1	-0.00008
31.565	31.562	-5 1 2	2.832	2.832	0.000	1	0.00001
33.466	33.494	-6 0 3	2.675	2.673	-0.002	1	-0.00013
36.937	36.918	8 0 1	2.432	2.433	0.001	1	0.00010
37.789	37.766	2 1 4	2.379	2.380	0.001	1	0.00013
44.330	44.298	8 1 2	2.042	2.043	0.001	1	0.00020
48.752	48.750	0 2 4	1.866	1.866	0.000	1	0.00001
50.444	50.466	-1 1 6	1.808	1.807	-0.001	1	-0.00015

R FACTOR 0.00000036

Appendix 3-6: CELL Refinement of AlTP-Ag

Cell parameters: a = 17.237(7) Å, b = 4.924(1) Å, c = 11.660(3) Å and β = 96.39(2) °.

Observed 2-θ (°)	Calculated 2-θ (°)	h k l	Observed d-spacing	Calculated d-spacing	Difference	Weight	Sin^2 (obs – calc)
10.298	10.285	2 0 0	8.583	8.594	0.011	1	0.00002
15.252	15.240	0 0 2	5.805	5.809	0.005	1	0.00003
17.437	17.446	-2 0 2	5.082	5.079	-0.003	1	-0.00002
19.423	19.373	2 0 2	4.566	4.578	0.012	1	0.00014
20.437	20.436	1 1 1	4.342	4.342	0.000	1	0.00000
20.707	20.690	4 0 0	4.286	4.290	0.004	1	0.00005
20.707	20.757	-2 1 0	4.286	4.276	-0.010	1	-0.00015
23.863	23.852	-1 1 2	3.726	3.728	0.002	1	0.00004
24.569	24.594	1 1 2	3.620	3.617	-0.004	1	-0.00009
27.415	27.428	-3 1 2	3.251	3.249	-0.001	1	-0.00005
29.359	29.330	-1 1 3	3.040	3.043	0.003	1	0.00012
29.359	29.350	3 1 2	3.040	3.041	0.001	1	0.00004
30.739	30.652	-1 0 4	2.906	2.914	0.008	1	0.00039
31.332	31.271	6 0 0	2.853	2.858	0.005	1	0.00028
31.770	31.759	-5 1 0	2.814	2.815	0.001	1	0.00005
31.770	31.827	1 0 4	2.814	2.809	-0.005	1	-0.00026
33.668	33.674	2 0 4	2.660	2.659	0.000	1	-0.00003
35.788	35.769	-1 1 4	2.507	2.508	0.001	1	0.00010
36.421	36.393	-6 1 1	2.465	2.467	0.002	1	0.00015
36.421	36.431	-2 1 4	2.465	2.464	-0.001	1	-0.00005
37.267	37.273	0 2 1	2.411	2.410	0.000	1	-0.00003
37.922	37.906	6 1 1	2.371	2.372	0.001	1	0.00009
39.014	39.019	2 2 1	2.307	2.307	0.000	1	-0.00003
39.707	39.711	0 2 2	2.268	2.268	0.000	1	-0.00002
39.707	39.745	1 0 5	2.268	2.266	-0.002	1	-0.00021
40.649	40.674	-2 2 2	2.218	2.216	-0.001	1	-0.00014
42.301	42.276	-4 2 0	2.135	2.136	0.001	1	0.00015
42.675	42.680	7 1 1	2.117	2.117	0.000	1	-0.00003
42.675	42.637	-5 1 4	2.117	2.119	0.002	1	0.00022
44.303	44.336	-4 2 2	2.043	2.041	-0.001	1	-0.00020
46.977	47.037	-5 2 2	1.933	1.930	-0.002	1	-0.00038
46.977	47.031	6 0 4	1.933	1.931	-0.002	1	-0.00034
48.446	48.443	0 2 4	1.877	1.878	0.000	1	0.00002
49.484	49.478	-4 0 6	1.840	1.841	0.000	1	0.00004
49.484	49.512	-7 1 4	1.840	1.839	-0.001	1	-0.00019
50.419	50.393	-1 1 6	1.809	1.809	0.001	1	0.00017
51.544	51.525	3 0 6	1.772	1.772	0.001	1	0.00013
57.784	57.795	2 0 7	1.594	1.594	0.000	1	-0.00008
58.751	58.748	0 1 7	1.570	1.570	0.000	1	0.00002
60.234	60.246	-3 3 2	1.535	1.535	0.000	1	-0.00009
60.829	60.817	-8 0 6	1.522	1.522	0.000	1	0.00009
62.730	62.683	-5 3 0	1.480	1.481	0.001	1	0.00037

R FACTOR 0.00000110

Appendix 4: Bond Valence Sum Data

A4.1 Bond Valence Sum Theory

The bond valence sum method[1] states that the valence (V) of an atom in a compound is a sum of the individual bond valences (v_i) surrounding the atom, Equation 1. Individual bond valences are calculated from observed bond lengths (R_i), ideal bond lengths (R_0) and an empirical constant (b) usually 0.37, via Equation 2. If the calculated valence equals the expected valence it is an indication the coordination environment for that atom is sensible.

$$V = \sum (v_i) \qquad \textbf{Equation 1}$$

$$v_i = exp\left(\frac{R_0 - R_i}{b}\right) \qquad \textbf{Equation 2}$$

A4.2 AlTP-Rb Data

Bond	R_i / Å	v_i
Rb-O1	3.06(1)	0.112
Rb-O2	2.919(9)	0.163
Rb-O3	3.23(1)	0.071
Rb-O4	3.154(9)	0.087
Rb-O4	3.35(1)	0.051
Rb-O4	3.93(1)	0.011
Rb-O4	3.97(1)	0.01
Rb-O4	4.01(1)	0.009
Rb-O5	3.70(1)	0.02
Rb-O5	3.79(1)	0.016
Rb-Ow	2.99(1)	0.135
Rb-Ow	2.96(1)	0.146
Rb-Ow	3.33(1)	0.054
Rb-Ow	3.04(1)	0.118
	V =	**1.003**

Bond	R_i / Å	v_i
P1-O1	1.531(7)	1.262
P1-O3	1.525(8)	1.282
P1-O4	1.454(7)	1.554
P1-O5	1.656(8)	0.9
	V =	**4.998**

Bond	R_i / Å	v_i
P2-O2	1.517(7)	1.31
P2-O2	1.517(7)	1.31
P2-O5	1.516(9)	1.314
P2-O5	1.516(9)	1.314
	V =	**5.248**

Bond	R_i / Å	v_i
Al-O1	1.847(5)	0.541
Al-O1	1.847(5)	0.541
Al-O2	1.913(6)	0.453
Al-O2	1.913(6)	0.453
Al-O3	1.853(6)	0.533
Al-O3	1.853(6)	0.533
	V =	**3.054**

A.4.3 AlTP-Cs Data

Bond	R_i / Å	v_i
Cs-O1	3.32(2)	0.091
Cs-O2	3.00(2)	0.216
Cs-O3	3.57(2)	0.046
Cs-O4	3.57(2)	0.046
Cs-O4	3.83(2)	0.023
Cs-O4	3.63(2)	0.039
Cs-O4	3.41(2)	0.071
Cs-O4	4.25(2)	0.007
Cs-O5	3.61(2)	0.041
Cs-O5	3.60(2)	0.043
Cs-Ow	3.27(2)	0.104
Cs-Ow	3.07(2)	0.179
Cs-Ow	3.20(2)	0.126
Cs-Ow	3.17(2)	0.136
	V =	**1.168**

Bond	R_i / Å	v_i
P1-O1	1.35(2)	2.058
P1-O3	1.55(2)	1.199
P1-O4	1.56(1)	1.167
P1-O5	1.62(2)	0.992
	V =	**5.416**

Bond	R_i / Å	v_i
P2-O2	1.60(1)	1.047
P2-O2	1.60(1)	1.047
P2-O5	1.56(1)	1.167
P2-O5	1.56(1)	1.167
	V =	**4.428**

Bond	R_i / Å	v_i
Al-O1	1.95(1)	0.446
Al-O1	1.95(1)	0.4146
Al-O2	1.86(1)	0.568
Al-O2	1.86(1)	0.568
Al-O3	1.93(1)	0.470
Al-O3	1.93(1)	0.470
	V =	**2.97**

References

1. I. D. Brown, *Acta Crystallogr.*, 1977, **B33**, 1305.

Appendix 5: AlTP-Cu EDX Data

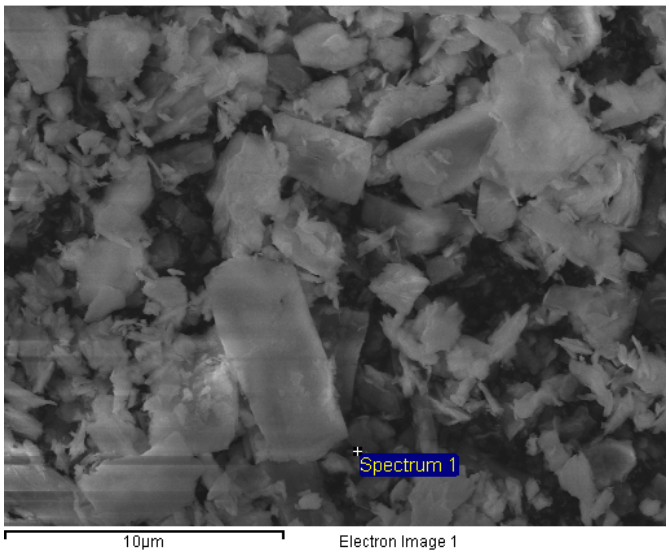

Element	Weight %	Molar Ratio	Composition Ratio
Al	6.61	0.245	1
Cu	17.55	0.276	1.13
P	21.46	0.549	2.24
O	54.38	3.399	13.87

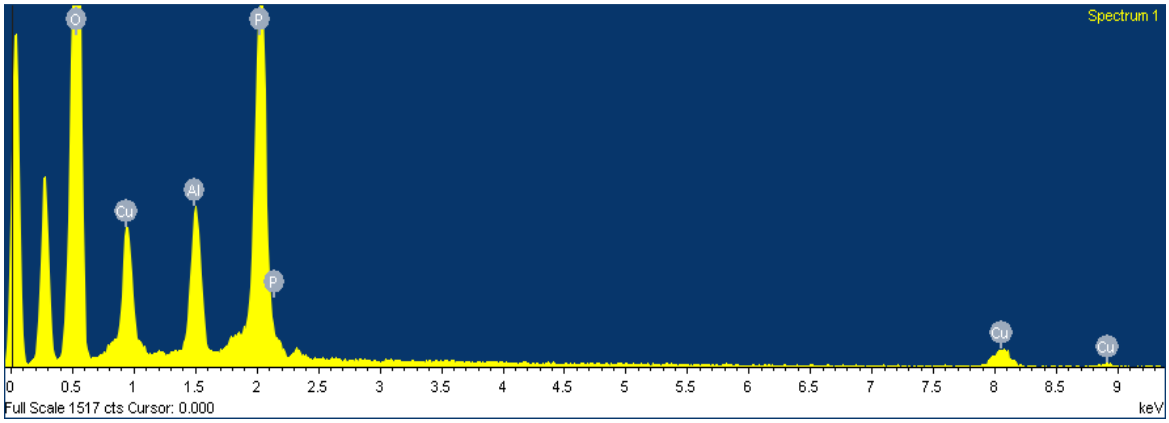

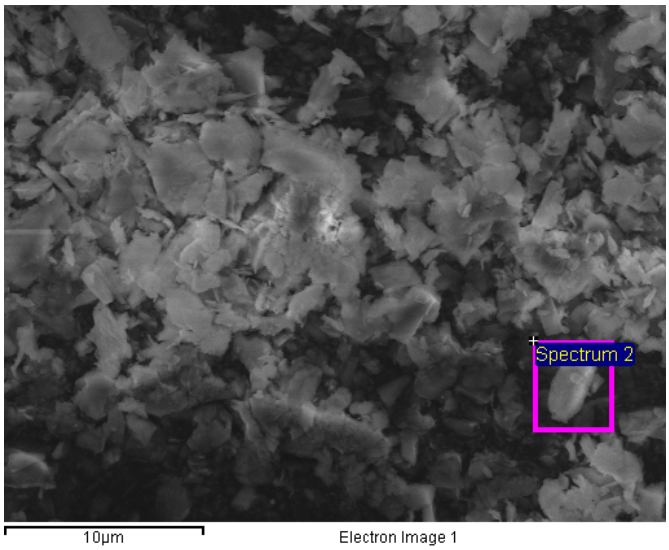

Element	Weight %	Molar Ratio	Composition Ratio
Al	6.19	0.229	1
Cu	19.87	0.313	1.37
P	19.09	0.488	2.13
O	54.85	3.428	14.97

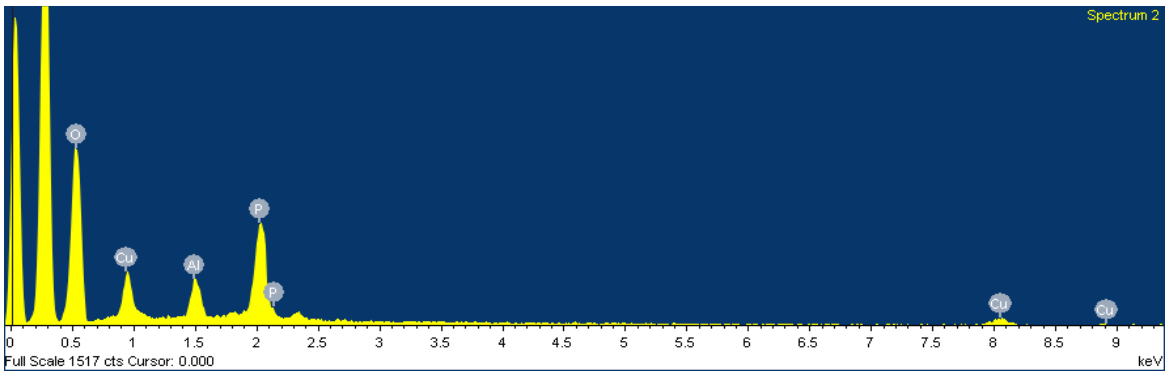

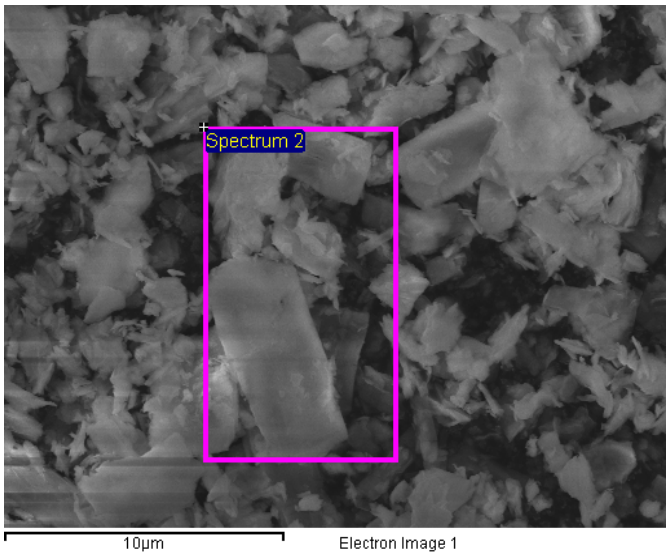

Element	Weight %	Molar Ratio	Composition Ratio
Al	6.71	0.249	1
Cu	18.71	0.294	1.13
P	23.02	0.589	2.37
O	51.56	3.223	12.94

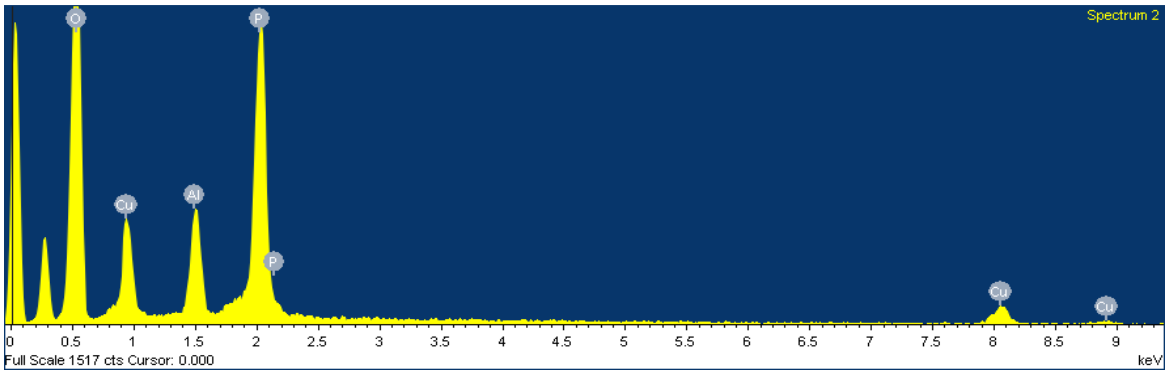

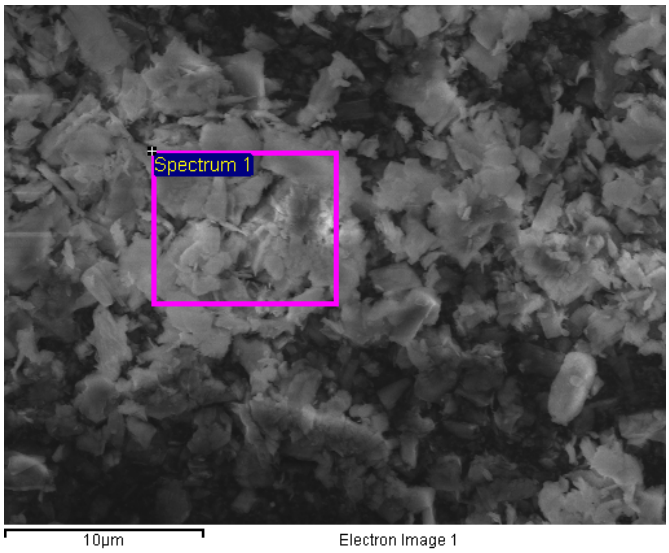

Element	Weight %	Molar Ratio	Composition Ratio
Al	6.5	0.241	1
Cu	20.9	0.321	1.33
P	23.98	0.613	2.54
O	49.12	3.07	12.74

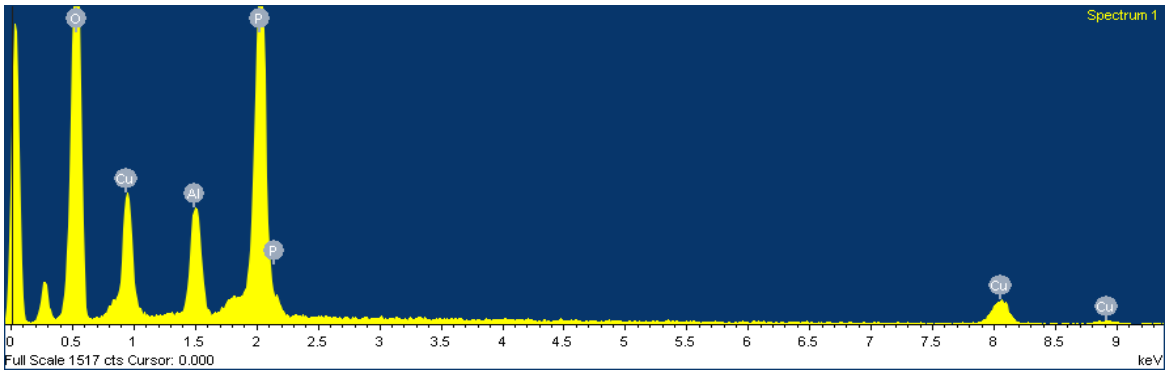

Appendix 6: HCN Elemental Analysis Data

A6.1 AlTP Data

Intercalated Amine	% C	% H	% N	C:N:H ratio	C:N:H ratio in amine	% C for full exchange	% exchange
Butylamine	21.57	5.63	6.49	4:1:12	4:1:11	22.44	96.12
Hexylamine	28.52	6.43	5.84	6:1:15	6:1:15	29.76	95.83
Dipropylamine	16.50	4.07	4.21	5:1:14	6:1:15	29.76	55.44
Dibutylamine	18.59	4.15	2.74	8:1:21	8:1:19	35.56	52.27
Tripropylamine	16.16	4.19	3.02	6:1:18	6:1:15	36.74	43.98
Tributylamine	18.68	4.68	3.04	8:1:21	8:1:19	44.17	48.45
6-AHA	19.07	4.52	3.76	6:1:16	6:1:13	26.48	72.01

A6.2 AlTP-Ag Data

Intercalated Amine	% C	% H	% N	C:N:H ratio	C:N:H ratio in amine	% C for full exchange	% exchange
Butylamine	15.0	3.66	4.26	4:1:12	4:1:11	14.97	100.2
Heptylamine	24.20	5.25	4.05	7:1:19	7:1:18	23.16	104.49
Butylanethiol	12.97	2.98	0	4:0:11	4:0:10	14.21	91.27
Hexanethiol	17.99	3.54	0	6:0:14	6:0:14	19.68	91.41
Cysteine	9.61	1.39	4.00	3:1:5	3:1:7	9.77	98.36